Preclinical pharmacokinetics and cerebral distribution of D-enantiomeric peptides for the treatment of Alzheimer's disease

Inaugural-Dissertation

zur Erlangung des Doktorgrades

der Mathematisch-Naturwissenschaftlichen Fakultät

der Heinrich-Heine-Universität Düsseldorf

vorgelegt von

Nan Jiang

aus China

Düsseldorf 2015

Aus dem Institut für Physikalische Biologie

der Heinrich-Heine-Universität Düsseldorf

Gedruckt mit der Genehmigung der Mathematisch-Naturwissenschaftlichen Fakultät der Heinrich-Heine-Universität Düsseldorf

Referent: Prof. Dr. Dieter Willbold

Korreferent: Prof. med. Dr. Karl-Josef Langen

Prüfer: Prof. Dr. Siegline Ott

Prof. Dr. Christine Rose

Prof. Dr. Eckhard Lammert

Vorsitzender der Prüfung: Prof. Dr. Peter Kern

Abgabedatum: September 16, 2015

Tag der mündlichen Prüfung: Dezember 15, 2015

Declaration

I hereby declare, on oath, that I have authored this thesis independently and without any undue assistance by third parties under consideration of the 'Principles for the Safeguarding of Good Scientific Practice at Heinrich Heine University Düsseldorf'". I have used no sources other than those quoted and the literatures I have used have been clearly cited in the text. Neither this, nor a similar work, has been published or presented to an examination committee.

Jülich,

Nan Jiang

Either I will find a way, or I will make one.

- Sir Philip Sidney

Acknowledgement

Firstly, I would like to use this opportunity to express my sincere gratitude to my boss, Prof. Dr. Dieter Willbold, not only for your support, motivation and patience throughout my doctoral study, but also for your great passion for science, your way of goal-orientated thinking and doing, as well as your immense knowledge covering a broad range of different research fields that impress me greatly and also shape my future. I thank you for offering me real freedom to do research that I could hardly believe to expect elsewhere. I specially appreciate those hard but pleasant discussions with you which guide and enlighten me a lot.

The next person I would mostly show my appreciation to, is my supervisor Dr. Antje Willuweit. Besides your guidance in my research and writing this thesis, I could not imagine how can I go through those dark times without your support and encourage. I sincerely thank you for those private talks and Emails, as well as you sharing your experience with me.

Then to my amazing supervisors in US: Prof. Dr. Thomas van Groen and Prof. Dr. Inga Kadish. I must say that it was really a great time with you at the sweet home Alabama.

Special thanks also to my second supervisor and referee Prof. med. Dr. Karl-Josef Langen, Prof. Dr. Jon. N. Shah, Prof. Dr. Jörg Breitkreutz as well as many other colleagues and friends in Forschungszentrum Jülich and Düsseldorf University.

Finally, I thank my parents, my wife, my little son and all my good friends in China. Thanks for your love, support and understanding.

Abbreviations

AD	Alzheimer's disease
%ID	Relative injected dose
ADDLs	Aβ-derived diffusible ligands
ADME	Absorption, distribution, metabolism and excretion
AGP	α_1-acid glycoprotein
APOE	Apolipoprotein
APP	Amyloid β precursor protein
ARM	Arginine-rich motif
AUC	Area under the concentration-time curve
AUMC	Area under the moment curve
Aβ	Amyloid β
BACE1	β-site APP cleaving enzyme-1
BBB	Blood-brain barrier
BCB	Blood-cerebrospinal fluid barrier
C	Concentration
CA	Cornu Ammonis
Cl	Clearance
CNS	Central nervous system
CPPs	Cell-penetrating peptides
CSF	Cerebrospinal fluid
CTF	Carboxy-terminal fragment
D	Dose
dpm	Disintegrations per minute
EC	Entorhinal cortex
ER	Endoplasmic reticulum
F	Bioavailability
FAD	Familial AD
FAM	5(6)-carboxyfluorescein
FITC	Fluorescein isothiocyanate
f_u	Unbound fraction
HIV	Human immunodeficiency virus
HSA	Human serum albumin
i.m.	Intramuscular
i.p.	Intraperitoneal
i.v.	Intravenoud
IC	Intermediate compartment
inf	Infinity
LC	Liquid chromatography
LPP	Lateral perforant pathway
MAPT	Microtubule-associated protein tau
MAT	Mean absorption time
MPP	Medial perforant pathway
MRT	Magnetic resonance tomography
MRT	Mean residence time
MS	Mass spectrometry
MW	Molecular weight
n.i.v.	Non-intravenous
NCA	Noncompartmental analysis
NEP	Neprilysin
NMDA	N-methyl-D-aspartic acid
NSAIDs	Nonsteroidal anti-inflammatory drugs
p.o.	Oral delivery
PBPK	Physiologically based pharmacokinetic
PET	Positron emission tomography
PK	Pharmacokinetics
PSEN	Presenilin
QWBA	Quantitative whole-body autoradiography
r^2	Correlation coefficient
RIP	Regulated intramembrane proteolysis
ROS	Reactive oxygen species
s.c.	Subcutaneous
SAD	Sporadic AD
scFvs	Single-chain variable fragments
SPECT	Single photon emission computed tomography
$t_{1/2}$	Terminal half-life
Tat	Trans-activator of transcription
TLC	Thin layer chromatography
V_{ss}	Distribution volume in steady state
V_z	Terminal distribution volume
WHO	World health organisation
λ_z	Terminal elimination rate constant

Table of Contents

I List of Figures

II List of Tables

1 Introduction

People around the world are expected to live longer. Due to great improvement in diet and lifestyle, as well as access to medical care, the global average life expectancy raised from 48 years in 1950 to 71 years in 2013 [1], in high-income countries like Germany, it is even 81 years. From another point of view, however, the average age of populations around the world is rapidly increasing. By 2050, 2 billion people will be aged 60 and older, which would be 22% of the world population (source: World Health Statistics 2015, WHO) that having high risk to develop neurodegenerative disorders, such as Parkinson's disease, Huntington disease and Alzheimer's disease.

1.1 Alzheimer's disease

On November 25, 1901, a 51-year-old woman, Auguste Deter, was admitted to a Frankfurt asylum, where she was examined by German psychiatrist and neuropathologist Alois Alzheimer (Fig. 1 A and B). She was suffering of disorientation, impaired memory, and troubles in reading and writing. Progressive symptoms like hallucinations and mental function disorders were developed later. After she died in 1906, Alzheimer presented a preliminary report based on her clinical and neuropathological features at a meeting of the South-West German Society of Alienists in Tübingen. He described it as "a peculiar disease of the cerebral cortex" and noted two abnormalities in the brain: neurofibrillary tangles and amyloid plaques (Fig. 1 C and D). On September 12, 1907, Alzheimer received a 56-year-old man, Johann F., who suffered from dementia and died three years later. Because these two cases showed similar changes in brain autopsy, Emil Kraepelin, a colleague of him and the most important German psychiatrist of that time, named this brain disorder after him as "Alzheimer's disease" [2-5].

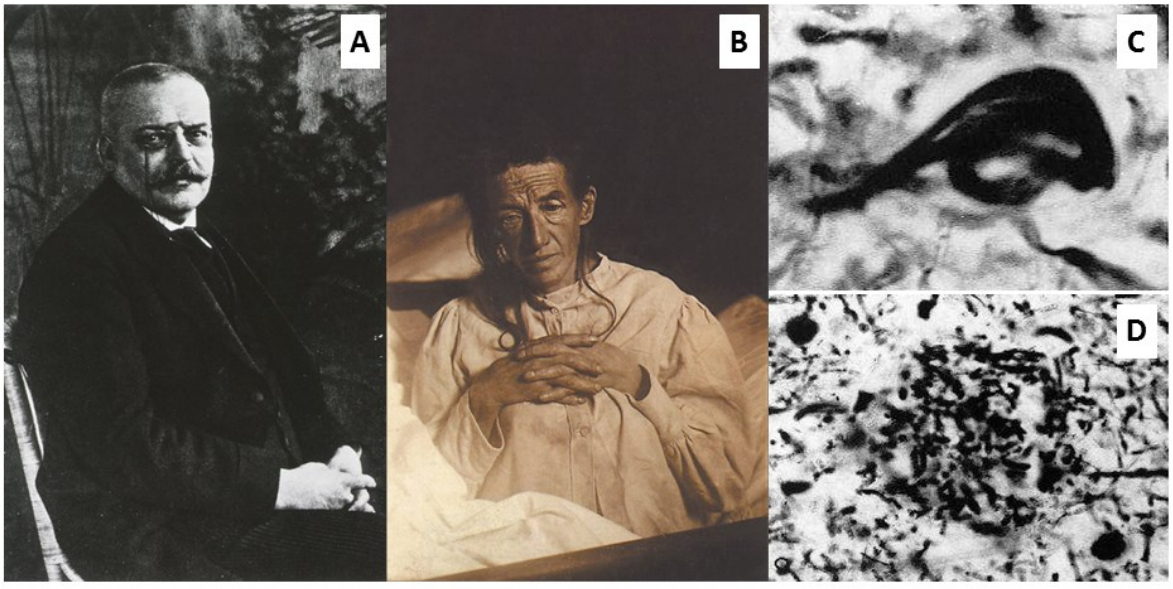

Fig. 1.The portraits of A) Alois Alzheimer (source: U.S. National Library of Medicine, History of Medicine Division), B) Auguste Deter (source: upload.wikimedia.org/wikipedia/commons/1/1d/

Auguste_D_aus_Marktbreit. jpg), C) A neurofibrillary tangle and D) Amyloid plaques in Bielschowsky (silver) stained tissue sections from the cerebral cortex of Auguste Deter (Images C and D are from the publication of Graeber et al. 1998 [6]).

Alois Alzheimer believed he had discovered a new but rare dementia occurring in the "presenile" period, because the first patient was 51 years old and the second was 56. However, the Alzheimer's cases accumulated rapidly over time and the "Alzheimer changes" (amyloid plaques and neurofibrillary tangles) in cerebral grey matter were also described in demented people of advanced age, which was then defined as senile dementia of the Alzheimer type [7].

Nowadays, Alzheimer's disease (AD) has become the most common cause of dementia (estimated 60-80% of cases) [8]. Clinical symptoms differ in different progressive stages. Major indications include loss of memory, inability to learn new things, hallucinations and delusions, loss of language function, deranged perception of space, depression, impulsive behaviour and many other signs [9]. Alzheimer's patients may survive 4 to 8 years on average after diagnosis and usually die of complications of chronic illness such as pneumonia [10]. According to the report 'Alzheimer's Disease 2015 Facts and Figures', between 2000 and 2012, the number of deaths from AD increased by 69%, which is more than that of breast cancer and prostate cancer combined. In the United States, AD is the 6th leading cause of death and the 5th leading cause of death for people over 65 years old (source: National Center for Health Statistics of the Centers for Disease Control and Prevention). While deaths from other major diseases like heart disease, cancer and HIV decreased, deaths from AD increased by 71% from 2000 to 2013 [11-13]. It is the only cause of death among the top 10 in America that cannot be prevented, cured, or even slowed. In 2015, about 700,000 people estimated will die with AD [14, 15]. Not only the person diagnosed Alzheimer's, but also their family members and caregivers suffer this devastating chronic disease [16, 17]. The psychological burden and economic impact of AD raise great issues to society and politics [18, 19].

1.1.1 Pathology

Macroscopic appearance may not distinguish a brain with AD from that of an age-matched elderly brain with normal cognitive function, especially in advanced age. But presenile AD brains (before 65-year-old) show obvious difference with age-matched controls, when comparing the brain weight or the atrophy of cerebral cortex [20]. Generally, AD brain shows extreme shrinkage in cortical region and hippocampus, as well as symmetrical enlargement of lateral ventricles (Fig. 2).

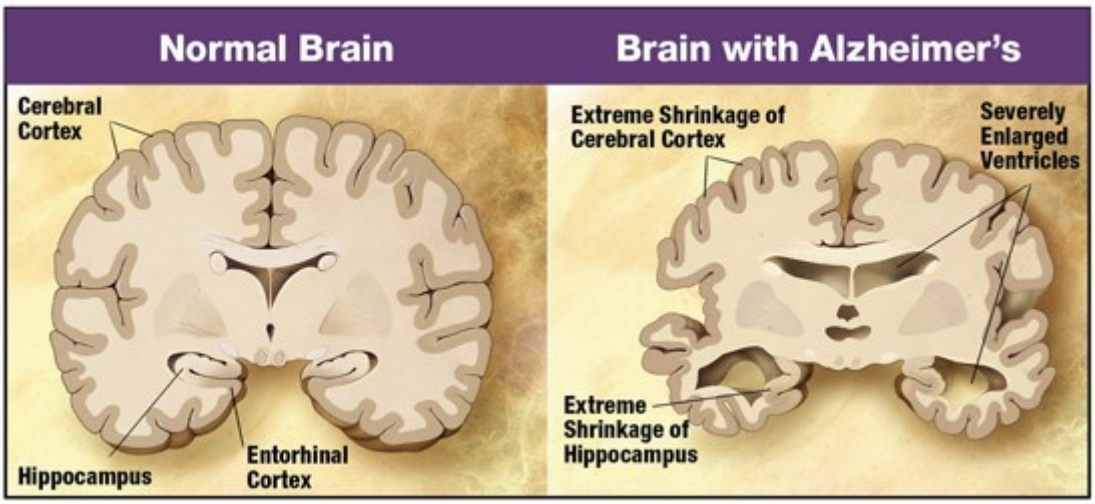

Fig.2. Diagram of a normal brain (left) and a brain with Alzheimer's Disease (right) (source: http://www.cpmedical.net/images/Brain-w550.jpg).

Under microscopic observation, AD can be more easily identified by histopathological features. The hallmark pathologies are the abnormal accumulation of neuritic plaques (the difference with amyloid plaque is explained below) and neurofibrillary tangles. Other neuropathological changes are for examples, cerebral amyloid angiopathy, astrogliosis, microglial cell activation, and neuronal and synaptic loss.

The neurofibrillary tangle consists of abnormally phosphorylated, twisted filaments of the microtubule-associated protein tau within the neural cells. Tau is an abundant protein in both central and peripheral nervous systems. In normal brain it is concentrated in axons, while in AD brain, it is found in nerve cell bodies, axons and dendrites in a hyperphosphorylated state [21, 22].

The other pathological significance in Alzheimer's brain with diagnostic meaning are extracellular neuritic plaques, which are composed primarily of 39- to 42-residue peptides, referred to as amyloid beta (Aβ). Neuritic plaques are defined by dystrophic neurites within or around Aβ deposits, and are characterized by local synapse loss and glial activation [23], thus it should not be confused with amyloid deposits [24]. The term "amyloid" was originally brought by the German botanist Matthias Schleiden in 1840's in botany [25], then later was introduced by the German physician Rudolph Virchow in 1854 to describe the polyglucosan bodies (corpora amylacea) in human being [26, 27]. He used iodine-sulphuric acid reaction [28] as a stain for glycogen-like substance in the human body [29]. Due to the limitation of scientific methodology and medical knowledge at that time, he concluded this structure contained cellulose and gave this iodine-stain-positive macroscopic abnormality the name "amyloid", derived from the Latin "amylum" and the Greek "amylon", meaning "starch-like" [30]. Here, the conception of starch, cellulose and glycogen, as well as the reaction mechanism of iodine test were misused and misunderstood. In 1859 Friedreich and Kekulé directly analysed amyloid-rich samples from the spleen of a patient with we now define

amyloidosis. They demonstrated the absence of carbohydrate and high nitrogen content in amyloid sample, suggesting amyloid consisted of protein [31].

In 1922 the young German chemist Herman Bennhold discovered the high affinity of Congo red to amyloid [32]. 5 years later, Divry and Florkin established the first diagnostic criterion of amyloidosis, namely Congo red stained amyloid showing apple-green birefringence under a polarizing optical microscope [33] (Fig. 3).

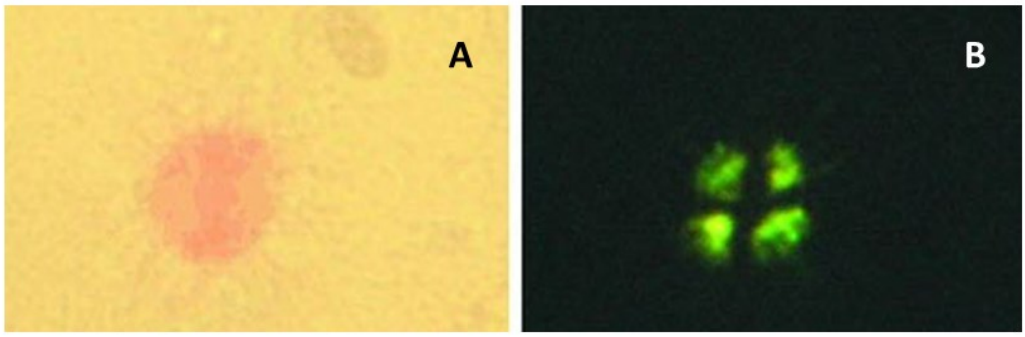

Fig. 3. Congo red stained amyloid plaque in linearly polarized white light (A) and between crossed polarizers showing apple-green birefringence (B). (Images A and B are from the publication of Jin L-W et al. 2003 [34]. Modified.).

The optical birefringence found in Congo red stained amyloid suggested that Congo red dye might intercalate in an ordered arrangement. This discovery led to more interests to investigate the ultrastructure of amyloid, which was initially considered as structurally amorphous [35]. Later studies identified that amyloid forms fibrils assembled through cross-β-sheet conformation which build up amyloid plaques [36]. The plaques also contain small amount of glycogen such as sulphated glycosaminoglycans [37] and heparan sulfate proteoglycan [38], thus explaining the congophilic as well as the iodine-stain positive characters of amyloid.

The neuropathological changes in different AD brain areas influence the regional brain function, resulting in corresponding clinical signs and symptoms of cognitive and behavioural changes when the neuropathological damages accumulate to certain extent. For example when hippocampus is affected, AD patients normally suffer from memory loss and disorientation [39, 40]. As a progressive disease, many efforts were made to retro-track the distribution of neuropathological changes of AD based on its clinical progression. In 1991, the German neuroanatomist Heiko Braak proposed a sequence of progression of the neuropathology of AD by mapping out the extent and distribution of lesions in 83 brain specimens, which is now called the Braak staging [41]. He described the spatiotemporal pattern of AD progression initially from areas of the transentorhinal region, then to the limbic system and in the final stage to the neocortex and occipital cortex (Fig. 4).

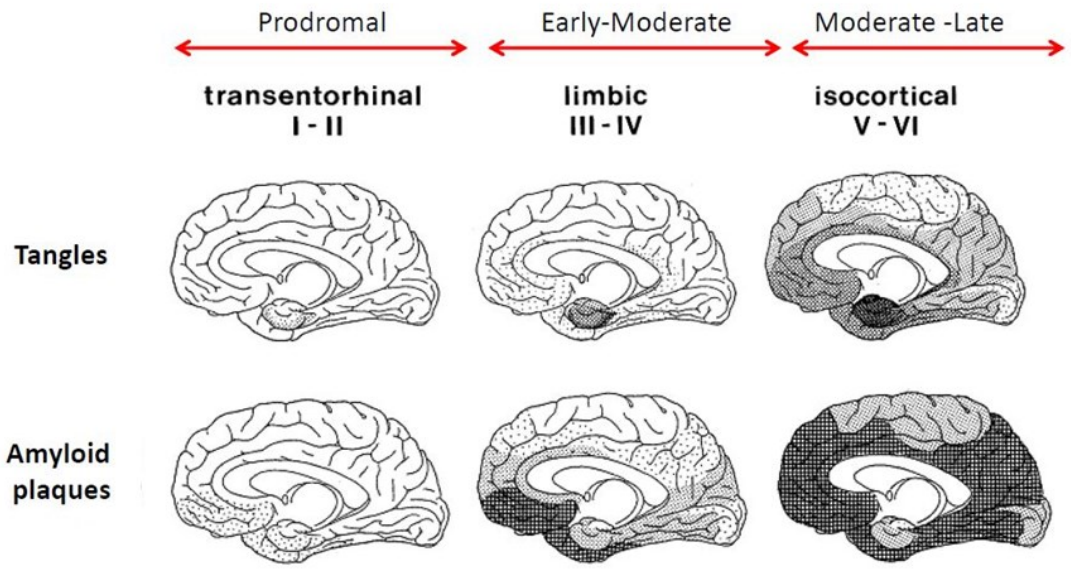

Fig. 4. Distribution of amyloid plaque and neurofibrillary tangles at different stages of Alzheimer's disease progression (Braak staging).
(source: http://www.iom.edu~media353F303C759D406C8B893618DF9260F7.ashx. Modified.)

Later the Braak staging was modified [42, 43], and also validated in animal models of AD [44, 45]. It provides a useful summary of Alzheimer's disease neuropathology and also reveals that the damages ascend progressively from the lower limbic regions to the higher brain centres [46], suggesting the function of neural circuits and pathways in spreading the AD pathology in brain (see Chapter 1.2).

1.1.2 APP, Aβ and amyloid cascade hypothesis

Aβ is a sequential proteolytic product of the amyloid β (A4) precursor protein (APP). APP is a type I transmembrane glycoprotein with a large extracellular domain containing N-terminus and a much smaller intracellular domain containing C-terminus [47, 48]. It has three principal isoforms of 695, 751, and 770 residues derived by alternative splicing. Among them the 695 residue isoform is expressed at very high level in neurons [23, 49]. The gene coding APP is highly conserved during evolution. In human it locates on chromosome 21 [47, 50]. Full-length APP and its proteolytic fragments have important functions in diverse biological and pathological processes such as axonal transport, cell adhesion, cholesterol metabolism and gene transcription [51].

APP can be processed by several proteolytic pathways involving α-, β- and γ-secretases [52] (Fig. 5). In the amyloidogenic pathway producing Aβ, the β-secretase firstly sheds a large part of the ectodomain of APP and generates an APP carboxy-terminal fragment (CTF or C99). After prior shedding, the γ-secretase cleaves consecutively the remaining small transmembrane part in the hydrophobic intramembrane at multiple sites, referring to as gamma-, zeta-, and epsilon-cleavages [52-54]. Before the release of the Aβ isoforms, a

stepwise cleavage of the APP CTF on these sites by γ-secretase is suggested, resulting in two distinct product lines. The major product line is Aβ49-Aβ46-Aβ43-Aβ40-Aβ37 from which the Aβ isoform with 40 amino acid residues, Aβ40, is the major end product, while the minor line is Aβ48-Aβ45-Aβ42-Aβ38 producing the pathogenic Aβ42 [54-56]. Thus, the γ-secretase generates predominately Aβ40 and 42 in the amyloidogenic pathway, namely 28 amino acids of the ectodomain and 12 or 14 amino acids of the transmembrane domain [57, 58].

In another proteolytic pathway involving α- and γ-secretase, APP is shedded by the α-secretase approximately in the middle of the Aβ domain and ultimately produces a truncated Aβ peptide called p3 [59]. p3 is irrelevant to the AD pathology and thus this pathway is called anti-amyloidogenic pathway.

Shorter and longer Aβ isoforms have been recently identified in cells and brain tissue [54, 60]. Studies show Aβ1-14, Aβ1-15, and Aβ1-16 are produced through catabolic pathway by β- followed by α-secretase [61], while all isoforms longer than and including Aβ1-17 were γ-secretase dependent [62]. The function of these isoforms is still under investigation.

Recently, another secretase has been reported as η-secretase by Michael Willem et al [63]. The CTF from this secretase cleavage can inhibit neuronal activity within the hippocampus.

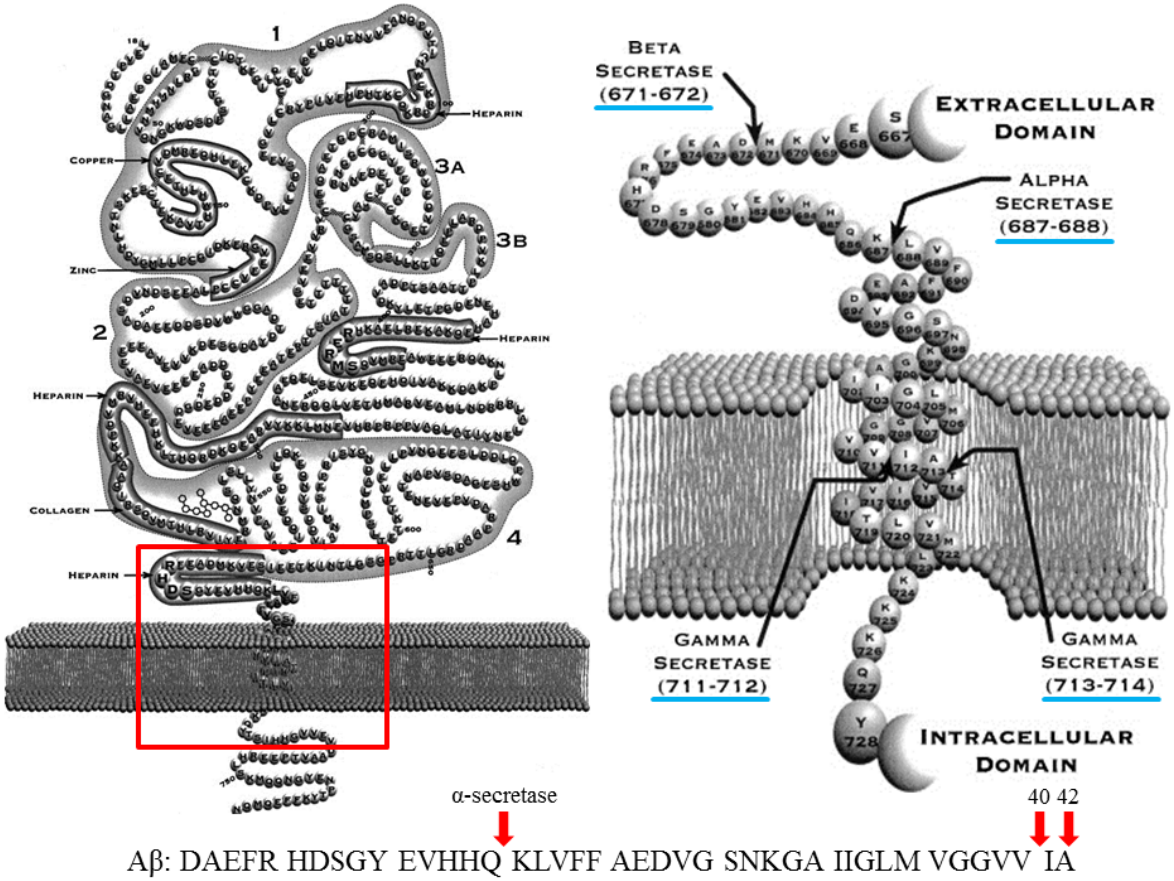

Fig. 5. Schematic representation of APP (left), enlarged view of red frame showing the membrane spanning and cleavage sites of secretases (right) and Aβ sequence. Modified from original figures in the publication of Turner et al. 2003 [51].

The processing of APP is now termed as regulated intramembrane proteolysis (RIP), which is found associated with many other membrane proteins [64-66]. The β-Secretase, or β-site APP cleaving enzyme-1 (BACE1) is more abundant in neurons [67, 68], so that the amyloidogenic processing of APP is dominant in nervous system, whereas the anti-amyloidogenic pathway is predominant elsewhere [69]. As APP is expressed ubiquitously, this helps to explain why brain is the most affected organ by Alzheimer's disease [53, 70].

The reason why γ-secretase has "sloppy" cleavage site is still unclear. Recent studies showed the cleavage of γ-secretase produces Aβ42 in the endoplasmic reticulum/intermediate compartment (ER/IC), while Aβ40 is produced in the trans-Golgi network and other cytoplasmic organelles. Based on the organelle-specific generation of different Aβ isoforms by γ-secretase, intracellular ER/IC-generated Aβ42 and secreted Aβ40 are supposed to be produced by different γ-secretases [71, 72].

Under non-pathogenic conditions, Aβ40 constitutes approximately 90% of total Aβ in human cerebrospinal fluid [72] and is the most abundant in the brain [73]. Aβ42 is much more prone to aggregation and more toxic to neurons than Aβ40, even though they differ from each other only by two residues [74, 75]. For a long time, it was thought that the Aβ plaques were toxic to neurons. However, recent studies have identified that the soluble Aβ oligomers, for example protofibrils, Aβ*56 (a dodecamer), annular assemblies and Aβ-derived diffusible ligands (ADDLs), are the key neurotoxic species in disrupting plasticity mechanisms and causing memory impairment [76-82], resulting in more studies concentrate on the aggregation states of those two predominant Aβ isoforms. They both form protofibrils and mature into fibrils, but recent studies show the difference in the initial phase of oligomerization due to the amino acids at position 41 and 42 [83]. Aβ40 exists as monomer, dimer, trimer and tetramer, while Aβ42 preferentially forms pentamer/hexamer units (paranuclei) (Fig. 6). The distinct behaviour between Aβ42 and Aβ40 in monomer oligomerization may explain their clinical, biological, and biophysical difference.

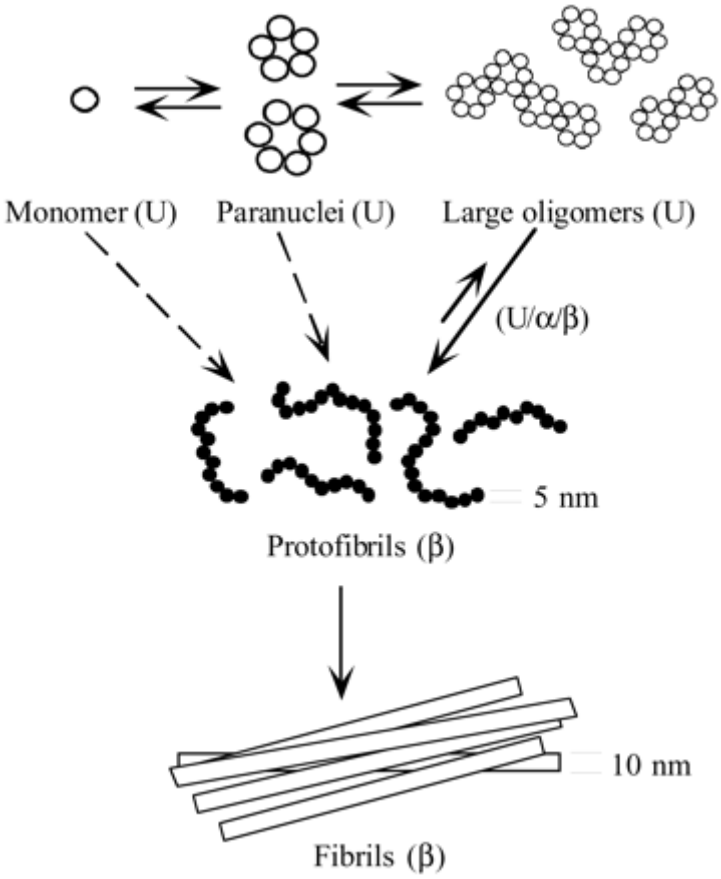

Fig. 6. A simple model of Aβ42 assembly. Monomers rapidly oligomerize into paranuclei, and then oligomerize to form larger, beaded structures. Monomers, paranuclei and large oligomers are predominately unstructured (U), but contain β-sheet/β-turn (β) and helical (α) elements. Protofibrils maturate to fibrils which seems to be a kinetically irreversible process. (The figure is from the publication of Bitan et al. 2003 [83].)

Based on pathological, biochemical and genetic findings, Selkoe established in 1991 a dynamic model to propose a rough temporal sequence of pathogenetic events of Alzheimer's disease (Fig. 7), which was later called the amyloid cascade hypothesis [84]. He concluded β-amyloidosis acts in initiating a chronic, multicellular degenerative response in selected brain regions of AD brain.

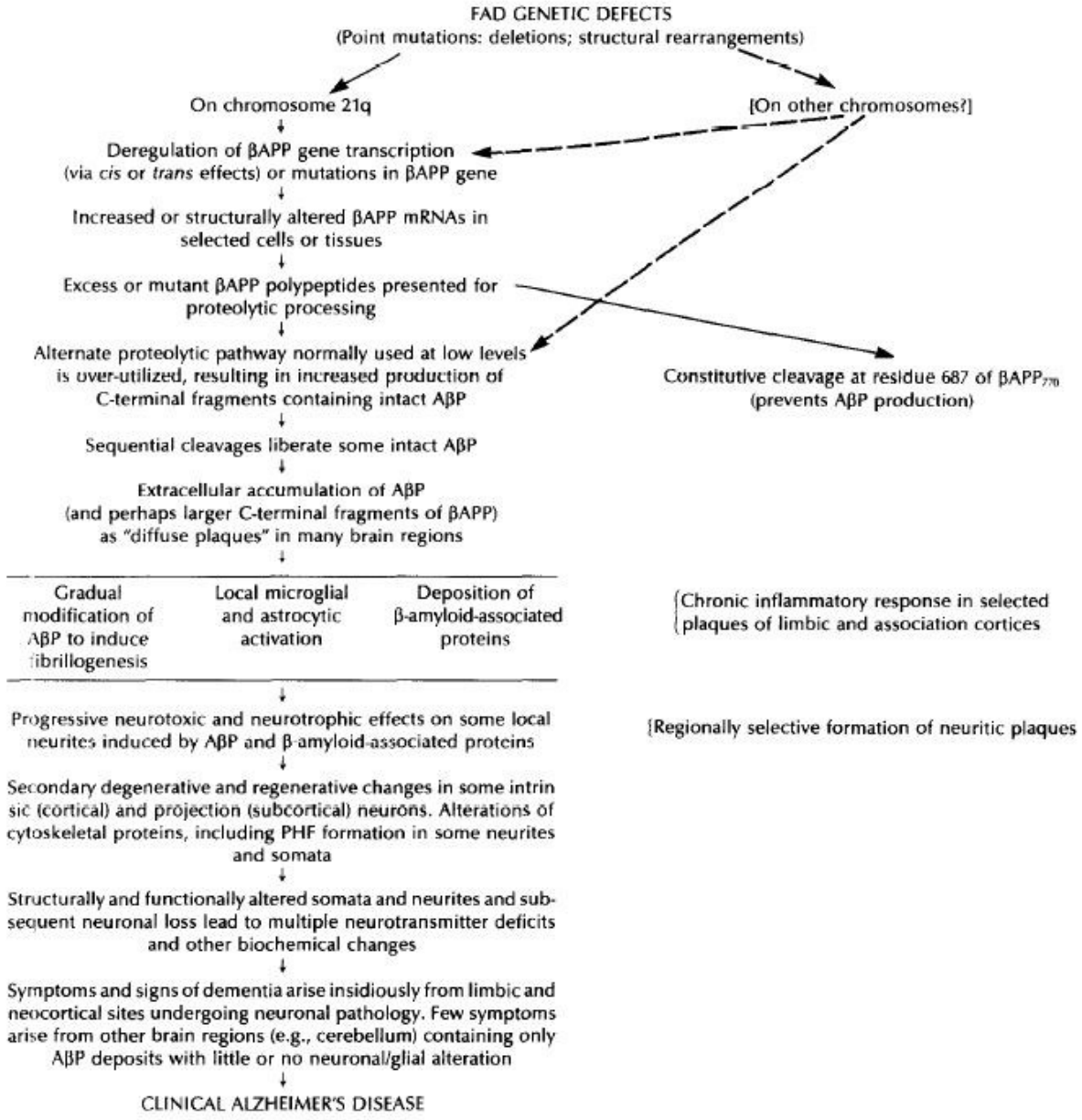

Fig. 7. Hypothetical model of the pathogenesis of familial forms of Alzheimer's disease based on currently available information. (The figure is from the publication of Selkoe 1991 [84].)

Over the past twenty years, the amyloid cascade hypothesis has been modified several times, as change from Aβ deposition dependent neuronal dysfunction to Aβ accumulation related (Fig. 8). Or in another word, to replace "amyloid hypothesis of Alzheimer's disease" with "Aβ hypothesis of Alzheimer's disease", because Aβ incorporates all the possible aggregated forms [85].

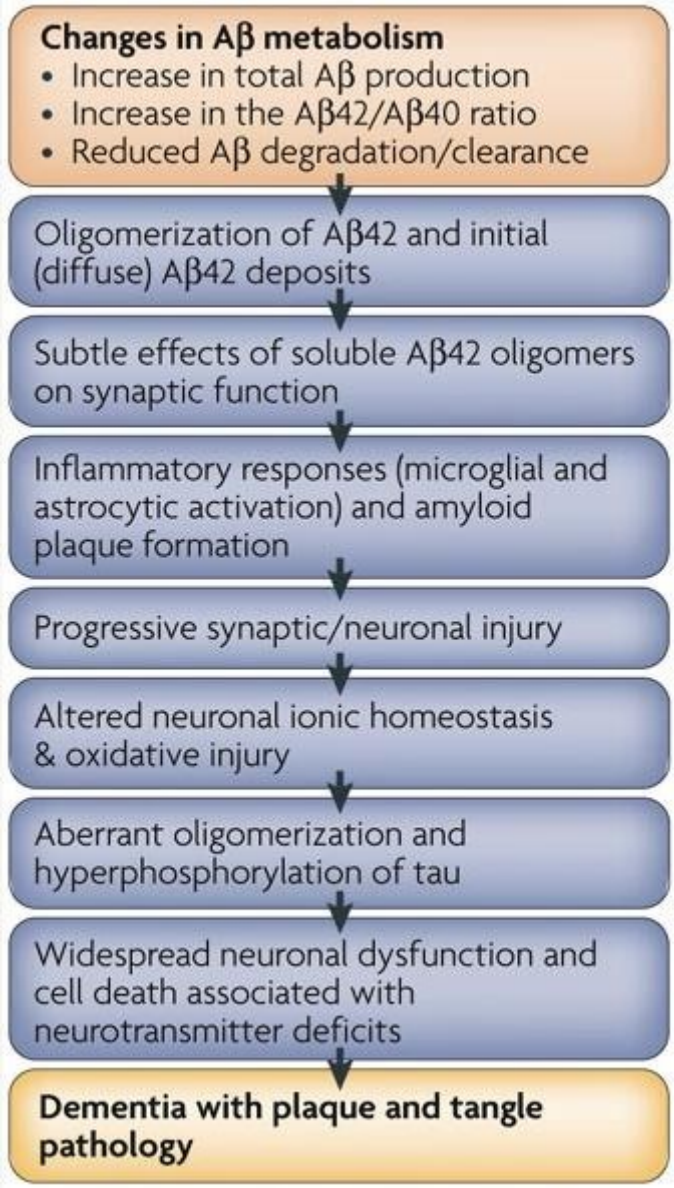

Fig. 8. Recently modified amyloid cascade hypothesis. (The figure is from the publication of Selkoe 2000 [85].)

The Aβ oligomers are toxic to neurons by a variety of mechanisms, for example, they cause lesions to plasma and intracellular membranes by a combination of radical-initiated lipid peroxidation through reactive oxygen species (ROS) [86] and formation of ion-permeable pores which causes an influx of Ca^{2+} into neurons and loss of calcium homeostasis [87, 88]. They also cause dysfunction of synapses through hyperphosphorylation of the tau protein, which interrupts the microtubule-supporting role of tau to maintain the axon structure, and ultimately leads to the death of neurons [89].

Expression of APP as well as production of Aβ can be found ubiquitously in the body [90, 91], suggesting they are part of biological processes. Aβ peptides are naturally present in nanomolar concentrations as circulating soluble monomers in the cerebrospinal fluid and blood of healthy individuals [92], which is much lower than the concentrations (in micomolar) used in in vitro and in vivo Aβ toxicological and pathological studies [93]. Recent studies

reveal its biological functions, such as protection of cells from hypoxia [94], stimulation of cholesterol transport [95], antimicrobial effect [96] or even being important for learning and memory [97]. Therefore, Alzheimer's disease should be considered as a downstream consequence of Aβ in pathological concentration.

1.1.3 Genetics

The greatest risk factor for acquiring Alzheimer's disease is aging, while rare cases (about 5%) of AD are inherited or "familial" [98, 99]. Therefore two types of AD are defined, the non-familial or sporadic AD (SAD) and the familial AD (FAD). These two types of AD have the same clinical features, incidence of risk factors for dementia, or MRI or PET features. But unlike the SAD, FAD can develop at any age, with mean age of onset before 65 years and often before 55 [100, 101]. FAD is caused by autosomal dominant mutations in either the amyloid beta (A4) precursor protein (APP) gene on chromosome 21 (10-15% of FAD), or the presenilin 1 (PSEN1) gene on chromosomes 14 (30-70% of FAD) and presenilin 2 (PSEN2) gene on chromosomes 1 (<5% of FAD) [102-104].

In 1989 Korenberg et al. discovered the first gene associated with Alzheimer's disease, the APP gene [105]. More than 50 different mutations in the APP gene have been identified in AD patients. APP mutations are located in exons 16 and 17 around the secretase processing sites. Mutations near the β-secretase site increase general Aβ levels and mutations near the γ-secretase site specifically increase Aβ42 [106-108]. Both presenilin 1 and 2 are the proteolytic subunits of the γ-secretase complex. More than 150 PSEN1 and 11 PSEN2 gene mutations have been identified in AD patients. Abnormal presenilin 1 and 2 proteins interfere with the function of the γ-secretase complex, which alter the processing of APP and leads to the increase of Aβ42/Aβ40-ratio [66].

Especially for sporadic AD, a genetic risk factor, apolipoprotein E (APOE) ε4 allele on chromosome 19 strongly promotes amyloid-β deposition in the brain [109]. The APOE gene encodes apolipoprotein E, which is essential for the normal catabolism of triglyceride-rich lipoprotein constituents. In brain it mediates extracellular transport of cholesterol, supports amyloid aggregation and clearance of deposits from the parenchyma [110, 111]. There are three alleles of APOE gene, called ε2, ε3 and ε4, which encode the apolipoprotein E2, E3 and E4, respectively. APOE4 is significantly associated with sporadic AD, whereas E2 might protect against AD [112, 113].

In addition to the three autosomal dominant mutations and APOE ε4 allele, which clearly play an important role in amyloid pathology of AD, several other genetic risk factors have recently been described [114]. However, microtubule-associated protein tau (MAPT) gene, which is located on chromosome 17 and encodes the tau protein, is a risk factor for Parkinson's disease but no clear genetic links have been found to AD [115-117].

Identified genetic factors or risk factors may contribute to a better chance to understand the complexity of Alzheimer's disease and to develop diagnostic and therapeutic strategies

through establishing transgenic animal or cell models [118]. Especially, transgenic mouse models developed in the last decade may provide a promising tool by reflecting behavioural cognitive deficits and neuropathological damages observed in human AD patients [119, 120]. Studies on a range of AD mouse models from single transgenic to multi-transgenic have already yielded significant research breakthroughs.

Considerations should also be taken, as none of the animal models can replicate all the aspects of human AD due to phylogenetic differences and fundamental differences in behavioural ecology [121]. Besides, those animal models only reflect the familial forms of the disease.

1.1.4 Diagnosis and treatment

AD is currently diagnosed based on clinical-neuropathologic assessment, such as cognitive tests and physical and neurologic examinations, laboratory testing of body fluid biomarkers (Aβ42 or tau in CSF or blood sample) and neuroimaging (MRT and PET), with approximately 80 to 90% accuracy [122, 123]. Confirmation of diagnosis is only possible post-mortem by analysis of neuropathological hallmarks at autopsy, including microscopic neuritic plaques, neurofibrillary tangles and amyloid angiopathy, which is still regarded as the gold standard for diagnosis [124].

No treatment is available today to cure or slow the Alzheimer's disease. Current pharmacologic treatment is only supportive against some of its symptoms, such as using acetylcholinesterase inhibitor or N-methyl-D-aspartic acid (NMDA) receptor antagonists which provides short-term benefits to AD patients based on enhancement of remaining cognitive function in a dose-dependent manner [125, 126]. Non-pharmacologic therapy for example music therapy and cognitive activity also aims on maintaining or improving cognitive function, the ability to perform daily activity or quality of life [127, 128]. Recently, Leinenga et al. used scanning ultrasound to internalize Aβ into the lysosomes of activated microglia in mouse brains, which provides a completely new non-pharmacological approach to remove Aβ and restore memory function in an AD mouse model [129].

As progress is made on discovering the molecular level of AD pathology, especially based on the concept of the amyloid cascade hypothesis, several strategies targeting different AD pathogenesis steps are developed.

Aimed on the Aβ concentration in brain, strategies to reduce production and/or increase the degradation/clearance of Aβ are being intensively tested. One strategy on the APP processing level is to decrease Aβ (especially Aβ42) production through inhibiting or reducing the activity of β- or γ-secretase. But consideration should be taken, as inhibition of γ-secretase activity also affects its physiological role on Notch proteolysis [130] and causes intestinal goblet cell metaplasia [131].

Another strategy is immunotherapy through vaccination with Aβ, which showed very encouraging results in transgenic mice. Through active or passive immunization, reduction of amyloid load and reversal of memory deficits could be achieved [132-134]. However, it may cause autoimmune response as demonstrated in a phase II clinical trial, in which some

patients treated by active immunization with vaccines against human Aβ42 showed an unacceptable incidence of meningoencephalitis [135].
To upregulate the expression of amyloid-degrading enzymes, for example neprilysin (NEP) is a strategy based on the degradation and clearance of Aβ [136]. Recent studies showed its therapeutic value in animal models [137, 138].
Metal ions for example Cu^{2+} and Zn^{2+} may play an important role in the pathogenesis of AD through mediation of Aβ aggregation and toxicity, as well as production of reactive oxygen species when bound to Aβ [139, 140]. Prevention of such toxic effects by certain metal chelators is also tested in clinical trials [141]. As epidemiologic evidence showed that nonsteroidal anti-inflammatory drugs (NSAIDs) delay onset of AD, administration of anti-inflammatory drugs may be of therapeutic importance by decreasing overall neuronal dysfunction and loss [142].
Because the focus of the AD pathological research has shifted to soluble Aβ oligomers, compounds that inhibit the transition of monomeric Aβ to toxic oligomers, or eliminate the toxic oligomers are attracting special interest. An advantage of this strategy is that it only targets a purely pathological species, rather than affecting processes which may have important biological functions. A range of compounds, such as nanoparticles, small organic molecules, peptides and peptidomimetics are identified [143-145]. An inositol stereoisomer called ELND005 is in now clinical phase 2 trials (source: ClinicalTrials.gov)

1.2 Hippocampal formation and axonal transport in AD

Neuropathological hall marks of Alzheimer's disease are mostly found in the limbic and association cortices, as well as in certain subcortical nuclei that project to them [84]. The progressive dysfunction and dystrophy of neurons in the different brain regions are associated with corresponding clinical signs and symptoms as discussed above (chapter 1.1.1).

Limbic (from the Latin *limbus* for border) means an intermediate or transitional state. In brain the limbic system acts as a border between the neocortex and the subcortical structures (diencephalon) [146]. It receives input from many parts of the cerebral cortex and contains association areas where gathering various aspects of sensory experience to form a single experience [147]. It consists of the phylogenetically old limbic lobe and other subcortical structures and their connections [148], in which the hippocampal formation is mostly implicated in the early stages of Alzheimer's disease [149, 150]. The components of hippocampal formation are disputed in different literatures. From the view adopted here, it is composed of dentate gyrus, hippocampus proper, subicular complex, and entorhinal cortex [151].

The word hippocampus comes from late Latin and means “sea horse” in Greek. This folded structure is also named 'Cornu Ammonis (CA)' or 'Ammon's horn' after an early Egyptian deity *Amun* with a ram's head [152]. The hippocampus proper, or simply hippocampus, is

divided into parts CA1 to 3. Unlike 6 layers in neocortex, hippocampus consists of 3 layers, including an outer molecular layer, a middle pyramidal layer and an inner polymorphic layer. In mammals, the anatomical details and the functional role of hippocampus are remarkably conserved across species [153], thus its neurophysiological or neuropathological studies with animal models like the mouse are closely predictive for human outcomes [154].

A variety of fibre pathways or circuits connect the hippocampus with other structures (Fig. 9). In general, two parallel excitatory pathways relay information through the hippocampus:

1. The tri-synaptic pathway, in which axons from layer II/IV of the entorhinal cortex project to the granule cells of the dentate gyrus through the perforant pathway. Then axons of the dentate gyrus project to CA3 pyramidal cells via Mossy fibres. Here the axons from the ipsilateral hippocampus through the Schaffer collaterals, or from the CA3 region of contralateral hippocampus through commissural fibres join together and project to CA1 pyramidal cells.
2. The monosynaptic pathway, in which layer III/V of the entorhinal cortex directly project to the pyramidal cells of the CA1 and the subiculum through the temporoammonic pathway.

Finally, axons of CA1 and subiculum project back to layer V of the entorhinal cortex.

Due to the different origins of fibres (from the lateral or medial entorhinal cortex), the perforant pathway is divided into lateral (LPP) and medial pathway (MPP), respectively.

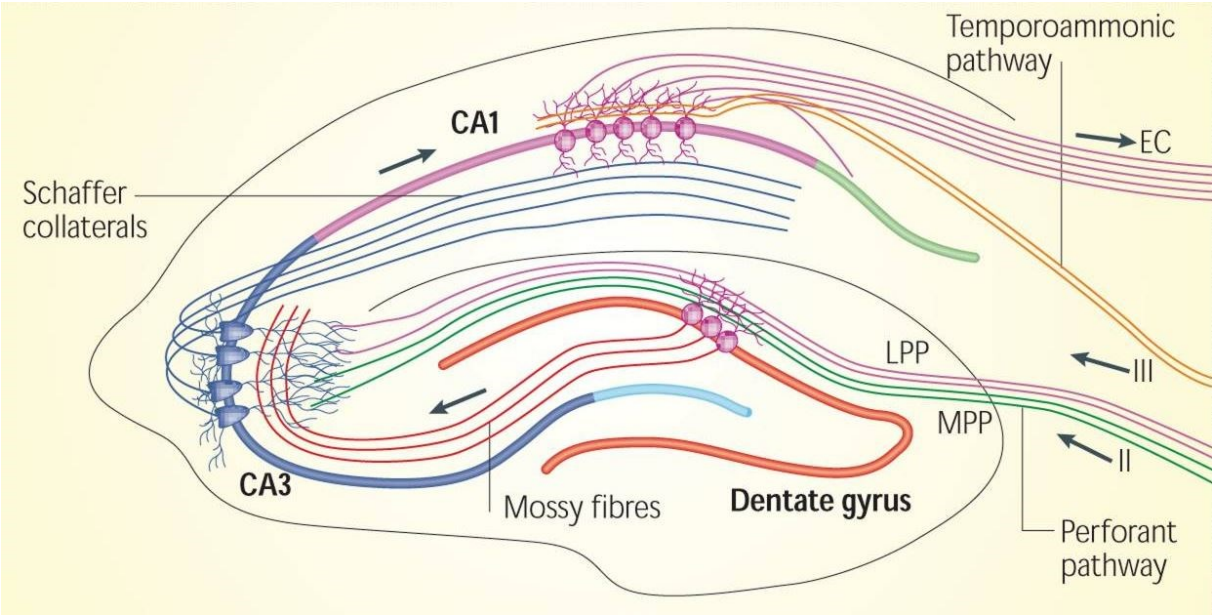

Fig. 9. The neural circuitry in the rodent hippocampal formation. Arrows show the "trisynaptic" perforant pathway. Orange lines show the "monosynaptic" temporoammonic pathway. (MPP: medial perforant pathway; LPP: lateral perforant pathway; EC: entorhinal cortex; II, III refer to layers II and III of the entorhinal cortex). The commissural fibres are not shown here. (The figure is from the publication of Deng et al. 2010 [155].)

Those projections are formed by the fibres or myelinated axons of interneurons. The axons transport a variety of substances to and from the neuron's cell body, such as proteins, lipids, synaptic vesicles, mitochondria and other organelles. The axonal transport manages intracellular informational communication and metabolic activities throughout the life and is essential to the neuron's growth and survival [156]. Two motor proteins decide direction of the axonal transport along the microtubule: the anterograde transport (from cell body to synapse) is mediated by kinesins; the retrograde transport (from synapse to cell body) is mediated by dynein [157]. Especially, endocytosis products destined for degradation are retrogradely transported to endolysosomes of the cell body [158].

In Alzheimer's disease, Aβ-deposition expands anterogradely from regions already exhibiting Aβ aggregates into regions that receive neuronal projections, following a distinct hierarchical sequence of neuropathology [159]. Lazarov et al. demonstrated in a transgenic mouse model that APP, synthesized by neurons in the entorhinal cortex, is transported via the perforant pathway to presynaptic terminals in the dentate gyrus and gives rise to local Aβ peptides which are deposited into extracellular plaques [160]. Other studies have identified the synaptic pathology, especially the altered transmission in hippocampal Schaffer collateral synapses, to be the earliest manifestation of AD pathology [161-163]. Since accumulating literature has emerged that links axonal transport deficits to synaptic dysfunction in neurodegenerative diseases like AD [164, 165], diagnosis based on clinical imaging of axonal transport would be of special interest. Furthermore, the delivery of therapeutic compounds through this high-speed, long distance and widely-spread route (or network) to the target region would provide novel strategies.

1.3 Pharmacokinetics

The current non-pharmacological treatments such as music or psychosocial interventions help AD patients to live with the disease. The pharmacological treatment aiming directly at the pathological aspects, on the other hand, mostly serves the therapeutic purpose with disease-modifying approaches. In the transition from a lead compound to clinically proven drug, the study of pharmacokinetics (PK) is one of the important steps during drug development. Before entering clinical trials, pre-clinical PK provides important information, such as selection of drug candidates that have the maximum potential of reaching the target or decision on the appropriate administration route. It also helps to estimate the frequency and duration of dosing in order to sustain drug with therapeutic concentration at target. Most importantly, the parameters from pre-clinical studies help to predict human pharmacokinetics.

1.3.1 ADME

Pharmacokinetics are defined as the study of the time course of drug absorption (A), distribution (D), metabolism (M) and excretion (E) [166]. When the drug is administered, it enters blood stream from its administration site (adsorption), and then blood circulation transports the drug to the target site as well as to other parts of body (distribution). During these processes, the drug may be transformed into smaller metabolites (metabolism), and finally the drug and its metabolites need to be removed from the body (excretion). Information about kinetics can be obtained through measuring the concentration of drug in different body fluids and tissues at different time points after administration. Blood, metabolism/excretion-related and target organs are mostly studied. Many factors affect the pharmacokinetics of a drug, such as the physiochemical properties of the drug (or its formulation), the route of administration, the duration and dose, and the animal species [167, 168].

Bioavailability is termed as the fraction of drug absorbed from the administration site into the systemic circulation, which should be considered when selecting the appropriate route of administration [169]. For example, intravenous administration has no absorption process and is guaranteed 100% bioavailability per definition, but is unfavourable for the patients. Oral drugs, on the contrary, can be simply administered and are well accepted by the patients, but are usually with low and unpredictable bioavailability due to complicated absorption in gastrointestinal tract, the first pass metabolism by gut and liver, as well as the enterohepatic circulation [170].

The metabolic stability of the drug, especially for peptide and protein drugs administered orally, should be well characterized. The metabolites of a drug are mostly pharmacologically inert, but for some drugs they could be also pharmacologically active or toxic [171] . Incomplete metabolism/excretion or accumulation of the unchanged drug and its metabolites from the previous doses may cause potential adverse effects with successive doses or continuous infusion. Because only unbound drug is pharmacologically active, its protein binding issue should be investigated for example through plasma protein binding assay [172, 173].

1.3.2 Pharmacokinetic parameters and models

PK parameters calculated from the concentration-time curves help to understand how the drug functions in the body and serve evaluation and communication of the results from different PK studies. They are basically divided into two categories. One category includes the parameters requiring no complex mathematical calculation. They are also called model-independent parameters, including the maximal observed concentration of a drug (C_{max}), the time to reach C_{max} (T_{max}) and the area under the concentration-time curve (AUC).

The other category includes parameters that require mathematical formula for calculation, such as mean residence times (MRT), clearance (Cl), volume of distribution (V_d) and the terminal half-life ($t_{1/2}$). Most of these parameters are generated through plotting the drug concentration in plasma/blood as a function of time.

The kinetic profile of a drug within the body involves various biological processes, and is highly complex that simplifications and empiricism of it are necessary in order to practically describe and predict these processes. Two most commonly used mathematical methods are noncompartmental and compartmental analysis.

The compartmental analysis regards tissues and/or fluids sharing similar kinetic properties (kinetic homogeneity) as a single compartment, and the body consists of one or more of these compartments with specified interconnections, inputs and losses. Each compartment can be mathematically described with an exponential function. The solution of an n-compartmental model is just n-exponential function(s).

The noncompartmental analysis (NCA) on the contrary, does not assume any specific compartmental model and thus also called model-independent analysis. It relies on empirical determination of AUC with the linear trapezoidal and/or log-linear trapezoidal rule. The rest of PK parameters are then calculated through AUC.

In theory, all parameters estimated using noncompartmental analysis can be recovered from the ones using compartmental analysis, but differences exist due to different numerical techniques used for parameter estimation (e.g. sums of exponentials versus trapezoidal integration) [174, 175]. If the primary requirement is to obtain basic parameters for characterizing the disposition of the drug in pilot PK studies, such as AUC, Tmax, Cmax, terminal half-life and clearance, then NCA is generally preferred to the compartmental analysis, especially when analysing sparse data [176, 177].

1.4 The brain barriers and peptide-based drugs

One therapeutic strategy against AD is based on a so-called “peripheral sink” hypothesis, which postulates that removal of Aβ from the periphery is sufficient to decrease Aβ levels in brain. However, recent studies on rodents and non-human primate indicate that peripheral Aβ clearance may not be a therapeutic option [178-180]. As the neurotoxic Aβ42 is predominately produced by neural cells, a direct action of potential therapeutics in the brain parenchyma is still the best choice. Many factors contribute to the difficulty of developing effective pharmacological treatments against AD. One of them is negligible transport of CNS targeting drugs in pharmacologically significant amounts through the protective structure of the brain, the blood-brain barrier (BBB).

1.4.1 The blood-brain barrier

BBB is a unique barrier that separates the brain from the circulating blood, which includes three cellular elements: endothelial cells, astrocyte end-feet and pericytes (Fig. 10). The BBB endothelial cells differ from peripheral endothelial cells by i) absence of fenestrae, ii) the presence of tight intercellular junctions, iii) low pinocytotic activity, and iv) high levels of efflux transporters at their luminal endothelial surface [181]. The tight junctions between endothelial cells provide the BBB with an extremely high trans-endothelial electrical

resistance and thus low para-cellular ion permeability [182]. Only water, some gases and lipid-soluble molecules that can freely diffuse through the endothelium may cross the BBB passively. Hydrophilic molecules must cross transcellularly through special transport mechanism such as carrier-/receptor-mediated transport [183], or through endocytotic mechanisms such as receptor-mediated or adsorptive transcytosis in case of bigger hydrophilic molecules like proteins [184]. Studies show that approximately 98% of small molecule (MW>500 D) and nearly all large molecule drugs (MW>1 kD) such as recombinant peptides, proteins, or gene-based medicines are normally excluded from the brain [185, 186].

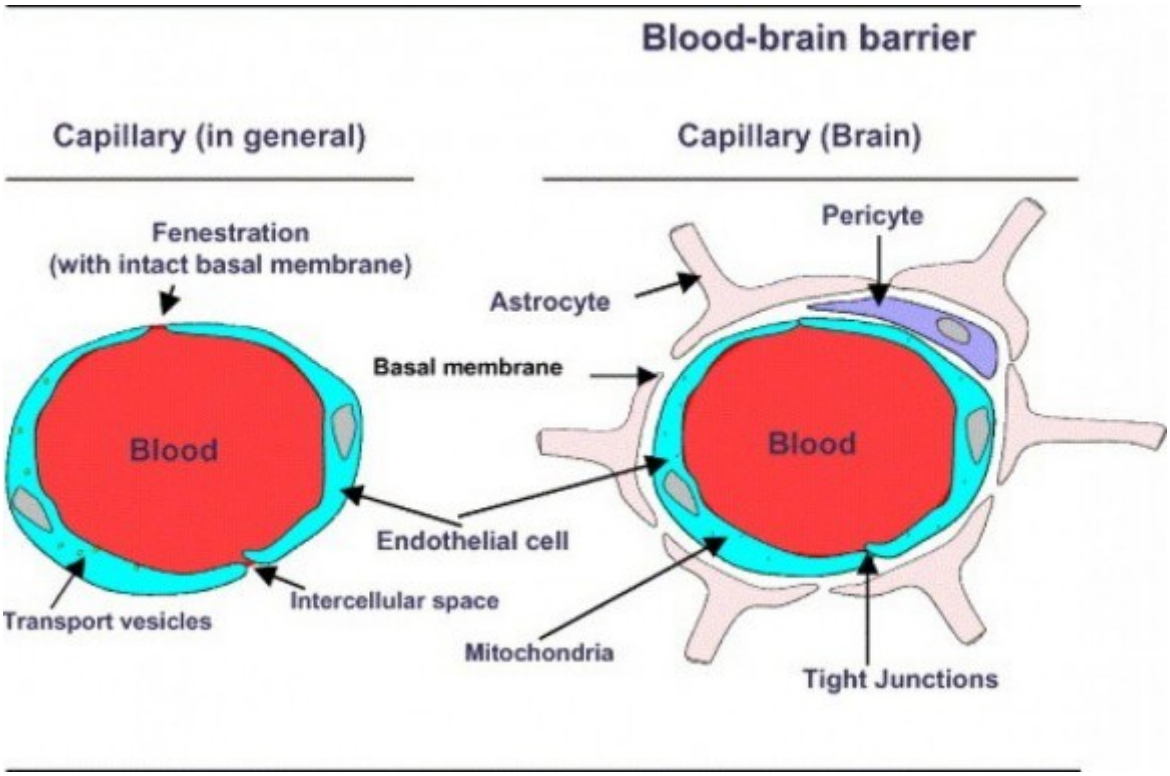

Fig. 10. Schematic comparison of a peripheral capillary (left) with a cerebral capillary (right) (source: http://www.midasletter.com/wp-content/uploads/2015/01/Blood-Brain-Barrier-Picture-2-581x383.jpg).

Besides the structural barrier, the BBB also possesses a metabolic barrier through expression of several ectoenzymes on the plasma membranes of the endothelial cells, pericytes and astrocytes, such as aminopeptidases, endopeptidases and cholinesterase [187-189].

The blood-cerebrospinal fluid barrier (BCB) also regulates blood-borne molecules entering the brain through CSF. It is formed by the choroid plexus epithelial cells and the arachnoid membrane which are linked by tight junctions [190, 191]. Some drugs and solutes enter the brain principally across this barrier. The BBB in the adult human has 12 to 18 m^2 surface area for exchange, which is 1000-fold greater than the surface area of the choroid plexus epithelium [192, 193], thus to enhance the brain delivery through the BBB is still the major strategy in design and optimization of most of the CNS drugs.

1.4.2 Peptide-based drugs and ARM of HIV-1 Tat

The therapeutic potential of peptide-based drugs with 5 to 50 amino acid residues is increasingly appreciated in the recent years. The peptide-based drugs combine the advantages of conventional “small molecule” drugs (<500 Da) and the protein-based drugs (>5000 Da), especially with high substrate specificity and affinity, as well as low toxicity [194]. With a better understanding of the cellular and molecular mechanisms of the BBB transport, several strategies to enhance brain delivery of peptide-based drugs have been developed in the past decades. One of these delivery technologies is based on cell-penetrating peptides (CPPs), for example the trans-activator of transcription (Tat) that is derived from human immunodeficiency virus type 1 (HIV-1) [195, 196]. The HIV-1 Tat is a regulatory protein with 86 to 101 amino acids depending on the subtype. It is produced in very early steps of viral infection and greatly enhances the transcriptional rates that results in a high viral gene expression. It also mediates viral spreading in disease progression [197]. It contains an arginine-rich transduction domain (YGRKKRRQRRR), and thus belongs to the family of arginine-rich motif (ARM) RNA binding proteins [198]. It is suggested to bind negatively charged cell membrane embedded molecules like heparan sulfate or sialinic acid, and passes the plasma-membranes passively [196, 199, 200]. Recent in vitro experiments based on artificial membrane systems suggest its formation of plasma-membrane pores [201]. Tat- and Tat motif-based drug delivery systems show in vivo BBB penetration when covalently attached to the macromolecules [202, 203]. With enhanced and sufficient brain delivery, the development of the peptide-based CNS drug would be particularly attractive.

1.5 Special aims of this thesis

In spite of the many advantages of peptide based drugs, their short half-life time *in vivo* due to rapid degradation by proteases, and low bioavailability by oral administration restrict their clinical usage. In comparison to naturally occurring L-form peptides, peptides derived from partial D-amino acid substitutions or D-enantiomeric peptides, which are composed entirely of D-amino acids, have advantages over L-enantiomers. Due to the stereoisomeric selectivity of proteolytic enzymes, they are less prone to proteolysis, therefore longer half-lives and higher bioavailability after oral administration are to be expected [204-206]. Furthermore, they are less or even not immunogenic at all [207].

Using mirror-image phage display [208, 209], a series of fully D-enantiomeric peptides have been identified to bind specifically to Aβ (1-42). These D-peptides have already proven to prevent Aβ fibril formation and to eliminate oligomers *in vitro*, as well as have shown therapeutic efficacy with reduction of amyloid plaques and inflammation in the brain, and reversing cognitive deficits in transgenic mouse models [210-213].

Despite knowing their therapeutic function, their exact distribution *in vivo* is yet unknown. Thus the purpose of this doctoral research is to examine the distribution of D-peptides in the body *in vivo*, their entrance into the brain and distribution within the brain in particular.

Aim #1. D-enantiomeric peptides are known to be very resistant to proteolysis *in vitro*. However, only limited information exists about their biodistribution, oral availability and biological half-life *in vivo*. So far, pharmacokinetic analyses have only been shown for peptides that only partially consisted of D-amino acids, thus a comprehensive preclinical pharmacokinetic study of solely D-enantiomeric peptides is strongly required. Studies on their metabolic stability and plasma protein binding property are important and help to understand PK parameters. Comparing the pharmacokinetic behaviour of lead peptide, D3, and its derivatives from rational design also provides important information on transfer of *in vitro* or *in silico* data to *in vivo*, as well as for the selection of promising candidates for the treatment of Alzheimer's disease.

Aim #2. As mentioned above, the "peripheral sink" hypothesis failed in many studies. Drugs developed as AD therapeutics still need to enter the brain to be therapeutically active. D3, as an arginine-rich peptide, shows similarity to the ARM of HIV-1 Tat and its BBB permeability was examined in an *in vitro* cell culture model. The studies of aim#1 suggested the distribution of D3, as well as other D-peptides, into the brain with different administration routes, but there is still no direct evidence to show D-peptides actually entre the brain. Therefore, the aim of this study is to use tritium and fluorescently labelled D3 to detect and visualize the brain delivery, as well as the specific binding to Aβ plaques in mouse models.

Aim #3. D3, as well as fluorescently labelled D3 are able to pass the BBB and bind to Aβ plaques *in vitro* and *in vivo* as shown in studies of aim #2. Here we go another step further, to see how they are transported as exogenous substances once they are introduced in the brain parenchyma. As mentioned above, the neuropathological changes of AD start at the region of hippocampal formation, thus we select this injection site as it is also easy to locate and suitable for tracking substance transport due to its anatomic character. D-peptides are labelled with fluorescence (FAM or FITC) for visualization purpose, so FITC is tested for control as well. By comparing the transport difference in wild type and AD transgenic mouse models, it is investigated whether those fluorescently labelled D-peptides can reveal the neuropathological changes of AD.

2 Publications

2.1 Structure characterization of unexpected covalent O-sulfonation and ion-pairing on an extremely hydrophilic peptide with CE-MS and FT-ICR-MS.

Published in: Analytical and Bioanalytical Chemistry

Impact Factor: 3.58

Contributions: 5%

Preparation of most samples; involved in measurements and discussions.

Anal Bioanal Chem (2015) 407:6637–6655
DOI 10.1007/s00216-015-8826-8

PAPER IN FOREFRONT

Structure characterization of unexpected covalent O-sulfonation and ion-pairing on an extremely hydrophilic peptide with CE-MS and FT-ICR-MS

Martin Pattky[1] · Simone Nicolardi[2] · Beatrix Santiago-Schübel[1] · Daniel Sydes[1] · Yuri E. M. van der Burgt[2] · Antonia N. Klein[3] · Nan Jiang[3] · Jeannine Mohrlüder[3] · Karen Hänel[3] · Janine Kutzsche[3] · S. A. Funke[3,4] · D. Willbold[3,5] · S. Willbold[1] · C. Huhn[1,6]

Received: 30 April 2015 / Revised: 22 May 2015 / Accepted: 3 June 2015 / Published online: 28 June 2015

Abstract In this study, we characterized unexpected side-products in a commercially synthesized peptide with the sequence RPRTRLHTHRNR. This so-called peptide D3 was selected by mirror phage display against low molecular weight amyloid-β-peptide (Aβ) associated with Alzheimer's disease. Capillary electrophoresis (CE) was the method of choice for structure analysis because the extreme hydrophilicity of the peptide did not allow reversed-phase liquid chromatography (RPLC) and hydrophilic interaction stationary phases (HILIC). CE-MS analysis, applying a strongly acidic background electrolyte and different statically adsorbed capillary coatings, provided fast and efficient analysis and revealed that D3 unexpectedly showed strong ion-pairing with sulfuric acid. Moreover, covalent O-sulfonation at one or two threonine residues was identified as a result of a side reaction during peptide synthesis, and deamidation was found at either the asparagine residue or at the C-terminus. In total, more than 10 different species with different *m/z* values were observed. Tandem-MS analysis with collision induced dissociation (CID) using a CE-quadrupole-time-of-flight (QTOF) setup predominantly resulted in sulfate losses and did not yield any further characteristic fragment ions at high collision energies. Therefore, direct infusion Fourier transform ion cyclotron resonance (FT-ICR) MS was employed to identify the covalent modification and discriminate O-sulfonation from possible O-phosphorylation by using an accurate mass analysis. Electron transfer dissociation (ETD) was used for the identification of the threonine O-sulfation sites. In this work, it is shown that the combination of CE-MS and FT-ICR-MS with ETD fragmentation was essential for the full characterization of this extremely basic peptide with labile modifications.

Keywords Extremely hydrophilic peptide · Capillary electrophoresis · Coating · Electron transfer dissociation · Alzheimer's disease

✉ C. Huhn
carolin.huhn@uni-tuebingen.de

[1] Central Institute for Engineering, Electronics, and Analytics (ZEA): Analytics (ZEA-3), Forschungszentrum Jülich GmbH, 52428 Jülich, Germany

[2] Leiden University Medical Center, Center for Proteomics and Metabolomics, 2333 ZA Leiden, The Netherlands

[3] Institute of Complex Systems, Structural Biochemistry (ICS-6), Research Centre Jülich, 52425 Jülich, Germany

[4] Bioanalytik, Hochschule für Angewandte Wissenschaften, 96450 Coburg, Germany

[5] Institut für Physikalische Biologie, Heinrich-Heine-Universität Düsseldorf, 40225 Düsseldorf, Germany

[6] Institute for Physical and Theoretical Chemistry, Eberhard Karls Universität Tübingen, 72076 Tübingen, Germany

Introduction

The prevalence of the neurodegenerative Alzheimer's disease (AD) as the most common form of dementia is strongly increasing because of the growing average age of the Western population, with more than 20 million people affected [1]. According to the modified amyloid cascade hypothesis, the disease is associated with the pathologic self-association of amyloid-β-peptide (Aβ), which leads to the formation of toxic Aβ oligomers and extracellular amyloid neuritic plaques. Aβ peptides are 37–43 amino acids long and are derived from

the amyloid precursor protein by proteolytic processing. Aβ aggregates are thought to play an important role in the development and progression of AD.

Based on the modified Aβ cascade theory, therapeutic approaches tackling Aβ aggregate formation include the developments of agents reducing the Aβ production by inhibiting secretases, interfering with the Aβ oligomerization and plaque formation, or increasing Aβ clearance from the brain.

Earlier, the D-enantiomeric peptide D3 was selected by phage display selection against monomeric or low molecular weight species of the mirror image of Aβ(1-42) using a phage displayed peptide library of more than $1•10^9$ different 12-mer peptides [2]. Such a mirror image phage display yields D-peptides that are known to have enhanced half-life via increased resistance against most proteases [3–5]. D3 was shown to bind to different Aβ1-42 conformers [6–8], to modulate Aβ aggregation and to reduce Aβ cytotoxicity and to reduce the plaque load and inflammation processes in transgenic mice [9, 10]. In addition, even oral application of D3 significantly improved cognition [11, 12]. D3 seems to convert toxic Aβ species into non-amyloidogenic, non-fibrillar, and non-toxic aggregates [12]. Interaction of D3 with Aβ may be based on electrostatic interaction of the cationic D3 moieties with anionic sites in Aβ oligomers.

The strong electrostatic interaction is due to the extreme characteristics of D3, being a very hydrophilic peptide (2/3 of the amino acids are hydrophilic) with 5 arginines and 2 histidines in its amino acid sequence: RPRTRLHTHRNR with an amidated C-terminus. The pI is calculated to be 12.6 [not taking into account the amidation of the C-terminus, http://web.expasy.org/compute_pi/)]. Other sources calculated the pI to be 14 with amidation at the C terminus (http://www.innovagen.se/custom-peptide-synthesis/peptide-property-calculator/peptide-property-calculator.asp) or 13.1 (https://www.genscript.com/ssl-bin/site2/peptide_calculation.cgi). These extreme values make the chromatographic separation of D3 challenging. For quality control and its analysis in cerebrospinal fluid and blood, chromatographic techniques are difficult to apply as either too strong or too low retention is observed. High separation selectivity was achieved using capillary electrophoresis coupled with ESI-MS to separate and identify the large number of modifications of D3 and other D3-related peptides including deamidation (DA), O-sulfonation at the threonine sites, and ion-pairing. Further in-depth analysis required high resolution accurate mass (HR/AM) mass spectrometry to determine deamidation and discriminate sulfate from phosphate, and different fragmentation techniques, including collision induced and electron transfer dissociation (CID and ETD). We used FTICR-ETD-MS to determine the O-sulfonation sites.

Materials and methods

Chemicals

Iodoacetamide (>99 %, TLC) and polybrene (>95 %, MW= 15,000) were purchased from Sigma-Aldrich (Steinheim, Germany). Dithiothreitol (DTT; molecular biology grade) was bought from BDH Prolabo (Darmstadt, Germany), trypsin (sequencing grade) from Promega (Mannheim, Germany) and ammonium hydrogen carbonate (>99 %) from AppliChem (Darmstadt, Germany). RapidGest was purchased from Waters (Eschborn, Germany), acetonitrile (LC-MS-grade) from Biosolve (Valkenswaard, The Netherlands), isopropanol (LC-MS-Chromasolv) from Fluka (Steinheim, Germany), and LN coating solution (concentrate) from Target Discovery (Palo Alto, CA, USA). Bovine serum albumin (BSA), ammonium acetate, glacial acetic acid (p.a.), and formic acid (p.a.) were bought from Merck (Darmstadt, Germany). All aqueous solutions were prepared with water that was purified by a Milli-Q purification system from Millipore (Bedford, MA, USA). The fused silica capillaries were purchased from Polymicro Technologies (Phoenix, AZ, USA). D3 and other peptides were synthesized by JPT Peptide Technologies GmbH, Berlin, Germany.

Recombinant production of L-D3

E. coli C43(DE3) competent cells (Avidis, Saint-Beauzire, France) and *E. coli* OmniMax T1(Invitrogen, Darmstadt, Germany) were employed. Custom synthesized DNA oligomers were obtained from BioTeZ (Berlin, Germany). Restriction enzymes were from MBI Fermentas. The original expression vectors pTKK19 and pET-20b/YUH were a generous gift of Dr. Toshiyuki Kohno. DNAse I was from AppliChem (Darmstadt, Germany), protease inhibitor complete EDTA free (Hoffmann-LA Roche, Basel, Switzerland), Ni^{2+}-NTA-agarose was purchased from Qiagen (Hilden, Germany), and SP Sepharose was obtained from GE Healthcare Life Science (Uppsala, Sweden). Hiload 16/60 Superdex 30 prep grade was from GE Healthcare Life Science, Uppsala, Sweden.

The plasmid pTKK19-LD3 allowed the production of the L-D3 peptide in *E.coli* as an N-terminal fusion protein with decahistidine tagged ubiquitin. The ubiquitin hydrolase is able to release the L-D3 12-mer peptide from ubiquitin without additional amino acids left from the cleavage site. The vector pTKK19 was modified by introducing the SacII restriction site as a still mutation at the C-terminal end of ubiquitin.

For cloning the L-D3 peptide expression vector DNA oligomers coding for L-D3 peptide (RPRTRLHTHRNR) were synthesized (BioTeZ, Berlin, Germany). The codon usage was optimized for the expression in *E. coli*. The 5′-phosphorylated oligomers (5′-GGCGGTCGTCCGCGTACCCGTCTG

CACACCCACCGTAACCGTTAAG and 5′-AGCTGAAT TGCCAATGCCACCCACACGTCTGCCCATGCGCCTGC TGGCGGCG) are able to hybridize to each other to build a DNA double strand with overhanging ends, which can hybridize with the SacII/ SalI digested and dephosphorylated vector pTKK19. After ligation of vector and DNA oligomers *E. coli* OmniMaxT1 competent cells (Invitrogen, Darmstadt, Germany) were transformed with the ligation reaction. The obtained colonies were analyzed, and the DNA sequence of the L-D3 peptide expression vector, referred to as pTKK19-LD3, was confirmed by DNA sequencing (SEQLAB, Göttingen, Germany).

E. coli C43(DE3) competent cells were transformed with plasmid pTKK19-LD3. A volume of 200 mL LB medium (100 μg/mL kanamycin and 2 % glucose) was inoculated with a single colony and incubated at 37 °C and 130 rpm overnight. The cells were harvested at 5000*g* for 20 min at 20 °C and resuspended in 1 L fresh LB-medium with a final $O.D._{600}$ of 0.2. The expression culture was incubated at 37 °C at 130 rpm until the $O.D._{600}$ value reached 1.6. The expression of the fusion protein was induced by addition of IPTG to a final concentration of 1 mM. After another 5 h of shaking at 37 °C at 130 rpm, cells were harvested by centrifugation at 5000*g* for 20 min at 4 °C. Cells were washed once with 30 mL PBS, centrifuged at 14,000*g* for 5 min at 4 °C, and stored at –20 °C.

For purification, the cell pellet was resuspended in 50 mL lysis buffer (PBS pH 7.4 with 5 mmol/L imidazole). The cell lysis took place with a cell disruptor at 1.7 bar for 3 cycles. Then 30 μg/mL DNAse I (5 mg/mL DNAse I dissolved in 10 mM HEPES-KOH, pH 7.9, 30 mmol/L $MgCl_2$, 30 mmol/L $CaCl_2$, 50 % glycerol) and one tablet protease inhibitor completely EDTA-free (Hoffmann-LaRoche, Basel, Schweiz) per 10 mL lysis buffer were added. After centrifugation at 50,000*g* for 30 min at 11 °C, the supernatant was loaded on a Ni^{2+}-NTA-agarose column (8 mL column material per liter expression pellet) equilibrated with lysis buffer. The column was washed with 10 column volumes PBS pH 7.4 containing 60 mmol/L imidazole, 10 column volumes PBS pH 7.4 containing 60 mmol/L imidazole and 1 mol/L urea, and 10 column volumes PBS pH 7.4 containing 60 mmol/L imidazole and 2 mol/L urea to remove non-specifically bound proteins. The His-tagged fusion protein was eluted from the column with six column volumes of 500 mmol/L imidazole in 50 mmol/L sodium phosphate buffer pH 7.5 and 700 mmol/L NaCl. Fusion protein containing fractions were pooled and dialyzed against 50 mmol/L sodium phosphate buffer pH 7.5, 400 mmol/L NaCl, and 1 mmol/L EDTA.

The N-terminal ubiquitin of the fusion protein was cleaved with yeast ubiquitin hydrolase (YUH) in 50 mmol/L sodium phosphate buffer pH 7.5, 400 mmol/L NaCl, and 1 mmol/L EDTA overnight at room temperature with a ratio YUH:fusion protein of 1:3. Expression and purification of YUH was done as described [13].

To remove YUH, ubiquitin and noncleaved fusion protein, a SP-Sepharose column was employed. The protein solution was diluted after cleavage with 50 mmol/L sodium phosphate buffer pH 7.5 1:4 to adjust the NaCl concentration to 100 mmol/L and loaded on an SP-Sepharose column (1 mL column material for 1 L expression culture) equilibrated with 50 mmol/L sodium phosphate buffer pH 7.5. The column was washed with increasing concentrations of ammonium acetate pH 8.8 (50, 100, 200, and 400 mmol/L, 2 column volumes each). During the washing procedure, the L-D3 peptide stuck to the column and YUH, ubiquitin, and non-cleaved fusion protein were washed away. To elute the L-D3 peptide, the column was incubated for 2 min with 6 column volumes 1 mol/L ammonium acetate pH 8.8.

To remove residual impurities, the L-D3 peptide solution was loaded on the size exclusion chromatography column Hiload 16/60 Superdex 30 prep grade (GE Healthcare Life Science, Uppsala, Sweden). The column was equilibrated with 1 mol/L ammonium acetate pH 8.8. The elution volume of L-D3 was 90 mL. The protein containing fractions were pooled, lyophilized, and stored at –80 °C.

HPLC-MS

Analyses were performed using an Agilent 1100 series binary HPLC system (Agilent Technologies, Waldbronn, Germany) coupled with a 4000Qtrap linear ion trap mass spectrometer (Applied Biosystem/MDS Sciex, Foster City, CA, USA), which was equipped with a TurboIon spray source. The mass spectrometer was operated in the positive Q1 mode scanning from 400 to 1200 Da. Parameters were first optimized performing a flow injection analysis with D3 and led to the following parameter settings: IS 5500 kV, declustering potential DP 80 V, curtain gas (N2) 10 arbitrary units (au), source temperature 550 °C, nebulizer gas (N2) 50 au, and heater gas (N2) 30 au.

Separation was tested on different C8/C18, HILIC-, and cation exchange columns (e.g., ProntoSIL 120-C8-SH, 3 μm, 150×2 mm (Bischoff Chromatography, Leonberg, Germany), Luna HILIC, 5 μm, 150×3 mm (Phenomenex, Aschaffenburg, Germany), or Luna WCX, 5 μm 150×2.1 mm (Phenomenex, Aschaffenburg, Germany). The column oven temperature was kept at 20 °C during analysis.

Gradient elution on C8/C18 columns was done with deionized water with 0.1 % formic acid, 20 mmol/L or 50 mmol/L ammonium acetate pH 3, 4.5, or 6 (solvent A), and acetonitrile with 0.1 % formic acid (solvent B) at a constant flow rate of 300 μL min^{-1}. The gradient profile was 5 % B for 2 min isocratic, from 2 to 20 min a linear increase from 5 % B to 95 % B, an isocratic step for 6 min, and a return to 5 % B at 27 min and 10 min isocratic for re-equilibration.

Gradient elution on HILIC column was tested with different ammonium acetate concentrations (30, 50, 100 mmol/L) with different pH (3, 4.5, and 6) (solvent A) and acetonitrile with 0.1 % formic acid (solvent B). The gradient profile was 95 % B for 5 min isocratic, from 5 to 35 min a linear decrease from 95 % B to 50 % B, an isocratic step for 6 min, a return to 95 % B at 42 min, and 15 min isocratic for re-equilibration. The flow rate was 150 μL/min.

Gradient elution on cation exchange was done with 100 mM ammonium acetate, pH 3.5 (solvent A) and acetonitrile with 0.1 % formic acid (B) 5 % B for 2 min isocratic, from 2 to 30 min a linear increase from 5 % B to 95 % B, an isocratic step for 6 min, a return to 5 % B at 37 min, and 10 min isocratic for re-equilibration. The injection volume was always 10 μL D3 (100 μmol/L).

CE-MS

An Agilent 7100 capillary electrophoresis system (Agilent Technologies, Waldbronn, Germany) was used for CE analysis. The capillaries (i.d. 50 μm, length 60 cm) were coated according to the standard coating procedure described in [14]. Briefly, the capillaries were rinsed consecutively with methanol and aqueous hydrochloric acid (c=1 mol/L) for 10 min at 1 000 mbar, followed by 25 min rinsing with sodium hydroxide (c=1 mol/L) for activation. Having rinsed with water for 10 min, the capillaries were flushed with the coating solution (a 5 % aqueous polybrene solution or the 1:5 diluted LN stock solution) for 30 min and the capillary was left overnight filled with coating solution. Having flushed it out with BGE, 20 min conditioning at –30 kV (polybrene) or +30 kV (LN) was accomplished and the capillary was ready to be used. The running buffer was a 3:1 (v/v) mixture of acetic acid:formic acid, each c=1 mol/L. The tryptic digests of bovine serum albumin (BSA) used as a reference were accomplished according to [14] and injected hydrodynamically (5 s at 50 mbar) without further treatment. Separations were carried out at +30 kV (LN coating) or –30 kV (polybrene coating). Before each run, the capillary was flushed with running buffer for 150 s. An Agilent 6520 Accurate-Mass QTOF-MS (Agilent Technologies, Santa Clara, CA, USA) was used for MS detection. The CE was coupled to the mass spectrometer via a coaxial sheath liquid interface from Agilent (Agilent Technologies, Waldbronn, Germany). An Agilent isocratic pump 1260 (Agilent Technologies, Waldbronn, Germany) delivered the sheath liquid, a 50:50 (v/v) mixture of water:isopropanol, containing 1 % acetic acid at a flow rate of 4 μL/min. The nebulizer pressure was set to 0.28 bar and the drying gas flow to 4 L/min. A fragmentation voltage of 175 V, a capillary voltage of –4000 V, a skimmer voltage of 65 V, and an octopol voltage of 750 V were used. The mass range was set to *m/z* 100–1700 and the data acquisition rate was 2 spectra/s. For the daily calibration of the MS we used the G1969-85000 QTOF standard calibration tune mix from Agilent. For the plotting of extracted ion electropherograms, the intensities of the isotopes of one signal were summed.

Direct infusion ESI-FTICR-MS

Direct infusion electrospray ionization (ESI) experiments were carried out using a 5 μg/mL solution of the synthetic D3 peptide with 0.05 % formic acid at an infusion rate of 2 μL per min. ESI-FTICR experiments were performed on a Bruker 15 Tesla solariX FTICR mass spectrometer, as previously described [15], using the same instrumental settings with some modifications. Briefly, the capillary voltage was 4500 V with dry gas flow, dry gas temperature, and nebulizer gas pressure set to 3.7 L/min, 200 °C, and 1.3 bar, respectively. A quadrupole (Q) was used for precursor ion selection and a hexapole collision cell for ETD. The ion funnels operated at 100 and 6.0 V, respectively, with the skimmers at 15 and 5 V. The trapping potentials were set at 0.995 and 0.985 V, the analyzer entrance was maintained at –10 V, and side kick technology was used to further optimize peak shape and signal intensity. The required excitation power was 19 % with a pulse time of 10 μs. MS and MS/MS spectra were acquired in the *m/z*-range from 153.5 to 3 000 and generated from the average of 8 and 100 scans, respectively, using an accumulation time in the hexapole collision cell of 0.15 and 4 s, respectively. MS/MS experiments were performed with the Q at an isolation window of 10 mass units, followed by ETD and fragment ion mass analysis in the ICR cell. The ETD reagent (fluoranthene from negative chemical ionization (NCI) source) accumulation and reaction time was 150 and 100 ms, respectively. Both positive and negative ions were trapped using a mirror rf amplitude of 180 V_{pp}.

Prior to the measurements, the FTICR system was externally calibrated using a commercially available peptide mix (Bruker Daltonics). DataAnalysis software ver. 4.0 SP 5 (Bruker Daltonics) was used for the visualization and the calibration of the ETD spectra. ETD fragments of the different D3 peptide forms were simulated using the MS-Product tool of the http://prospector.ucsf.edu/prospector/mshome.htm website.

Results

LC-MS

D3 analysis was first tested using RP-HPLC with a C18 column, though D3 eluted close to the void volume with hardly any retention (data not shown), despite various optimization strategies (different columns, salt concentration, pH, see the Materials and methods section). In contrast, the peptide was irreversibly bound to a weak cation exchange column (data

not shown). In order to obtain reasonable but not too strong binding of D3 on the stationary phase, HILIC separation with a column covered by cross-linked diol groups was tested (see Fig. 1). Very strong retention also at elevated pH was observed with peak base widths of 6 min, revealing doubly and triply charged peptides in the deconvoluted MS spectra with *m/z* values of 1599.7, 1679.6, and 1759.4. These correspond to D3 and isoforms differing in one or two modifications with a mass difference of +80 Da pointing to phosphorylation or O-sulfonation.

CE-MS separation and identification of modifications

We applied our standard CE-MS method for peptide analysis [14] involving an acidic background electrolyte composed of a mixture of acetic acid and formic acid (3:1, each c= 1 mol/L). In order to avoid adsorption of the highly charged D3 peptide cations to the capillary wall, different coatinging strategies were applied using the neutral acrylamide-based LN coating and polybrene, both well suited for the analysis of highly charged and, thus, highly mobile peptides [14]. With LN coating, very short analysis times below 6 min were obtained (see Fig. 2a). Already from the analysis with LN coating, an astonishingly high number of D3 species was observed migrating in three major groups. The mass spectra for two signals of the very basic D3 with a corresponding high charge state of 4 (the D3 species were detected with 3–5 charges) are exemplarily shown in Fig. 3. The signal of free D3 is observed together with two signals with nominal mass differences of 80 (Fig. 3a) and 98 (Fig. 3b) (or 178 from a combination of both). These could later be assigned to a single O-sulfonation at the threonines, the formation of an ion-pair with sulfate, or a combination of covalent O-sulfonation and ion-pairing with sulfate via FTICR-MS (see section ESI-FTICR-MS fragmentation with ETD). Care has to be taken in the interpretation of the results as in-source decay is present for the labile ion-pairs and SO_3-moieties (see below) and many isobaric species are present, not yet sufficiently resolved (Fig. 2b).

A higher resolution, especially of isobaric species with single or double O-sulfonation and ion-pairs was obtained matching the effective electrophoretic mobility of the fast D3 and its modified forms with the electroosmotic mobility using the cationic polybrene coating inducing a high EOF [16] as visible in Fig. 4. As O-sulfonation and ion-pairing are prone to in-source decay, this good separation is vital for unambiguous identification of compounds present either in the sample or stemming from neutral loss reactions. The mass spectra of all electrophoretic peaks showed O-sulfonation and/or ion-pairing of D3 (potentially with deamidation) plus the signals

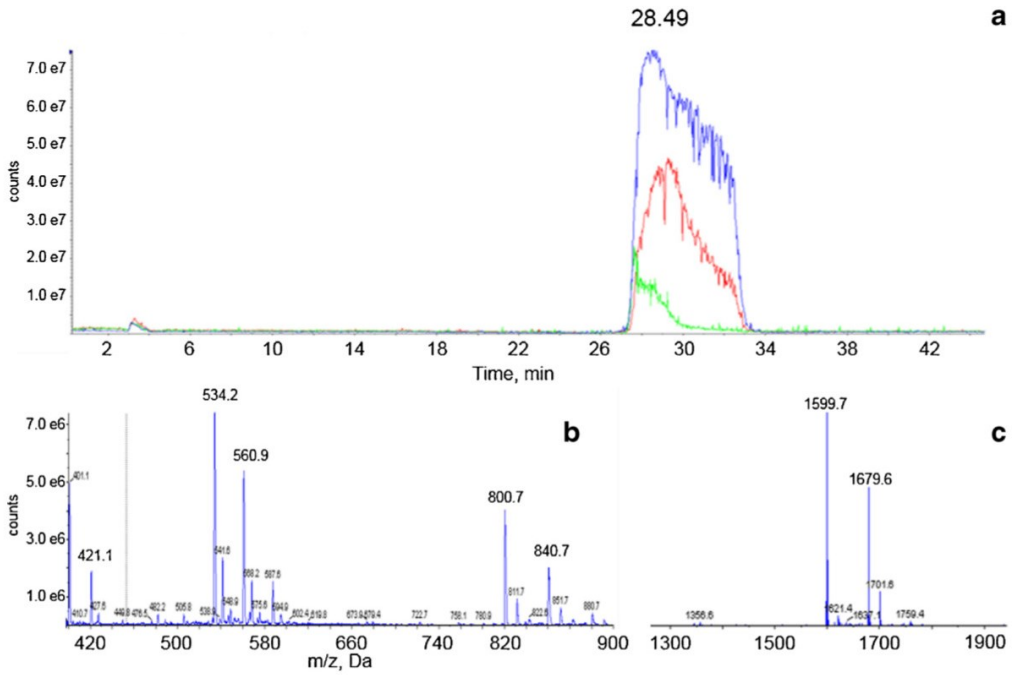

Fig. 1 (**a**) HILIC-MS chromatogram with mass traces for 535 (blue), 561 (red), and 587 (green); (**b**) mass spectrum as well as (**c**) deconvoluted mass spectrum over retention time range 27.5–29.0 min; separation was done with 100 mmol/L ammonium acetate, pH 6, as described in Materials and Methods

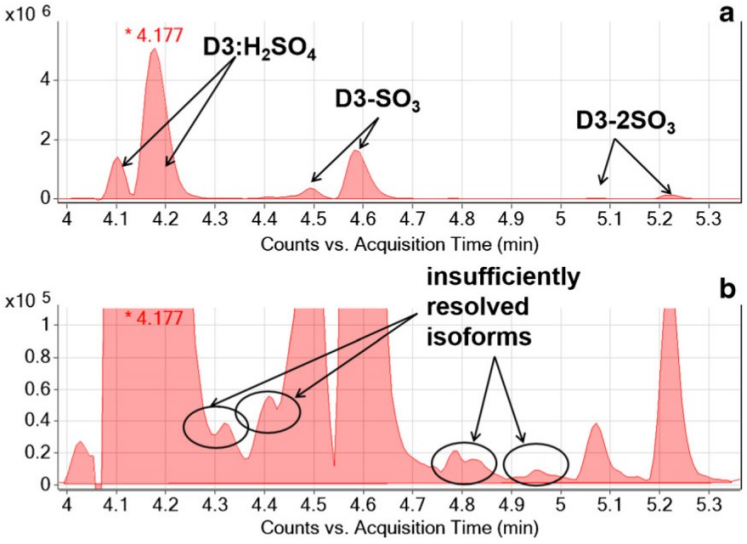

Fig. 2 Electropherogram from CE-MS separation using LN coating; BGE: 3:1 (v/v) mixture of acetic acid:formic acid, each c=1 mol/L; +30 kV; sheath liquid: a 50:50 (v/v) water:isopropanol mixture with 1 % acetic acid, flow rate of 4 μL/min; injection 5 s×50 mbar; (**a**) overview; (**b**) enlargement. The mass trace of *m/z* 320.59 is shown (unmodified D3 present from in-source decay)

from neutral losses. An example is presented in Fig. 3 for D3-SO_3:H_2SO_4, where the D3-SO_3 as well as the free D3 can be observed. A comparison of the separation profiles obtained with the respective coating materials reveals the strong impact of the capillary coating and, thus the EOF velocity on the separation profiles: although the LN coating is perfectly suited for a fast screening of larger sample cohorts, only the highly cationic capillary coating polybrene enables the in-depth evaluation of the complex D3 isoform pattern.

Owing to in-source decay with its neutral losses, the mass of the native D3 (or the deamidated form) can be observed underlying every signal, but no "free" D3 was observed during our CE-MS analysis. For data representation in Fig. 4a, we used this presence of the *m/z* signal of 320.59 (5-fold charged D3 from in-source decay) to illustrate the impressive sample complexity of the commercially synthesized D3 sample. In addition, deamidation is indirectly visualized: note that the resolving power of the QTOF system does not allow accurate detection of a 0.984 Da mass shift (i.e., the first isotope of the deamidated species cannot be resolved from the second isotope of the amidated peptide signal). However, because of the separation capabilities of the CE-method, deamidation can be visualized when plotting the

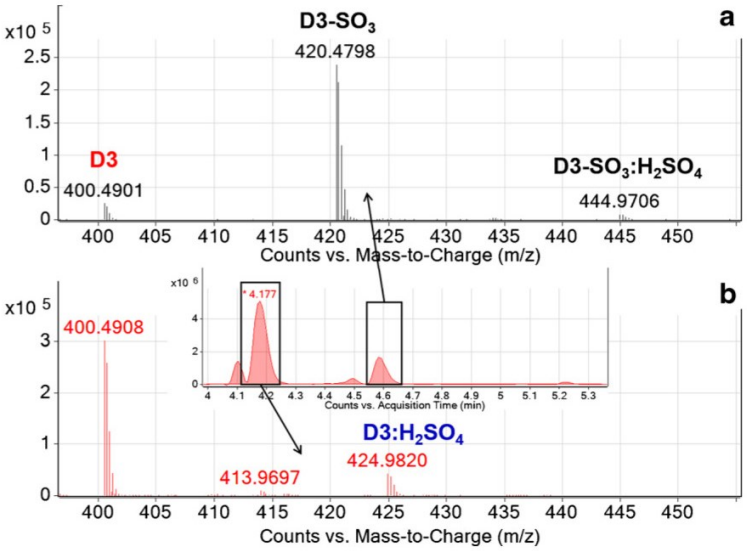

Fig. 3 Details of the mass spectra (charge state +4) of two selected D3 species [D3-SO_3 (**a**) and D3:H_2SO_4 (**b**)] in the separation presented in Fig. 2 (see also insert); further separation conditions, see Fig. 2

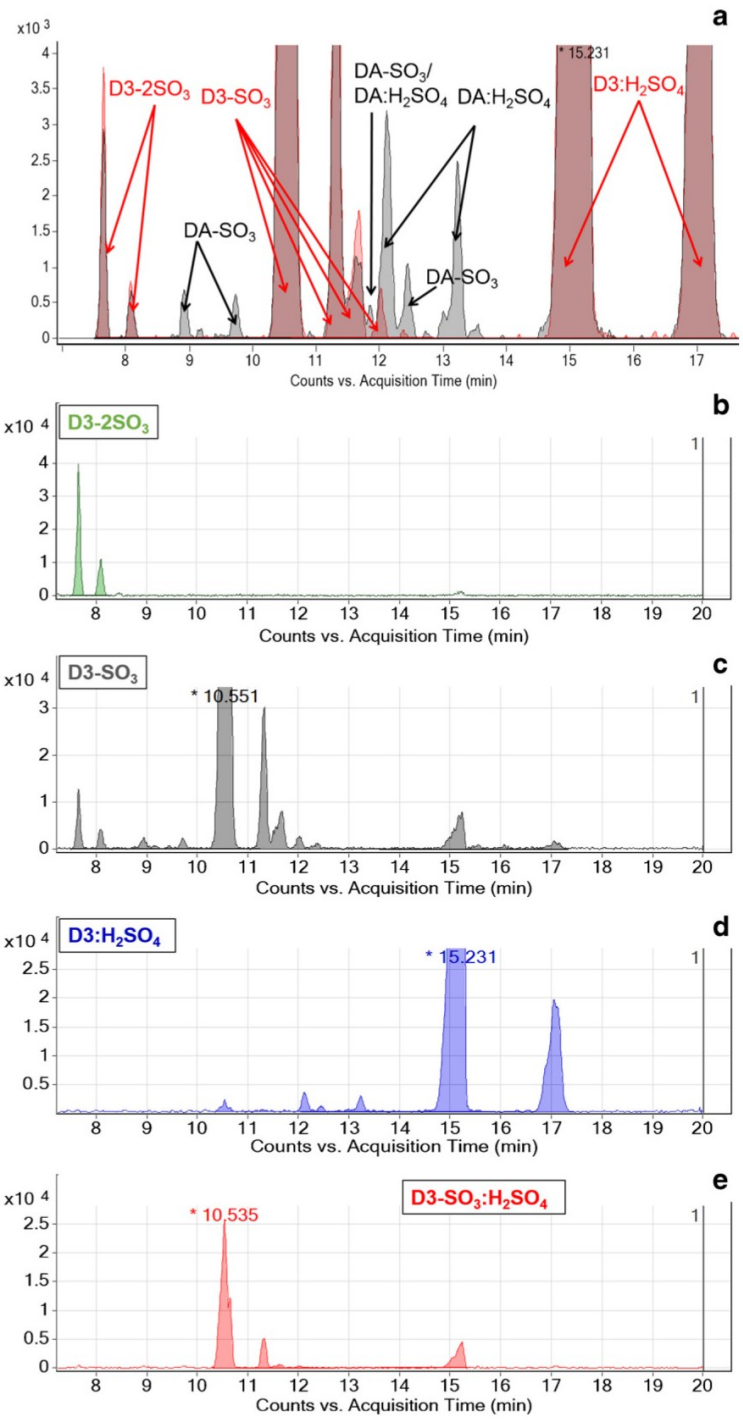

Fig. 4 Electropherograms from separations using a PB-coated capillary, other separation conditions as in Fig. 2. (**a**) Electropherogram overview including the sum of the mass traces of *m/z* 320.59 (unmodified D3 present from in-source decay); (**c**)–(**e**) extracted ion electropherograms of modified D3 forms including deamidated forms; (**b**) D3-2SO_3 (*m/z* 440.47); (**c**) D3-SO_3 (*m/z* 420.48); (**d**) D3:H_2SO_4 (*m/z* 424.98); (**e**) D3-SO_3:H_2SO_4 (*m/z* 444.97)

extracted ion electropherograms of the first and second isotope masses of the amidated species (*m/z* values 320.59 and 320.79), as presented in Fig. 4a. Signals of species with deamidation are present where a large difference in the signal intensities of these mass traces is observed.

A summary of all species identified from CE-MS using polybrene-coated capillaries is given in Table 1.

Table 1 Characterization of the heterogeneity of D3: theoretical mass, modification, theoretical, and observed mass of charge state +4 (for CE-MS and FTICR-MS). As visualized in Fig. 4, the masses of the D3 species occur at multiple positions in the electropherogram. The average of the measured masses at the different positions is listed. For migration times please refer to Fig. 4

MW (theor)	Deamidation	O-sulfonation	Ion-pair	Theoretical mass at charge state +4 *m/z*-values	Observed mass at charge state +4 in CE-MS: *m/z*-values	Delta (ppm)	Observed mass at *m/z*-values (charge state +4) FTICR-MS
1597.92529**	-	-	-	400.4885	400.4902	4	400.4885
1598.90931**	1 DA	-	-	400.7345	400.7355	2	
1757.83893	-	2 SO_3	-	440.4666	440.4683	4	440.4670
1677.88211	-	1 SO_3	-	420.4777	420.4781	1	420.4778
1678.86609	1 DA	1 SO_3	-	420.7237	420.7247	2	
1775.84948*	-	1 SO_3	1 H_2SO_4	444.9696	444.9704	2	444.9696
1695.89268	-	-	1 H_2SO_4	424.9804	424.9814	2	424.9804
1696.87668	1 DA	-	1 H_2SO_4	425.2264	425.2250	-3	

* The mass referring to D3-SO_3:H_2SO_4 was detected at different migration times as also shown in Fig. 4e. A clear identification was possible at migration times of 10.3–10.6 min; for other signals, an unexpected isotopic pattern was observed varying within a peak over time. Further species, where a similar effect was observed, are not listed as the identification is ambiguous (see also section on Determination of O-sulfonation sites).

** D3 and DA without modification were only observed as a result of in-source decay.

ESI-FTICR-MS fragmentation with ETD

Direct infusion ESI-FTICR-MS analysis of the D3 peptide confirmed the presence of five out of eight species detected by CE-QTOF-MS. A typical example of an ESI-FTICR-MS spectrum is depicted in Fig. 5a. The signal detected at *m/z* 400.4885 was identified via ETD experiments as the quadruply protonated form of the D3 peptide amidated on the C-Terminus (data now shown). The high accuracy of the 15 T ESI-FTICR-MS measurements allowed the identification of ion adducts and modified forms of the same peptide by accurate measurement of the mass differences between signals in the spectrum. Following this strategy and measuring the mass differences from the D3 peptide observed at *m/z* 400.4885, all species in the spectrum were identified: the mass difference of 21.9820 Da corresponding to a sodium adduct was calculated for the peptide detected at *m/z* 405.9841, whereas a mass difference of 79.9568 Da corresponding to an O-sulfonation was calculated for the peptide observed at *m/z* 420.4778. The peptide observed at *m/z* 424.9804 was 97.9676 Da heavier than the D3 peptide, indicating the formation of an ion-pair with sulfate, whereas the peptide observed at *m/z* 440.4670 was 159.9136 Da (i.e., twice 79.9568 Da) heavier than the D3 peptide, indicating the presence of a second O-sulfonation. Finally, the mass difference of 97.9672 Da was calculated between the peptide at *m/z* 420.4778 and the peptide at *m/z* 444.9696, indicating both the presence of one O-sulfonation and an ion-pair with sulfate. All the identified species are summarized in Table 1.

To corroborate the identification and localize the modification sites, ETD ESI-FTICR-MS/MS experiments were performed on selected precursor ions. The ETD spectrum of quadruply protonated mono-sulfonated D3 peptide is depicted in Fig. 5b. Here, only the precursor ion and ETD c- and z-fragment ions were annotated. The high sequence coverage (i.e.,10 out of 11 peptide bonds cleaved) allowed the localization of this modification mainly on threonine-8.

Since the mass differences between a sulfonated and a phosphorylated peptide is only 9.5 mDa, the unambiguous identification of this kind of modification was proven after internal calibration of the spectrum. To this end, the c9- (*m/z*-value 621.1877), the c4- (*m/z*-value 528.3365), the z4- (*m/z*-value 565.3192), and the c6-fragment (*m/z*-value 797.5217) that do not contain the modification were used to internally calibrate the ETD spectrum. As depicted in Fig. 5c, the measured *m/z* value of the modified c8-fragment was in excellent agreement with sulfonation with a mass measurement error (MME) below 0.2 ppm for both the c4- and the c8-fragment. Note that HSO_3-containing fragment ions had an MME between 0.13 and 0.50 ppm. MMEs would have been higher than 5 ppm in case of phosphorylated fragment ions. Note that ETD fragments (i.e., c4, c5, and c7) of the D3 peptide mono-O-sulfonated at threonine-4 were also detected. However, the signal intensity of these fragments was very low and the mono-sulfonated D3 peptide was considered as modified mainly at threonine-8. The ETD experiment performed on the modified D3 peptide of *m/z* value 440.4670 confirmed the presence of one O-sulfonation on both threonine-4 and threonine-8 simultaneously (data not shown).

Analysis of L-D3 obtained from *E. coli*

Figure 6 shows the CE-MS analysis of the peptide L-D3 expressed in *E. coli*, with only L-D3:H_2SO_4 and minor

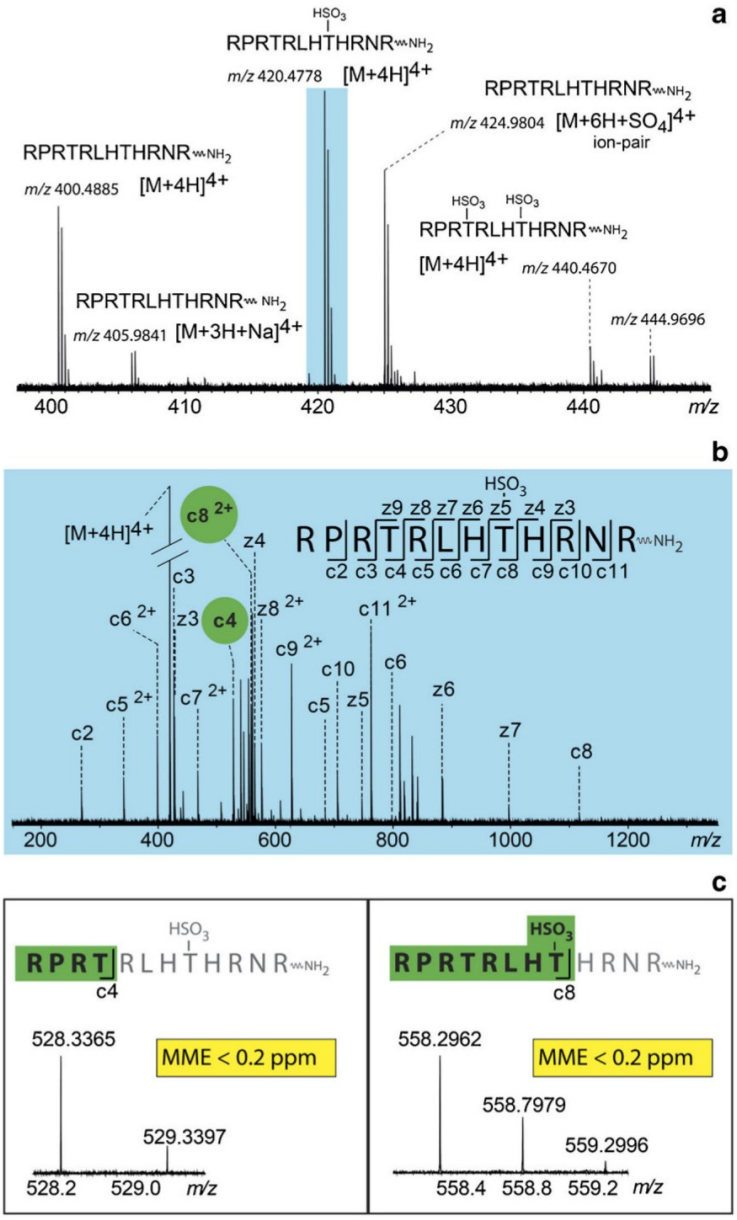

Fig. 5 ETD-MS spectra from direct infusion FTICR-MS of D3

impurities not related to L-D3 present. No O-sulfonated species were detected.

Application to D3-related peptides

Peptides with slightly modified amino acid sequences were synthesized to investigate the impact of a modified amino acid sequence on the pharmacologic potency of the respective peptides as well as to understand the impact of the amino acid sequence on the number of O-sulfonated forms and ion-pairing. The CE-MS results in Fig. 7 show that only single but not double O-sulfonation was always observed on the single threonine present. Deamidation was only recorded in case of RD2. Ion-pairs are present, though only detected with a higher degree of in-source decay compared with D3, pointing to a higher stability of its ion-pairs in the gas phase. No combinations of O-sulfonation and ion-pairing or deamidation were detected. Overall, the complexity of the peptides with a varied amino acid sequence was clearly lowered.

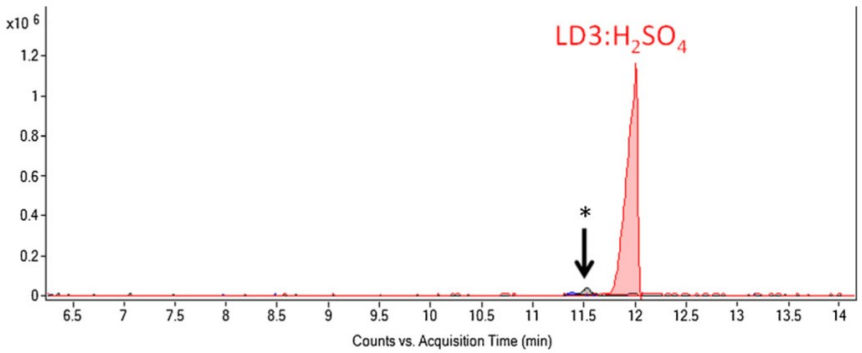

Fig. 6 Electropherogram of L-D3 separated in polybrene-coated capillaries at –30 kV; further separation conditions as in Fig. 2. MS traces of extracted ion electropherograms of 320.59 (unmodified L-D3). *Marks an impurity not related to L-D3

Discussion

Analysis of the extremely hydrophilic peptide D3 and separation of sulfated/phosphorylated species

Both the chromatographic and electrophoretic separation of extremely hydrophilic and highly basic peptides such as the peptide D3 in this study are challenging.

Chromatography

The very hydrophilic peptide D3 with its large number of polar amino acid moieties (mainly lysine and arginine) showed negligible retention on reverse phase columns, like other very polar peptides [17, 18] , though in principle the analysis of phosphorylated, sulfated, and sulfonated peptides is possible [19, 20]. An optimization via ion-pairing [9, 17, 18, 21] or using normal phase chromatography with a high content of organic solvents in the mobile phase of high surface tension and low induced ionization efficiency [22, 23] is not possible. Too strong up to irreversible retention of very basic peptides, also for D3, was observed using weak cation exchange phases (see also [24]).

HILIC is often used for weakly acidic or basic compounds in general [25], including hydrophilic (glyco-)peptides [26, 27] with aqueous-organic mobile phases of >50 % organic solvent, well compatible with mass spectrometry [26]. In order to avoid excessive retention, we applied here a non-ionic diol-stationary phase without anionic surface charge (e.g., of zwitterionic sulfobetaine phases) to prevent Coulombic attraction of D3 on the surface. However, no successful separation of different D3 species was obtained. Even decreasing the percentage of organic solvent or utilizing the salting-out effect [25] for the non-ionic HILIC phase did neither reduce the retention times below 30 min nor enhance separation efficiency (6 min peak base width), see Fig. 1. The negligible selectivity may stem from the strong ion-pairing of the peptide with sulfate and O-sulfonation, with an increase in hydrophobicity as also observed by Singer et al. [28] for phosphorylated peptides.

In the future, we will test other HILIC stationary phases including amide- and amine-bonded phases at low pH in order to induce Coulombic repulsion, thus lowering the retention

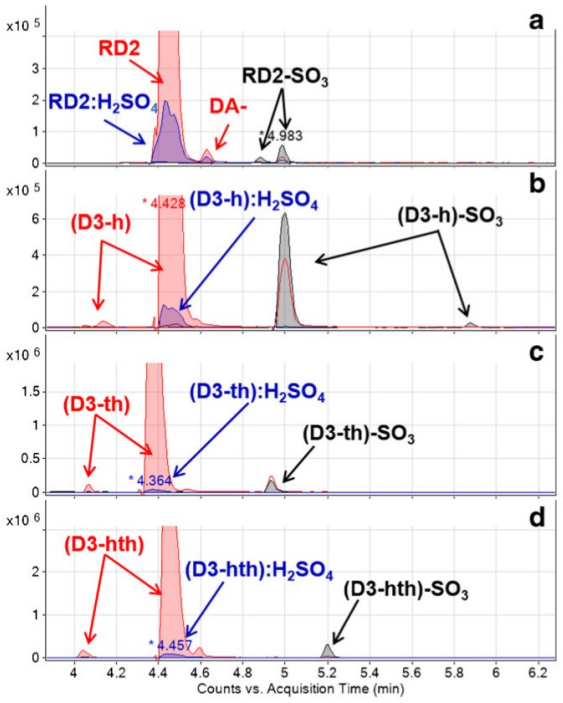

Fig. 7 Electropherograms from the analysis of D3 variants separated in polybrene-coated capillaries at -30 kV; further separation conditions as in Fig. 2. (**a**) **PTLHTHNRRRRR** with mass traces: RD2 400.74 (1598.92); RD2-SO_3 420.73 (1678.87); RD2:H_2SO_4 424.23 (1776.85); DA-RD2 400.98 (1599.90). (**b**) **RPRTRLTHRNR** with mass traces D3-h: 366.47; (1461.86); D3-h-SO_3 386.46 (1541.82); D3-h:H_2SO_4 390.96 (1559.825). (**c**) **RPRTRLHRNR**, with mass traces D3-th 341.21 (1360.81); D3-th-SO_3 361.20 (1440.77); D3-th:H_2SO_4 365.70 (1458.78). (**d**) **RPRTRLRNR** with mass traces D3-hth 408.92 (1223.75); D3-hth-SO_3 435.58 (1303.71); D3-hth:H_2SO_4 440.58 (1321.73)

(ERLIC-approach; electrostatic repulsion-hydrophilic interaction chromatography) [29]. Likewise, mixed-mode stationary phases may be used [30–33].

Capillary electrophoresis

An alternative to chromatography with its inherently limited range of encompassed analyte polarities [32] are capillary electromigrative separation techniques, where the polarity of the analyte, despite the need of being soluble in the separation medium, is not of concern for the separation. Only charge is required for separation (either on the analyte or on a separation carrier). CE-MS coupling is frequently applied for peptide analysis [34, 35]; mostly very acidic BGEs (pH 2–3) are used with volatile acetic acid and formic acid as buffer constituents. This ensures cationic migration of most peptides, especially tryptic peptides, which mostly have a charge of +2 in these aqueous buffers. D3 with its high pI and, thus, high charge can be regarded a nearly ideal analyte for capillary electrophoresis as it has a very high electrophoretic mobility and a good solubility. However, because of its very basic character and high cationic charge, adsorption problems onto the capillary wall are likely to occur with the use of acidic BGEs attributable to ionic interactions. Thus, neutral or cationic coatings had to be applied for high separation efficiency and repeatability. The neutral LN coating provided extremely fast measurements with less than 6 min separation time (see Fig. 2); however, only with low resolution (compare [16]). Counter-electroosmotic migration with the help of polybrene with its high EOF (-6.2×10^{-4} cm^2/Vs with the running buffer applied here) to provide an efficient transport of D3 to the MS yielded increased resolution, very high separation efficiency, and increased robustness [14]; however, in a somewhat longer separation time of 20 min. Only with the brilliant separation obtained, we were able to clearly discriminate the large number of isobaric compounds, including ion-pairs and sulfonated species together with their deamidated analogs, without quenching effects. More importantly, a clear assignment of all species despite the labile nature of the ion-pairs as well as the covalent bond of the sulfonate was now possible (see Fig. 4), in contrast to direct infusion experiments or HILIC-MS with coeluting analytes.

Identification of D3 species

Deamidation

With CE-MS using the polybrene coating, a clear baseline separation of several D3 peptide species differing in mass by +0.98 Da was observed, pointing to deamidation converting a neutral into an acidic side chain and, thus, leading to lower mobilities and higher migration times in the electropherogram (see Fig. 4). It is also possible that the ion-pair changes its three dimensional structure. Resolution is further aided by the counter-electroosmotic migration. A shift of more than 1 min was observed for D3-SO_3 versus DA-SO_3 (9 and 9.8 versus 10.5, 11.5 and 12 min, although a clear assignment of corresponding isobaric species is not possible) corroborating the good experiences for this type of modification by Gennaro and Salas-Solano [36] for CE, and Gaus et al. [37] for MEKC but not for RPLC [36–38].

The number of isobaric analogs observed may stem from the isomerization process into aspartate and iso-aspartate, two isomers that may well be separated by CE as described by Lai et al. [39]. Isobaric deamidated D3 analogs may also stem from isomers differing in the deamidation site as D3 has two possible deamidation sites: at the amidated C-terminus or on asparagine, though only one seems to be deamidated at a time (some signals with very low intensity may tentatively be identified as doubly deamidated species, though mass accuracy is too poor at these low intensities). As we did not obtain viable CID fragment spectra using CE-MS, no clear assignment is possible. However, deamidation was not observed for the L-D3 peptides synthesized in *E. coli* (see section Analysis of L-D3 obtained from *E. coli*), which does not possess the amidated C-terminus, making it likely that this is the point of deamidation in D3.

FTICR-MS did not reveal signals related to deamidation even though the mass resolving power of the instrument of more than 200,000 can be considered to be sufficient to distinguish between deamidated and non-deamidated D3 species (87,000 would be sufficient in case of similar signal intensities, which are, however, not present). Possibly, discrimination effects are present that hinder the detection of the relatively low abundant deamidated species without prior separation. We can rule out in-source decay or deamidation reactions during the electrophoretic run as we achieved baseline separation of deamidated species without tailing effects.

Ion-pairing with sulfuric acid

CE-MS revealed several electrophoretic signals, the mass spectra of which showed the native D3 (or its deamidated analog) plus signals with a nominal mass difference of 98 to the native D3 peptide (or its deamidated analog) as exemplified in Fig. 3. Strong in-source decay is thus present, depending on the fragmentation voltage. At 250 V, the intensity of the mass trace for native D3 dominated but was clearly reduced at 70 V (data not shown). For complex analogs with both O-sulfonation and ion-pairing present, e.g., in D3-SO_3:H_2SO_4 (see Fig. 3), also the gas-phase dissociation of the ion-pair to D3-SO_3 was visible (as the Coulombic attraction is obviously weaker than the covalent O-sulfonation).

The reduction in the electrophoretic mobility upon addition of HSO_4^- to the D3 peptide forming an ion-pair with protonated D3 (D3:H_2SO_4) leads to a lower shift in migrations times

compared with covalent O-sulfonation (D3-SO_3). It is likely that the hydrodynamic radius of the ion-pair is smaller as the peptide winds around the sulfate moiety. Thus, a higher effective electrophoretic mobility and a shorter migration time can be anticipated.

FTICR-MS confirmed the presence of D3 singly and doubly O-sulfonated species. Likewise, an ion-pair of D3 with sulfate was detected, which was also stable enough in the gas phase to survive the long measuring time in FTICR-MS. Using only direct infusion experiments, the ion-pair would most probably have been identified as an adduct formation from sulfuric acid in the sample, not as a sample constituent as demonstrated by CE analysis. For all ion-paired species, several isobaric signals were observed pointing to isomers with the sulfate present at different positions in the molecule. With several structural motifs of Arg-X-Arg in the D3 sequence (with X being proline, threonine, or asparagine), such a differential binding to sulfate with corresponding differences in charge density and hydrodynamic radius is easy to comprehend.

The results allow the conclusion that amidation or O-sulfonation events or ion-pair formation are independent: e.g., amidation does not seem to play a role in the O-sulfonation/sulfation processes as both D3-SO_3 and DA-SO_3 as well as the ion-paired counterparts are present (see Fig. 4 and Table 1). It is also very interesting to report that CE-MS as well as FTICR-MS results clearly revealed that O-sulfonation and ion-pairing occur simultaneously in D3 as species with *m/z* 444.9696 (FTICR) and 444.97 (CE-MS) (each charge state +4) for D3 with covalently bound sulfate and ion-pair formation were observed, that is D3-SO_3:H_2SO_4. In CE-MS, these signals had only a low intensity, but had an expected intermediate effective electrophoretic mobility and, thus, migrated between doubly sulfonated and ion-paired species. This means that even the covalent modification with –SO_3 does not hinder the formation of ion-pairing (or vice versa), obviously because of the large number of basic amino acid moieties in the D3 amino acid sequence and most likely several different binding sites in the peptide.

In contrast to electrophoretic separations, only covalent modifications were observed in HILIC-MS. Obviously the ion-pairing constant is strong enough to yield a stable ion-pair within the CE buffer, but not strong enough when competing binding sites on the HILIC column are present or when electrosprayed from the HILIC eluent. In general, CE is well known to be useful for the analysis of stable metal complexes in speciation analysis [40]. In our case, CE was able to partially keep the D3:sulfate ion-pairs intact. Interestingly, in solution the ion-pair proved to be extremely stable as attempts to break the ion-pair using sodium hydroxide or surfactants at low concentration were not successful, as proven by non-changing CE-MS electropherograms (data not shown). With high concentrations of ammonia and overnight incubation, only hydrolysis (CE-MS signals with mass of D3 minus 18) was observed to a low extent.

We have not found similar stable ion-pairs of peptides with strong acids described in literature. However, Schug and Lindner [41] discussed noncovalent binding between guanidinium and anionic groups with a focus on arginine interactions with phosphonate and sulfonate residues. Electrostatic interactions as well as hydrogen binding are the key interactions involved here because of the "planar forklike guanidinium functionality with six potential hydrogen bond donors available" [41]. The authors also discuss special binding motifs with RR (as in the twin arginine translocase binding domain) and RKR for binding acidic residues. These motifs are not present for D3, though similarly strong binding is possible via folding of the molecule with its five arginines for similar binding sites.

Identification of O-sulfonation versus phosphorylation

Electromigrative separation techniques are especially suited when modifications with changes of the charge state of the analyte occur [42], among them O-sulfonation/phosphorylation, glycosylation with sialic acids [43], formation of C-terminal pyroglutamate, or deamidation reactions (see discussion in Deamidation). Especially phosphorylation analysis has been addressed [35] showing that in cation analysis, phosphorylated species have a clearly lower effective electrophoretic mobility and can well be separated from the non-modified peptides because of their relatively low isoelectric point, regardless of the modified amino acid being serine, threonine, or tyrosine [44]. Both with CE and MEKC, phosphopeptide isomers with multiple phosphorylation sites have been separated [45–47].

For mass spectrometric analysis, it has to be taken into account that O-sulfonation and phosphorylation are near-isobaric modifications with a mass difference of only 0.0095 u. For their discrimination on the D3 peptide amidated at the C-terminus (*m/z* value 420.4778 for the quadruply charged mono-sulfated D3), a mass resolution of about 180,000 is necessary to resolve the modification's mass difference, which requires an FTICR-MS instrument. Even upon ETD fragmentation, for the smaller fragments C4 and C8, the required mass resolution is still 56,000 and 120,000.

O-sulfonation of serine and threonine has been described by Medzihradszky et al. [20] as a post-translational modification for proteins in a number of species besides the more common O-sulfonation of tyrosine residues. The authors observed peptide signals largely differing in retention time in RPLC but showing the same sequence information from CID fragmentation. Upon inspection of the results, a mass difference of 80 Da proved to be present, pointing to either phosphorylation or O-sulfonation. Several hints on O-sulfonation were considered: (1) loss of –80 Da from serine

and threonine residues instead of the more commonly observed –98 Da due to H_3PO_4; (2) FTICR-MS clearly pointed to O-sulfonation; (3) comparison with the spectra and retention times of synthesized peptides and their sulfonated and phosphorylated counterparts; (4) chemical β-elimination and O-sulfonation reactions.

CE-MS did not allow the discrimination of O-sulfonation versus phosphorylation; hints on sulfonation were: phospho-NMR did not reveal a signal. Cleavage reactions using sulfatases and phosphatases were unsuccessful (identical CE-MS runs) after enzymatic treatment. In CE-MS, we mainly observed neutral losses of –80 u instead of –98 u during in-source decay and/or CID. It was shown that for phosphorylated and sulfonated peptides, CID fragmentation mostly leads to either the neutral loss of phosphoric or sulfuric acid (H_3PO_4 and H_2SO_4) with a mass difference of –98 Da or gas-phase elimination of HPO_3 and SO_3 (–80 Da) when applying positive mode [48]. In case of aliphatic phosphorylation at threonine and serine, mostly neutral loss of H_3PO_4 is observed mainly from a charge-directed E2-elimination process, whereas in case of phosphorylation at tyrosine (aromatic), the loss of HPO_3 is preferred as H_3PO_4 cannot be lost upon E2 elimination and as the C–O bond is stronger than the P–O bond because of resonance stabilization of the resulting product [48]. However, in cases where basic moieties are present, such as in D3, neutral loss of H_3PO_4 may be observed either from cation–π interaction or from a concurrent loss of HPO_3 and water [48]. So a neutral loss of –80 is not suitable for an ambiguous identification of the modification. To this end, a 15 Tesla ESI-FTICR-MS instrument with ETD option was applied that allowed the unambiguous identification of O-sulfonation at direct infusion with a mass accuracy at 0.2 ppm (versus 5 ppm for a potential phosphorylation), see Fig. 5.

Determination of O-sulfonation sites

The D3 peptide in our study has two threonine residues, one of them or both were observed to be sulfonated (see Figs. 4 and 5). O-sulfonation site identification requires either fragmentation of the D3 peptide in mass spectrometry or its tryptic digestion, the latter impossible for the D-amino acids involved.

As seen in Fig. 4, many isobaric species can be observed for the singly sulfonated species D-SO_3 and DA-SO_3 (and also D3-SO_3:H_2SO_4), pointing to structural isomers, differing in the O-sulfonation site of threonine-8 versus threonine-4 and the site of ion-pairing. A similar separation of singly or doubly phosphorylated isomers with two phosphorylation sites has been shown by Dong et al. [45]. CID fragmentation in CE-MS was unsuccessful as either the collision energy was too low to reveal peptide backbone cleavage in addition to the strong neutral loss of SO_3 or the collision energy was too high and no fragment could be identified. However, we observed also two isomers of D3-2SO_3, clearly separated from each other (see Fig. 4b) with both threonines being O-sulfonated. Sterical isomers may be present. In literature, several chemical attempts for O-sulfonation and (more often) phosphorylation site determination have been presented: O-sulfonation on tyrosine (for review see [49]) (serine and threonine O-sulfonation have only very recently been described in eukaryotes [20]) may be identified (1) via the modification of remaining free tyrosines in a peptide (e.g., via acetylation) followed by enzymatic release of the sulfonation [50, 51]; (2) via β-elimination and derivatization by bromination or reaction with ethane diol [51, 52]; or (3) by mass spectrometry with concurrent neutral loss at the sulfonated/phosphorylated tyrosines [53] or using noncovalent stabilizers in MALDI [54]. Several attempts were made to enable CID identification of phosphorylation and O-sulfonation: several studies describe the β-elimination of the phosphorylation moiety (either hydrolysis or sulfatase/phosphatase) with subsequent derivatization reactions on serine [51–53] to determine the stoichiometry and the sites of the modification. Stabilization of the modification in the gas phase may be achieved with derivatization, complex formation, or the use of negative ionization mode [54].

Alternatively, fragmentation of the amino acid backbone can be achieved using ECD or ETD [49, 55–59] or infrared multiphoton dissociation (IRMPD) [60]. Whereas in CID the energy upon collision is quickly spread via vibrational processes leading to the break of the weakest bond (mostly with the modification attached), the electron transfer leads to radical anions with the charge at the most electronegative points in the molecule leading to the break of most N–Cα bonds and to c/z fragment ion series.

With the success of ETD for phosphorylated and sulfonated peptides, we decided to use FTICR-MS with an ETD option for further evaluation of the O-sulfonation sites. With our direct infusion experiments, indeed a successful fragmentation of the amino acid backbone with a high sequence coverage of 10 out of 11 fragments in ETD was obtained (see Fig. 5). Clearly, mainly threonine-8 was shown to be sulfonated. With direct infusion FTICR-MS, also double-O-sulfonation at both threonine-4 and threonine-8 was confirmed.

Overall modification of D3

More than 15 signals, many of them isobaric related to D3, were observed, detected with charge stages of +3 to +5 inversely correlating with a higher degree of O-sulfonation or ion-pairing as can be expected from these acidic moieties. From the exact mass and the mass differences to the native D3, the presence of D3 species with one deamidation (mass difference of 0.98), 1–2 O-sulfonations (mass differences of 79.96 or 159.97) as well as 1–2 ion-pairs with sulfate (mass differences of 97.97 or 195.94) can be deduced, further identified via FTICR-MS (see section Identification of O-sulfonation versus phosphorylation). Also, combinations of these modifications such as D3-SO_3:H_2SO_4 are present as well as deamidation events giving rise to a large heterogeneity. An overview of the species

observed is presented in Table 1. Notably, the mass of the native (deamidated or non-deamidated) D3 (Fig. 4a) was only observed underlying all signals, even dominating in case of the gas-phase labile ion-pairs. Additional signals of low intensity were recorded, tentatively identified as (e.g., D3-2SO_3:H_2SO_4 or D3:2H_2SO_4). However, the isotopic pattern within these signals changed during the passage of the peak, preventing a clear assignment of these species. To a lesser degree, the same inconsistencies regarding the isotope pattern were observed for some of the D3-SO_3:H_2SO_4 signals as well, even though the species was clearly identified by FTICR-MS. It is possible that the unexpected isotopic pattern of these signals is related to the instability of the D3-species after entering the MS giving rise to metastable ions, which decompose in the flight path of the TOF. Nevertheless, we can clearly state that D3 can carry more than one negatively charged modification (2 SO_3, 1 SO_3 and 1 H_2SO_4 or 2 H_2SO_4) and there are some hints for even three anionic modifications.

Overall, there is a clear group separation of D3 species in polybrene-coated capillaries with (1) ion-pairs with relatively high overall charge and high effective electrophoretic mobility (high migration times when cationic coatings are used), (2) singly, and (3) doubly sulfonated species with reduced charge and effective electrophoretic mobility (reduced migration times with polybrene coating). Co-migration of (e.g., D3-SO_3:H_2SO_4 and D3-SO_3) as possibly read from mass spectra such as in Fig. 3 is thus unlikely and points to in-source decay. However, the separation and sample are more complicated because of the occurrence of deamidation, also changing the charge distribution on D3 species and, thus, migration times. Overall, a very good separation of deamidated and amidated species is observed when using polybrene-coated capillaries (e.g., D3-SO_3 and DA-SO_3 at 10.5 and 11.5 versus 9 and 10 min, see Fig. 4a). Clearly, deamidation leads to lower effective electrophoretic mobilities as the –$CONH_2$ moiety reacts to the acidic –COOH group. Thus, even in the relatively crowded region of 10–14 min (Fig. 4a), a clear discrimination of D3 species present in the sample versus species derived from in-source decay is possible. This discrimination was not possible with just direct infusion experiments using FTICR-MS. FTICR-MS with its ETD option was vital for the identification of O-sulfonation versus phosphorylation and for the site -specific analysis revealing a considerably higher degree of O-sulfonation on threonine-8 versus threonine-4.

From the CE-MS results, we know that 1 deamidation, 1–2 O-sulfonation at two different sites in the peptide, and 1–2 ion-paired sulfates may be present. Theoretically, with 1–2 O-sulfonation, 1–3 ion-pairs, and 1–2 deamidation events, up to 40 different combinations, including the native amidated D3 peptide may be expected, as—according to our results—the different modifications do not counteract each other. However, first we do not see the native D3 peptide as a signal of its own. Signals for *m/z* 400.4885 (quadruply charged) or 320.59 (charge state 5+) corresponding to this species are only present underlying other signals, thus being only derived from in-source decay of the ion-pair or sulfonated analog. The same holds true for D3 analogs being deamidated. Second, we do not observe all combinations or some only at a very low intensity, making an unambiguous identification difficult. Third, on total, a large number of isobaric signals were observed, some of them but clearly not all attributable to site-specificity (O-sulfonation at threonine-8 versus –4, deamidation at C-terminus versus asparagine, as well as ion-pairing at different parts of the peptide with its high number of Arg-X-Arg motifs) (see discussion in section Determination of O-sulfonation sites). Most likely sterical effects leading to differences in the effective electrophoretic mobility are induced, which are well known to be separable with CE as was impressively demonstrated by Gaus et al. [37]. The possible formation of aspartic versus iso-aspartic acid may also have to be taken into account. It has to be noted that this site-specific information would be difficult or impossible to obtain by direct-infusion experiments and most likely by competing chromatographic interaction.

Reasons for complexity

According to the producer, no sulfate salt or sulfuric acid were used during the manufacturing process. However, covalent O-sulfonation was already observed in the LC-MS data provided by the vendor (data not shown). Screening the relatively scarce literature on threonine O-sulfonation, we came across two publications from 1993 [61], which describe O-sulfonation of serine and threonine as a side reaction in Fmoc solid state synthesis. The arginine side chain is most often protected via different arene sulfonyl chlorides leading to protecting groups such as MTR (4-methoxy-2,3,5-trimethylphenylsulfonyl) or PMC (2,2,5,7,8-pentamethylchroman-6-sufonyl) as well as PBF (2,2,4,6,7-pentamethyldihydrobenzofuran-5-sulfonyl) used for the synthesis here. This derivatization efficiently blocks the guanidino side chain but also requires a relatively long treatment with TFA for removal, which may lead to modifications of tryptophan (alkylation, transfer of full PMC residue), tyrosine (O-sulfonation), and arginine moieties (*N*-sulfonation at the side chain) [62]. Originally, PMC was optimized with regard to higher acid lability but increased compatibility for peptides with multiple arginine residues; however, the problem of tryptophan O-sulfonation was not completely abandoned despite the fast hydrolysis and, thus, a lower chance of intramolecular transfer [61, 63, 64]. Jaeger et al. [61] also observed O-sulfonation of serine and threonine side chains, which are O-tert-butyl protected. Relatively high yields from the transfer of the SO_2-group of PMC or MTR to threonines in case of disadvantageous cleavage conditions were reported. The reaction mechanism remained unclear, but it was discussed that the reaction may be scavenged upon addition of 5 % water to

TFA. It is likely that also PBF with its very similar structure faces the same problems.

From these results, the very high degree of O-sulfonation of threonine-8 in case of D3 can easily be anticipated by the high number of arginines present in the amino acid sequence, which requires a high number of PBF protecting groups. We can only speculate on the higher degree of threonine-8 versus threonine-4 O-sulfonation being due to the distance of the arginines to this residue probably facilitating the intramolecular transfer or the nucleophilic attack. Further work has to be done for the cleavage of the protection groups to suppress these side reactions. It is very interesting to note that the covalent O-sulfonation was not observed in case of L-D3 being synthesized in *E. coli*, further proving that side reactions in solid state synthesis are relevant for this modification (and not, as we first thought, covalent modification of D3 due to the very stable ion-pairs formed leading to a condensation reaction and, thus, covalent modification). However, for both L-D3 and D3, strong ion-pairing with sulfate is observed. This strong ion-pairing seems to be a characteristic of the molecule with its high number of guanidine side chains, most likely enhanced by the R-X-R motifs.

Variation of the amino acid sequence

Changes in the order of the amino acid sequence as well as deletion of histidines and/or threonines clearly change the observed binding pattern. As shown in Fig. 7, with just one threonine present, only single O-sulfonation is present as can be expected. Ion-pairing was observed for all modified D3 sequences, also when all arginines are present at the C-terminus of the peptide (Fig. 7a). However, from the ratio of the mass trace abundance of the ion-pair versus the free peptide, it can be concluded that the ion-pair formation constant in the gas phase is lowered.

The data presented in Fig. 7 also stress the covalent modification being related to threonine moieties. In contrast, ion-pairing with sulfate seems to depend on the arginine moieties (not histidines). Interestingly, all these peptides do not show a combination of both modifications, that is, O-sulfonation and ion-pairing present in one species. This may be reflected in the linker sequence LHTH present in D3, which gives rise to both peptide tails rich in arginines. In the other peptide sequences, this linker is reduced to only LTH, LH, or L, which is not sufficient to detect species with multiply bound sulfate and covalent sulfonate.

Conclusion

We here shown that CE-MS in contrast to HILIC-MS is a valuable tool for the characterization of extremely basic peptides, which show several modifications, here O-sulfonation, ion-pairing with sulfate and deamidation. The high separation selectivity of the electrophoretic separation of all evolving species differing in charge and/or structure was advantageously combined with impressive resolution optimization using coating strategies. O-sulfonation was confirmed with HR/AM FTICR-MS and the site of covalent O-sulfonation via ETD fragmentation. Overall, the efficient electrophoretic separation was vital because of the many isobaric species and the lability of the modifications prone to in-source decay. The method was also applied to D3 variants differing in the amino acid composition as well as L-D3 produced via *E. coli*. The comparison as well as literature work suppose that the covalent modification is an artifact from a side reaction (from the arginine protecting groups) during solid state synthesis. In contrast, the formation of very stable ion-pairs with sulfate is a basic characteristic of D3 and related species as it is also observed for D3 produced biotechnologically.

Currently we do not know if the strong formation of ion-pairs may be related to the therapeutic action of D3. Possibly, methionine autoxidation described due to Aβ peptides ability to catalyze H_2O_2 formation (similarity to superoxide dismutase), with the formation of S=O and O=S=O motifs is relevant here [65]. Further studies on the binding of Aβ to D3 are envisaged, which will advantageously be conducted with capillary electrophoresis. Here, no limitation on polarity (with D3 being extremely hydrophilic and Aβ peptides being very hydrophobic) is present as long as no adsorption onto the capillary coating occurs.

Acknowledgments The authors thank the Helmholtz Initiative and Networking Fund as well as the German Excellence Initiative commissioned by the German Research Foundation (DFG) for financial support.

References

1. Wimo A, Prince M (2010) World Alzheimer report 2010: the global economic impact of dementia. Alzheimer's Disease International, London. https://www.alz.co.uk/research/files/WorldAlzheimerReport2010.pdf. **Accessed 13 Jan 2015**
2. van Groen T, Wiesehan K, Funke SA, Kadish I, Nagel-Steger L, Willbold D (2008) Reduction of Alzheimer's disease amyloid plaque load in transgenic mice by D3, a D-enantiomeric peptide identified by mirror image phage display. Chem Med Chem 3: 1848–1852
3. Wiesehan K, Willbold D (2003) Mirror-image phage display: aiming at the mirror. Chem Bio Chem 4:811–815
4. Funke SA, Willbold D (2009) Mirror image phage display—a method to generate d-peptide ligands for use in diagnostic or therapeutical applications. Mol BioSyst 5:783–786
5. Sun N, Funke SA, Willbold D (2012) Mirror image phage display—generating stable therapeutically and diagnostically active peptides with biotechnological means. J Biotechnol 161:121–125
6. van Groen T, Kadish I, Wiesehan K, Funke SA, Willbold D (2009) In vitro and in vivo staining characteristics of small, fluorescent, Aβ42-binding D-enantiomeric peptides in transgenic AD mouse models. Chem Med Chem 4:276–282
7. Bartnik D, Funke SA, Andrei-Selmer L-C, Bacher M, Dodel R, Willbold D (2009) Differently selected D-enantiomeric peptides act on different Aβ species. Rejuvenation Res 13:202–205

8. Olubiyi OO, Frenzel D, Bartnik D, Gluck JM, Brener O, Nagel-Steger L, Funke SA, Willbold D, Strodel B (2014) Amyloid aggregation inhibitory mechanism of arginine-rich D-peptides. Curr Med Chem 21:1448–1457
9. Wang X, Carr PW (2007) An unexpected observation concerning the effect of anionic additives on the retention behavior of basic drugs and peptides in reversed-phase liquid chromatography. J Chromatogr A 1154:165–173
10. van Groen T, Kadish I, Funke A, Bartnik D, Willbold D (2012) In: Rossen D (ed) Advances in protein chemistry and structural biology. Academic Press: Elsevier, Amsterdam
11. van Groen T, Kadish I, Funke SA, Bartnik D, Willbold D (2013) Treatment with D3 removes amyloid deposits, reduces inflammation, and improves cognition in aged AβPP/PS1 double transgenic mice. J Alzheimers Dis 34:609–620
12. Funke SA, van Groen T, Kadish I, Bartnik D, Nagel-Steger L, Brener O, Sehl T, Batra-Safferling R, Moriscot C, Schoehn G, Horn AHC, Müller-Schiffmann A, Korth C, Sticht H, Willbold D (2010) Oral treatment with the d-enantiomeric peptide D3 improves the pathology and behavior of Alzheimer's disease transgenic mice. ACS Chem Neurosci 1:639–648
13. Kohno T, Kusunoki H, Sato K, Wakamatsu K (1998) A new general method for the biosynthesis of stable isotope-enriched peptides using a decahistidine-tagged ubiquitin fusion system: an application to the production of mastoparan-X uniformly enriched with 15N and 15N/13C. J Biomol NMR 12:109–121
14. Pattky M, Huhn C (2013) Advantages and limitations of a new cationic coating inducing a slow electroosmotic flow for CE-MS peptide analysis: a comparative study with commercial coatings. Anal Bioanal Chem 405:225–237
15. Nicolardi S, Giera M, Kooijman P, Kraj A, Chervet J-P, Deelder A, van der Burgt YM (2013) On-line electrochemical reduction of disulfide bonds: improved FTICR-CID and -ETD coverage of oxytocin and hepcidin. J Am Soc Mass Spectrom 24:1980–1987
16. Huhn C, Ramautar R, Wuhrer M, Somsen GW (2010) Relevance and use of capillary coatings in capillary electrophoresis-mass spectrometry. Anal Bioanal Chem 396:297–314
17. Lam MY, Siu SO, Lau E, Mao X, Sun HZ, Chiu PN, Yeung WB, Cox D, Chu I (2010) Online coupling of reverse-phase and hydrophilic interaction liquid chromatography for protein and glycoprotein characterization. Anal Bioanal Chem 398:791–804
18. McCalley DV (2005) Comparison of an organic polymeric column and a silica-based reversed-phase for the analysis of basic peptides by high-performance liquid chromatography. J Chromatogr A 1073:137–145
19. Aitken A, Learmonth M (2003) In: Smith B (ed) Protein sequencing protocols, vol 211. Methods in molecular biology. Humana Press, New York
20. Medzihradszky KF, Darula Z, Perlson E, Fainzilber M, Chalkley RJ, Ball H, Greenbaum D, Bogyo M, Tyson DR, Bradshaw RA, Burlingame AL (2004) O-sulfonation of serine and threonine : mass spectrometric detection and characterization of a new post-translational modification in diverse proteins throughout the eukaryotes. Mol Cell Proteomics 3:429–440
21. Shibue M, Mant CT, Hodges RS (2005) Effect of anionic ion-pairing reagent concentration (1–60 mM) on reversed-phase liquid chromatography elution behavior of peptides. J Chromatogr A 1080:58–67
22. Lerro KA, Orlando R, Zhang HZ, Usherwood PNR, Nakanishi K (1993) Separation of the sticky peptides from membrane proteins by high-performance liquid chromatography in a normal-phase system. Anal Biochem 215:38–44
23. Kostiainen R, Kauppila TJ (2009) Effect of eluent on the ionization process in liquid chromatography–mass spectrometry. J Chromatogr A 1216:685–699
24. Neubert H, James I (2009) Online capillary weak cation exchange enrichment hyphenated to nanospray mass spectrometry for quantitation of a basic pegvisomant derived peptide. J Chromatogr A 1216:6151–6154
25. Jandera P (2011) Stationary and mobile phases in hydrophilic interaction chromatography: a review. Anal Chim Acta 692:1–25
26. Yoshida T (2004) Peptide separation by hydrophilic-interaction chromatography: a review. J Biochem Biophys Methods 60:265–280
27. Zauner G, Deelder AM, Wuhrer M (2011) Recent advances in hydrophilic interaction liquid chromatography (HILIC) for structural glycomics. Electrophoresis 32:3456–3466
28. Singer D, Kuhlmann J, Muschket M, Hoffmann R (2010) Separation of multiphosphorylated peptide isomers by hydrophilic interaction chromatography on an aminopropyl phase. Anal Chem 82:6409–6414
29. Alpert AJ (2008) Electrostatic repulsion hydrophilic interaction chromatography for isocratic separation of charged solutes and selective isolation of phosphopeptides. Anal Chem 80:62–76
30. Jiang W, Fischer G, Girmay Y, Irgum K (2006) Zwitterionic stationary phase with covalently bonded phosphorylcholine type polymer grafts and its applicability to separation of peptides in the hydrophilic interaction liquid chromatography mode. J Chromatogr A 1127:82–91
31. Lämmerhofer M, Nogueira R, Lindner W (2011) Multi-modal applicability of a reversed-phase/weak-anion exchange material in reversed-phase, anion-exchange, ion-exclusion, hydrophilic interaction, and hydrophobic interaction chromatography modes. Anal Bioanal Chem 400:2517–2530
32. Boysen RI, Yang Y, Chowdhury J, Matyska MT, Pesek JJ, Hearn MTW (2011) Simultaneous separation of hydrophobic and hydrophilic peptides with a silica hydride stationary phase using aqueous normal phase conditions. J Chromatogr A 1218:8021–8026
33. Wilce MCJ, Aguilar M-I, Hearn MTW (1995) Physicochemical basis of amino acid hydrophobicity scales: evaluation of four new scales of amino acid hydrophobicity coefficients derived from RP-HPLC of peptides. Anal Chem 67:1210–1219
34. Schmitt-Kopplin P, Frommberger M (2003) Capillary electrophoresis-mass spectrometry: 15 years of developments and applications. Electrophoresis 24:3837–3867
35. Fonslow BR, Yates JR III (2009) Capillary electrophoresis applied to proteomic analysis. J Sep Sci 32:1175–1188
36. Gennaro LA, Salas-Solano O (2009) Characterization of deamidated peptide variants by micropreparative capillary electrophoresis and mass spectrometry. J Chromatogr A 1216:4499–4503
37. Gaus HJ, Beck-Sickinger AG, Bayer E (1993) Optimization of capillary electrophoresis of mixtures of basic peptides and comparison with HPLC. Anal Chem 65:1399–1405
38. Timm V, Gruber P, Wasiliu M, Lindhofer H, Chelius D (2010) Identification and characterization of oxidation and deamidation sites in monoclonal rat/mouse hybrid antibodies. J Chromatogr B 878:777–784
39. Lai M, Skanchy D, Stobaugh J, Topp E (1998) Capillary electrophoresis separation of an asparagine containing hexapeptide and its deamidation products. J Pharm Biomed Anal 18:421–427
40. Timerbaev AR (2000) Element speciation analysis by capillary electrophoresis. Talanta 52:573–606

41. Schug KA, Lindner W (2004) Noncovalent binding between guanidinium and anionic groups: focus on biological- and synthetic-based arginine/guanidinium interactions with phosph[o-n]ate and sulf[on]ate residues. Chem Rev 105:67–114
42. Kim J, Zand R, Lubman DM (2002) Electrophoretic mobility for peptides with post-translational modifications in capillary electrophoresis. Electrophoresis 23:782–793
43. Pattky M, Huhn C (2010) Protein glycosylation analysis with capillary-based electromigrative separation techniques. Bioanal Rev 2:115–155
44. Young SY, Ye SH, Moo JS, Park J (1997) Analysis of phosphopeptides by capillary electrophoresis and matrix-assisted laser-desorption ionization-time-of-flight mass spectrometry. J Chromatogr A 763: 285–293
45. Dong Y-M, Chien K-Y, Chen J-T, Lin S-J, Yu J-S, Wang T-CV (2013) Site-specific separation and detection of phosphopeptide isomers with pH-mediated stacking capillary electrophoresis-electrospray ionization-tandem mass spectrometry. J Sep Sci 36:1582–1589
46. Tadey T, Purdy WC (1995) Capillary electrophoretic resolution of phosphorylated peptide isomers using micellar solutions and coated capillaries. Electrophoresis 16:574–579
47. Dawson JF, Boland MP, Holmes CFB (1994) A capillary electrophoresis-based assay for protein kinases and protein phosphatases using peptide substrates. Anal Biochem 220:340–345
48. Boersema PJ, Mohammed S, Heck AJR (2009) Phosphopeptide fragmentation and analysis by mass spectrometry. J Mass Spectrom 44:861–878
49. Seibert C, Sakmar TP (2008) Toward a framework for sulfoproteomics: synthesis and characterization of sulfotyrosine-containing peptides. Pept Sci 90:459–477
50. Drake SK, Hortin GL (2010) Improved detection of intact tyrosine sulfate-containing peptides by matrix-assisted laser desorption/ionization time-of-flight mass spectrometry in linear negative ion mode. Int J Biochem Cell Biol 42:174–179
51. Kim J-S, Song S-U, Kim H-J (2011) Simultaneous identification of tyrosine phosphorylation and sulfation sites utilizing tyrosine-specific bromination. J Am Soc Mass Spectrom 22:1916–1925
52. Li W, Backlund PS, Boykins RA, Wang G, Chen H-C (2003) Susceptibility of the hydroxyl groups in serine and threonine to β-elimination/Michael addition under commonly used moderately high-temperature conditions. Anal Biochem 323:94–102
53. Yu Y, Hoffhines AJ, Moore KL, Leary JA (2007) Determination of the sites of tyrosine O-sulfation in peptides and proteins. Nat Methods 4:583–588
54. Cantel S, Brunel L, Ohara K, Enjalbal C, Martinez J, Vasseur J-J, Smietana M (2012) An innovative strategy for sulfopeptides analysis using MALDI-TOF MS reflectron positive ion mode. Proteomics 12:2247–2257
55. Stensballe A, Jensen ON, Olsen JV, Haselmann KF, Zubarev RA (2000) Electron capture dissociation of singly and multiply phosphorylated peptides. Rapid Commun Mass Spectrom 14:1793–1800
56. Macek B, Mann M, Olsen JV (2009) Global and site-specific quantitative phosphoproteomics: principles and applications. Annu Rev Pharmacol Toxicol 49:199–221
57. Monigatti F, Hekking B, Steen H (2006) Protein sulfation analysis—a primer. Biochim Biophys Acta Proteins Proteomics 1764: 1904–1913
58. Bakhtiar R, Guan Z (2006) Electron capture dissociation mass spectrometry in characterization of peptides and proteins. Biotechnol Lett 28:1047–1059
59. Mikesh LM, Ueberheide B, Chi A, Coon JJ, Syka JEP, Shabanowitz J, Hunt DF (2006) The utility of ETD mass spectrometry in proteomic analysis. Biochim Biophys Acta Proteins Proteomics 1764:1811–1822
60. Crowe MC, Brodbelt JS (2004) Infrared multiphoton dissociation (IRMPD) and collisionally activated dissociation of peptides in a quadrupole ion trap with selective IRMPD of phosphopeptides. J Am Soc Mass Spectrom 15:1581–1592
61. Jaeger E, Remmer HA, Jung G, Metzger J, Oberthür W, Rücknagel KP, Schäfer W, Johann S, Zetl I (1993) Nebenreaktionen bei peptidsynthesen, V. O-sulfonierung von serin und threonin während der abspaltung der pmc- und mtr-schutzgruppen von argininresten bei fmoc-festphasen-synthesen. Biol Chem 374: 349–362
62. Beck-Sickinger AG, Schnorrenberg G, Metzger J, Jung G (1991) Sulfonation of arginine residues as side reaction in Fmoc-peptide synthesis. Int J Pept Protein Res 38:25–31
63. Green J, Ogunjobi OM, Ramage R, Stewart ASJ, McCurdy S, Noble R (1988) Application of the NG-(2,2,5,7,8-pentamethylchroman-6-sulphonyl) derivative of FMOC-arginine to peptide synthesis. Tetrahedron Lett 29:4341–4344
64. Ramage R, Green J (1987) NG-2,2,5,7,8-pentamethylchroman-6-sulphonyl-L-arginine: a new acid labile derivative for peptide synthesis. Tetrahedron Lett 28:2287–2290
65. Head E, Garzon-Rodriguez W, Johnson JK, Lott IT, Cotman CW, Glabe C (2001) Oxidation of Aβ and plaque biogenesis in Alzheimer's disease and Down syndrome. Neurobiol Dis 8:792–806

Martin Pattky is a Postdoctoral Researcher at the Eberhard Karls Universität Tübingen, Germany. His work focuses on the development and optimization of CE-MS methods for bioanalytical questions in pharmacy, medicine, and environmental analysis.

Simone Nicolardi is Postdoctoral Researcher at the Center for Proteomics and Metabolomics of the Leiden University Medical Center in the Netherlands. His work focuses on the development of ultra-high resolution mass spectrometry-based methods for the analysis of body fluid-derived peptides and proteins in a clinical setting.

Daniel Sydes is a PhD student in analytical chemistry in the working group of Professor Carolin Huhn at the Eberhard Karls Universität Tübingen, Germany. He studied BSc "Water Science" in Duisburg/Essen, Germany, and graduated with the degree of MSc. in analytical chemistry, at the Leibniz Universität Hannover, Germany. He is working on instrumental and method development of multidimensional electrophoretic separation platforms, with a special regard to the coupling of 2D CIEF/CE-MS for protein analysis.

Yuri E.M. van der Burgt obtained his PhD in bio-organic chemistry at Utrecht University in the Netherlands. He works as an Associate Professor at the Leiden University Medical Center and is responsible for multiple MS-platforms that are applied both for in-depth analyses and high-throughput clinical proteomics studies.

Antonia Nicole Klein is a Scientist at the Institute of Complex Systems, Structural Biochemistry (ICS-6) at the Research Center Jülich, Germany. She obtained a diploma in biosystems engineering in 2012 from the Otto-von-Guericke University Magdeburg. Her research focuses on the development and characterization of D-peptides for the treatment of Alzheimer's disease. Currently, she is carrying out her PhD in biology at the University of Düsseldorf.

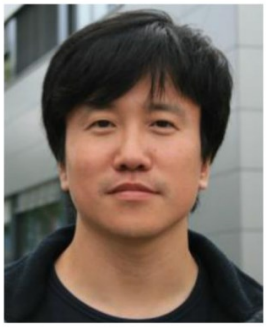

Nan Jiang is Research Assistant at the Institute of Complex Systems (ICS-6) in Forschungszentrum Jülich, Germany. He is working on preclinical pharmacokinetic, therapeutic, and diagnostic studies of Aβ-aggregation modulating D-peptides on mouse models for the treatment of Alzheimer's disease.

Jeannine Mohrlüder is a Scientist at the Research Centre in Jülich, Germany. Her current work focuses on the identification and characterization of protein–protein interactions. She majored in Biology at Gutenberg University of Mainz, Germany, at University of Montpellier II, Faculté des sciences, France, and at University of Cologne, Germany, where she passed her diploma thesis in biochemistry. She obtained a PhD from the Heinrich-Heine University of Düsseldorf, Germany.

Janine Kutzsche is Group Leader at the Institute of Complex Systems–Structural Biochemistry (ICS-6), Forschungszentrum Jülich, Germany. She is working on the development of Aβ-aggregation modulating D-peptides for the therapy of Alzheimer's disease.

Susanne Aileen Funke is Professor for molecular biology at the University of Applied Sciences in Coburg, Germany. Her research focuses on the investigation of protein–protein interactions, especially in the fields of neurodegenerative diseases, diagnostics, and food technology.

Carolin Huhn is Professor for Effect-based Environmental Analysis at the Eberhard Karls Universität Tübingen and has been a speaker of the platform Environmental System Analysis since 2013. Her research interests cover all aspects of analytical chemistry: instrumental development, analytical basic research, method development, and application. Major focuses are electromigrative separation techniques and their application in forensics, pharmacy, clinics, and environmental bioanalysis.

Dieter Willbold is Full Professor for physical biology at the Heinrich Heine University, Düsseldorf, and Director of the Institute of Complex Systems at the Research Centre Jülich. He uses state-of-the-art techniques to decipher the complex three-dimensional structures of proteins and their interactions. This provides the basis for an understanding of how these proteins work, thus contributing to the development of methods for early diagnosis and treatment of neurodegenerative diseases

2.2 Preclinical pharmacokinetic studies of the tritium labelled D-enantiomeric peptide D3 developed for the treatment of Alzheimer´s disease.

Published in: PloS ONE

Impact Factor: 3.23

Contributions: 80%

Involved in the conception and design of the experiments; except for protein-binding assay, conducted all the rest of experimental parts and data analysis; involved in data analysis of protein-binding assay; involved in writing the manuscript.

PLOS | ONE

RESEARCH ARTICLE

Preclinical Pharmacokinetic Studies of the Tritium Labelled D-Enantiomeric Peptide D3 Developed for the Treatment of Alzheimer´s Disease

Nan Jiang[1], Leonie H. E. Leithold[1], Julia Post[1], Tamar Ziehm[1], Jörg Mauler[2], Lothar Gremer[1], Markus Cremer[3], Elena Schartmann[1], N. Jon Shah[2], Janine Kutzsche[1], Karl-Josef Langen[2,4], Jörg Breitkreutz[5], Dieter Willbold[1,6]*, Antje Willuweit[2]*

1 Structural Biochemistry, Institute of Complex Systems (ICS-6), Forschungszentrum Jülich GmbH, Jülich, Germany, **2** Medical Imaging Physics, Institute of Neuroscience and Medicine (INM-4), Forschungszentrum Jülich GmbH, Jülich, Germany, **3** Structural and functional organisation of the brain, Institute of Neuroscience and Medicine (INM-1), Forschungszentrum Jülich GmbH, Jülich, Germany, **4** Department of Nuclear Medicine, Universitätsklinikum der RWTH Aachen, Aachen, Germany, **5** Institute of Pharmaceutics and Biopharmaceutics, Heinrich-Heine-Universität Düsseldorf, Düsseldorf, Germany, **6** Institut für Physikalische Biologie, Heinrich-Heine-Universität Düsseldorf, Düsseldorf, Germany

* D.Willbold@fz-juelich.de (DW); A.Willuweit@fz-juelich.de (AW)

OPEN ACCESS

Citation: Jiang N, Leithold LHE, Post J, Ziehm T, Mauler J, Gremer L, et al. (2015) Preclinical Pharmacokinetic Studies of the Tritium Labelled D-Enantiomeric Peptide D3 Developed for the Treatment of Alzheimer´s Disease. PLoS ONE 10(6): e0128553. doi:10.1371/journal.pone.0128553

Academic Editor: Riqiang Yan, Cleveland Clinic Foundation, UNITED STATES

Received: March 4, 2015

Accepted: April 28, 2015

Published: June 5, 2015

Data Availability Statement: All relevant data are within the paper and its Supporting Information files.

Funding: DW was supported by grants from the "Portfolio Technology and Medicine" and the Helmholtz-Validierungsfonds of the Impuls und Vernetzungs-Fonds der Helmholtzgemeinschaft; KJL and DW were supported by the "Portfolio Drug Design" of the Impuls und Vernetzungs-Fonds der Helmholtzgemeinschaft (http://www.helmholtz.de/ueber_uns/impuls_und_vernetzungsfonds; no grant numbers available). The funders had no role in study

Abstract

Targeting toxic amyloid beta (Aβ) oligomers is currently a very attractive drug development strategy for treatment of Alzheimer´s disease. Using mirror-image phage display against Aβ1-42, we have previously identified the fully D-enantiomeric peptide D3, which is able to eliminate Aβ oligomers and has proven therapeutic potential in transgenic Alzheimer´s disease animal models. However, there is little information on the pharmacokinetic behaviour of D-enantiomeric peptides in general. Therefore, we conducted experiments with the tritium labelled D-peptide D3 (^{3}H-D3) in mice with different administration routes to study its distribution in liver, kidney, brain, plasma and gastrointestinal tract, as well as its bioavailability by i.p. and p.o. administration. In addition, we investigated the metabolic stability in liver microsomes, mouse plasma, brain, liver and kidney homogenates, and estimated the plasma protein binding. Based on its high stability and long biological half-life, our pharmacokinetic results support the therapeutic potential of D-peptides in general, with D3 being a new promising drug candidate for Alzheimer´s disease treatment.

Introduction

After the initial description by Alois Alzheimer in 1906 [1], Alzheimer's disease (AD), a progressive neurodegenerative disorder, has become nowadays the most common form (60–80%) of dementia [2]. According to the World Alzheimer Report 2014, nearly 36 million people worldwide are suffering from AD or related dementia. Even after years of intensive

design, data collection and analysis, decision to publish, or preparation of the manuscript.

Competing Interests: The authors have declared that no competing interests exist.

investigation and research, it is still an incurable disease [3]. Current treatments are only supportive against some of its symptoms. Clinical duration of AD varies from one to 25 years, typically eight to ten years [4].

Amyloid beta (Aβ) is produced by sequential cleavage of a type I integral transmembrane protein, called amyloid precursor protein (APP) by β- and γ-secretases. Variable lengths of Aβ isomers differing at the C-terminus are produced due to imprecise cleavage by γ-secretase [5, 6]. The most abundant isomers are Aβ1–40 (approximately 80–90%) and Aβ1–42 (approximately 5–10%). Aβ1–42 is more hydrophobic and fibrillogenic, and therefore the main component of Aβ plaques in the brain of AD patients [7]. It also aggregates readily into oligomers, which are considered to be the most toxic form of Aβ [8–10].

In recent years, many substances have been developed targeting Aβ production and clearance [11], including peptide-based drugs [12, 13]. In spite of the many advantages of peptide drugs, for example high specificity and low toxicity, their short half-life time *in vivo* due to rapid degradation by proteases, and low bioavailability by oral administration, restrict their clinical usage. In comparison to naturally occurring L-form peptides, peptides derived from partial D-amino acid substitutions or D-enantiomeric peptides, which are composed entirely of D-amino acids, have advantages over L-enantiomers. Because of the stereoisomeric selectivity of proteolytic enzymes they are less prone to proteolysis, therefore longer half-lives and higher bioavailability after oral administration are to be expected [14–16]. Furthermore, they are less or even not immunogenic at all [13].

The fully D-enantiomeric peptide D3, which was identified by mirror-image phage display [17, 18] for binding to Aβ (1–42), has been shown to have interesting properties. D3 inhibits Aβ fibril formation and eliminates Aβ-oligomers *in vitro*. *Ex vivo*, D3 has been shown to specifically bind to amyloid plaques in transgenic mice [19]. *In vivo*, D3 was able to reduce plaque load and inflammation markers in the brains of treated transgenic mice, as well as improve their cognition even after oral administration [20–23]. Here we investigate the pharmacokinetic properties of D3 in mice.

We present the first comprehensive preclinical pharmacokinetic study of a peptide consisting solely of D-enantiomeric amino acid residues in general and in particular for such a D-peptide developed for the treatment of Alzheimer's disease.

Materials and Methods

Materials

^{3}H-D3 (rprtr-(4,5-^{3}H-Leu)-hthrnr) and its L-form enantiomer ^{3}H-(L)-D3 (RPRTR-(4,5-^{3}H-Leu)-HTHRNR) were purchased from Quotient Bioresearch (Radiochemicals) Ltd. (Cardiff, United Kingdom) with 10–100 Ci/mmol, 1 mCi/ml and purity >95%.

All chemicals were supplied by Fluka Chemie AG (Buchs, Switzerland), Merck (Darmstadt, Germany), AppliChem (Darmstadt, Germany) and VWR (Darmstadt, Germany) in research grade. Micro-osmotic pumps (model 1007D) were purchased from Alzet DURECT Corporation, (Cupertino, CA, USA).

Animals

Male C57Bl/6 mice (Charles River, Sulzfeld Germany) with an average age of 13 weeks and body weight of 28.5 g were used in this study. For micro-osmotic pump i.p. implantation experiment, 19 months old mice were used with average body weight of 34 g. The mice were hosted in the animal facility of the Forschungszentrum Juelich under standard housing conditions with free access to food and water for at least 2 weeks before experiment. All animal experiments were approved by the Animal Protection Committee of the local government

(LANUV (Landesamt für Natur, Umwelt und Verbraucherschutz), North-Rhine-Westphalia, Germany, AZ84-02.04.2011. A359 and AZ84-02.04.2011. A356) according to the Deutsche Tierschutzgesetz). All sections of this study adhere to the ARRIVE Guidelines for reporting animal research [24]. A completed ARRIVE guidelines checklist was included in Supporting Information (S1 File).

Pharmacokinetic studies

Mice were administered with 100 μl radioactive working solution consisting of 5 μCi ^{3}H-D3 in 5 μl with 95 μl buffer (0.1 M phosphate buffer, pH 8) as a single bolus dose either i.v. (tail vein), i.p. or p.o. (gavaging). In order to achieve the desired total D3 concentration, non-radioactive D3 was added to a concentration of 1 mg/ml (i.v.) or 3 mg/ml (i.p. and p.o.). Doses were selected from previous tolerability studies and were not causing any adverse effects. I.v. injections and i.p micro-osmotic pump implantations were performed under anaesthesia with ketamine/medetomidine per i.p. administration. Antisedan was administered s.c. to reverse the anaesthesia directly after the intervention, which took about 10 min. Sampling times were chosen depending on the route of administration (i.p.: 10, 20, 30, 60, 120, 240, 360, 1440 and 2880 min.; p.o.: 10, 20, 30, 60, 120, 240, 360, 1080, 1440, 2880 and 4320 min.; i.v.: 3, 5, 10, 15, 30, 60, 240, 1440 and 2880 min.; 3 animals per time point). For i.p. micro-osmotic pump implantation, delivery dose of pumps was set to 5 μCi ^{3}H-D3 plus 0.3 mg non-radioactive D3 per 24 hours per mouse. Sampling times were 2, 4 and 6 days after implantation (3 mice per time point).

Upon sampling time, blood was drawn per heart puncture under isoflurane anaesthesia and heparinized plasma was isolated. A small piece of liver (approx. 0.2 g), the left kidney and the right brain hemisphere were sampled. To study the gastrointestinal absorption and elimination by p.o. administration, mice were fasted 18 hours before the experiment and their complete gastrointestinal tracts were prepared. Small intestine was dissected into 4 equal parts and marked from oral to aboral as 1 to 4, respectively. Organ samples were weighted and homogenized in homogenizer tubes (Precellys Ceramic Kit 1.4 mm, Precellys 24, Bertin technologies SAS, Montigny le Bretonneux, France) with 500 μl PBS. 10 ml scintillation cocktail (Ultima Gold XR, PerkinElmer, Waltham, Massachusetts, USA) was added to 100 μl of each organ homogenate or plasma (diluted 1:1 with PBS) and mixed well. Disintegrations per unit time (dpm) were obtained in triplicates with a liquid scintillation counter (Packard Tri-Carb 2100TR Liquid Scintillation Analyser, PerkinElmer, Waltham, MA, USA). Blank values of each sample were obtained by omitting radioactive substance following the same protocol.

Radioactivity counted in each sample was adjusted (subtraction of the blank value) and was expressed as percentage injected dose per gram tissue or millilitre plasma (%ID/g or %ID/ml), or as milligram of total D3 per gram tissue or millilitre plasma (mg/g or mg/ml).

Pharmacokinetic analysis

Pharmacokinetic parameters were calculated with non-compartmental analysis using Phoenix WinNonlin, version 6.3 (Pharsight Corp., St. Louis, USA). Mean D3 concentrations per time point were used to calculate the PK parameters (model type: plasma (200–202); calculation method: linear trapezoidal linear interpolation; dose options: "IV Bolus" for i.v. or "Extravascular" for i.p. and p.o. administration). The same model setting was used to estimate pharmacokinetic parameters of brain. For i.v. administration, plasma concentration at time zero (C0) was back extrapolated with a log-linear regression of the first two observed plasma concentrations, while brain C0 was set to be zero. For the i.p. and p.o. administrations, all concentrations at time zero were set to be zero.

The last three to five observed mean plasma concentrations were used to estimate the first order rate constant in the terminal elimination phase (Lambda_z) based on the largest adjusted square of the correlation coefficient (R^2) of the log-linear regression lines. The area under the curve (AUC) from C0 extrapolated to infinity ($AUC_{C0\text{-}inf}$) was calculated as the sum of $AUC_{C0\text{-}last}$+(Clast/Lambda_z), calculated from the last determined concentration derived by Lambda_z, and $AUC_{C0\text{-}last}$ representing the AUC from time point zero to the last observed concentration (Clast). Parameters that do not require Lambda_z were calculated for brain data: time of maximal observed concentration (Tmax), maximal observed concentration (Cmax), maximal observed concentration normalized to dose (Cmax/D), $AUC_{C0\text{-}last}$ and mean residence time from the time of dosing to the last time point ($MRT_{C0\text{-}last}$). Additional parameters requiring estimated Lambda_z were calculated for plasma data: Lambda_z, terminal half-life (HL_Lambda_z), $AUC_{C0\text{-}inf}$, terminal volume of distribution (Vz), plasma clearance (Cl), $MRT_{C0\text{-}inf}$ and volume of distribution at steady state (Vss). Absolute bioavailability of i.p. and p.o. administration was calculated with $AUC_{C0\text{-}inf}$ by: F(bioavailability) = [AUC(non-iv)*Dose (iv)]/[AUC(iv)*Dose(non-iv)]*100.

To minimize the time dependence of brain-plasma ratio by bolus dosing, brain-plasma ratio was calculated from the areas under the brain and plasma concentration curves in the terminal elimination phase starting from 4 hours to infinity ($brain\_AUC_{4h\text{-}inf}$/$plasma\_AUC_{4h\text{-}inf}$).

Plasma protein binding

Plasma protein binding was estimated by incubation of D3 with varying concentrations of protein using TRANSIL^{XL} binding kits (Sovicell GmbH, Leipzig, Germany). K_D values were determined by titrating a constant drug concentration against different concentrations of human serum albumin (HSA) and α_1-acid glycoprotein (AGP). Experiments were performed as recommended for the kit. To obtain the desired D3 stock solution of 80 μM, non-radioactively labelled D3 was dissolved in PBS and 5% ^{3}H-labelled D3 solution was added for detection purposes. A final concentration of 5 μM D3 was applied in the assay. After incubation and centrifugation 15 μl supernatant were taken and scintillation cocktail was added. This was done in triplicate. Radioactivity was then quantified using liquid scintillation counting. After measuring the disintegrations per minute (dpm) of the supernatant containing the unbound peptide, the D3 fraction bound to the titrated protein was calculated and plotted against the protein concentrations. The curves were fitted to the Michaelis Menten ligand binding equation (SigmaPlot 11.0, Systat Software, Inc., San Jose, California, USA) to obtain the K_D. Mean and relative standard error (%) of multiple measurements are given (AGP n = 3, HSA n = 2).

For bioavailability determination, the unbound fraction of D3 (f_u) was calculated using the equation below:

$$f_u = 100 * \frac{\frac{C_{D3}-K_D-C_{physiol}}{2} + \sqrt{K_D * C_{D3} + \left(\frac{C_{D3}-K_D-C_{physiol}}{2}\right)^2}}{C_{D3}} \quad (1)$$

For very low D3 concentrations in blood (C_{D3}), Eq (1) can be simplified by Eq (2), where the unbound fraction of D3 can be calculated independently of the applied D3 concentration. Since this is true for our *in vivo* experiments we used Eq (2) for the total free fraction of D3, combining the binding of D3 to HSA and AGP. For calculation of the overall unbound fraction according to Eq (2), physiological concentrations ($C_{physiol}$) of 0.65 mM HSA and 0.02 mM

AGP were assumed.

$$f_{u,total} = 100 * \frac{1}{1 + \frac{C_{physiolHSA}}{K_D HSA} + \frac{C_{physiolAGP}}{K_D AGP}} \quad (2)$$

Calibration curves and internal standard

Calibration curves were prepared by adding a corresponding ^{3}H-D3 dilution series with certain dpm range to plasma or organ homogenates in comparison to those diluted in PBS. The dpm ranges of each ^{3}H-D3 dilution series were set to cover the measured dpm ranges of each sample (for plasma 400–40000; for brain 100–1200; for liver 3000–15000; for kidney 40000–400000). Plasma and organ homogenates obtained from C57Bl/6 mice were prepared following the same procedure as outlined above.

No differences were found comparing the calibration curves of ^{3}H-D3 in organ homogenates or plasma to those in PBS. The measured dpm values of the internal standard with ^{3}H-D3 in PBS matched closely the expected ones.

Thin layer chromatography

In order to study the proteolytic stability of peptides in biological extracts, tritium labelled peptides were incubated with liver microsomes (pooled from mouse (CD-1), Sigma-Aldrich), freshly prepared mouse plasma or extracts of brain, liver and kidney at 37°C for different time periods (from 0 min to 2 days). 1 μCi (approx. 0.08–0.8 μg) radioactive labelled peptide was mixed with 1 μl microsomes stock solution, plasma or organ extracts, respectively (in great excess to peptide). Mixtures containing tritium-labelled peptides were applied onto HPTLC Silica Gel 60 plates (OMNILAB, Essen, Germany) for thin layer chromatography (TLC) with a mobile solvent (2-Butanol/Pyridine/Ammonia(28%)/Water(39/34/10/26)). After development, a phosphor imaging plate for ^{3}H-autoradiography (FUJIFILM, Tokyo, Japan) was exposed to the TLC plates for 3 days. Images were acquired with a BAS reader and AIDA software (Raytest, Freiburg, Germany). Retardation factor (Rf) of each substance was defined as the ratio of the migration distance of the centre of a separated spot to the migration distance of the solvent front.

Results

Proteolytic stability of D3 in comparison to its L-enantiomer

Before meaningful pharmacokinetic studies could be performed with ^{3}H-D3, it was essential to show that the D-peptide is stable under near *in vivo* conditions. First, we compared the stability of ^{3}H-D3 with its exact enantiomer, ^{3}H-(L)-D3 in plasma (Fig 1). ^{3}H-(L)-D3 shows significant degradation already after 60 min incubation in plasma as concluded by the appearance of additional bands as compared to the mixture at 0 min on the TLC plate after detection by autoradiography. In contrast, ^{3}H-D3 did not show any degradation products even after 2 d incubation in the same plasma preparation.

More importantly, ^{3}H-D3, was neither degraded after 2 h incubation in liver microsomes nor after 2 days incubation in homogenates of kidney, brain and liver as shown by TLC and detection by autoradiography (Fig 2). Microsomes were checked for proteolytic activity using L-peptide substrates.

Due to high but unspecific affinity of D3 and (L)-D3 to the TLC plate support material (glass), artefacts were observed at the starting points of the TLC as well as light smears

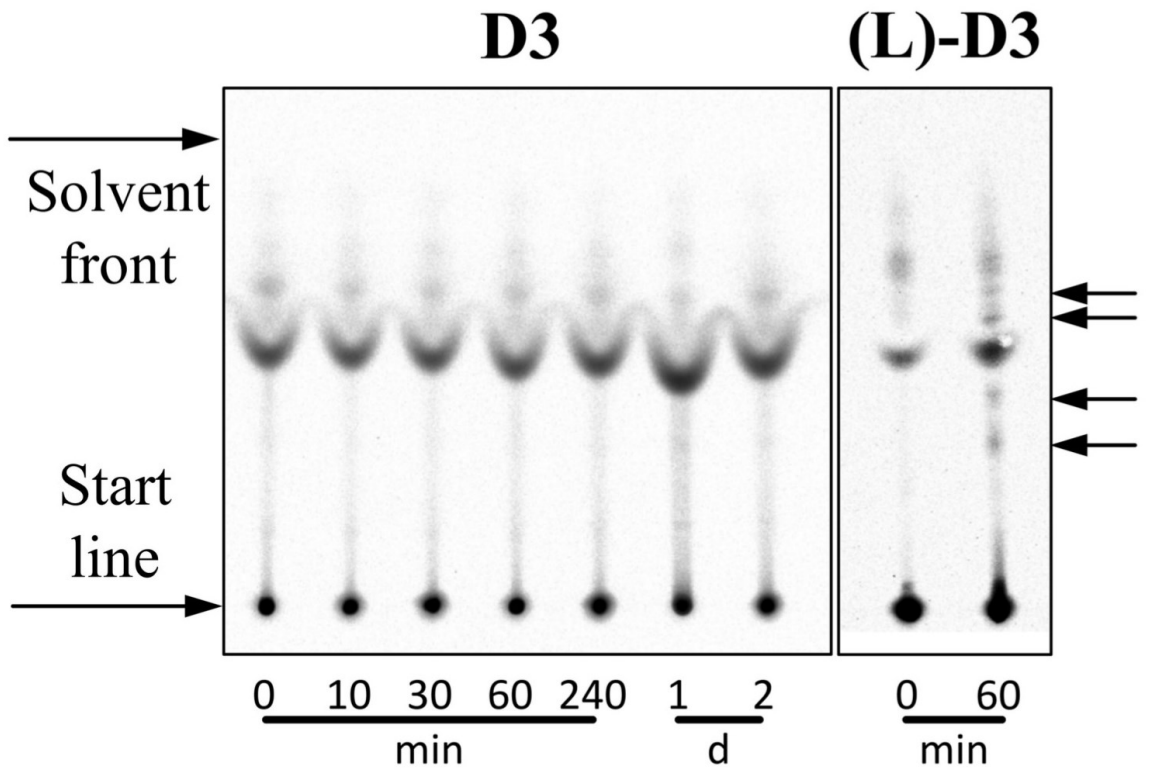

Fig 1. Autoradiogram demonstrating proteolytic stability of ^{3}H labelled peptides in plasma. ^{3}H-D3 was incubated with plasma for different times at 37°C and developed on TLC plates. For comparison, the exact enantiomer of D3, (L)-D3, was used in this stability assay. ^{3}H-(L)-D3 was incubated with plasma for 0 and 60 min at 37°C. Please note that free ^{3}H-(L)-D3 and free ^{3}H-D3 are perfect enantiomers to each other and because the TLC material is not chiral, both compounds show identical Rf values. Additional bands in the 0 min lanes of ^{3}H-(L)-D3 and ^{3}H-D3 that arise from binding and co-migration of ^{3}H-D3 and ^{3}H-(L)-D3 to plasma components do not necessarily have identical Rf values in the 0 min lanes of ^{3}H-(L)-D3 and ^{3}H-D3, because some of the plasma components are enantiomers themselves. Therefore, any effect of degradation will lead to extra additional bands as compared to the 0 min lane of the very same compound. Obvious proteolytic degradation can be observed for ^{3}H-(L)-D3 already after 60 min incubation with plasma leading to additionally appearing bands (black arrows) as compared to the 0 min lane ^{3}H-(L)-D3. Additionally appearing bands as compared to 0 min incubation are not observed for ^{3}H-D3 even after 2 days incubation.

doi:10.1371/journal.pone.0128553.g001

originating thereof. To prove that these compounds were not located in the layer of the TLC matrices, a control experiment was performed by placing a new TLC plate to a freshly developed plate to transfer only the ^{3}H-peptides within matrices, but not those on the glass surface support (Fig 3). Artefacts could thus be eliminated.

Pharmacokinetics

Time dependent distribution of D3 in organs and plasma after different administration routes was analysed using tritium labelled D3 (^{3}H-D3) as shown in Fig 4. The corresponding pharmacokinetic parameters calculated with non-compartmental analysis based on the absolute amount of administered D3 are shown in Tables 1 and 2.

After i.v. and i.p. administration, pharmacokinetic curves showed similar patterns with highest concentration of tritium per gram tissue found in kidney, followed by liver and plasma.

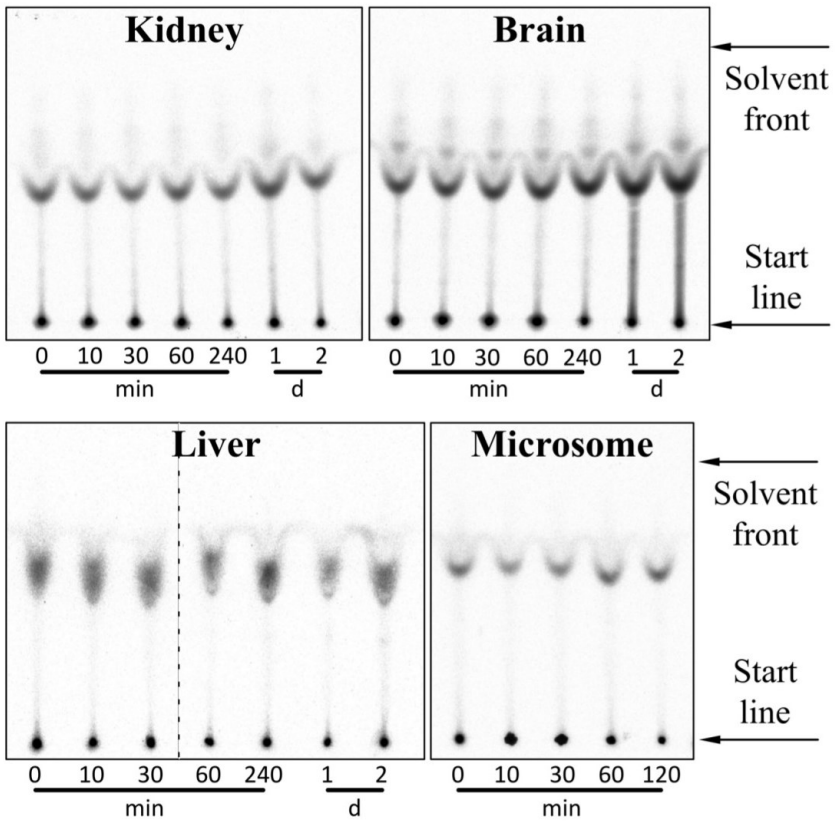

Fig 2. Autoradiogram demonstrating proteolytic stability of ^{3}H labelled peptides in liver microsomes and organ homogenates. ^{3}H-D3 was incubated with kidney, brain and liver homogenate for 0, 10, 30, 60, 240 min and 1, 2 days at 37°C and developed on TLC plates. For liver microsomes, the incubation time was 0, 10, 30, 60 and 120 min. Slight difference in Rf values of ^{3}H-D3 in liver homogenate might be due to incompletely homogenized liver tissues, which was not observed after incubation with liver microsomes. (Two autoradiograms of liver homogenate were presented in one image and separated through a dashed line.) No obvious proteolytic degradation of D3 can be observed in all the organ homogenates with up to two days' incubation.

doi:10.1371/journal.pone.0128553.g002

However, after oral administration ^{3}H-D3 concentrations measured in kidney and liver did not exceed concentrations in plasma (Fig 4). Plasma Cmax/D after i.v. administration reached 78 μg/ml/mg at Tmax 3 min (the first sampling time point), while after i.p. and p.o. administration plasma Cmax/D were 47 μg/ml/mg at 10 min and 1.5 μg/ml/mg at 240 min (Table 1). In brain, the Cmax/D and their corresponding Tmax values for i.v., i.p. and p.o. administration were 2.8, 2.2 and 1.3 μg/ml/mg at 3, 20 and 240 min, respectively (Table 2). However, after 4 hours concentrations in brain reached similar concentrations irrespectively of the administration route (Fig 4). Although plasma concentrations after p.o. administration appeared to be very low in comparison to i.v. and i.p. administration, comparable concentrations of ^{3}H-D3 were found in the brain resulting in high brain/plasma ratio after 4 h (Fig 5).

4 hours after a ^{3}H-D3 bolus dose, brain/plasma ratio of all administration routes reached a plateau between 0.7 and 1.0 (Fig 5). To minimize the time dependence of brain/plasma ratio, the absolute ratios were calculated from the area under the brain and plasma concentration

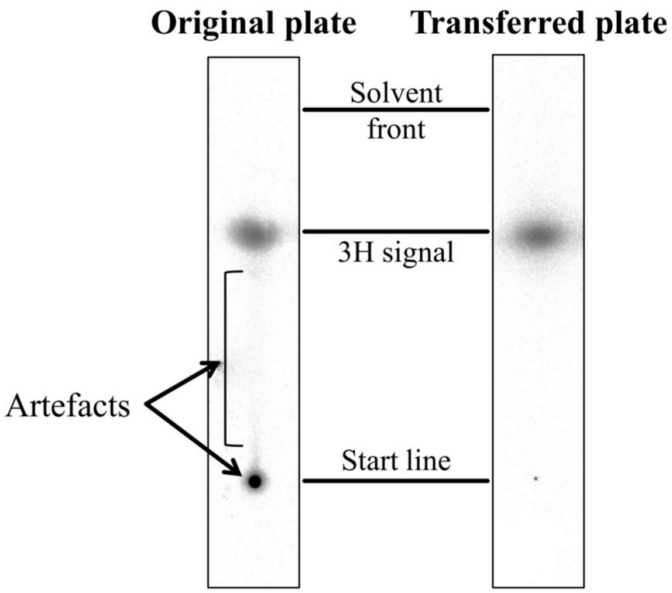

Fig 3. Plate-transfer of ^{3}H-D3 in TLC matrices. A control experiment was performed by placing a new TLC plate to a freshly developed plate to transfer only the ^{3}H-D3 within matrices. On the mirror image of the transferred plate, the ^{3}H signals at the start points as well as the smears were obviously reduced, while the intensity of separated ^{3}H-D3 did only change slightly. This result suggests that the observed artefacts arise from unspecific ^{3}H-D3 binding to the glass surface.

doi:10.1371/journal.pone.0128553.g003

curves from 4 hours to infinity (brain_$AUC_{4h\text{-}inf}$/plasma_$AUC_{4h\text{-}inf}$) with 1.07 for i.v., 0.69 for i.p., and 0.85 for p.o. administration.

After bolus administration, D3 showed relatively long elimination half-lives in plasma of 31.8 h, 41.2 h and 40.7 h after i.v., i.p. and p.o. administration, respectively. Plasma clearance was 0.12 ml/min after i.v. administration. Apparent volumes of distribution were different among i.v., i.p. and p.o. administration with 316, 444 and 684 ml, respectively (Table 1).

Absolute bioavailability was high with 92.2% after i.p. administration and 58.3% after p.o. administration (Table 1). When studying gastrointestinal distribution of D3 after p.o. administration (Fig 6), most of the radioactivity was found in the lower intestinal tract after 4 hours, which suggested that the majority of D3 did not enter the system circulation within 4 hours. Still, the AUC of D3 in brain after p.o. administration was comparable to those after i.p. and i.v. administration (Table 2).

We were also interested in answering the question, whether continuous dosing over several days using an i.p. implanted osmotic pump is showing specific effects in D3 distribution. We found linearly increasing D3 concentrations in plasma and all tested organs over 6 days (Fig 7). Although D3 highly accumulated in liver and kidney at day 6, the mice did not show any obvious signs of intoxication. The brain/plasma ratio increased with time from 0.53 at day 2 to 0.77 at day 6.

Plasma protein binding of D3

To estimate the free fraction of D3 in plasma *in vivo* ($f_{u,total}$), D3 was incubated with human serum albumin (HSA) and α_1-acid glycoprotein (AGP) in an *in vitro* assay (Fig 8). The plasma

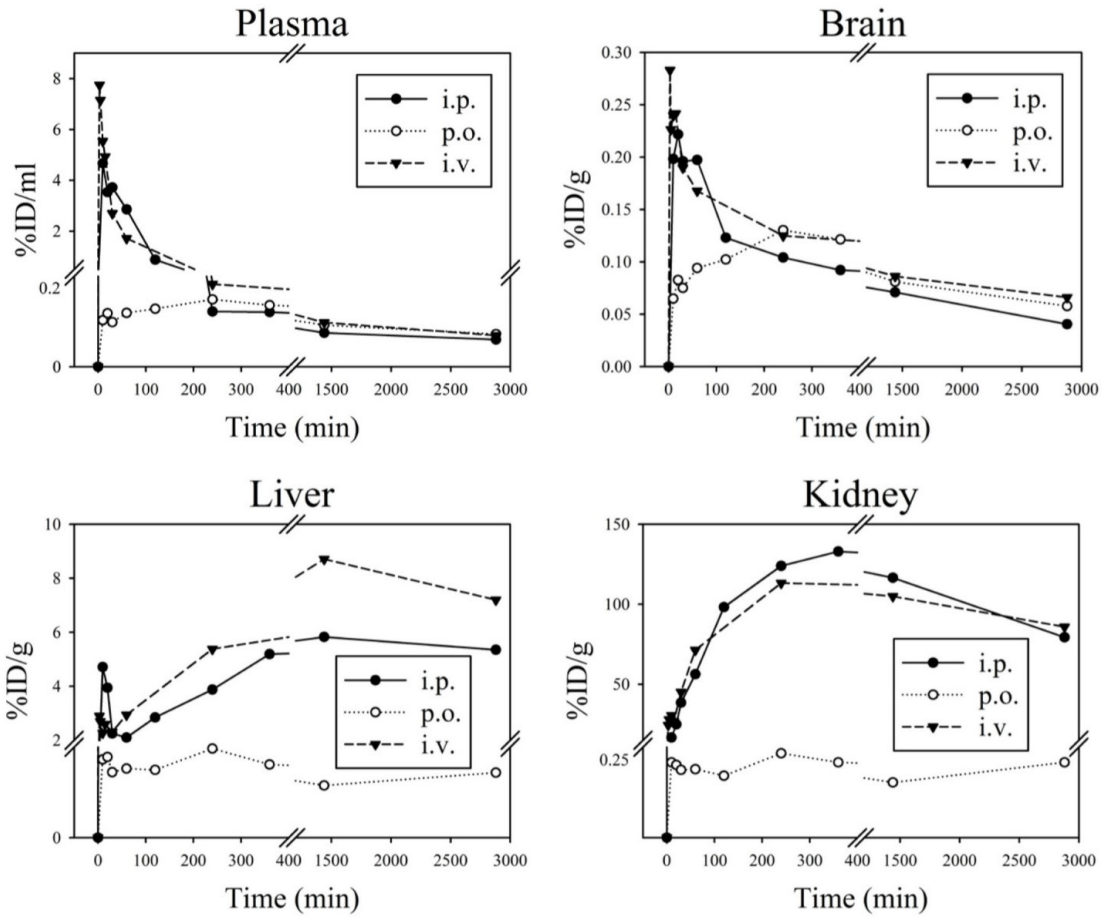

Fig 4. Mean pharmacokinetic profiles of ^{3}H-D3 in organs and plasma after i.p., p.o. and i.v. administration. ^{3}H-D3 (5 μCi) mixed with D3 in a total concentration of 3.5 mg/kg (i.v.) or 10.5 mg/kg (i.p. and p.o.) was applied per mouse. D3 concentrations are shown as percentage of injected dose per gram tissue or milliliter plasma (%ID/g or %ID/ml) dependent of time after administration. Mean values from 3 mice are shown.

doi:10.1371/journal.pone.0128553.g004

protein binding assay for AGP resulted in a K_D of 1.8 μM ± 7.9%. Assuming a D3 concentration in blood of 0.1 μM (C_{D3}, measured 4 h after i.p. injection) calculation of binding to AGP according to Eq (1) predicts a free fraction of 8.3%. For HSA, the K_D was above the detection limit of the kit (> 1.4 mM) indicating very low affinity of D3 to HSA. Nevertheless, calculation of the free fraction with an assumed K_D of 1.4 mM resulted in 68.3% free D3. Taken together, using Eq (2), the estimated free fraction of D3 in plasma was calculated to be approximately 8%.

Discussion

In the current study we have analysed the distribution of the D-enantiomeric peptide D3 after single intravenous, intraperitoneal and per oral administration, as well as continuous dosing

Table 1. Pharmacokinetic parameters for D3 from noncompartmental analysis of plasma.

Parameter	Units	i.v. (3.5 mg/kg)	i.p. (10.5 mg/kg)	p.o. (10.5 mg/kg)
Tmax	min	3	10	240
Cmax	µg/ml	7.75	14	0.45
Cmax/D	µg/ml/mg	77.5	46.7	1.48
$AUC_{C0\text{-}last}$	min*µg/ml	679	1763	1095
$MRT_{C0\text{-}last}$	min	547	527	1718
Lambda_z	1/min	0.00036	0.00028	0.00028
HL_Lambda_z	min	1907	2471	2439
$AUC_{C0\text{-}inf}$	min*µg/ml	869	2404	1521
$MRT_{C0\text{-}inf}$	min	1658	2104	3430
Vz	ml	317	445	684
Cl	ml/min	0.115	N.A.	N.A.
Vss	ml	190	N.A.	N.A.
Bioavailability	%	N.A.	92.2	58.3

N.A.: Parameters not applicable for this administration route. For abbreviations see methods section.

doi:10.1371/journal.pone.0128553.t001

via intraperitoneally implanted osmotic pumps. To the best of our knowledge, this is the first report of a comprehensive pharmacokinetic study of a peptide consisting solely of D-enantiomeric amino acid residues in rodents demonstrating excellent proteolytic stability, long plasma half-life and very high oral bioavailability.

D3 showed high proteolytic resistance exactly as it was shown *in vitro* previously with other all-D-peptides [14–16]. Thanks to this stability, metabolites can be neglected and the measured ^{3}H radioactivity represents the concentration of D3 after administration *in vivo*.

Estimated terminal plasma half-lives of D3 were between 32 and 41 h and were thus much higher than those reported for L-enantiomeric peptides which are typically only a few minutes [25]. Four hours after administration, irrespective of the administration routes, the temporal distribution of D3 in brain closely followed that in plasma resulting in brain/plasma ratios between 0.7 and 1.0 (Fig 5). While substances with a brain/plasma ratio larger than 0.3 are considered to have sufficient access to the central nervous system [26], our results suggest that D3 efficiently overcomes the blood-brain barrier.

Interestingly, by p.o. administration of D3, in spite of only a small rate of D3 being absorbed via the enteric tract, the bioavailability was 58.3% (Table 1), which is relatively high in comparison to that of L-peptide drugs, which were described to be less than 1% without delivery enhancement [27–30]. This finding can be explained by slow oral absorption of D3 and particularly long terminal half-life in plasma resulting in high AUC-values after p.o.

Table 2. Pharmacokinetic parameters for D3 from noncompartmental analysis of brain.

Parameter	Units	i.v. (3.5 mg/kg)	i.p. (10.5 mg/kg)	p.o. (10.5 mg/kg)
Tmax	min	3	20	240
Cmax	µg/g	0.283	0.665	0.390
Cmax/D	µg/g/mg	2.83	2.22	1.30
$AUC_{C0\text{-}last}$	min*µg/g	275	643	935
$MRT_{C0\text{-}last}$	min	1173	1108	1693

For abbreviations see methods section.

doi:10.1371/journal.pone.0128553.t002

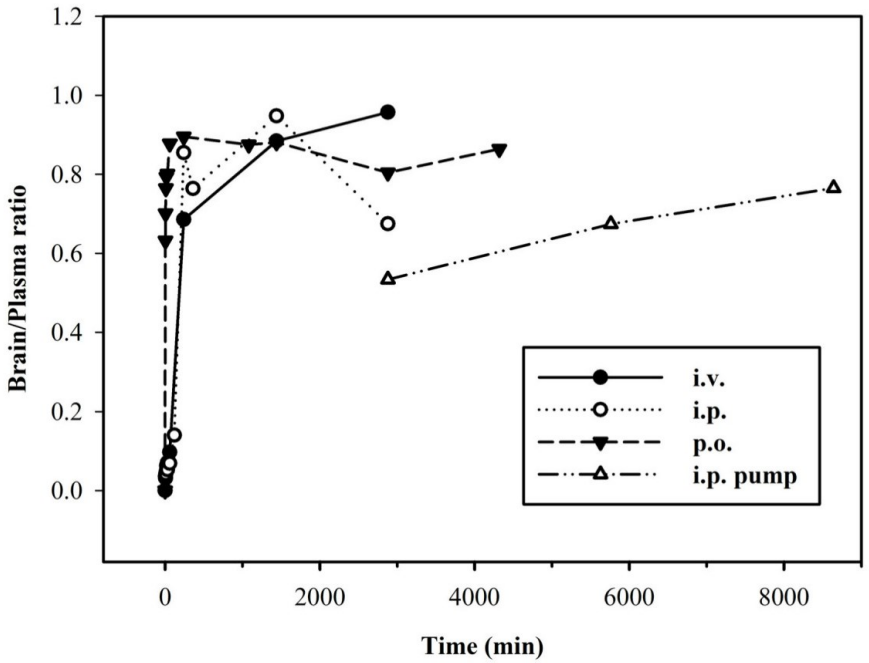

Fig 5. Temporal distribution of brain/plasma ratio of ^{3}H-D3 after different administration routes. Following bolus dose administration, low brain/plasma ratios were found at the starting time points. After 4 hours, the ratios reached relative high values and varied between 0.7–1.0. Upon i.p. pump implantation the ratio increased constantly with time.

doi:10.1371/journal.pone.0128553.g005

administration (Table 1). Low concentrations of D3 as found in kidney and liver after p.o. administration are desirable because this lowers the risk of possible intoxication of important organs. With absorption enhancers and a more suitable formulation of D3, even higher oral bioavailabilities seem to be feasible. Due to the observed high stability of D3 against proteolysis under biological conditions and its hydrophilic properties, elimination via biliary excretion (without re-absorption) and renal clearance in unchanged form could be expected.

Estimated volumes of distribution were 11.1 (i.v.), 15.6 (i.p.) and 24.0 l/kg (p.o.), respectively considering the body weight of the mice (28.5 g in average). The total body water in C57Bl/6 mice is approximately 0.6 l/kg [31], suggesting a distribution of D3 beyond the body fluid and some uptake in peripheral tissues.

Plasma volume of distribution at steady state was also high with 191 ml and 6.69 l/kg considering the body weight of the mice and the fraction of unbound D3 in plasma was predicted to be around 8%. High volume of distribution promotes low plasma clearance, which in our study was approximately between 0.12–0.19 ml/min observed in all routes of administration.

In summary, the current study demonstrates high proteolytic stability for the D-enantiomeric peptide D3. Furthermore, D3 enters the brain very efficiently and shows high oral bioavailability. The terminal half-life in mice after p.o. administration was approximately 41 hours with a brain/plasma ratio between 0.7 and 1.0, and a bioavailability of about 60%.

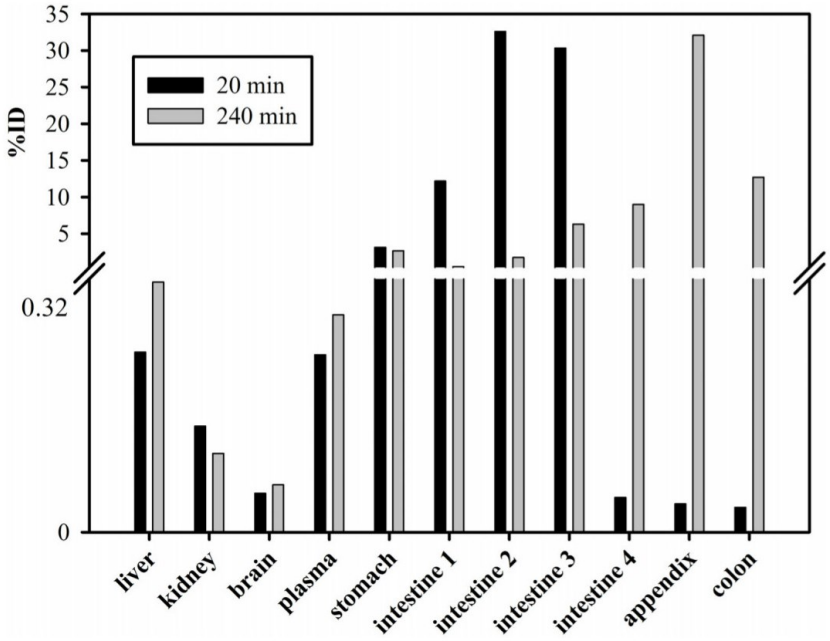

Fig 6. Distribution of ^{3}H-D3 after p.o. administration in organs and plasma. 20 min after gavaging of 100 µl, 5 µCi ^{3}H-D3 with a total D3 concentration of 10.5 mg/kg, most of the radioactivity was located in the middle of small intestine (intestine 2 and 3); 4 hours later, it spread to the lower intestinal tract. Of note is the high concentration of D3 observed in the appendix. At this time point, D3 could already be detected in feces. In comparison to the gastrointestinal tract, the amount of D3 in other organs or plasma after p.o. administration was very low.

doi:10.1371/journal.pone.0128553.g006

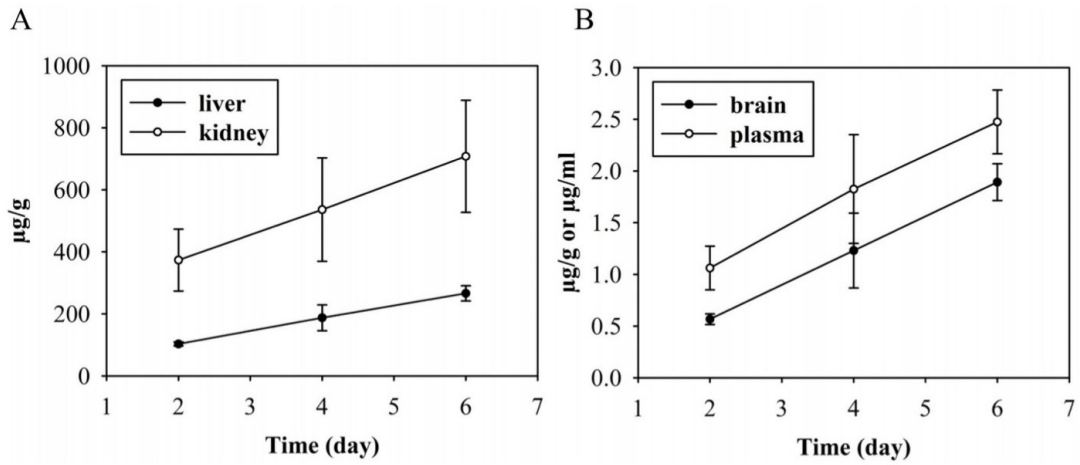

Fig 7. Concentration of ^{3}H-D3 in kidney, liver, brain and plasma administered via i.p. implanted osmotic pump. Alzet mini pumps with a delivery rate of 0.3 mg D3 (plus 5 µCi ^{3}H-D3) per 24 hours were implanted i.p. and organs were sampled after 2 to 6 days. Similar to bolus i.p. administration, more ^{3}H-D3 was found in kidney than in liver (A), whereas D3 concentrations in plasma and brain were considerably lower (B). The concentration of D3 was increasing linearly over time suggesting that the saturation concentration in the respective organs and plasma was not reached by 6 days of continuous dosing.

doi:10.1371/journal.pone.0128553.g007

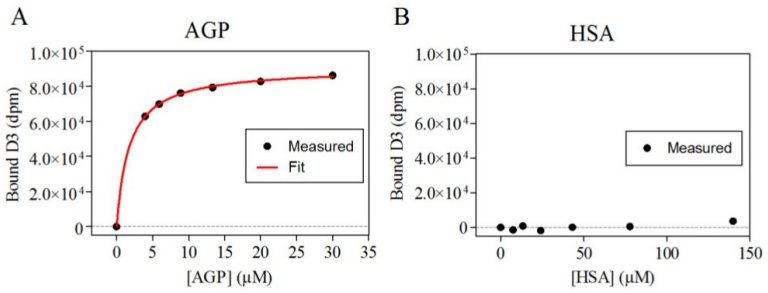

Fig 8. The bound D3 (in dpm) over the protein concentration as determined using the TRANSIL^{XL} kits. Each sample contained 5 μM D3 added to varying concentrations of AGP or HSA. (A) AGP fitted to the Michaelis Menten equation (red). (B) The binding of D3 to HSA was below the detection limit of the kit (K_D > 1.4 mM).

doi:10.1371/journal.pone.0128553.g008

In our previous studies, D3 already proved to be therapeutically active in reversing cognitive deficits and amyloid plaque load *in vivo*. Given its high oral bioavailability, suitably formulated D3 with multiple dosing might be a promising drug candidate against Alzheimer's disease.

Supporting Information

S1 File. ARRIVE Checklist. Completed "The ARRIVE Guidelines Checklist" for reporting animal data in this manuscript.
(DOCX)

Acknowledgments

We thank Michael Schöneck, Nicole Niemietz and Daniela Schumacher for excellent technical assistance and Dr. Dagmar Jürgens for discussions on the data analysis.

Author Contributions

Conceived and designed the experiments: NJ LL JB LG MC NJS JK KJL DW AW. Performed the experiments: NJ LL JP ES. Analyzed the data: NJ LL JP TZ JM DW AW. Wrote the paper: NJ LL NJS JB DW AW.

References

1. Berchtold NC, Cotman CW. Evolution in the conceptualization of dementia and Alzheimer's disease: Greco-Roman period to the 1960s. Neurobiology of aging. 1998; 19(3):173–89. Epub 1998/07/14. PMID: 9661992.
2. Fletcher LC, Burke KE, Caine PL, Rinne NL, Braniff CA, Davis HR, et al. Diagnosing Alzheimer's disease: are we any nearer to useful biomarker-based, non-invasive tests? GMS health technology assessment. 2013; 9:Doc01. Epub 2013/06/12. doi: 10.3205/hta000107 PMID: 23755087; PubMed Central PMCID: PMC3677379.
3. Nygaard HB. Current and emerging therapies for Alzheimer's disease. Clinical therapeutics. 2013; 35 (10):1480–9. Epub 2013/10/22. doi: 10.1016/j.clinthera.2013.09.009 PMID: 24139420.
4. TD B. Alzheimer Disease Overview. 1993. In: GeneReviews(R) [Internet]. University of Washington, Seattle.
5. Mikulca JA, Nguyen V, Gajdosik DA, Teklu SG, Giunta EA, Lessa EA, et al. Potential novel targets for Alzheimer pharmacotherapy: II. Update on secretase inhibitors and related approaches. Journal of clinical pharmacy and therapeutics. 2014; 39(1):25–37. Epub 2013/12/10. doi: 10.1111/jcpt.12112 PMID: 24313554.

6. Stockley JH, O'Neill C. Understanding BACE1: essential protease for amyloid-beta production in Alzheimer's disease. Cellular and molecular life sciences: CMLS. 2008; 65(20):3265–89. Epub 2008/08/13. doi: 10.1007/s00018-008-8271-3 PMID: 18695942.
7. Selkoe DJ. Alzheimer's disease: genes, proteins, and therapy. Physiological reviews. 2001; 81(2):741–66. Epub 2001/03/29. PMID: 11274343.
8. Bitan G, Kirkitadze MD, Lomakin A, Vollers SS, Benedek GB, Teplow DB. Amyloid beta-protein (Abeta) assembly: Abeta 40 and Abeta 42 oligomerize through distinct pathways. Proceedings of the National Academy of Sciences of the United States of America. 2003; 100(1):330–5. Epub 2002/12/31. doi: 10.1073/pnas.222681699 PMID: 12506200; PubMed Central PMCID: PMC140968.
9. Kayed R, Lasagna-Reeves CA. Molecular mechanisms of amyloid oligomers toxicity. Journal of Alzheimer's disease: JAD. 2013; 33 Suppl 1:S67–78. Epub 2012/04/26. doi: 10.3233/JAD-2012-129001 PMID: 22531422.
10. Tamaoka A. [The pathophysiology of Alzheimer's disease with special reference to "amyloid cascade hypothesis"]. Rinsho byori The Japanese journal of clinical pathology. 2013; 61(11):1060–9. Epub 2014/01/24. PMID: 24450113.
11. Schenk D, Basi GS, Pangalos MN. Treatment strategies targeting amyloid beta-protein. Cold Spring Harbor perspectives in medicine. 2012; 2(9):a006387. Epub 2012/09/07. doi: 10.1101/cshperspect.a006387 PMID: 22951439; PubMed Central PMCID: PMC3426815.
12. Citron M. Alzheimer's disease: strategies for disease modification. Nature reviews Drug discovery. 2010; 9(5):387–98. doi: 10.1038/nrd2896 PMID: 20431570
13. Sun N, Funke SA, Willbold D. A Survey of Peptides with Effective Therapeutic Potential in Alzheimer's Disease Rodent Models or in Human Clinical Studies. Mini-Rev Med Chem. 2012; 12(5):388–98. PMID: ISI:000303103600005.
14. Liu M, Li C, Pazgier M, Mao Y, Lv Y, Gu B, et al. D-peptide inhibitors of the p53-MDM2 interaction for targeted molecular therapy of malignant neoplasms. Proceedings of the National Academy of Sciences of the United States of America. 2010; 107(32):14321–6. Epub 2010/07/28. doi: 10.1073/pnas.1008930107 PMID: 20660730; PubMed Central PMCID: PMC2922601.
15. Zawadzke LE, Berg JM. A Racemic Protein. Journal of the American Chemical Society. 1992; 114 (10):4002–3. doi: 10.1021/Ja00036a073 PMID: ISI:A1992HT80100073.
16. Milton RCD, Milton SCF, Kent SBH. Total Chemical Synthesis of a D-Enzyme—the Enantiomers of Hiv-1 Protease Show Demonstration of Reciprocal Chiral Substrate-Specificity. Science. 1992; 256 (5062):1445–8. doi: 10.1126/science.1604320 PMID: ISI:A1992HX33700036.
17. Wiesehan K, Willbold D. Mirror-image phage display: aiming at the mirror. Chembiochem: a European journal of chemical biology. 2003; 4(9):811–5. Epub 2003/09/10. doi: 10.1002/cbic.200300570 PMID: 12964153.
18. Schumacher TN, Mayr LM, Minor DL Jr., Milhollen MA, Burgess MW, Kim PS. Identification of D-peptide ligands through mirror-image phage display. Science. 1996; 271(5257):1854–7. PMID: 8596952
19. van Groen T, Kadish I, Wiesehan K, Funke SA, Willbold D. In vitro and in vivo staining characteristics of small, fluorescent, Abeta42-binding D-enantiomeric peptides in transgenic AD mouse models. ChemMedChem. 2009; 4(2):276–82. Epub 2008/12/17. doi: 10.1002/cmdc.200800289 PMID: 19072935.
20. van Groen T, Kadish I, Funke SA, Bartnik D, Willbold D. Treatment with D3 removes amyloid deposits, reduces inflammation, and improves cognition in aged AbetaPP/PS1 double transgenic mice. J Alzheimers Dis. 2013; 34(3):609–20. Epub 2012/12/29. doi: 10.3233/JAD-121792 PMID: 23271316.
21. van Groen T, Kadish I, Funke A, Bartnik D, Willbold D. Treatment with Abeta42 binding D-amino acid peptides reduce amyloid deposition and inflammation in APP/PS1 double transgenic mice. Advances in protein chemistry and structural biology. 2012; 88:133–52. Epub 2012/07/21. doi: 10.1016/B978-0-12-398314-5.00005-2 PMID: 22814708.
22. Aileen Funke S, van Groen T, Kadish I, Bartnik D, Nagel-Steger L, Brener O, et al. Oral treatment with the d-enantiomeric peptide D3 improves the pathology and behavior of Alzheimer's Disease transgenic mice. ACS chemical neuroscience. 2010; 1(9):639–48. Epub 2010/09/15. doi: 10.1021/cn100057j PMID: 22778851; PubMed Central PMCID: PMC3368690.
23. van Groen T, Wiesehan K, Funke SA, Kadish I, Nagel-Steger L, Willbold D. Reduction of Alzheimer's disease amyloid plaque load in transgenic mice by D3, A D-enantiomeric peptide identified by mirror image phage display. ChemMedChem. 2008; 3(12):1848–52. Epub 2008/11/19. doi: 10.1002/cmdc.200800273 PMID: 19016284.
24. Kilkenny C, Browne WJ, Cuthill IC, Emerson M, Altman DG. Improving Bioscience Research Reporting: The ARRIVE Guidelines for Reporting Animal Research. Plos Biol. 2010; 8(6). ARTN e1000412 doi: 10.1371/journal.pbio.1000412 PMID: ISI:000279355600022.

25. Pollaro L, Heinis C. Strategies to prolong the plasma residence time of peptide drugs. MedChemComm. 2010; 1(5):319–24. doi: 10.1039/c0md00111b

26. Reichel A. The role of blood-brain barrier studies in the pharmaceutical industry. Current drug metabolism. 2006; 7(2):183–203. Epub 2006/02/14. PMID: 16472107.

27. Wong TW. Design of oral insulin delivery systems. Journal of drug targeting. 2010; 18(2):79–92. Epub 2009/12/09. doi: 10.3109/10611860903302815 PMID: 19968567.

28. Takagi H, Hiroi T, Hirose S, Yang L, Takaiwa F. Rice seed ER-derived protein body as an efficient delivery vehicle for oral tolerogenic peptides. Peptides. 2010; 31(8):1421–5. Epub 2010/05/12. doi: 10.1016/j.peptides.2010.04.032 PMID: 20457197.

29. Mason JM. Design and development of peptides and peptide mimetics as antagonists for therapeutic intervention. Future medicinal chemistry. 2010; 2(12):1813–22. Epub 2011/03/25. doi: 10.4155/fmc.10.259 PMID: 21428804.

30. Lalatsa A, Garrett NL, Ferrarelli T, Moger J, Schatzlein AG, Uchegbu IF. Delivery of Peptides to the Blood and Brain after Oral Uptake of Quaternary Ammonium Palmitoyl Glycol Chitosan Nanoparticles. Molecular pharmaceutics. 2012; 9(6):1764–74. doi: 10.1021/Mp300068j PMID: ISI:000304728700022.

31. Chapman ME, Hu L, Plato CF, Kohan DE. Bioimpedance spectroscopy for the estimation of body fluid volumes in mice. American journal of physiology Renal physiology. 2010; 299(1):F280–3. Epub 2010/05/14. doi: 10.1152/ajprenal.00113.2010 PMID: 20462974; PubMed Central PMCID: PMC2904176.

2.3 Pharmacokinetic properties of a novel D-peptide developed to be therapeutically active against toxic β-amyloid oligomers.

Published in: PHARMACEUTICAL RESEARCH

Impact Factor: 3.42

Contributions: 40%

Involved in the conception and design of the experiments; conducted large fraction of experimental parts; involved in the data analysis and manuscript writing.

Pharm Res (2016) 33:328–336
DOI 10.1007/s11095-015-1791-2

RESEARCH PAPER

Pharmacokinetic Properties of a Novel D-Peptide Developed to be Therapeutically Active Against Toxic β-Amyloid Oligomers

Leonie H. E. Leithold[1] • Nan Jiang[1] • Julia Post[1] • Tamar Ziehm[1] • Elena Schartmann[1] • Janine Kutzsche[1] • N. Jon Shah[2] • Jörg Breitkreutz[3] • Karl-Josef Langen[2,4] • Antje Willuweit[2] • Dieter Willbold[1,5]

Received: 29 April 2015 / Accepted: 8 September 2015 / Published online: 17 September 2015

ABSTRACT

Purpose It has been shown that amyloid β (Aβ) oligomers play an important role in the pathology of Alzheimer's disease (AD). D3, a peptide consisting solely of D-enantiomeric amino acid residues, was developed to specifically eliminate Aβ oligomers and is therapeutically active in transgenic AD mice. D-peptides have several advantages over L-peptides, but little is known about their pharmacokinetic potential *in vivo*. Here, we analysed the pharmacokinetic properties of RD2, a rationally designed and potent D3 derivative.

Methods The pharmacokinetic analysis was performed using ^{3}H-RD2 after administration via several routes in mice. The time dependent amount of radiolabelled RD2 was measured in plasma and several organ homogenates by liquid scintillation counting. Furthermore, binding to plasma proteins was estimated.

Results RD2 penetrates into the brain, where it is thought to implement its therapeutic function. All administration routes result in a maximal brain concentration per dose (C_{max}/D) of 0.06 (μg/g)/(mg/kg) with brain/plasma ratios ranging between 0.7 and 1.0. RD2 shows a small elimination constant and a long terminal half-life in plasma of more than 2 days. It also exhibits high bioavailability after i.p., s.c. or p.o. administration.

Conclusions These excellent pharmacokinetic properties confirm that RD2 is a very promising drug candidate for AD.

KEY WORDS Alzheimer's disease · D-enantiomer · peptide · pharmacokinetics · preclinical

ABBREVIATIONS

%ID	Relative injected dose
AD	Alzheimer's disease
AGP	α_1-acid glycoprotein
AUC	Area under the concentration-time curve
AUMC	Area under the moment curve
Aβ	Amyloid β
C	Concentration
Cl	Clearance
D	Dose
dpm	Disintegrations per minute
F	Bioavailability
f_u	Unbound fraction
HSA	Human serum albumin
i.p.	Intraperitoneal
i.v.	Intravenous
inf	Infinity
MAT	Mean absorption time
MRT	Mean residence time
n.i.v.	Non-intravenous
p.o.	*per os*, oral delivery
r^2	Correlation coefficient
s.c.	Subcutaneous
$t_{1/2}$	Terminal half-life
TLC	Thin layer chromatography

✉ Antje Willuweit
a.willuweit@fz-juelich.de

✉ Dieter Willbold
d.willbold@fz-juelich.de

1 Institute of Complex Systems, Structural Biochemistry (ICS-6), Forschungszentrum Jülich GmbH, 52425 Jülich, Germany

2 Institute of Neuroscience and Medicine, Medical Imaging Physics (INM-4), Forschungszentrum Jülich GmbH, 52425 Jülich, Germany

3 Institute of Pharmaceutics and Biopharmaceutics, Heinrich-Heine-Universität Düsseldorf, Düsseldorf, Germany

4 Clinic for Nuclear Medicine, RWTH Aachen University, Aachen, Germany

5 Institut für Physikalische Biologie, Heinrich-Heine-Universität Düsseldorf, Düsseldorf, Germany

V_{ss} Distribution volume in steady state
V_z Terminal distribution volume
λ_z Terminal elimination rate constant

INTRODUCTION

Alzheimer's disease (AD) is a progressive neurodegenerative disorder and the most common form of dementia. It currently affects about 24 million people worldwide, but to date, no curative treatment exists (1,2).

The pathology of Alzheimer's disease is mainly characterised by extracellular amyloid plaques and intracellular neurofibrillary tangles. Research suggests that amyloid β (Aβ) aggregation plays a major role in the development of AD (3,4), while Aβ oligomers are thought to be the most toxic species (5–7). Therefore, various strategies to develop AD therapeutics address Aβ, trying to reduce its formation, inhibit aggregation to fibrils or enhance its clearance (3,8). Several studies on potential therapeutics considered peptides, e.g. designed to prevent β-sheet conformation (3,9). However, peptide drugs show several disadvantages since they can be immunogenic, instable due to degradation by proteases and often show rapid clearance (10). Additionally, they generally have a very low oral bioavailability and short *in vivo* half-lives (11).

D-peptides, which are entirely composed of D-amino acids, are more protease resistant than L- peptides, due to the stereoisomeric selectivity of most proteolytic enzymes (12,13). As a result, system elimination is slower and they remain stable in the body for longer periods of time than L-peptides, thereby providing more time to be therapeutically active *in vivo* (14,15). This was for instance shown for all D-enantiomeric peptides in rat plasma and Rhesus monkey cerebrospinal fluid (16,17). In addition it has been shown that they are not immunogenic or at least significantly less than L-peptides (15).

Previously, a D-peptide, called D3, has been identified by mirror image phage display for binding to Aβ (18,19). It has been shown that it is able to improve both pathology and cognition of AD transgenic mice e.g. after 4 weeks of i.p. treatment or after 8 weeks of oral delivery (20–24).

RD2 is a derivative of D3 consisting of a rationally repositioned sequence, resulting in improved binding to Aβ oligomers (25) which are currently widely believed to be the most toxic Aβ species (26,27).

Here, we determined and compared the pharmacokinetic properties of RD2 in mice after intraperitoneal, subcutaneous, oral and intravenous delivery. This is the first systematic preclinical pharmacokinetic study of a D-enantiomeric peptide to such an extent.

METHODS

Peptides

RD2 (H-ptlhthnrrrrr-NH_2, all amino acid residues are D-enantiomers, 1.6 kDa) was purchased from Cambridge Peptides Ltd. (Birmingham, United Kingdom). The Lewis structure of RD2 can be found in Fig. 1.

Radioactively labelled peptides were purchased from Quotient Bioresearch (Radiochemicals) Ltd. (Cardiff, United Kingdom) containing 1 mCi/ml and were supplied as solution in water:ethanol (1:1). RD2 (H-pt-[4,5-^{3}H-D-Leu]-hthnrrrrr-NH_2) was supplied with > 95% purity, containing 124 Ci/mmol. Radioactively labelled L-peptide (H-RPRTR-[4,5-^{3}H-Leu]-HTHRNR-NH_2), 103 Ci/mmol was used as control for stability assessment.

Animals

C57BL/6 mice (Charles River Laboratories, Sulzfeld, Germany) were housed in groups of up to four mice in standard mouse individually ventilated cages with standard chip aspen bedding, a nestlet was provided as cage enrichment. Water as well as food were available *ad libitum*. Housing rooms were maintained on a 12/12 h light–dark cycle (7 a.m. – 7 p.m.), with a temperature of 22°C and approx. 54% humidity. All animal experiments were carried out in conformance with the German Protection of Animals Act (TierSchG §§ 7–9) and with permit of an Animal Protection Committee (AZ84-02.04.2011.A356).

Proteolytic Stability

To assess the stability of RD2 in different organs, thin layer chromatography (TLC) was applied using the ^{3}H-radioactively labelled RD2. As positive control an L-peptide was included. Blood and organs were sampled from C57BL/6 mice (25 g body weight). The animal was anaesthetised with isoflurane (Actavis Deutschland GmbH & Co. KG, Langenfeld, Germany) and blood was taken by cardiac puncture with a heparin containing needle before the mouse was sacrificed by cervical dislocation. Blood was spun down at 4°C and 1200 g for 15 min and plasma was taken. A small piece of liver (approx. 0.2 g), the left kidney and the right brain hemisphere were taken. All organ weights were measured and homogenised with 500 µl PBS per 0.2 g organ weight. Afterwards, organ homogenates were centrifuged at 4°C and 1200 g for 10 to 15 min and supernatant was taken off. 5 µl radioactively labelled peptide (5 µCi) were then added to 1 µl mouse plasma or organ homogenate supernatant. After different incubation times the reaction was stopped by adding 4 µl mobile solvent (2-butanol/pyridine/ammonia (28%)/water, 39/34/10/26 ml respectively) to each sample which was

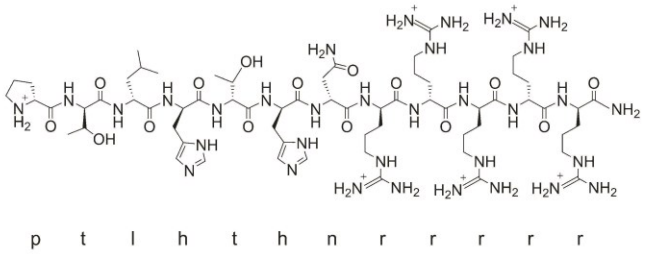

Fig. 1 Lewis structure and single letter amino acid code of the D-enantiomeric peptide RD2 (1.6 kDa).

then stored at - 20°C until further use. Samples were then dotted on the TLC membrane (HPTLC Silica 60 gel plates, Merck, Darmstadt, Germany) and placed into the solvent. Upon drying, start- and endpoint were marked with spots of ^{3}H-labelled peptide. For ^{3}H detection plates were then placed on phosphor imaging plates (Fujifilm, Tokyo, Japan) for 3 days and afterwards detected using a BAS reader with AIDA software (Raytest GmbH, Freiburg, Germany).

Pharmacokinetic Studies

Pharmacokinetic properties of ^{3}H-radioactively labelled RD2 in male C57BL/6 mice were studied using different administration routes. The applied amount contained 10 mg/kg for subcutaneous (s.c.) and intraperitoneal (i.p.) injection as well as oral gavage (p.o.) and 3.3 mg/kg for intravenous (i.v.) injection.

To achieve sufficiently high total concentrations of RD2, a combination of ^{3}H-labelled "hot" RD2 and non-radioactive "cold" RD2 was used, as detailed below. The working solution was prepared in phosphate buffer (0.1 M, pH 8.0). To achieve the appropriate dose each mouse received ^{3}H-labelled RD2 together with non-radioactive "cold" RD2, resulting in a total dose of 10 mg/kg (i.p., p.o., s.c.) or 3.3 mg/kg (i.v.) RD2 per mouse. I.v. injection was given into the tail vain under anaesthesia. Animals were sacrificed after different incubation times as detailed in Table I, for each time point three mice were used. Just before sampling time, the animal was anaesthetised with isoflurane and blood was taken by cardiac puncture with a heparin containing needle before the mouse was sacrificed by cervical dislocation. Blood was spun down at 4°C and 1200 g for 15 min and plasma was taken. A small piece of liver, the left kidney and the right brain hemisphere were taken at all time points. Additionally, at the late time points of 7 and 28 days, the spleen and the inguinal lymph nodes were harvested (spleen all administration routes, lymph nodes i.p. and i.v. only). 24 h after i.v. and i.p. administration urine and faeces were taken freshly (urine $n=2$ (i.p.) $n=4$ (i.v.), faeces $n=5$). All weights were measured and organs were homogenised with 500 µl PBS. After mixing with 10 ml scintillation cocktail (Ultima Gold XR, PerkinElmer, Waltham, MA, USA) ^{3}H-radioactivity was then measured in triplicate with a liquid scintillation analyser beta radiation counter (PerkinElmer, Waltham, MA, USA) in form of disintegrations per minute (dpm). The same procedure was performed on three animals without RD2 application, thereby creating blank reference values for each organ that were subtracted from all dpm values.

From the activity of the working solution subtracted with blank values and the organ weight the relative injected dose (%ID/g or %ID/ml) and total amount of RD2 (mg/g or mg/ml) per gram organ or millilitre plasma were calculated. All calculations of pharmacokinetic parameters were based on the total RD2 concentration. For calculation of pharmacokinetic parameters of the brain the radioactivity resulting from residual blood was subtracted assuming a plasma fraction of 1.5% in brain. The relative injected dose was only used for presentation purposes of the time dependent distribution in organs and plasma and displayed as mean and standard error of the mean where numbers are given.

Calculation of Pharmacokinetic Parameters

A non-compartmental analysis of pharmacokinetic parameters was performed. The area under the curve (AUC) as well as the area under the moment curve (AUMC) for the total RD2 concentrations was calculated (SigmaPlot 11.0, Systat Software, Inc., San José, CA, USA). The mean residence time (MRT) was calculated according to MRT = AUMC/AUC. The RD2 concentration at time zero was assumed to be zero for all applications except for plasma after i.v. delivery where it was back extrapolated from the first two observed concentrations in the semi-logarithmic time-concentration plot (SigmaPlot). The terminal elimination rate constant (λ_z) was obtained by logarithmic extrapolation based on the last observed concentrations starting from 2 days post administration (the correlation coefficient (r^2) was between 0.92 and 1.0 for all extrapolations). Parameters containing the suffix "0–28" were calculated from the measured data points while "0-inf" denotes values reaching into infinity being calculated based on λ_z. The AUC and AUMC reaching into infinity were

Table I Pharmacokinetic Experiments were Performed According to this Scheme

Administration method	Time points	RD2 dose
i.v.	3 min, 5 min, 10 min, 15 min, 30 min, 1 h, 4 h, 1 d, 2 d, 7 d, 28 d	3.3 mg/kg
i.p.	10 min, 20 min, 30 min, 1 h, 2 h, 4 h, 6 h, 1 d, 2 d, 7 d, 28 d	10 mg/kg
s.c.	10 min, 20 min, 30 min, 1 h, 2 h, 4 h, 6 h, 1 d, 2 d, 7 d, 28 d	10 mg/kg
p.o.	30 min, 1 h, 2 h, 4 h, 6 h, 8 h, 18 h, 1 d, 2 d, 3 d, 7 d, 28 d	10 mg/kg

Assessed durations post administration and concentrations of RD2 per route of administration are given. For each time point three mice were used

calculated by $AUC_{0-inf}=AUC_{0-28}+C_{28}/\lambda_z$ and $AUMC_{0-inf}=AUMC_{0-28}+(C_{28}*t_{28})/\lambda_z+C_{28}/\lambda_z^2$. The bioavailability (F) was calculated on the basis of the respective AUC according to $F=100*(D_{i.v.}*AUC_{n.i.v.})/(D_{n.i.v.}*AUC_{i.v.})$ with n.i.v. denoting the respective extravascular administration route. Parameters describing the terminal elimination phase were calculated based on λ_z: the terminal half-life ($t_{1/2}=\ln 2/\lambda_z$) and clearance ($Cl_{i.v.}=\lambda_z*V_z$), the terminal distribution volume ($V_z=D/(\lambda_z*AUC_{inf})$ (for n.i.v. Cl and V_z were calculated including the bioavailability: $Cl_{n.i.v.}=\lambda_z*V_z/F$ and $V_z=(D*F)/(\lambda_z*AUC_{inf})$) was calculated as well as the distribution volume in steady state ($V_{ss}=(D*AUMC)/AUC^2$).

The overall brain/plasma ratio was determined using the respective AUC_{0-28} whereas the brain/plasma ratio over time was calculated from the individual values of each time point, both with subtracted radioactivity from residual blood, assuming a plasma fraction of 1.5% in brain (28).

Plasma Protein Binding

Plasma protein binding was estimated by incubation of RD2 with varying concentrations of protein using TRANSIL^{XL} binding kits (Sovicell GmbH, Leipzig, Germany). K_D values were determined by titrating a constant drug concentration against different concentrations of human serum albumin (HSA) and α_1-acid glycoprotein (AGP). Experiments were performed as recommended for the kit. To obtain the desired RD2 stock solution of 80 µM, non-radioactively RD2 was dissolved in PBS and 5% ^{3}H-labelled RD2 solution was added for detection purposes. A final concentration of 5 µM RD2 was applied in the assay. After incubation and centrifugation 15 µl supernatant were taken and scintillation cocktail was added for detection using liquid scintillation counting. This was done in triplicate. After measuring the disintegrations per minute (dpm) of the supernatant containing the unbound RD2, the fraction bound to the titrated protein was calculated and plotted against the protein concentrations. The curves were fitted to the Michaelis Menten ligand binding equation (SigmaPlot) to obtain a K_D. Mean and relative standard error (%) of multiple measurements are given where applicable (AGP $n=2$).

For determination of the unbound fraction of RD2 (f_u) Eq. (1) was used:

$$f_u = 100*\frac{\frac{C_{RD2}-K_D-C_{physiol}}{2}+\sqrt{K_D*C_{RD2}+\left(\frac{C_{RD2}-K_D-C_{physiol}}{2}\right)^2}}{C_{RD2}} \quad (1)$$

For very low RD2 concentrations in blood (C_{RD2}), Eq. (1) can be simplified by Eq. (2), where the unbound fraction of RD2 can be calculated independently of the applied RD2 concentration. Since this is true for our *in vivo* experiments we used Eq. (2) for the total free fraction of RD2, combining the binding of RD2 to HSA and AGP. For calculation of the unbound fraction according to Eq. (2), physiological concentrations ($C_{physiol}$) of 0.65 mM HSA and 0.02 mM AGP were assumed.

$$f_{u,total} = 100*\frac{1}{1+\frac{C_{physiol,HSA}}{K_{D,HSA}}+\frac{C_{physiol,AGP}}{K_{D,AGP}}} \quad (2)$$

RESULTS

Proteolytic Stability of RD2

To confirm stability of ^{3}H-labelled RD2 in mouse plasma, thin layer chromatography (TLC) was performed after incubation of ^{3}H-RD2 with plasma for up to 1 day and detected via autoradiography. This experiment was essential to consider potential metabolites in later pharmacokinetic analyses. TLC results showed that RD2 remained stable in mouse plasma (Fig. 2) for at least 24 h while a comparable L-peptide was proteolytically degraded within 2 h as is deduced from the appearance of additional bands at that time (marked by arrows) in comparison to those present at 0 h. Similarly, the pattern of RD2 after incubation with organ homogenates did not change over time, indicating that no proteolytic degradation took place (Fig. 2). Of note, the peptides bind to different components of the plasma and organ samples resulting in different patterns and intensities for each peptide.

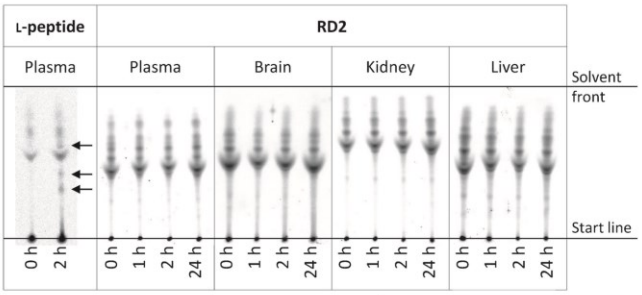

Fig. 2 Autoradiography of thin layer chromatogram demonstrating proteolytic stability of ^{3}H-labelled RD2 in mouse plasma, brain, kidney and liver. ^{3}H-RD2 was incubated at 37°C with mouse plasma for different durations and developed on TLC plates. For comparison, a very similar L-peptide was also incubated with mouse plasma. Multiple bands in the 0 h lanes arise from binding and co-migration of the ^{3}H-peptides with plasma and tissue components. Therefore, any effect of degradation will lead to extra additional bands as compared to the 0 h lane of the very same compound. Obvious proteolytic degradation can be observed for the ^{3}H-L-peptide already after 2 h of incubation with plasma leading to additionally appearing bands (*black arrows*) as compared to the 0 h lane. Additionally appearing bands as compared to 0 h incubation are not observed for ^{3}H-RD2 even after 24 h of incubation in plasma and tissue homogenates.

However, since the overall composition did not change with time, it can be concluded that RD2 was not subject to proteolytic degradation. The L-peptide showed appearance of additional bands after 2 h incubation, while the pattern of RD2 remained unchanged. Therefore, metabolites were considered negligible and the measured radioactivity was used to back calculate the total RD2 concentration.

Pharmacokinetic Properties

Pharmacokinetic analyses were performed using ^{3}H-labelled RD2 after i.v., i.p., s.c. or oral administration in mice. Graphs showing the relative injected dose per organ weight over time of the different administration routes can be found in Fig. 3.

Significant amounts of ^{3}H-RD2 were found in the analysed organs after i.v., i.p. or s.c. injection with highest concentrations present in kidney, followed by liver and plasma (Fig. 3). Oral administration resulted in very low ^{3}H-RD2 levels in liver, kidney and plasma. Interestingly, in brain ^{3}H-RD2 was found in amounts similar to the other administration routes. Exposure to all analysed organs was quite stable for a couple of days and declined gradually until 28 days after injection where it was still detectable in very low amounts.

Additionally, ^{3}H-RD2 amounts in urine and faeces were evaluated 24 h post i.p. and i.v. injection, showing only low doses in faeces (0.28±0.05 (i.p.) and 0.35±0.02%ID/g (i.v.), n=5). The amount of ^{3}H-RD2 in urine was higher, following i.p. administration it reached 2.3±0.09%ID/ml and 4.3±0.07%ID/ml upon i.v. administration (i.p. n=2; i.v. n=4). Furthermore, at 7 and 28 days post injection the presence of ^{3}H-RD2 in spleen and lymph nodes was determined, showing only low concentrations at 7 days (0.4 – 0.6±0.11%ID/g) decreasing with time (0.01 – 0.2±0.02%ID/g, except spleen i.v. 0.6 ±0.02%ID/g). Remarkably, upon oral application nearly no ^{3}H-RD2 was found in the spleen at 7 days post injection (0.04±0.004%ID/g).

Plasma Pharmacokinetic Parameters

A summary of all pharmacokinetic parameters in mouse plasma can be found in Table II, parameters were determined based on the back-calculated total RD2 concentration from measured radioactivity.

In contrast to the other administration routes, i.v. injection was performed with 3.3 mg/kg body weight. Results show low rate of terminal plasma clearance with Cl/F=1.68 ml/(kg*min) and a relatively long terminal half-life ($t_{1/2}$) of 59 h. Since the extrapolated part of the area under the curve (AUC) is small (≤1%) the AUC_{0-28} and $AUC_{0\text{-inf}}$ are very similar with $AUC_{0\text{-inf}}$=1.97 mg/ml*min.

Upon extravascular administration, absorption happened rapidly, as t_{max} was between 0.5 and 1 h, with oral administration showing the slowest absorption. The maximal observed concentration relative to the dose (C_{max}/D) was highest for i.v. administration (3.04 (µg/ml)/(mg/kg)), lower after i.p. and s.c. injection (0.79 and 0.98 (µg/ml)/(mg/kg)) and lowest following oral administration (0.09 (µg/ml)/(mg/kg)). The drug exposure in plasma, calculated as $AUC_{0\text{-inf}}$, showed the highest values after s.c. injection (5.42 mg/ml*min) and similar values upon i.p. and p.o. administration (4.57 and 4.54 mg/ml*min). The mean residence time (MRT), however, appeared to be comparable between all administration routes. The terminal half-life was about 60 h and independent of the administration route. The bioavailability (F) was similar for i.p. and p.o. administration (approx. 76%) and even higher upon s.c. injection (91%).

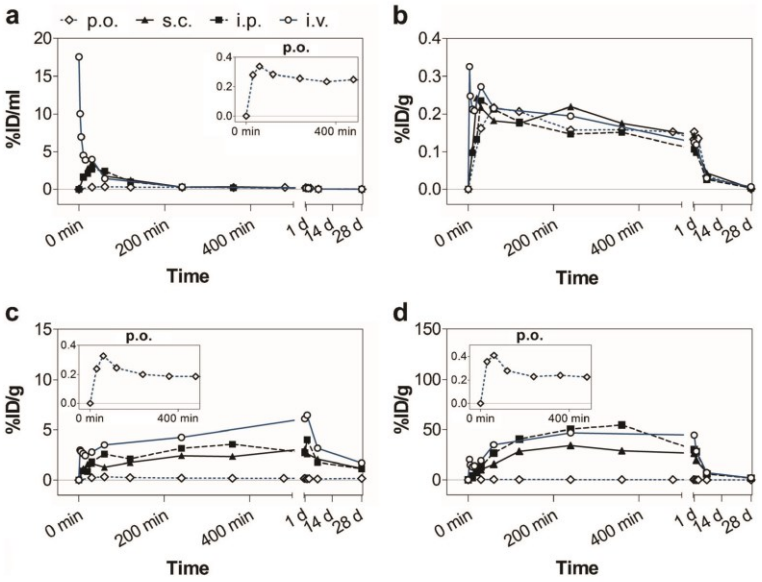

Fig. 3 Time dependent distribution of ^{3}H-RD2 in mouse organs and plasma after different administration routes. ^{3}H-RD2 was administered together with non-radioactive RD2 via different routes at 10 mg/kg or 3.3 mg/kg (i.v.). The concentration of ^{3}H-RD2 as expressed in relative injected dose per gram organ (%ID/g) or millilitre plasma (%ID/ml) is shown for plasma (**a**), brain (**b**), liver (**c**) and kidney (**d**) over time after different administration routes (p.o. *dashed line*, *open square*; s.c. *triangle*; i.p. *dashed line*, *closed square*; i.v. *open circle*). Graphs show the mean of three mice per time point.

Pharmacokinetic Parameters of RD2 in the Brain

Table III shows a summary of parameters calculated for the brain as this is expected to be the therapeutically relevant organ. The present study was performed in healthy C57BL/6 mice. The resulting pharmacokinetic parameters may be different in transgenic AD mouse models. Measured ^{3}H-RD2 radioactivity was used to extrapolate the total RD2 concentration in brain.

Brain/plasma ratios increased over time for i.v., i.p. and s.c. injection (Fig. 4), whereas for oral administration it remained relatively stable, all delivery routes almost reaching

Table II Determined Pharmacokinetic Parameters in Mouse Plasma for Different Administration Routes, based on Measured ^{3}H-RD2

Parameter	Units	i.v.	i.p.	s.c.	p.o.
Dose (D)	mg/kg	3.3	10	10	10
t_{max}	min	3	30	30	60
C_{max}/D	(μg/ml)/(mg/kg)	3.04	0.79	0.98	0.09
AUC_{0-28}	mg/ml*min	1.95	4.54	5.39	4.51
$AUMC_{0-28}$	min^{2}*mg/ml	9908	22,154	26,169	23,355
MRT_{0-28}	h	84.8	81.4	80.9	86.3
λ_z	min^{-1}	0.00020	0.00019	0.00019	0.00020
$t_{1/2}$	h	59	62	60	58
AUC_{0-inf}	mg/ml*min	1.97	4.57	5.42	4.54
$AUMC_{0-inf}$	min^{2}*mg/ml	10,794	23,676	27,514	24,748
MRT_{0-inf}	h	91.4	86.4	84.6	90.8
V_z	l/kg	8.57	8.95	8.77	8.46
Cl/F	ml/(min*kg)	1.68	2.19	1.84	2.20
V_{ss}	l/kg	9.20			
F_{AUC-28}	%		76.9	91.4	76.5
% AUC extrapolated	%	1.0	0.7	0.5	0.7

For comparison of absolute values, note that i.v. was administered at lower dose than extravascular administration. Clear fields are not applicable for this respective administration route. For abbreviations please refer to the abbreviation and methods sections

Table III Calculated Pharmacokinetic Parameters in Mouse Brains for Different Administration Routes, based on Measured ^{3}H-RD2

Parameter	Units	i.v.	i.p.	s.c.	p.o.
Dose (D)	mg/kg	3.3	10.0	10.0	10.0
t_{max}	min	3	30	20	60
C_{max}/D	(μg/g)/(mg/kg)	0.06	0.06	0.06	0.06
AUC_{0-28}	mg/g*min	1.48	3.37	4.51	4.49
$AUMC_{0-28}$	min^2*mg/g	11,408	22,656	31,419	27,039
MRT_{0-28}	h	128.4	111.9	116.1	100.3
λ_z	min^{-1}	0.00019	0.00019	0.00012	0.00016
$t_{1/2}$	h	60	61	94	73
F_{AUC-28}	%		75.2	100.6	100.1
Brain/plasma ratio AUC_{0-28}		0.8	0.7	0.8	1.0

Clear fields are not applicable for this respective administration route. For abbreviations please refer to the abbreviation and methods sections

1 at 2 days post administration. Overall, a good penetration of the brain was reached with AUC-based brain/plasma ratios reaching 0.8 (i.v. and s.c.) and even 1.0 (p.o.). Interestingly, C_{max}/D in brain was similar for all administration routes (0.06 (μg/ml)/(mg/kg)). The AUC_{0-28} was high for s.c. and p.o. administration (4.5 mg/g*min) but lower following i.p. injection (3.4 mg/g*min). After i.v. injection the AUC_{0-28} was found to be 1.5 mg/g*min but was performed using a lower dose of RD2. The terminal half-life of ^{3}H-RD2 in brain was very comparable to that in plasma, i.e. 61 h (i.v. and i.p.), 73 h (p.o.) and 94 h (s.c.). The bioavailability in the brain was calculated to be 75% for i.p. injection and 100% for s.c. and oral administration.

Plasma Protein Binding

For estimation of the *in vivo* free fraction of RD2 in blood ($f_{u,\,total}$), an *in vitro* assay was used, incubating RD2 with human serum albumin (HSA) and α_1-acid glycoprotein (AGP) (Fig. 5). For AGP this assay resulted in a K_D of 2.77 μM ± 9.97% (r^2 = 99.4%). The fraction unbound to AGP (f_u) was estimated using Eq. (1) under assumption of a RD2 blood concentration of 0.23 μM (C_{RD2}, measured 4 h after p.o. administration). This predicts a free fraction of 12.3%. For HSA, the K_D was above the detection limit of the kit (≥1.4 mM) indicating a very low affinity for HSA and leaving AGP as the main binding partner. Nevertheless, calculation of the RD2 fraction unbound to HSA with an assumed K_D of 1.4 mM results in 68.3% free RD2. Taken together, using Eq. (2), the estimated free fraction of RD2 in plasma was calculated to be approximately 11.5%.

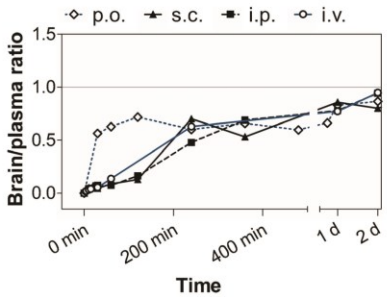

Fig. 4 Time dependent development of the brain/plasma ratio for different administration routes, corrected for residual blood in the brain.

DISCUSSION

In the present study we have analysed the pharmacokinetic properties of the D-peptide RD2, an improved derivative of D3, which has previously been shown to be therapeutically active *in vivo* (20,22).

It has previously been shown *in vivo* for rat plasma and rhesus monkey CSF that D-peptides are proteolytically more stable than their L-forms (16,17). Here, we also demonstrated that RD2 remains intact in mouse plasma and organ homogenates for at least 24 h. Thus, we considered metabolites negligible and used the measured ^{3}H-radioactivity to calculate the RD2 concentrations *in vivo*. Nevertheless, it needs to be clearly stated that all obtained pharmacokinetic values are based on the assumption that the measured radioactivity represents the non-metabolised RD2. Although we have shown that RD2 is stable for at least 24 h in plasma and tissue homogenates, we cannot exclude for later time points partial conversion of RD2 into metabolites that may or may not have reduced therapeutic activities. However, because we did not see any RD2 metabolism at 24 h, there was no reason to expect significant metabolism at 48 h or even 7 days. Furthermore, incubation in organ homogenates or plasma beyond 24 h appeared not to be meaningful because after longer incubation times enzymes

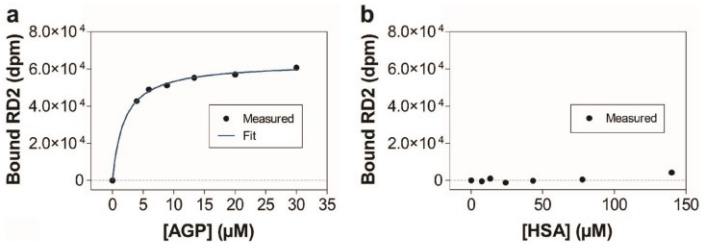

Fig. 5 Plasma protein binding of RD2. Bound ^{3}H-RD2 (in dpm) dependent on AGP (**a**) and HSA (**b**) concentration (*dots*). For binding of RD2 to AGP the fit according to the Michaelis Menten binding equation (*line*) is shown, indicating an almost perfect fit ($r^2 = 99.4\%$, **a**). Binding of RD2 to HSA was below the detection limit of the applied kit ($K_D \geq 1.4$ mM).

in those biological samples will have digested themselves leading to artefacts.

In the present study non-compartmental analysis was performed because a simplistic analysis of the data at hand is possible without making assumptions regarding the number of compartments as is necessary for other analyses such as compartmental or physiologically based models. We quantified RD2 in plasma and brain by measuring the radioactivity and assumed based on the 24 h stability data in plasma and organ homogenates that the measured radioactivity parallels RD2 concentration. Any minor metabolite would influence a more complex model, e.g. a minimal physiologically based model, to produce inaccurate data. However, non-compartmental analysis assumes linear kinetics and may therefore not be the optimal model for pharmacokinetic analysis of RD2. This may result in over- or under-estimation of certain values. Nevertheless, non-compartmental analysis is often used to give an indication of the pharmacokinetic properties of a candidate. Therefore, the more simple non-compartmental analysis was used to avoid additional over-interpretation of our data towards the pharmacokinetic properties of RD2.

Summarised, the pharmacokinetic results yielded a low terminal plasma clearance (Cl/F = 1.68 ml/(min*kg)) of RD2 resulting in long terminal half-lives of about 60 h upon all assessed administration routes. Since L-peptides are typically cleared from the blood relatively fast after administration, often within minutes, this long half-life represents a major advantage of RD2 since it provides more time to reach the target tissue and to be therapeutically active (10,29). The plasma bioavailability was exceptionally high following extravascular administration, with 77% upon intraperitoneal and oral administration and 91% after subcutaneous injection. In comparison to other peptide drugs especially the bioavailability upon oral application is very high (11,30).

It is noteworthy that irrespective of the administration route similar concentrations of RD2 reached the brain where it is thought to be therapeutically active. Irrespective of the administration route an overall brain/plasma ratio of 1 was reached. This indicates sufficient transport of RD2 into the target organ.

RD2 levels found in urine at 24 h post injection agree with the relatively high values obtained at the 24 h time point in the kidney. In general, values are higher upon i.v. injection than those obtained following i.p. administration. Hence, even 1 day after dosing the kidney still seems to be a major excretion route, illustrated also by the high RD2 concentrations observed in the kidney for at least 2 days. Additionally, excretion of RD2 also appears to take place via faeces although rather low doses of RD2 are measured at 24 h post i.v. or i.p. administration, indicating that this excretion pathway is not the dominating one for these administration routes. Furthermore, measurements of RD2 in spleen and inguinal lymph nodes indicate that after 28 days post administration only very low amounts of RD2 remain in the lymphatic system.

Prediction of plasma protein binding based on binding to HSA and AGP suggested a plasma free fraction of about 12%, which is also a very favourable property of RD2 as potential AD drug candidate. It has been reported that only the minority of the examined drugs developed for the central nervous system exhibit free plasma fractions above 10% (31).

Here, we compare RD2 distribution after different administration routes as well as the predicted plasma protein binding. In this pharmacokinetic study we were able to demonstrate high stability, long plasma half-life of several days and favourable oral and subcutaneous bioavailability of this all D-enantiomeric peptide in mice.

CONCLUSION

Taken together, the current study demonstrates favourable pharmacokinetic properties of the D-enantiomeric peptide RD2. Based on the long terminal half-life, high oral bioavailability and drug exposure to the brain it can be concluded, that D-peptides in general may be very well suited as drug candidates. Particularly, providing therapeutic efficiency

in vivo, RD2 may be a very promising candidate for the treatment of Alzheimer's disease.

ACKNOWLEDGMENTS AND DISCLOSURES

We thank Daniela Schumacher, Elias Bissong and Nicole Niemietz for the excellent technical assistance. Additionally, we thank Jörg Mauler for helping with the data analysis. D.W. was supported by grants from the "Portfolio Technology and Medicine" and the Helmholtz-Validierungsfonds of the Impuls und Vernetzungs-Fonds der Helmholtzgemeinschaft; K.J.L. and D.W. were supported by the "Portfolio Drug Research" of the Impuls und Vernetzungs-Fonds der Helmholtzgemeinschaft. The authors declare that they have no conflict of interest.

REFERENCES

1. Reitz C, Mayeux R. Alzheimer disease: epidemiology, diagnostic criteria, risk factors and biomarkers. Biochem Pharmacol. 2014;88(4):640–51.
2. Alzheimer's Association. 2014 Alzheimer's disease facts and figures. Alzheimers Dement. 2014;10(2):e47–92.
3. Soto C. Plaque busters: strategies to inhibit amyloid formation in Alzheimer's disease. Mol Med Today. 1999;5(8):343–50.
4. Hardy JA, Higgins GA. Alzheimer's disease: the amyloid cascade hypothesis. Science. 1992;256(5054):184–5.
5. Benilova I, Karran E, De Strooper B. The toxic a beta oligomer and Alzheimer's disease: an emperor in need of clothes. Nat Neurosci. 2012;15(3):349–57.
6. DaRocha-Souto B, Scotton TC, Coma M, Serrano-Pozo A, Hashimoto T, Serenó L, *et al.* Brain oligomeric beta-amyloid but not total amyloid plaque burden correlates with neuronal loss and astrocyte inflammatory response in amyloid precursor protein/tau transgenic mice. J Neuropathol Exp Neurol. 2011;70(5):360–76.
7. Decker H, Lo KY, Unger SM, Ferreira ST, Silverman MA. Amyloid-beta peptide oligomers disrupt axonal transport through an NMDA receptor-dependent mechanism that is mediated by glycogen synthase kinase 3 beta in primary cultured hippocampal neurons. J Neurosci. 2010;30(27):9166–71.
8. Hardy J, Selkoe DJ. The amyloid hypothesis of Alzheimer's disease: progress and problems on the road to therapeutics. Science. 2002;297(5580):353–6.
9. Sun N, Funke SA, Willbold D. A survey of peptides with effective therapeutic potential in Alzheimer's disease rodent models or in human clinical studies. Mini Rev Med Chem. 2012;12(5):388–98.
10. Sato AK, Viswanathan M, Kent RB, Wood CR. Therapeutic peptides: technological advances driving peptides into development. Curr Opin Biotechnol. 2006;17(6):638–42.
11. Pauletti GM, Gangwar S, Siahaan TJ, Aubé J, Borchardt RT. Improvement of oral peptide bioavailability: peptidomimetics and prodrug strategies. Adv Drug Deliv Rev. 1997;27(2–3):235–56.
12. van Regenmortel MHV, Muller S. D-peptides as immunogens and diagnostic reagents. Curr Opin Biotechnol. 1998;9(4):377–82.
13. Soto C, Kindy MS, Baumann M, Frangione B. Inhibition of Alzheimer's amyloidosis by peptides that prevent beta-sheet conformation. Biochem Biophys Res Commun. 1996;226(3):672–80.
14. Sela M, Zisman E. Different roles of D-amino acids in immune phenomena. FASEB J. 1997;11(6):449–56.
15. Dintzis HM, Symer DE, Dintzis RZ, Zawadzke LE, Berg JM. A comparison of the immunogenicity of a pair of enantiomeric proteins. Proteins Struct Funct Genet. 1993;16(3):306–8.
16. Findeis MA, Musso GM, Arico-Muendel CC, Benjamin HW, Hundal AM, Lee JJ, *et al.* Modified-peptide inhibitors of amyloid beta-peptide polymerization. Biochemistry. 1999;38(21):6791–800.
17. Poduslo JF, Curran GL, Kumar A, Frangione B, Soto C. beta-sheet breaker peptide inhibitor of Alzheimer's amyloidogenesis with increased blood–brain barrier permeability and resistance to proteolytic degradation in plasma. J Neurobiol. 1999;39(3):371–82.
18. Schumacher TNM, Mayr LM, Minor DL, Milhollen MA, Burgess MW, Kim PS. Identification of D-peptide ligands through mirror-image phage display. Science. 1996;271(5257):1854–7.
19. Wiesehan K, Willbold D. Mirror-image phage display: aiming at the mirror. Chembiochem. 2003;4(9):811–5.
20. Funke SA, van Groen T, Kadish I, Bartnik D, Nagel-Steger L, Brener O, *et al.* Oral treatment with the D-enantiomeric peptide D3 improves the pathology and behavior of Alzheimer's disease transgenic mice. ACS Chem Neurosci. 2010;1(9):639–48.
21. van Groen T, Kadish I, Funke A, Bartnik D, Willbold D. Treatment with a beta 42 binding D-amino acid peptides reduce amyloid deposition and inflammation in APP/PS1 double transgenic mice. Adv Protein Chem Struct Biol. 2012;88:133–52.
22. van Groen T, Wiesehan K, Funke SA, Kadish I, Nagel-Steger L, Willbold D. Reduction of Alzheimer's disease amyloid plaque load in transgenic mice by D3, a D-enantiomeric peptide identified by mirror image phage display. ChemMedChem. 2008;3(12):1848–52.
23. van Groen T, Kadish I, Wiesehan K, Funke SA, Willbold D. In vitro and in vivo staining characteristics of small, fluorescent, Aβ42-binding D-enantiomeric peptides in transgenic AD mouse models. ChemMedChem. 2009;4(2):276–82.
24. van Groen T, Kadish I, Funke SA, Bartnik D, Willbold D. Treatment with D3 removes amyloid deposits, reduces inflammation, and improves cognition in aged AbetaPP/PS1 double transgenic mice. J Alzheimers Dis. 2013;34(3):609–20.
25. Olubiyi OO, Frenzel D, Bartnik D, Glück JM, Brener O, Nagel-Steger L, *et al.* Amyloid aggregation inhibitory mechanism of arginine-rich D-peptides. Curr Med Chem. 2014;21(12):1448–57.
26. Larson ME, Lesne SE. Soluble Abeta oligomer production and toxicity. J Neurochem. 2012;120 Suppl 1:125–39.
27. Ferreira ST, Klein WL. The Abeta oligomer hypothesis for synapse failure and memory loss in Alzheimer's disease. Neurobiol Learn Mem. 2011;96(4):529–43.
28. Brown RP, Delp MD, Lindstedt SL, Rhomberg LR, Beliles RP. Physiological parameter values for physiologically based pharmacokinetic models. Toxicol Ind Health. 1997;13(4):407–84.
29. Pollaro L, Heinis C. Strategies to prolong the plasma residence time of peptide drugs. Med Chem Commun. 2010;1(5):319–24.
30. Renukuntla J, Vadlapudi AD, Patel A, Boddu SH, Mitra AK. Approaches for enhancing oral bioavailability of peptides and proteins. Int J Pharm. 2013;447(1–2):75–93.
31. Kratochwil NA, Huber W, Muller F, Kansy M, Gerber PR. Predicting plasma protein binding of drugs: a new approach. Biochem Pharmacol. 2002;64(9):1355–74.

2.4 Pharmacokinetic properties of tandem D-peptides designed for treatment of Alzheimer's disease.

Published in: European Journal of Pharmaceutical Sciences

Impact Factor: 3.35

Contributions: 45%

Involved in the conception and design of the experiments; conducted large fraction of the experiments and data analysis; involved in writing the manuscript.

European Journal of Pharmaceutical Sciences 89 (2016) 31–38

Contents lists available at ScienceDirect

European Journal of Pharmaceutical Sciences

journal homepage: www.elsevier.com/locate/ejps

Pharmacokinetic properties of tandem D-peptides designed for treatment of Alzheimer's disease

Leonie H.E. Leithold [a,1], Nan Jiang [a,1], Julia Post [a], Nicole Niemietz [b], Elena Schartmann [a], Tamar Ziehm [a], Janine Kutzsche [a], N. Jon Shah [b,c], Jörg Breitkreutz [d], Karl-Josef Langen [b,e], Antje Willuweit [b,*], Dieter Willbold [a,f,**]

[a] Institute of Complex Systems, Structural Biochemistry, Forschungszentrum Jülich GmbH, 52425 Jülich, Germany
[b] Institute of Neuroscience and Medicine, Medical Imaging Physics, Forschungszentrum Jülich GmbH, 52425 Jülich, Germany
[c] Department of Neurology, Universitätsklinikum der RWTH Aachen, 52074 Aachen, Germany
[d] Institute of Pharmaceutics and Biopharmaceutics, Heinrich-Heine-Universität Düsseldorf, 40225 Düsseldorf, Germany
[e] Department of Nuclear Medicine, Universitätsklinikum der RWTH Aachen, 52074 Aachen, Germany
[f] Institut für Physikalische Biologie, Heinrich-Heine-Universität Düsseldorf, 40225 Düsseldorf, Germany

ARTICLE INFO

Article history:
Received 19 November 2015
Received in revised form 6 April 2016
Accepted 12 April 2016
Available online 13 April 2016

Keywords:
Pharmacokinetics
Alzheimer's disease
D-enantiomeric peptide
Beta amyloid ligand
Therapy

ABSTRACT

Peptides are more and more considered for the development of drug candidates. However, they frequently exhibit severe disadvantages such as instability and unfavourable pharmacokinetic properties. Many peptides are rapidly cleared from the organism and oral bioavailabilities as well as *in vivo* half-lives often remain low. In contrast, some peptides consisting solely of D-enantiomeric amino acid residues were shown to combine promising therapeutic properties with high proteolytic stability and enhanced pharmacokinetic parameters. Recently, we have shown that D3 and RD2 have highly advantageous pharmacokinetic properties. Especially D3 has already proven promising properties suitable for treatment of Alzheimer's disease. Here, we analyse the pharmacokinetic profiles of D3D3 and RD2D3, which are head-to-tail tandem D-peptides built of D3 and its derivative RD2. Both D3D3 and RD2D3 show proteolytic stability in mouse plasma and organ homogenates for at least 24 h and in murine and human liver microsomes for 4 h. Notwithstanding their high affinity to plasma proteins, both peptides are taken up into the brain following i.v. as well as i.p. administration. Although both peptides contain identical D-amino acid residues, they are arranged in a different sequence order and the peptides show differences in pharmacokinetic properties. After i.p. administration RD2D3 exhibits lower plasma clearance and higher bioavailability than D3D3. We therefore concluded that the amino acid sequence of RD2 leads to more favourable pharmacokinetic properties within the tandem peptide, which underlines the importance of particular sequence motifs, even in short peptides, for the design of further therapeutic D-peptides.

1. Introduction

Despite remarkable efforts to develop curative and disease modifying treatments against Alzheimer's disease (AD), thus far only symptomatic treatment is available (Nygaard, 2013). Among other substance classes, peptides are being investigated as promising drug candidates (Sun et al., 2012). Currently, however, most peptides have shown severe disadvantages due to their immunogenicity and instability as well as unfavourable pharmacokinetic properties such as rapid clearance, low oral bioavailability and short *in vivo* half-lives (Pauletti et al., 1997; Sato et al., 2006).

To overcome those disadvantages, D-enantiomeric peptides are being developed. They combine high protease resistance due to stereoisomeric selectivity of mammalian proteolytic enzymes with low, if any, immunogenicity, leading to slower system elimination and thereby providing more time for therapeutic activity (Dintzis et al., 1993; van Regenmortel and Muller, 1998).

Abbreviations: %ID, relative injected dose; AD, Alzheimer's disease; AGP, α_1-acid glycoprotein; AUC, area under the concentration-time curve; AUMC, area under the moment curve; Aβ, β-amyloid; C, concentration; Cl, clearance; D, dose; dpm, disintegrations per minute; F, bioavailability; f_u, unbound fraction; HSA, human serum albumin; i.p., intraperitoneal; i.v., intravenous; inf, infinity; K_D, dissociation constant; MRT, mean residence time; r^2, correlation coefficient; $t_{1/2}$, terminal half-life; TLC, thin layer chromatography; V_{ss}, distribution volume in steady state; V_z, terminal distribution volume; λ_z, terminal elimination rate constant.

* Correspondence to: A. Willuweit, Institute of Neuroscience and Medicine, Medical Imaging Physics (INM-4), Forschungszentrum Jülich GmbH, 52425 Jülich, Germany.
** Correspondence to: D. Willbold, Institute of Complex Systems, Structural Biochemistry (ICS-6), Forschungszentrum Jülich GmbH, 52425 Jülich, Germany.
E-mail addresses: l.hofmann@fz-juelich.de (L.H.E. Leithold), n.jiang@fz-juelich.de (N. Jiang), j.post@fz-juelich.de (J. Post), n.niemietz@fz-juelich.de (N. Niemietz), e.schartmann@fz-juelich.de (E. Schartmann), t.ziehm@fz-juelich.de (T. Ziehm), j.kutzsche@fz-juelich.de (J. Kutzsche), n.j.shah@fz-juelich.de (N.J. Shah), joerg.breitkreutz@uni-duesseldorf.de (J. Breitkreutz), k.j.langen@fz-juelich.de (K.-J. Langen), a.willuweit@fz-juelich.de (A. Willuweit), d.willbold@fz-juelich.de (D. Willbold).
[1] Authors contributed equally.

http://dx.doi.org/10.1016/j.ejps.2016.04.016
0928-0987/

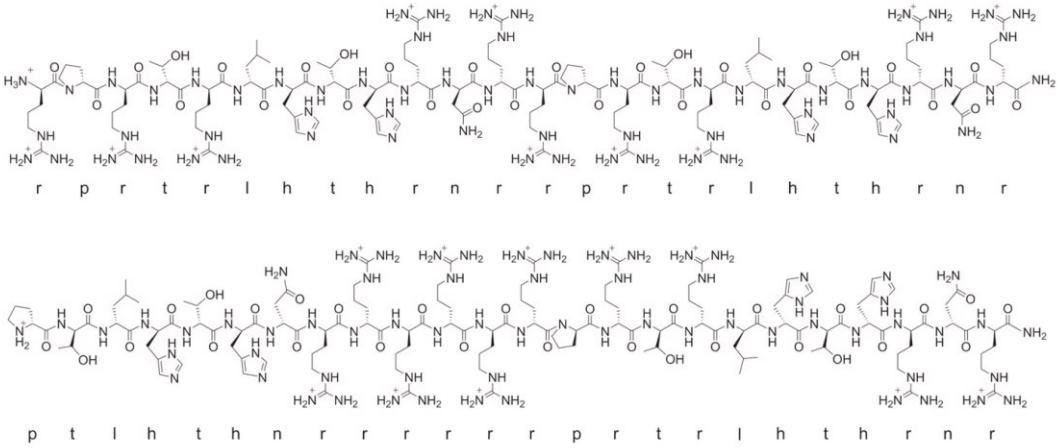

Fig. 1. Lewis structure and single letter amino acid code of D3D3 (top) and RD2D3 (bottom). Both peptides are D-enantiomeric peptides (3.2 kDa).

Using mirror image phage display against β-amyloid (Aβ) monomers as target (Schumacher et al., 1996; Wiesehan and Willbold, 2003), we have previously identified the D-peptide D3 which has been shown to improve pathology and cognition in transgenic AD mice (Funke et al., 2010; van Groen et al., 2012; van Groen et al., 2013; van Groen et al., 2008). Additionally, a number of derivatives have also been designed. Among those, RD2 has shown enhanced properties *in vitro* and *in silico*, while containing the same D-amino acid residues in a rationally reordered sequence (Olubiyi et al., 2014). Studies assessing pharmacokinetic properties of both D3 (Jiang et al., 2015)

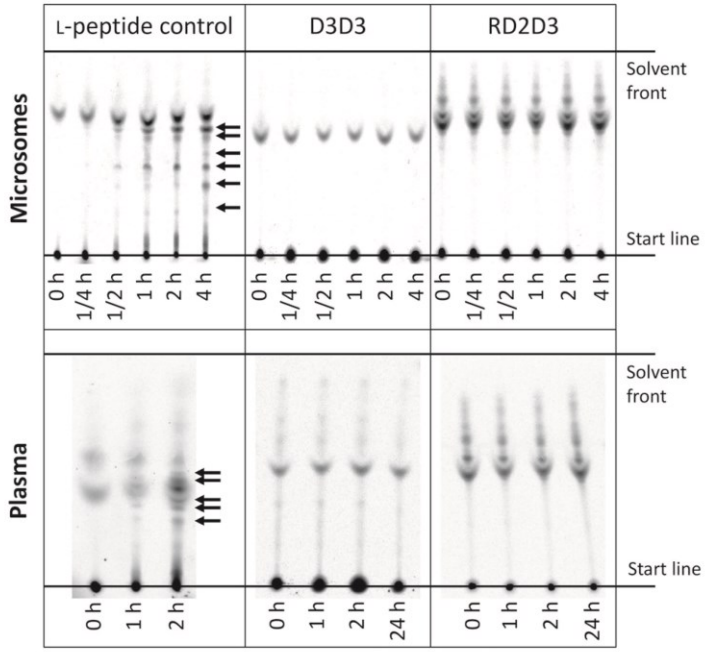

Fig. 2. Autoradiography of thin layer chromatogram, showing proteolytic stability of ^{3}H-D3D3 and ^{3}H-RD2D3 in mouse plasma and liver microsomes in comparison to an L-peptide control. The peptides were incubated with plasma or microsomes at 37 °C for the given amount of time and applied to thin layer chromatography plates. Proteolytic degradation is apparent from time dependent appearance of additional bands, as was obvious for the L-peptide control (arrows). In contrast, D3D3 and RD2D3 remained stable for 4 h in liver microsomes and plasma for up to 24 h of incubation.

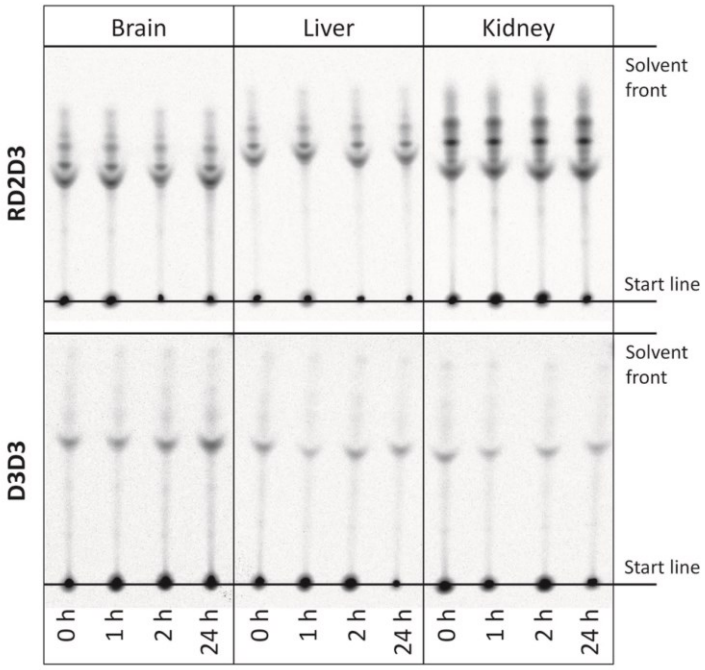

Fig. 3. Autoradiography of thin layer chromatogram, showing proteolytic stability of ^{3}H-D3D3 and ^{3}H-RD2D3 in mouse organ homogenates. The peptides were incubated with brain, liver and kidney homogenates at 37 °C for the given amount of time and applied to thin layer chromatography plates. No proteolytic degradation is apparent for both peptides for up to 24 h of incubation.

and RD2 (Leithold et al., 2015) have demonstrated auspicious characteristics such as long half-lives and high oral bioavailability.

Here, we determined the pharmacokinetic properties of D3D3 and RD2D3, which can be thought of as head-to-tail tandem homo- and heteropeptides made of D3 and RD2. The rationale behind the design of the tandem peptides is that multivalent D-peptides can be expected to target their multivalent target molecules, here Aβ oligomers, with increased efficiency. Recently, this was shown to be true for D3D3 *in vitro* and *in vivo* (Brener et al., 2015).

2. Methods

2.1. Peptides

D3D3 (H-rprtrlhthrnrrprtrlhthrnr-NH_2, 3.2 kDa) and RD2D3 (H-ptlhthnrrrrrrprtrlhthrnr-NH_2, 3.2 kDa) were purchased from peptides&elephants GmbH (Potsdam, Germany). All peptides consist solely of D-enantiomeric amino acids. The Lewis structures of both peptides can be found in Fig. 1.

The tritium-labelled peptides ^{3}H-D3D3 (H-rprtrlhthrnrrprtrlhthrnr-NH_2, 110 Ci/mmol) and ^{3}H-RD2D3 (H-ptlhthnrrrrrrprtrlhthrnr-NH_2, 73 Ci/mmol) were purchased from Quotient Bioresearch (Radiochemicals) Ltd. (Cardiff, United Kingdom) to contain 1 mCi/ml respectively 37 MBq/ml and were supplied as solution in water and ethanol (1:1). The radioactively labelled L-enantiomer of D3 (H-RPRTRLHTHRNR-NH_2, 103 Ci/mmol, Quotient Bioresearch), was used as control peptide for stability assessment.

2.2. Proteolytic stability

Proteolytic stability of ^{3}H-D3D3 and ^{3}H-RD2D3 in mouse organ homogenates was assessed as described previously (Leithold et al., 2015). Additionally, 2 µl of a ^{3}H-L-peptide were incubated with 1 µl mouse plasma as control.

Furthermore, proteolytic stability of all peptides against degradation by microsomes was analysed using microsomes from mouse and human liver (pooled from CD-1 mice; pooled from male human liver; protein content approx. 20 mg/ml, Sigma-Aldrich). 6 µl ^{3}H-peptide were added to 4 µl pre-warmed microsome solution and incubated at 37 °C. After different incubation times the reaction was stopped by addition of 6 µl mobile solvent (2-butanol/pyridine/ammonia (28%)/water, 39/34/10/26 ml respectively) and samples were stored at −20 °C until further use. For detection, thin layer chromatography and autoradiography were performed as described before (Leithold et al., 2015).

2.3. Pharmacokinetic studies

Pharmacokinetic analysis of the ^{3}H-peptides was assessed as previously described, with the exceptions explained below (Leithold et al., 2015). For pharmacokinetic analysis different doses and time points of organ harvesting were chosen per route of administration: i.v. injection 3.3 mg/kg, 3 min, 5 min, 10 min, 15 min, 30 min, 1 h, 4 h, 18 h, 1 d, 2 d; i.p. administration 10 mg/kg, 10 min, 20 min, 30 min, 1 h, 2 h, 4 h, 6 h, 1 d, 2 d. For each time point three mice were administered with the respective dose. The terminal elimination rate constant (λ_z) was obtained

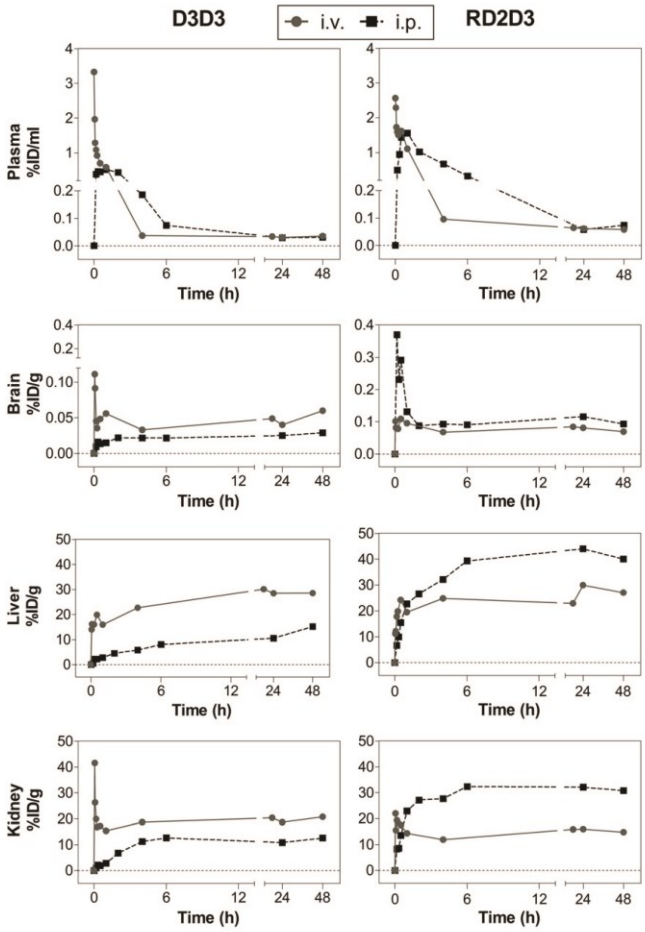

Fig. 4. Time-dependent distribution of ^{3}H-D3D3 and ^{3}H-RD2D3 in mouse plasma, brain, liver and kidney after i.v. and i.p. administration. Radioactively labelled D3D3 or RD2D3 was administered together with non-labelled peptide at total concentrations of 10 mg/kg (i.p.) or 3.3 mg/kg (i.v.). The concentration of D3D3 and RD2D3 is shown as percent of the injected dose per millilitre plasma (%ID/ml) or gram organ (%ID/g). Graphs show the means of three mice per time point.

by logarithmic extrapolation of the last five to six observed concentrations based on the highest correlation coefficient obtained ($r^2 = 0.99$ for all calculations).

2.4. Plasma protein binding

The plasma protein binding assay was performed twice per peptide as described previously (Leithold et al., 2015).

2.5. Animals

C57BL/6 mice were used for plasma extraction and pharmacokinetic studies. All animal experiments were carried out in conformance with the German Protection of Animals Act (TierSchG §§ 7–9) and with permit from an Animal Protection Committee (AZ84-02.04.2011.A356).

3. Results

3.1. Proteolytic stability

It was shown previously that both D3 and RD2 are proteolytically stable in organ homogenates and plasma (Jiang et al., 2015; Leithold et al., 2015). To confirm the proteolytic stability for both tandem peptides, ^{3}H-D3D3 and ^{3}H-RD2D3 were incubated with mouse plasma (Fig. 2) and organ homogenates (Fig. 3) for up to 24 h and analysed by thin layer chromatography (TLC). It is noteworthy that under TLC conditions the peptides bound differently to plasma and organ constituents, thereby exhibiting different patterns and intensities on the TLC plate as detected by autoradiography. Results show that overall composition of both D3D3 and RD2D3 did not change over time, but remained stable for at least 24 h. In contrast, the L-peptide used for control was proteolytically degraded within 2 h as visible by the time dependent appearance of additional bands (Fig. 2).

Table 1
Pharmacokinetic parameters determined from mouse plasma for i.v. and i.p. administration. Clear fields are not applicable for the respective administration route. For abbreviations please refer to the abbreviations section.

Parameter	Units	D3D3		RD2D3	
		i.v.	i.p.	i.v.	i.p.
Dose (D)	mg/kg	3.3	10	3.3	10
t_{max}	min	3	60	3	60
C_{max}/D	(μg/ml)/(mg/kg)	0.54	0.16	0.58	0.47
$AUC_{0\text{-last}}$	mg/ml * min	0.18	0.61	0.32	1.82
$AUMC_{0\text{-last}}$	min^2 * mg/ml	131	424	229	1091
$MRT_{0\text{-last}}$	h	11.9	11.6	11.9	10.0
λ_z	min^{-1}	0.0155	0.0075	0.0137	0.0050
$t_{1/2}$	h	0.7	1.5	0.8	2.3
$AUC_{0\text{-inf}}$	mg/ml * min	0.18	0.62	0.32	1.87
$AUMC_{0\text{-inf}}$	min^2 * mg/ml	137	461	240	1225
$MRT_{0\text{-inf}}$	h	12.3	12.3	12.3	10.9
V_z	l/kg	1.15	2.37	0.74	1.99
Cl/F	ml/(min * kg)	17.9	16.1	10.2	5.4
V_{ss}	l/kg	13.2		7.5	
$F_{AUC\text{-last}}$	%		110		187
% AUC extrapolated	%	1.1	1.9	1.2	2.3

Moreover, neither D-peptide was degraded after 4 h incubation with liver microsomes, in contrast to the L-peptide (Fig. 2). Confirmation of proteolytic stability of D3D3 and RD2D3 was important to ensure that measured radioactivity in the pharmacokinetic studies correlated with ^{3}H-D3D3 and ^{3}H-RD2D3 total concentrations.

3.2. Pharmacokinetic properties

To assess pharmacokinetic parameters ^{3}H-labelled D3D3 and RD2D3 were used for i.p. and i.v. administration in mice. Following the radioactive label, both peptides were successfully quantitated in all analysed organs and upon all administration routes. Fig. 4 shows the relative injected dose per millilitre plasma or gram brain, liver and kidney over the time course of two days as well as the brain/plasma ratio.

Remarkably, for RD2D3 intraperitoneal rather than intravenous administration resulted in higher values in all organs, whereas this was the opposite for D3D3 where i.v. resulted in higher amounts present in all assessed organs. Higher concentration of D3D3 and RD2D3 in the liver as compared to the kidney suggests the liver as the major pathway for excretion for both peptides. It is noteworthy that after 2 days post administration both peptides were still present in all organs and especially high in liver and kidney. RD2D3 reached higher levels than D3D3 in the brain as well as in liver and kidney (Fig. 4), which is most prominent following i.p. administration.

3.2.1. Plasma pharmacokinetic parameters

Plasma pharmacokinetic parameters were calculated based on back calculated peptide concentrations from measured radioactivity in plasma and are summarised in Table 1. The maximally observed concentration relative to the Dose (C_{max}/D) was similar for i.v. injection (D3D3 0.54 and RD2D3 0.58 (μg/ml)/(mg/kg)) but differed upon i.p. administration between 0.16 (μg/ml)/(mg/kg) for D3D3 and 0.47 (μg/ml)/(mg/kg) for RD2D3. For both D-peptides the areas under the curve $AUC_{0\text{-last}}$ and $AUC_{0\text{-inf}}$ do not differ much, which is due to the very low extrapolated part of the $AUC_{0\text{-inf}}$ (< 3%). RD2D3 showed higher plasma $AUC_{0\text{-inf}}$ for both administration routes (i.v. 0.32 mg/ml * min and i.p. 1.87 mg/ml * min) as compared to D3D3 (i.v. 0.18 mg/ml * min and i.p. 0.62 mg/ml * min). The mean retention time ($MRT_{0\text{-inf}}$) was around 11 and 12 h and similar for all administration routes and both peptides. The rate of i.v. terminal plasma clearance was higher for D3D3 with Cl/F = 17.9 ml/(min * kg) than for RD2D3 with Cl/F = 10.2 ml/(min * kg). Additionally, upon i.p. administration the clearance was found to be lower than after i.v. administration for both peptides. This results in longer half-lives ($t_{1/2}$) for RD2D3 (i.v. 0.8 h and i.p. 2.3 h) compared to D3D3 (i.v. 0.7 h and i.p. 1.5 h). Furthermore, the bioavailability (F) upon i.p. administration of RD2D3 was very high with about 190%, while D3D3 reached 110%.

3.2.2. Brain pharmacokinetic parameters

Since the brain is thought to be the therapeutically relevant target organ, pharmacokinetic parameters were also calculated for the brain (Table 2). Both peptides showed an increasing brain/plasma ratio over time, reaching 1 after about 6 to 12 h (Fig. 5), which resulted in an overall brain/plasma ratio based on the $AUC_{0\text{-last}}$ of 0.6 (i.v.) and 0.3 (i.p.) for D3D3 and 0.6 (i.v.) and 0.5 (i.p.) for RD2D3. The time-dependent The brain exposure ($AUC_{0\text{-last}}$) was higher for RD2D3 than for D3D3, especially upon i.p. administration (RD2D3 i.v. 0.19 and i.p. 0.88 mg/g * min and D3D3 i.v. 0.12 and i.p. 0.20 mg/g * min). The C_{max}/D was 0.02 (μg/g)/(mg/kg) for i.v. administration. I.p. injection lead to a C_{max}/D of 0.01 for D3D3 and was higher for RD2D3 with 0.11 (μg/g)/(mg/kg). The MRT was calculated to be about one day for both peptides and administration routes. Furthermore, the bioavailability of the i.p. administration was low for D3D3 with 55% and very high for RD2D3 with 157%.

3.3. Plasma protein binding

In vivo plasma protein binding was estimated by *in vitro* incubation of ^{3}H-labelled D3D3 and RD2D3 with human serum albumin (HSA) and α_1-acid glycoprotein (AGP) (Fig. 6). For AGP the binding curves of both peptides reached saturation even at the lowest AGP concentration. This indicates strong binding affinities to AGP. Results yielded for RD2D3 a K_D of 0.04 μM ± 18% and for D3D3 a K_D of 0.03 μM ± 18%. Binding to HSA did not reach saturation and could therefore not be determined reliably, with K_D values being in the hundreds micromolar range. It could be deduced that both peptides showed much higher affinity to AGP than to HSA and plasma protein binding therefore is mainly determined by AGP binding. The expected free fraction in plasma was calculated disregarding HSA binding and under the assumption of peptide concentrations in plasma of C_{RD2D3} = 0.027 μM and C_{D3D3} = 0.013 μM (concentrations 24 h after administration). Results showed a fraction unbound (f_u) for RD2D3 of 0.20% and for D3D3 of 0.16%.

3.4. Proteolytic stability in human samples

To confirm that the peptides are not only stable in mouse tissue, proteolytic stability was additionally assessed and ^{3}H-D3D3 and ^{3}H-RD2D3 and the ^{3}H-L-peptide control were incubated with human liver microsomes and analysed by TLC (Fig. 7). Results show that overall composition of both D3D3 and RD2D3 remained stable for at least 24 h both in human microsomes. In contrast, the L-peptide used for control was quickly proteolytically degraded.

Table 2
Brain pharmacokinetic parameters determined for i.v. and i.p. administration. Clear fields are not applicable for the respective administration route. For abbreviations please refer to the abbreviations section.

Parameter	Units	D3D3		RD2D3	
		i.v.	i.p.	i.v.	i.p.
Dose (D)	mg/kg	3.3	10	3.3	10
t_{max}	min	3	2880	30	10
C_{max}/D	(μg/g)/(mg/kg)	0.02	0.01	0.02	0.11
$AUC_{0\text{-last}}$	mg/g * min	0.12	0.20	0.19	0.88
$AUMC_{0\text{-last}}$	min^2 * mg/g	189	315	269	1264
$MRT_{0\text{-last}}$	h	26.8	26.5	24.2	23.8
$F_{AUC\text{-last}}$	%		55		157
Brain/plasma ratio $AUC_{0\text{-last}}$		0.6	0.3	0.6	0.5

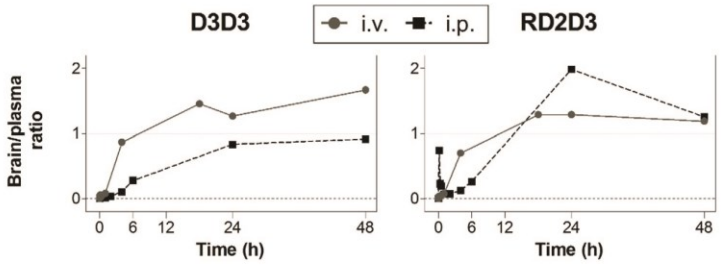

Fig. 5. Time-dependent development of ^{3}H-D3D3 and ^{3}H-RD2D3 brain/plasma ratio after i.v. and i.p. administration. Graphs show the means of three mice per time point, corrected for residual blood in the brain.

4. Discussion

Here, we have assessed the pharmacokinetic properties of two D-peptides which are head-to-tail tandem derivatives of the previously described peptides D3 and its derivative RD2. D3 has been selected by mirror image phage display for binding against Aβ(1–42) and both D3 and RD2 have demonstrated therapeutic potential *in vitro* and *in vivo* (Bartnik et al., 2010; Funke et al., 2010; Olubiyi et al., 2014; van Groen et al., 2008). Furthermore, D3 and RD2 exhibited excellent pharmacokinetic properties as has been shown previously (Jiang et al., 2015; Leithold et al., 2015). In a next step, tandem peptides were created in order to enhance the affinity to Aβ (Brener et al., 2015). Thereafter, pharmacokinetic assessment was performed to determine their ability to reach the target organ brain.

For both D3 and RD2 it could previously be shown that they remain stable in mouse organ homogenates and plasma (Jiang et al., 2015; Leithold et al., 2015). Here, we demonstrated that the homo- and heteropeptides D3D3 and RD2D3 are likewise proteolytically stable for at least 24 h in mouse plasma, organ homogenates and liver microsomes. We used the measured ^{3}H-radioactivity of the administered peptides in the pharmacokinetic study to calculate the peptide concentrations. This assumes that the non-metabolised peptides are represented by the measured radioactivity which is then used to obtain the pharmacokinetic parameters. Although we have shown that the peptides are stable in mouse plasma for 24 h we cannot exclude partial metabolism at later time points which might or might not influence their therapeutic effectivity. Incubation in plasma and organ homogenates beyond 24 h and microsomes beyond 4 h appeared not to be meaningful since enzyme activities in biological samples cannot be expected to last for long incubation times at 37 °C. Furthermore, due to the complete lack of metabolism of RD2D3 and D3D3 after 24 h incubation with organ homogenates as well as after incubation with microsomes there was no reason to expect significant metabolism at 48 h. Nevertheless, for pharmacokinetic assessment we performed a non-compartmental analysis since this is a simplistic analysis without the need for assumptions regarding the number of compartments. Any minor metabolite would influence more complex pharmacokinetic models and would lead to inaccurate data. The authors are aware that non-compartmental analysis may not be the optimal model for the pharmacokinetic analysis. It assumes linear kinetics and may therefore result in over- or under-estimation of certain parameters. However, it is often used as an initial indication of the pharmacokinetic properties of a substance and avoids additional over-interpretation of the data at hand. The present study was performed in healthy C57BL/6 mice. The

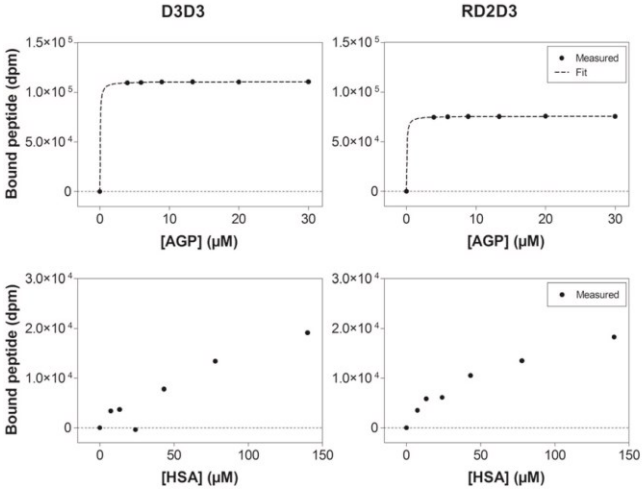

Fig. 6. Plasma protein binding of ^{3}H-D3D3 and ^{3}H-RD2D3. Graphs display the determined amount of D-peptide bound (in dpm) to α_1-acid glycoprotein (AGP) or human serum albumin (HSA) at different concentrations. Binding affinity to AGP was roughly estimated based on the Michaelis Menten binding equation (dotted lines). Dissociation constants for binding to HSA could be estimated to be in the hundreds μM range as the saturation was not reached even above 100 μM.

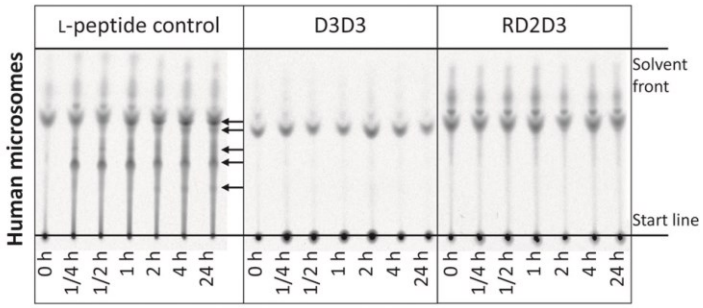

Fig. 7. Autoradiography of thin layer chromatogram, showing proteolytic stability of ^{3}H-D3D3 and ^{3}H-RD2D3 in human liver microsomes. The peptides were incubated with human liver microsomes at 37 °C for the given amount of time and applied to thin layer chromatography plates. No proteolytic degradation is apparent for both peptides for up to 24 h of incubation whereas the L-peptide control is degraded rapidly as indicated by the appearance of additional bands (arrows).

resulting pharmacokinetic parameters may be different in transgenic AD mouse models. Existing preliminary pharmacokinetic data for D3, however, does not suggest any significant difference in pharmacokinetic properties between wild type mice and transgenic AD mice.

To summarise, the pharmacokinetic analysis showed that RD2D3 has a lower clearance than D3D3, resulting in higher drug exposure in plasma and brain as well as a high bioavailability after i.p. administration. Both peptides have higher AUC values upon i.p. administration compared to i.v. administration. However, both D3D3 and RD2D3 have relatively high elimination rate constants and therefore short half-lives of only few hours that are in the same range as other peptides assessed as potential drugs (Pollaro and Heinis, 2010). Furthermore, D3D3 and RD2D3 have a low predicted free fraction in plasma and may therefore only be available for therapeutic action in the target organ in small amounts. However, it was shown that high plasma protein binding does not necessarily impede drug efficacy, and newly approved drugs often show high plasma protein binding (Liu et al., 2014; Smith et al., 2010; Zhang et al., 2012). This is also the case for the available drugs indicated for the central nervous system, Kratochwil et al. (2002) found no general preference for high or low HSA binding.

The i.p. plasma drug exposure especially of RD2D3 is considerably higher than upon i.v. administration. This could possibly be explained by the higher rate of clearance observed for i.v. administration. Entero-hepatic recirculation or renal reabsorption can lead to a prolonged presence of the peptide in the organism (Bendayan, 1996; Roberts et al., 2002). This is underlined by the results showing no apparent decrease of the peptide concentration in liver and kidney after 2 days (Fig. 4). For RD2D3 the concentration in both organs is higher than for D3D3, indicating that this effect is more pronounced for RD2D3, explaining the much higher bioavailability of RD2D3 than D3D3. The bioavailability upon oral administration for the tandem peptides remains to be analysed, however, both monovalent peptides D3 and RD2 were shown to exhibit promising pharmacokinetic properties for oral application (Jiang et al., 2015; Leithold et al., 2015).

It was shown that D3 itself has a half-life in plasma of 32 h for i.v. and >40 h upon i.p. or oral administration (Jiang et al., 2015). Remarkably, RD2 showed a plasma half-life of about 60 h for all assessed administration routes (Leithold et al., 2015). In contrast, both tandem peptides have remarkably short half-lives of only few hours. This is also reflected in the clearance, with D3D3 exhibiting the highest rate, followed by RD2D3, D3 and RD2 having the slowest clearance. Interestingly, the MRT in both plasma and brain was higher for the tandem peptides than for D3 for both i.p. and i.v. administration, while RD2 had much higher MRT values for all administration routes. RD2 also showed the highest brain/plasma ratio when calculated using the $AUC_{0\text{-last}}$ of all peptides. Since also the drug exposure in plasma, as calculated by plasma $AUC_{0\text{-inf}}$, is highest in RD2 and D3, it is concluded that the larger size of the tandem peptides results in less favourable pharmacokinetic parameters. Furthermore, resorption from the peritoneum into the blood seems to be least effective for the tandem peptides. Plasma levels of D3D3 are very low, higher for RD2D3 followed by D3, while RD2 is resorbed very efficiently. Similarly, peptide levels in the brain are highest for RD2, followed by D3 and the tandem peptides with RD2D3 exhibiting higher levels than D3D3. Considering the brain/plasma ratios which do not differ much, the low brain levels of the tandem peptides may result primarily from their insufficient resorption rather than from an inferior ability to enter the brain.

Additionally, we were able to show that D3D3 and RD2D3 are proteolytically stable in human liver microsomes for at least 24 h. The stability in human tissue is important knowledge for the further development of these D-peptides into clinical application.

5. Conclusions

Taken together, the tandem peptides exhibit less favourable pharmacokinetic properties than the single peptides. Resorption of D3D3 and RD2D3 is less effective, resulting in lower brain concentrations as compared to the single peptides D3 and RD2. This disadvantage of the tandem peptides could possibly be outweighed by higher efficiency of the tandem compounds as was indicated by recent data for D3D3 (Brener et al., 2015). Furthermore, it is concluded that the sequence order of the D-enantiomeric amino acid residues has a considerable impact on pharmacokinetic properties of the peptide. Peptides harbouring the amino acid residue sequence of RD2 were found to exhibit enhanced pharmacokinetic properties than those harbouring the D3 sequence. This can be seen both in RD2 alone when compared to D3 and similarly within RD2D3 in comparison to D3D3.

Conflict of interest

The authors declare that they have no conflict of interest.

Acknowledgements

We thank Jörg Mauler for helping with the data analysis. D.W. and N.J.S. were supported by grants from the "Portfolio Technology and Medicine" of the Impuls und Vernetzungs-Fonds der Helmholtzgemeinschaft. D.W. was supported by the Helmholtz-Validierungsfonds of the Impuls und Vernetzungs-Fonds der Helmholtzgemeinschaft; K.J.L. and D.W. were supported by the "Portfolio Drug Research" of the Impuls und Vernetzungs-Fonds der Helmholtzgemeinschaft.

References

Bartnik, D., Funke, S.A., Andrei-Selmer, L.C., Bacher, M., Dodel, R., Willbold, D., 2010. Differently selected D-enantiomeric peptides act on different Abeta species. Rejuvenation Res. 13, 202–205.

Bendayan, R., 1996. Renal drug transport: a review. Pharmacotherapy 16, 971–985.

Brener, O., Dunkelmann, T., Gremer, L., van Groen, T., Mirecka, E.A., Kadish, I., Willuweit, A., Kutzsche, J., Jurgens, D., Rudolph, S., Tusche, M., Bongen, P., Pietruszka, J., Oesterhelt, F., Langen, K.J., Demuth, H.U., Janssen, A., Hoyer, W., Funke, S.A., Nagel-Steger, L., Willbold, D., 2015. QIAD assay for quantitating a compound's efficacy in elimination of toxic Abeta oligomers. Sci. Rep. 5, 13222.

Dintzis, H.M., Symer, D.E., Dintzis, R.Z., Zawadzke, L.E., Berg, J.M., 1993. A comparison of the immunogenicity of a pair of enantiomeric proteins. Protein Struct. Funct. Genet. 16, 306–308.

Funke, S.A., van Groen, T., Kadish, I., Bartnik, D., Nagel-Steger, L., Brener, O., Sehl, T., Batra-Safferling, R., Moriscot, C., Schoehn, G., Horn, A.H.C., Mueller-Schiffmann, A., Korth, C., Sticht, H., Willbold, D., 2010. Oral treatment with the D-enantiomeric peptide D3 improves the pathology and behavior of Alzheimer's disease transgenic mice. ACS Chem. Neurosci. 1, 639–648.

Jiang, N., Leithold, L.H.E., Post, J., Ziehm, T., Mauler, J., Gremer, L., Cremer, M., Schartmann, E., Shah, N.J., Kutzsche, J., Langen, K.-J., Breitkreutz, J., Willbold, D., Willuweit, A., 2015. Preclinical pharmacokinetic studies of the tritium labelled D-enantiomeric peptide D3 developed for the treatment of Alzheimer's disease. PLoS One 10, e0128553.

Kratochwil, N.A., Huber, W., Muller, F., Kansy, M., Gerber, P.R., 2002. Predicting plasma protein binding of drugs: a new approach. Biochem. Pharmacol. 64, 1355–1374.

Leithold, L.H.E., Jiang, N., Post, J., Ziehm, T., Schartmann, E., Kutzsche, J., Shah, N.J., Breitkreutz, J., Langen, K.J., Willuweit, A., Willbold, D., 2015. Pharmacokinetic Properties of a Novel D-Peptide Developed to Be Therapeutically Active Against Toxic β-Amyloid Oligomers. Pharm. Res.

Liu, X., Wright, M., Hop, C.E.C.A., 2014. Rational use of plasma protein and tissue binding data in drug design. J. Med. Chem. 57, 8238–8248.

Nygaard, H.B., 2013. Current and emerging therapies for Alzheimer's disease. Clin. Ther. 35, 1480–1489.

Olubiyi, O.O., Frenzel, D., Bartnik, D., Glück, J.M., Brener, O., Nagel-Steger, L., Funke, S.A., Willbold, D., Strodel, B., 2014. Amyloid aggregation inhibitory mechanism of arginine-rich D-peptides. Curr. Med. Chem. 21, 1448–1457.

Pauletti, G.M., Gangwar, S., Siahaan, T.J., Aubé, J., Borchardt, R.T., 1997. Improvement of oral peptide bioavailability: peptidomimetics and prodrug strategies. Adv. Drug Deliv. Rev. 27, 235–256.

Pollaro, L., Heinis, C., 2010. Strategies to prolong the plasma residence time of peptide drugs. Medchemcomm 1, 319–324.

Roberts, M.S., Magnusson, B.M., Burczynski, F.J., Weiss, M., 2002. Enterohepatic circulation: physiological, pharmacokinetic and clinical implications. Clin. Pharmacokinet. 41, 751–790.

Sato, A.K., Viswanathan, M., Kent, R.B., Wood, C.R., 2006. Therapeutic peptides: technological advances driving peptides into development. Curr. Opin. Biotechnol. 17, 638–642.

Schumacher, T.N.M., Mayr, L.M., Minor, D.L., Milhollen, M.A., Burgess, M.W., Kim, P.S., 1996. Identification of D-peptide ligands through mirror-image phage display. Science 271, 1854–1857.

Smith, D.A., Di, L., Kerns, E.H., 2010. The effect of plasma protein binding on in vivo efficacy: misconceptions in drug discovery. Nat. Rev. Drug Discov. 9, 929–939.

Sun, N., Funke, S.A., Willbold, D., 2012. A survey of peptides with effective therapeutic potential in Alzheimer's disease rodent models or in human clinical studies. Mini Rev. Med. Chem. 12, 388–398.

van Groen, T., Wiesehan, K., Funke, S.A., Kadish, I., Nagel-Steger, L., Willbold, D., 2008. Reduction of Alzheimer's disease amyloid plaque load in transgenic mice by D3, a D-enantiomeric peptide identified by mirror image phage display. ChemMedChem 3, 1848–1852.

van Groen, T., Kadish, I., Funke, A., Bartnik, D., Willbold, D., 2012. Treatment with a beta 42 binding D-amino acid peptides reduce amyloid deposition and inflammation in APP/PS1 double transgenic mice. Adv. Protein Chem. Struct. Biol. 88, 133–152.

van Groen, T., Kadish, I., Funke, S.A., Bartnik, D., Willbold, D., 2013. Treatment with D3 removes amyloid deposits, reduces inflammation, and improves cognition in aged AbetaPP/PS1 double transgenic mice. J. Alzheimers Dis. 34, 609–620.

van Regenmortel, M.H.V., Muller, S., 1998. D-peptides as immunogens and diagnostic reagents. Curr. Opin. Biotechnol. 9, 377–382.

Wiesehan, K., Willbold, D., 2003. Mirror-image phage display: aiming at the mirror. Chembiochem 4, 811–815.

Zhang, F., Xue, J., Shao, J., Jia, L., 2012. Compilation of 222 drugs' plasma protein binding data and guidance for study designs. Drug Discov. Today 17, 475–485.

2.5 Blood-brain barrier penetration of an Aβ-targeted, arginine-rich, D-enantiomeric peptide

Published in: BBA - Biomembranes

Impact Factor: 3.84

Contributions: 80%

Involved in the conception and design of the experiments; except for oral treatment part, conducted all the rest of experiments and data analysis; involved in writing the manuscript.

Biochimica et Biophysica Acta 1858 (2016) 2717–2724

Contents lists available at ScienceDirect

Biochimica et Biophysica Acta

journal homepage: www.elsevier.com/locate/bbamem

Blood-brain barrier penetration of an Aβ-targeted, arginine-rich, D-enantiomeric peptide

Nan Jiang [a], Daniel Frenzel [a,b], Elena Schartmann [a], Thomas van Groen [c], Inga Kadish [c], N. Jon Shah [d], Karl-Josef Langen [d,e], Dieter Willbold [a,f,*], Antje Willuweit [d,**]

[a] Forschungszentrum Jülich, Institute of Complex Systems, Structural Biochemistry, 52428 Jülich, Germany
[b] European Molecular Biology Laboratory, Meyerhofstraße 1, 69117 Heidelberg, Germany
[c] Department of Cell, Developmental and Integrative Biology, University of Alabama at Birmingham, Birmingham, AL 35294, USA
[d] Forschungszentrum Jülich, Institute of Neuroscience and Medicine, Medical Imaging Physics, 52428 Jülich, Germany
[e] Department of Neurology, Faculty of Medicine, JARA, RWTH Aachen University, Aachen, Germany
[f] Heinrich-Heine-Universität Düsseldorf, Institut für Physikalische Biologie, 40225 Düsseldorf, Germany

ARTICLE INFO

Article history:
Received 11 February 2016
Received in revised form 1 July 2016
Accepted 12 July 2016
Available online 14 July 2016

Keywords:
Blood-brain barrier penetration
Arginine-rich motif of HIV-Tat protein
D-Enantiomeric peptide
Alzheimer's disease
Amyloid beta
Transgenic mouse models

ABSTRACT

The application of small peptides targeting amyloid beta (Aβ) is one of many drug development strategies for the treatment of Alzheimer's disease (AD). We have previously identified several peptides consisting solely of D-enantiomeric amino acid residues obtained from mirror-image phage display selection, which bind to Aβ in different assembly states and eliminate toxic Aβ aggregates. Some of these D-peptides show both diagnostic and therapeutic potential *in vitro* and *in vivo*. Here we have analysed the similarity of the arginine-rich D-peptide D3 to the arginine-rich motif (ARM) of the human immunodeficiency virus type 1 transactivator of transcription (HIV-Tat) protein, and examined its *in vivo* blood-brain barrier (BBB) permeability using wild type mice and transgenic mouse models of Alzheimer's disease. We are able to demonstrate that D3 rapidly enters the brain where it can be found associated with amyloid plaques suggesting a direct penetration of BBB.

1. Introduction

Currently, two molecular weight categories classify drugs into conventional "small molecule" drugs (<500 Da) and "biologics" which are generally referred to as protein-based drugs (>5000 Da) [1]. Small molecules are often associated with favorable oral bioavailability and their production is considered scalable and economical. During drug discovery, they can be rationally designed, for example, altering the structure to optimize physiochemical properties for enhanced brain delivery [2,3]. Frequently, however, small molecules show low target selectivity, which may ultimately result in side effects. Protein-based drugs, for example antibodies, possess high selectivity, mainly because their large size allows formation of specific and high affinity binding sites for their target molecules. Usually they have poor oral bioavailability due to low membrane permeability and proteolytic instability [4]. Small peptide based molecules consisting of 5 to 50 amino acid residues may fill the molecular weight gap and combine the advantages of small molecules and protein based drugs.

Well-known examples of peptide-based drugs with high medical and economic impact are the peptide hormones insulin and glucagon. Diseases like diabetes, cancer, inflammation and cardiovascular diseases, are strong drivers for the development of peptide based drugs [5]. Peptide drugs have the potential for high substrate specificity and affinity. Their degradation usually doesn't lead to toxic metabolites. They are smaller than proteins and thus can be obtained synthetically by well-established and cost-efficient methods [6]. A drawback of peptide drugs is their relatively low bioavailability due to degradation and the resulting short half-lives. Several approaches have been developed to enhance the bioavailability of peptide based drug candidates. The application of D-enantiomeric amino acids is an effective way to enhance the resistance to degradation, because most proteolytic enzymes have substrate specificity for L-peptide bonds. This even allows the oral administration of D-enantiomeric peptides [7,8]. Furthermore, D-peptides are less, if at all, immunogenic [9].

The application of peptide based drugs for the treatment of central nervous system (CNS) diseases is hindered by the blood-brain barrier (BBB) [10,11]. Blood capillaries at the BBB have specialized structures and are characterized by the i) absence of fenestrae, ii) the presence of tight intercellular junctions, iii) low pinocytotic activity, and iv) high

* Corresponding author at: Forschungszentrum Jülich, Institute of Complex Systems, Structural Biochemistry, 52428 Jülich, Germany.
** Corresponding author.
E-mail addresses: D.Willbold@fz-juelich.de (D. Willbold), A.Willuweit@fz-juelich.de (A. Willuweit).

http://dx.doi.org/10.1016/j.bbamem.2016.07.002
0005-2736/

levels of efflux transporters at their luminal endothelial surface. This efficiently limits the penetration potential of 95% of all known drugs into the brain [12]. In the absence of active transport mechanisms, the ability of peptides to permeate through membranes usually decreases with increasing mass and hydrophilicity. Studies have shown that most drugs with molecular weights above 500 Da already show poor brain penetration potential and compounds with molecular weights above 1000 Da are usually widely excluded from the passive transmembrane transport system [13,14]. In spite of poor BBB permeability in general, some peptides can be transported into the brain *via* specific transporters expressed in brain endothelium under physiological or pathological conditions [15,16]. Furthermore, several BBB penetration mechanisms such as receptor-mediated, adsorptive-mediated or carrier-mediated mechanism are intensively studied [17]. Properties such as the presence of basic clusters have been found to trigger the uptake of compounds into the cell by an as yet unresolved mechanism. A well-known example is the human immunodeficiency virus type 1 (HIV-1) transactivator of transcription (Tat) [18–20]. The HIV-1 Tat is a regulatory protein with 86 to 101 amino acids depending on the subtype. It is produced in the very early stages of viral infection and greatly enhances the transcriptional rates which result in high viral gene expression. It also mediates viral spreading in disease progression [21]. The basic region of HIV-1 Tat protein involved in RNA binding is rich in arginines and lysines, and thus belongs to the family of arginine-rich motif (ARM) RNA binding proteins [22]. Such ARMs have been identified first in lentiviral Tat proteins, *e.g.* from HIV and equine infectious anaemia virus (EIAV), and later in a variety of nucleic acid binding proteins. Functional and structural details have been described for Tat proteins [23–26]. Currently there are several hypotheses about the potential mechanism for HIV-1 Tat uptake; these all incorporate the fact that HIV-1 Tat binds negatively-charged targets such as heparane sulfate/glycosaminoglycans, sialic acid and phospholipids, and traverses the plasma-membranes passively. Furthermore, recent *in vitro* experiments based on artificial membrane systems suggest the formation of plasma-membrane pores [18–20,27]. The exact mechanism of ARM transduction is still unknown, but the relative abundance of arginines is suggested to play a decisive role [28,29]. Although lysine presents the same positive net charge as arginine, the substitution of arginines with lysines decreases the transduction efficiency [30,31]. Studies show that arginine-rich peptides, which demonstrate membrane permeation, lack secondary structure, and D-enantiomeric arginine as well as guanidino peptoids work equivalently [28,31,32], which demonstrate that the guanidinium groups are the critical structural component responsible for the transduction [28,30,33]. Such mechanisms may be beneficial for peptide design.

We have identified several D-peptides by mirror-image phage display [34] for binding to Aβ [35,36]. They show promising abilities, *e.g.* elimination of Aβ oligomers and inhibition of Aβ fibril formation *in vitro* [37], and fluorescently labelled D-peptides bind to amyloid plaques in transgenic mice after direct brain infusion. [38]. One of those D-peptides, D3, was able to reduce plaque load and inflammation markers in the brains of aged APP/PS1 double transgenic mice and improved cognition even after oral administration [39–42]. Recently, the first comprehensive preclinical pharmacokinetic study of D3 was reported [7] and its BBB permeability was evaluated in an *in vitro* cell culture model [43].

D3 (rprtrlhthrnr) is an arginine-rich peptide containing five arginines out of twelve amino acid residues and shares sequence homology to ARM of HIV-1 Tat (HXB2) [44] (Fig. 1). HXB2 is a recombinant inbred strain derived from a cross of SHR/OlaIpcv with BN-Lx/Cub (HXB) of the first HIV-1 isolate, regarding as a standard reference strain [45,46]. The ARM mediates HIV-1 Tat's activity to overcome plasma membranes. Given the amino acid sequence similarity of D3 to the ARM of HIV-1 Tat, the ability of D3 to penetrate the BBB may be based on the same mechanism.

```
HIV-1 (HXB2) Tat 53-64:  RQRRRAHQNSQT
D3 1-12:                 rprtrlhthrnr
                         * * * *
```

Fig. 1. Alignment of D3 with human immunodeficiency virus type 1 (HIV-1), strain HXB2, transactivator (Tat) protein. D3 shows sequence similarity to the arginine-rich motif (ARM) of a recombinant inbred strain (HXB2) of HIV-1 Tat protein.

To test this hypothesis, we have studied the *in vivo* localization of D3 in the CNS and its potential to pass the BBB as well as to bind amyloid plaques *in vivo* and *in vitro* in mouse brain sections.

Our results suggest that the BBB penetration of D3 may indeed have the same mechanism as HIV-1 Tat. This may offer a strategy to design and select peptide-based drugs and suggests that D3 and its derivatives are promising candidates for the future treatment of Alzheimer's disease.

2. Materials and methods

2.1. Peptides and other chemicals

^{3}H-D3 (rprtr-(4,5-^{3}H-Leu)-hthrnr) was purchased from Quotient Bioresearch (Radiochemicals) Ltd. (Cardiff, United Kingdom) with 10–100 Ci/mmol, 1 mCi/ml and purity >95%. D3 (rprtrlhthrnr), FAM-D3 (H-rprtrlhthrnr-Lys(5(6)-carboxyfluorescein)-NH2) and FAM-LP (LRMMLQIKRIPR-Lys(5(6)-carboxyfluorescein)-NH2) was purchased from JPT peptide Technologies GmbH (Berlin, Germany). Molecular weight of D3 is 1599, while FAM-D3 is 2086; The FAM tagging through 5-FAM lysine introduced one negative charge to D3 from a carboxylic acid at 5-FAM molecule. Thioflavine S was from Sigma-Aldrich (Munich, Germany). All other chemicals were supplied by Fluka Chemie AG (Buchs, Switzerland), Merck (Darmstadt, Germany), AppliChem (Darmstadt, Germany) and VWR (Darmstadt, Germany) in research grade.

2.2. Animals

To study the distribution of ^{3}H-D3, male C57Bl/6 mice (Charles River, Sulzfeld Germany) with an average body weight of 33.4 g were used. The mice were hosted in our animal facility under standard housing conditions for at least 2 weeks before experiment. All animal experiments were approved by the Animal Protection Committee of the local government (LANUV, North-Rhine-Westphalia, Germany, AZ84-02.04.2011. A359 and AZ84-02.04.2011. A356) according to the German Protection of Animals Act.).

For the experiment of FAM-D3 oral administration, seven male four-month old APP and PS1 double transgenic mice (APPswe/PS1ΔE9) were used in the present study. It has been shown that animals from this line exhibit numerous plaques and cerebral amyloid angiopathy within the brain, especially within cortex and hippocampus but also in other brain areas including the cerebellum [47–49]. The APPswe/PS1ΔE9 mice were acquired from JAX at the age of six weeks and housed in 4/cage in a controlled environment (temperature 22 °C, humidity 50–60%, and light from 07:00–19:00) until the treatments; food and water were available *ad libitum*. The experiment was conducted in accordance with the local Institutional Animal Care and Use Committee (IACUC) guidelines. All animal studies comply with the ARRIVE guidelines [50]. A completed ARRIVE guidelines checklist was included in S1 ARRIVE Checklist.

2.3. ^{3}H-D3 distribution in brain, plasma and CSF

^{3}H-D3 was mixed with non-radioactive D3 in a 0.1 M phosphate buffer (pH 8) to a total D3 concentration of 3 mg/ml with a specific radioactivity of 16.7 μCi per mg D3. 5 μCi D3 (100 μl) were administered as a single bolus intraperitoneally. Doses were selected according to

tolerability studies and did not cause adverse reactions. The total D3 concentration was calculated through 3H radioactivity assuming radioactive/non-radioactive ratio of the working solution stays the same during bio-distribution. Sampling times were 30, 60, 240 and 1440 min after administration (3 mice per time point). The administration method and the sampling time were selected based on our previous pharmacokinetic study [7]. Mice were anaesthetized with ketamine/medetomidine 10 min before samples were collected. Cerebrospinal fluid (CSF) was collected with a glass capillary tube (Round Boro Capillaries, CM Scientific, New Jersey, USA) from the *cisterna magna* as described by Liu and Duff [51]. About 8 to 9 μl CSF was obtained from each mouse. Blood was drawn by heart puncture and heparinized to isolate blood plasma. The right brain hemisphere was isolated directly after euthanasia through cervical dislocation.

The brain hemisphere was weighed and homogenized in homogenizer tubes (Precellys Ceramic Kit 1.4 mm, Precellys 24, Bertin technologies SAS, Montigny le Bretonneux, France) with 500 μl PBS. 10 ml scintillation cocktail (Ultima Gold XR, PerkinElmer, Waltham, Massachusetts, USA) was added to 100 μl of brain homogenate or plasma (diluted 1:1 with PBS) and mixed well. Disintegrations per unit time (dpm) were obtained in triplicates with a liquid scintillation counter (Packard Tri-Carb 2100TR Liquid Scintillation Analyser, PerkinElmer, Waltham, MA, USA). CSF was mixed directly with 10 ml scintillation cocktail.

Radioactivity was quantified in each sample as the percentage of injected dose (ID) per weight unit for brain tissue (%ID/g), or dose per volume unit for plasma/CSF samples (%ID/ml). Analogously, for cold material the concentration was expressed as weight unit of total D3 per weight unit of brain tissue (μg/g), or as weight unit per volume unit for plasma/CSF samples (μg/ml). Ratios were calculated from the values of brain, CSF and plasma, respectively. Mean values with standard error (SEM) of three mice were presented.

2.4. In vitro autoradiography (^3H) with mouse brain sections

Brain from a homozygous 18.5 months old APP/PS1 (ARTE 10) transgenic mouse is a generous gift from Andre Manook (Nuklearmedizinische Klinik und Poliklinik, Klinikum rechts der Isar, Technische Universität München, Munich, Germany). Homozygous ARTE10 mice of this age exhibit extensive plaque load and to a lesser extent cerebral amyloid angiopathy especially in cortex and hippocampus, but also in other areas except the cerebellum [42,52]. The brain was fixed in 4% formaldehyde (Carl Roth, Karlsruhe, Germany) in PBS for one week at room temperature then transferred into 30% sucrose in PBS for 2 days at 4 °C. A series of 30 μm free floating cryosections were cut sagittal and post-fixed in 4% paraformaldehyde for 30 min at room temperature. After washing and 10 min permeabilization with 1% Triton X-100 in Tris-buffered saline (TBS), sections were transferred into a staining dish containing ^{3}H-D3 solution in 1% Triton-TBS (2.5 k-becquerel (kBq) per section) and incubated for 3 days at room temperature. After washing in TBS and a rapid washing step in H_2O, sections were mounted on glass slides and dried at 37 °C for 2 h, then exposed against a phosphor-imaging plate for ^{3}H-autoradiography (FUJIFILM, Tokyo, Japan) in an autoradiography cassette for 7 days. The imaging plate was scanned with a phosphor film imager (Fujifilm BAS-5000, FUJIFILM Life Science, Japan) and images were acquired with BAS reader and AIDA software (Raytest, Freiburg, Germany).

2.5. Thioflavine S staining

Sections from *in vitro* autoradiography were immersion-fixed in 4% paraformaldehyde for 20 min, and then equilibrated in water twice for 2 min. After incubation in freshly filtrated 1% (w/v in water) Thioflavine S for 30 min at RT in a dark chamber, sections were washed twice for 2 min in $_{dd}H_2O$, and differentiated in two changes of 80% ethanol for 5 and 1 min, respectively. After washing three times in water (2 min per iteration), sections were covered with a glass slide and Aqua Poly/Mount (Polysciences, Warrington, US). Images were acquired with a Lumar V12 SteREO microscope (Zeiss, Oberkochen, Germany) with AxioCamMR3 camera (Zeiss, Oberkochen, Germany) and processed with AxioVs40 software (Release 4.5 SP1) and ImageJ (1.48 s).

2.6. Oral administration of D3 and FAM-D3

We chose oral administration for this long term experiments as it is favorable for animals. In order to achieve the desired total D3 concentration, non-labelled D3 (90%) was added to FAM-D3 (10%) with a final concentration of 0.25 mg/ml. Seven four-month old APPswe/PS1ΔE9 transgenic mice were treated for eight weeks with FAM-D3 and D3 in the drinking water. On average, the mouse drank ca. 2 to 3 ml water per day. The stability of D3 in water containing mouse saliva was verified using reversed phase HPLC analysis. Briefly, D3 was dissolved in double-distilled water, drinking water and drinking water containing 0.05% (v/v) mouse saliva to a final concentration of 27 μM. Freshly prepared solution and solution incubated for 24 h at 37 °C were analysed through reversed phase HPLC with a C18 column (Phenomenex, Aschaffenburg, Germany) and compared. No obvious degradation was observed. Eight weeks after the start of treatment, the mice were sacrificed for histopathological analysis (see below).

2.7. Immunohistochemistry and immunofluorescence

Brain sections from the transgenic mouse orally administered with FAM-D3 were treated with a monoclonal mouse anti-Aβ(4–10) (W0–2) antibody (EMD Millipore). The sections were incubated overnight in a solution of TBS; then the sections were treated for 30 min in a heated (85 °C) sodium citrate solution (0.05 M, pH 6.0) and allowed to cool down. Afterwards, the series of sections were transferred into TBS-T (TBS with 0.5% Triton X-100) containing the primary antibody (mouse anti-Aβ(4–10), USA) for 24 h at 20 °C in a dark room. The sections were washed three times in TBS-T and transferred into a solution containing the secondary antibody (biotinylated goat anti mouse; Sigma) for 2 h. Again, the sections were washed three times with TBS-T and transferred to a solution containing ExtrAvidin for 2 h. Then the sections were incubated for approximately 3 min with Ni-enhanced diaminobenzidine (DAB) (12.5 mg DAB in 25 ml 0.1 M phosphate buffer, pH 7.4, 30 μl H_2O_2 (30%), with 1 ml of a 15% ammonium Ni-sulfate solution added). The stained sections were mounted on gelatinized slides and coverslipped.

Cerebral blood vessels were visualized with GLUT-1 antibody (rabbit anti-GLUT-1 antibody EMD Millipore). The staining was performed exactly as described for Aβ, with the exception that no pretreatment was performed and a fluorescent secondary antibody (goat anti rabbit, Jackson ImmunoResearch) was applied. The stained sections were mounted on gelatinized slides and coverslipped.

2.8. Thin layer chromatography

Untreated wildtype mouse brain was homogenized with the same method as described above. After centrifuge at 20,000 ×*g* for 15 min at 4 °C to clarify the homogenate, extract of mouse brain was obtained from supernatant. FAM labelled peptide was incubated with the brain extract at 37 °C for different time periods (from 0 to 2 days). 2 μg FAM labelled peptide was mixed with 1 μl brain extract (in excess to peptide [53,54]). Mixtures containing FAM-labelled peptides were applied onto a HPTLC cellulose plate (OMNILAB, Essen, Germany) for thin layer chromatography (TLC) with mobile solvent (2-butanol/pyridine/acetic acid/water (30/20/6/24)). Images were acquired using the ChemDoc MP imaging system (Bio-RAD, Munich, Germany) under the fluorescein channel. The retardation factor (R_f) of each substance was defined as the ratio of the migration distance of the centre of a separated spot to the migration distance of the solvent front.

3. Results

3.1. Temporal distribution of ^{3}H-D3 in brain, plasma and CSF after intraperitoneal administration

To study the temporal and spatial distribution of D3 *in vivo*, we have analysed the concentrations of radioactively labelled D3 in brain, plasma and CSF. The time-concentration profiles of ^{3}H-D3 in whole brain, plasma and CSF after *i.p.* administration are shown in Fig. 2. Brain/plasma, CSF/plasma and brain/CSF ratios are shown in Fig. 3.

As expected, the highest concentration of D3 was measured in plasma shortly after administration with 8.4 μg/ml after 4 h and subsequently decreased to 0.53 μg/ml, whereas the concentration of D3 in brain and CSF started at about 0.6 μg/ml and decreased only slightly (Fig. 2). The brain/plasma ratio reached 0.8 to 0.9 after 4 h. D3 concentration in CSF remained slightly higher in comparison to that in the brain at all four time points, resulting in a relatively constant brain/CSF ratio of about 0.8 (Fig. 3).

3.2. Binding of ^{3}H-D3 on Aβ plaques by in vitro autoradiography

In order to study the influence of ^{3}H-D3 within cerebral blood vessels on the total radioactivity detected in the whole brain, brain slices of a transgenic APP/PS1 (ARTE 10) mouse were incubated with ^{3}H-D3 and subsequently developed by *in vitro* autoradiography (Fig. 4A). Additionally, the same slices were stained with Thioflavine S to stain beta-sheet rich structure elements (Fig. 4B), which is regarded as a robust and easy method for Aβ plaque quantification in this mouse model [55]. Co-localization of ^{3}H-D3 and Thioflavine S is an indicator of the specific binding of D3 to the amyloid plaques (Fig. 4C). Furthermore, the use of 1% Thioflavine S causes the strong non-specific staining of blood vessels [56], which also visualizes cerebral blood vessels on the section (Fig. 4D).

The APP/PS1 (ARTE 10) mouse model used is characterized by the lack of Aβ plaques in the cerebellum [55], which is in agreement with the Thioflavine S stain, as well as the autoradiography with ^{3}H-D3 in this study. No ^{3}H-D3 labelled structures of blood vessels in either the cerebrum or cerebellum could be observed in the autoradiogram, even though some of the vessels were clearly stained by Thioflavine S (Fig. 4D). This shows that ^{3}H-D3 bound specifically to Aβ plaques in the parenchyma and any specific binding of ^{3}H-D3 to cerebral blood vessels was negligible.

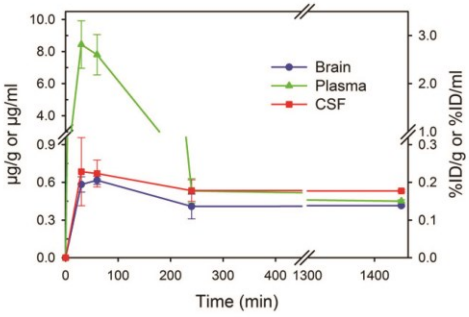

Fig. 2. Temporal distribution of ^{3}H-D3 in brain, plasma and cerebrospinal fluid (CSF) after *i.p.* administration in C57Bl/6 mice. ^{3}H-D3 (5 μCi) mixed with non-radioactive D3 to a total amount of 0.3 mg D3 was applied as single bolus per mouse. The concentration of D3 is shown as the mean value ± SEM (n = 3) at each time point. Units are given in μg/g (left Y-axis) or %ID/g (percentage of injected dose per gram tissue, right Y-axis) for brain, μg/l or %ID/ml (percentage of injected dose per milliliter) for CSF and plasma. ^{3}H-D3 concentration in brain and CSF were quite stable (about 0.6 μg/ml), whereas plasma concentration dropped rapidly initially until it reached similar levels to those in brain and CSF 4 h post injection (from 8.4 μg/ml to 0.53 μg/ml).

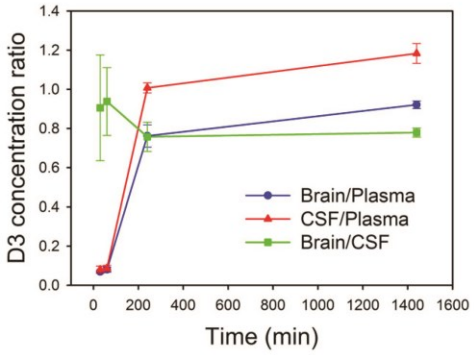

Fig. 3. Temporal development of ^{3}H-D3 concentration ratios after *i.p.* administration in C57Bl/6 mice. Illustrated are the brain/plasma, cerebrospinal fluid (CSF)/plasma, and brain/CSF ratios as the mean value ± SEM (n = 3) at different time points post injection. Following bolus dose administration, low brain/plasma and CSF/plasma ratios were found at the starting time points (about 0.1), whereas the brain/CSF ratio was high with about 0.9. After 4 h, all the ratios reached relative stable values.

3.3. Oral administration of FAM-D3

As demonstrated recently in a pharmacokinetic study, oral administration yielded similar D3 concentrations after 4 h in the brain as *i.p.* and *i.v.* administrations did [7]. Here we used fluorescently labelled D3 for the purpose of direct visualization. After eight weeks of oral administration of 5(6)-carboxyfluorescein labelled D3 (FAM-D3) in an APPswe/PS1ΔE9 transgenic mouse, fluorescence was observed associated with Aβ plaques in brain parenchyma (Fig. 5A). Colocalization of FAM-D3 fluorescence with Aβ aggregates was validated by immunohistochemistry using anti-Aβ antibody (W0-2) based staining on adjacent sections (Fig. 5B and C). Cerebral blood vessels were visualized using an *anti*-glucose transporter GLUT-1 antibody (Fig. 5D). No specific binding of FAM-D3 on cerebral blood vessels was observed (Fig. 5E). An anti-GLUT-1 positive structure was found in the middle of an Aβ deposition, suggesting this plaque was formed around the blood vessel (Fig. 5D and E, white arrows).

3.4. Proteolytic stability of FAM-D3 in comparison to FAM labelled L-enantiomeric peptide

In order to support the interpretation that FAM fluorescence correlates with binding of intact FAM-D3, an *ex vivo* stability test was performed with brain homogenate. The proteolytic stability of D3 peptide within its amino acid sequence has been reported earlier [7]. In this study, the stability of D3 bound to FAM *via* an L-Lys linker was tested additionally. As a control, a 12-mer peptide consisting of L-enantiomeric amino acid residues (LP) coupled to FAM was used. FAM-D3 and FAM-LP were incubated with brain homogenate at 37 °C and applied to thin layer chromatography (TLC) (Fig. 6). Under the same experimental conditions, Rf values of FAM-D3 and FAM-LP were different due to their different amino acid sequences. Most of the FAM-LP was degraded in brain homogenate after 2 h, whereas FAM-D3 was resistant to proteolysis within the same time frame.

4. Discussion

The all-D-enantiomeric peptide D3 contains five arginines out of twelve amino acid residues. Three arginines at the N-terminus and two at C-terminus are separated by single spacing amino acids, respectively. This arginine arrangement in peptide backbone may increase its

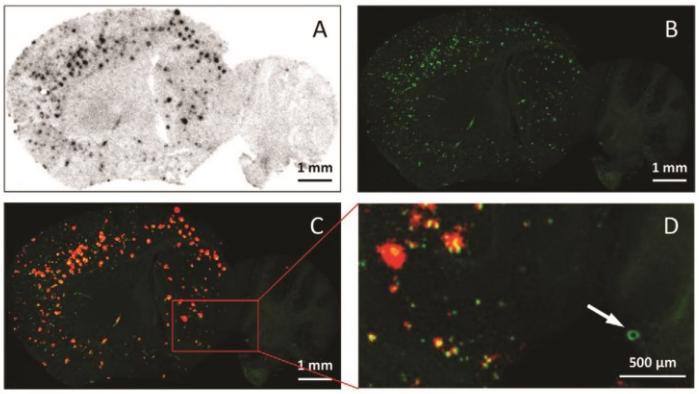

Fig. 4. *In vitro* autoradiography of ^{3}H-D3 on mouse brain cross-sections. (A) Autoradiogram of an APP/PS1 (ARTE 10) transgenic mouse brain section (sagittal) incubated with ^{3}H-D3. A stronger ^{3}H-signal correlates to a higher blackening of the image. (B) Thioflavine S staining for amyloid of section A performed after autoradiography. (C) Merged image based on the fluorescence signal after Thioflavine S staining (green) and autoradiography (converted to red). Yellow indicates colocalization of Thioflavine S and ^{3}H-D3. (D) Merged image with higher magnification. White arrow points to a blood vessel in cerebellum which is not positive for ^{3}H-D3. Other small spots that only showed Thioflavine S positive stain but were not stained by ^{3}H-D3 could be either plaques that were only weakly stained by ^{3}H-D3 or small cerebral blood vessels.

cellular uptake as studies have shown that increase of the distance between arginine residues enhances the uptake of ARMs [57,58]. The arrangement of arginines at the C-terminus may contribute to the overall similarity of D3 to ARM of HIV-1 Tat, which may lead to the ability to penetrate plasma membranes and the BBB. In order to elucidate this observation, further *in vivo* experiments using tritium labelled (^{3}H-D3) and fluorescently labelled (FAM-D3) peptide were carried out.

The systemic administration of ^{3}H-D3 (*i.p.*) led to similar concentrations of radioactivity in CSF, plasma and whole brain after 4 h. As ^{3}H-D3 has been shown to be proteolytically stable, D3 concentrations can be calculated from measured radioactivity and its metabolites can be neglected [7]. Also, temporal distribution of ^{3}H-D3 in the plasma and brain fitted well with recently reported pharmacokinetic data [7]. The fast appearance and constant presence of D3 in the brain suggests direct penetration into brain parenchyma via the blood brain barrier. It must be noted that, as radioactivity from CSF remained in the ventricles or from the blood in the cerebrovasculature, this may have contributed to the radioactivity detected in the whole brain to some extent. But because the CSF space was destroyed during preparation of the brain hemispheres, the amount of remaining CSF in the brain hemisphere was considered negligible. Since we could not detect specific binding of ^{3}H-D3 to cerebral blood vessels in *in vitro* autoradiography, it is unlikely that radioactivity bound to the vessel walls contributed significantly to the amount detected in the whole brain. Furthermore, the cerebral blood volume decreases dramatically in the absence of any cardiac activity once the mouse is euthanized [59]. Derivation of theoretical concentration in intact brain assuming well preserved cerebral blood and CSF volume was also performed. When maximal blood and CSF compartments (using measured plasma and CSF concentrations) were excluded, there was still about half of the concentration left in the brain. Thus, the ^{3}H-D3 concentration detected in the brain likely represents its real concentration in the brain parenchyma and the vascular fraction is negligible.

The amount of ^{3}H-D3 measured up to 4 h post-administration in the brain is 0.14% to 0.21% of the total administered dose, which is clearly above the known bias concentration of 0.10% for BBB permeating agents [60]. Clinically applied CNS drugs consisting of L-polypeptides with proven BBB penetration potential, like Colistin, have CSF/serum ratios in the range of 0.051 to 0.057, or 0.16 [61]. In contrast, the CSF/plasma ratio of D3 started at 0.1 and reached 1.2 after 4 h post-administration, suggesting distribution in brain parenchyma. Even if drug entry into the CSF alone is not a proper measure of BBB permeability [62], CSF concentrations of

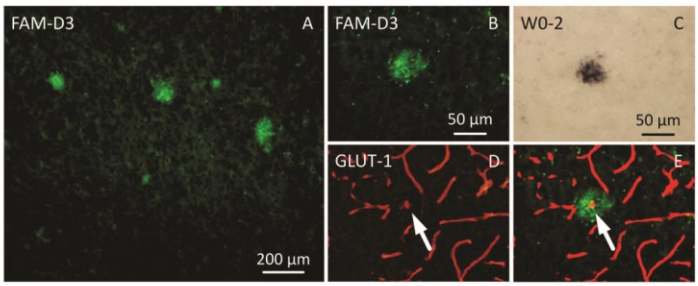

Fig. 5. Colocalization of FAM-D3 and Aβ in APPswe/PS1ΔE9 transgenic mouse brain sections after eight weeks' oral administration of FAM-D3. (A and B) Fluorescence images detecting FAM-D3 in cortex with low-magnification (A) and high-magnification (B), respectively. (C) High-magnification of photomicrograph showing adjacent section of B stained with anti-Aβ antibody (W0-2). (D) Microvasculature stained with anti-GLUT-1 antibody on the same section of B. (E) Merged image of B and D. White arrows highlight anti-GLUT-1 positive structure in the center of Aβ aggregate.

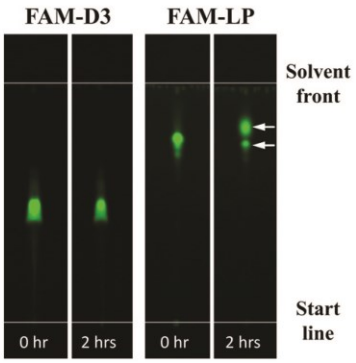

Fig. 6. Comparison of the proteolytic stability of FAM-D3 in comparison to a FAM labelled L-peptide (LP) of similar molecular weight as D3. FAM-D3 and FAM-LP were incubated in brain homogenate at 37 °C for 0 and 2 h and developed on TLC plate. Degradation of FAM-LP but not FAM-D3 is indicated by formation of additional bands and change in intensity and retardation factor (Rf) value (white arrows).

drugs are still considered as discriminating factors of drugs and their bioavailabilities in the CNS, especially for hydrophilic or large molecular weight compounds [63,64].

BBB permeability of D3 was demonstrated and further confirmed by oral administration of FAM labelled D3 in a transgenic AD mouse model. Aβ plaques in the brain were visualized under fluorescent light indicating FAM-D3 entered the brain parenchyma and bound to Aβ plaques. Together with the proteolytic stability test, results showed that D3 was orally active. D3 is selected to specifically bind to Aβ(1–42) [7], which is the major component of parenchymal Aβ, whereas the major Aβ species in cerebral amyloid angiopathy (CAA) is Aβ(1–40) (however, upon aging, more and more Aβ1–42 can be found in CAA) [65,66]. No specific binding of FAM-D3 on cerebral blood vessels was found, which is in accordance with our observations during the study when incubating ^{3}H-D3 with mouse brain sections. We also detected blood vessels in close proximity to Aβ plaques (Fig. 5E), supporting the hypothesis that every plaque seems to be associated with a vessel [67,68].

In our study, BBB penetration of D3 was quantified by measuring its brain concentration after *i.p.* administration (using ^{3}H-D3) and visualized through its binding to Aβ plaques inside the brain (using FAM-D3 and ^{3}H-D3). However, all those methods have their restrictions and thus needed to be validated by each other: D3 concentration in brain was calculated from radioactivity of tritium labelled D3, assuming that ^{3}H-D3 is proteolytically stable as shown previously [7]. Also, we showed that D3 did not bind to the CNS vasculature, which otherwise would have lead us to misinterpreted brain levels (Fig. 4). In addition, labelling with a bulky, hydrophobic 5-FAM lysine molecule adding one extra negative charge to D3 could have an influence on its BBB penetration and Aβ binding. Thus combination of experiments in Figs. 2 and 4 demonstrated that ^{3}H-D3, which preserves the original physical and chemical properties of D3 to the fullest extent, could pass the BBB and bind Aβ plaques.

Re-analysis and interpretation of the data reported previously [7] and in combination with Figs. 2 and 3, suggests that high concentrations of D3 in plasma do not directly translate into similarly high D3 concentrations either in brain or in CSF. After *i.p.* administration the plasma concentration of D3 rises rapidly to reach its maximum before dropping away within the first hours. In contrast, brain concentrations do not follow the same pattern but rise until certain and very stable levels are reached. Similar brain levels could previously be found after *i.v.* and even after *p.o.* administration despite huge differences by the order of several magnitudes in the initial plasma levels after *i.v.*, *i.p.* and *p.o.* administration. Those obviously constant brain levels may suggest that the responsible transport mechanism from plasma into the CNS is kinetically limited and that elevating the plasma concentration dose not directly lead to a proportional increase of brain concentration. This is in perfect agreement with a previous report on the permeability of D3 in an *in vitro* BBB model [43]. On a co-culture of rat brain microvascular endothelial cells and rat astrocytes in a transwell filter system, D3 passed through the *in vitro* BBB model and showed a partially saturated apical-to-basolateral (blood to brain) transport pattern, whereas another D-peptide (qshyrhispaqv) used as a control containing only one arginine did not pass the *in vitro* BBB model. This pattern was further investigated and it was suggested that D3 might be transported *via* adsorptive-mediated transcytosis [43,69].

Arginine-rich HIV-Tat-like peptides were suggested to bind negatively-charged cell membrane embedded molecules such as heparan sulfate and sialinic acid [70–72]. If the cell membrane-permeating property of Tat is independent of cell surface receptor proteins, it is likely that this process is rather dependent on the overall charge density, than on the presence of any specific sequence or secondary structure elements. Thus, the configuration of peptides (chirality) should not be relevant for cell membrane penetration. In the study of Tünnemann et al., D-enantiomeric arginine-rich peptides showed improved ability to cross the cell membrane as compared to their L-enantiomers, which was explained as a result of difference in proteolytic stability [73]. The observed BBB permeability of D3 in the hereby presented *in vivo* study is in agreement with this concept. Tünnemann et al. also investigated the cell penetration ability of oligo-arginines (with 5 to 12 arginine residues) coupled directly to fluorescein or 5,6-carboxytetramethylrhodamine (TAMRA). Their results show that the transduction ability of arginines increase with the number of consecutive residues and the best performance associated with a tolerable toxicity is achieved with 9 and 10 arginines [73]. Other studies reported that not only linear peptides but also branched-chain peptides show efficient transduction with an optimum number of approximately 8 arginines [74,75]. In this study, D3 achieved the *in vivo* BBB permeability through 5 arginine residues almost equally distributed over the whole molecule, which suggests a cation (guanidinium) dependent and sequence/structure related electrostatic interaction of D3. This special feature not only enables protease-resistant D3 to interact with Aβ, but also has advantage over the strategy to add extra arginine-rich peptides to achieve BBB permeability, as more arginine residues are usually accompanied with increased toxicity and production costs [73,76].

Another study showed that arginine-rich peptides are able to directly penetrate the plasma membrane independent of endocytosis [77]. The formation of nonselective pores was also excluded, because simultaneously added fluorophores were not taken up together with the arginine-rich peptides. BBB penetration of D3 might follow a similar mechanism as HIV-Tat assuming the limited transport pattern mentioned above. In fact, no complex transport mechanism is necessary to explain the distribution pattern of D3 in the body. It could be described as a rapid absorption phase from peritoneal cavity into systemic circulation followed by slower passive entry into intracellular compartments of brain and other organs, after which the proteolytically stable D3 remains equilibrated throughout the body. Remarkably, our results showed a relatively constant brain/CSF ratio over all time points, which also indicated a distribution equilibrium of D3 between brain and CSF. The most straight forward explanation would be that this equilibrium, as well as differences in brain/plasma and CSF/plasma ratios may simply reflect reduced distribution to non-aqueous compartments in brain that do not exist in CSF. In addition, this constant brain/CSF ratio might also provide a possibility to monitor D3 concentrations in brain, because CSF sampling can be performed several times or even continuously in living animals.

Taken together, our results strongly suggest that D3 penetrates the blood brain barrier and specifically binds to Aβ plaques after systemic administration. Being orally active, D3 might be a promising drug

candidate for therapeutic intervention in Alzheimer's disease. Additionally, being a middle-sized peptide of synthetic origin, D3 allows easy chemical modifications *e.g.* radiolabelling for early diagnosis of the disease.

Supplementary data to this article can be found online at http://dx.doi.org/10.1016/j.bbamem.2016.07.002.

Conflict of interest

There is no conflict of interest regarding this manuscript.

Author contributions

Conceived and designed the experiments: NJ, DF, TVG, IK, NJS, KJL, DW, AW

Performed the experiments: NJ, ES, TVG, IK

Analysed the data: NJ, TVG, IK, DW, AW

Wrote the paper: NJ, TVG, IK, KJL, DW, AW

Transparency document

The Transparency document associated with this article can be found, in the online version.

Acknowledgements

D.W. was supported by grants from the "Portfolio Technology and Medicine" and the Helmholtz-Validierungsfonds of the Impuls und Vernetzungs-Fonds der Helmholtzgemeinschaft; K.J.L. and D.W. were supported by the "Portfolio Drug Design" of the Impuls und Vernetzungs-Fonds der Helmholtzgemeinschaft. We thank Ashish Kumar and Monique Dozier-Sharpe for the excellent technical assistance.

References

[1] D.J. Craik, D.P. Fairlie, S. Liras, D. Price, The future of peptide-based drugs, Chem. Biol. Drug Des. 81 (2013) 136–147.
[2] C.A. Lipinski, F. Lombardo, B.W. Dominy, P.J. Feeney, Experimental and computational approaches to estimate solubility and permeability in drug discovery and development settings, Adv. Drug Deliv. Rev. 64 (2012) 4–17.
[3] J.L. Mikitsh, A.M. Chacko, Pathways for small molecule delivery to the central nervous system across the blood-brain barrier, Perspect. Med. Chem. 6 (2014) 11–24.
[4] M.T. Weinstock, J.N. Francis, J.S. Redman, M.S. Kay, Protease-resistant peptide design-empowering nature's fragile warriors against HIV, Biopolymers 98 (2012) 431–442.
[5] Watching peptide drugs grow up, Chem. Eng. News Arch. 83 (2005) 17–24.
[6] D. Goodwin, P. Simerska, I. Toth, Peptides as therapeutics with enhanced bioactivity, Curr. Med. Chem. 19 (2012) 4451–4461.
[7] N. Jiang, L.H.E. Leithold, J. Post, T. Ziehm, J. Mauler, et al., Preclinical pharmacokinetic studies of the tritium labelled D-enantiomeric peptide D3 developed for the treatment of Alzheimer's disease, PLoS One 10 (2015), e0128553.
[8] L. Leithold, N. Jiang, J. Post, T. Ziehm, J. Kutzsche, et al., Pharmacokinetic properties of a novel D-peptide developed to be therapeutically active against toxic β-amyloid oligomers, Pharm. Res. (2015).
[9] P. Chong, C. Sia, B. Tripet, O. James, M. Klein, Comparative immunological properties of enantiomeric peptides, Lett. Pept. Sci. 3 (1996) 99–106.
[10] B.V. Zlokovic, M.B. Segal, D.J. Begley, H. Davson, L. Rakic, Permeability of the blood cerebrospinal-fluid and blood-brain barriers to thyrotropin-releasing-hormone, Brain Res. 358 (1985) 191–199.
[11] B.V. Zlokovic, D.J. Begley, D.G. Chaineliash, Blood-brain barrier permeability to leucine-enkephalin, D-Alanine2-D-Leucine5-enkephalin and their N-terminal amino-acid (tyrosine), Brain Res. 336 (1985) 125–132.
[12] A. Lalatsa, V. Lee, J.P. Malkinson, M. Zloh, A.G. Schatzlein, et al., A prodrug nanoparticle approach for the oral delivery of a hydrophilic peptide, leucine(5)-enkephalin, to the brain, Mol. Pharm. 9 (2012) 1665–1680.
[13] W.M. Pardridge, CNS drug design based on principles of blood-brain barrier transport, J. Neurochem. 70 (1998) 1781–1792.
[14] W.M. Pardridge, Drug targeting to the brain, Pharm. Res. 24 (2007) 1733–1744.
[15] B.V. Zlokovic, S. Hyman, J.G. Mccomb, M.N. Lipovac, G. Tang, et al., Kinetics of arginine-vasopressin uptake at the blood-brain-barrier, Biochim. Biophys. Acta 1025 (1990) 191–198.
[16] B.V. Zlokovic, R. Deane, A.P. Sagare, R.D. Bell, E.A. Winkler, Low-density lipoprotein receptor-related protein-1: a serial clearance homeostatic mechanism controlling Alzheimer's amyloid beta-peptide elimination from the brain, J. Neurochem. 115 (2010) 1077–1089.
[17] J.A. Vazquez, M. Raghunath, S.A. Adibi, Uptake and hydrolysis of Glycylglutamine at the blood-brain-barrier, Metab. Clin. Exp. 41 (1992) 121–124.
[18] E. Vives, P. Brodin, B. Lebleu, A truncated HIV-1 Tat protein basic domain rapidly translocates through the plasma membrane and accumulates in the cell nucleus, J. Biol. Chem. 272 (1997) 16010–16017.
[19] H. Brooks, B. Lebleu, E. Vives, Tat peptide-mediated cellular delivery: back to basics, Adv. Drug Deliv. Rev. 57 (2005) 559–577.
[20] F. Salomone, F. Cardarelli, M. Di Luca, C. Boccardi, R. Nifosi, et al., A novel chimeric cell-penetrating peptide with membrane-disruptive properties for efficient endosomal escape, J. Control. Release 163 (2012) 293–303.
[21] M. Zeitler, J.P. Steringer, H.M. Muller, M.P. Mayer, W. Nickel, HIV-Tat forms phosphoinositide dependent membrane pores implicated in unconventional protein secretion, J. Biol. Chem. (2015).
[22] T.H. Tahirov, N.D. Babayeva, K. Varzavand, J.J. Cooper, S.C. Sedore, et al., Crystal structure of HIV-1 Tat complexed with human P-TEFb, Nature 465 (2010) 747–751.
[23] M.J. Seewald, A.U. Metzger, D. Willbold, P. Rosch, H. Sticht, Structural model of the HIV-1 Tat(46-58)-TAR complex, J. Biomol. Struct. Dyn. 16 (1998) 683–692.
[24] A.U. Metzger, T. Schindler, D. Willbold, M. Kraft, C. Steegborn, et al., Structural rearrangements on HIV-1 Tat (32-72) TAR complex formation, FEBS Lett. 384 (1996) 255–259.
[25] D. Willbold, R. Rosin-Arbesfeld, H. Sticht, R. Frank, P. Rosch, Structure of the equine infectious anemia virus Tat protein, Science 264 (1994) 1584–1587.
[26] P. Bayer, M. Kraft, A. Ejchart, M. Westendorp, R. Frank, et al., Structural studies of HIV-1 Tat protein, J. Mol. Biol. 247 (1995) 529–535.
[27] D. Sun, J. Forsman, M. Lund, C.E. Woodward, Effect of arginine-rich cell penetrating peptides on membrane pore formation and life-times: a molecular simulation study, Phys. Chem. Chem. Phys. 16 (2014) 20785–20795.
[28] J.B. Rothbard, T.C. Jessop, R.S. Lewis, B.A. Murray, P.A. Wender, Role of membrane potential and hydrogen bonding in the mechanism of translocation of guanidinium-rich peptides into cells, J. Am. Chem. Soc. 126 (2004) 9506–9507.
[29] I. Nakase, T. Takeuchi, G. Tanaka, S. Futaki, Methodological and cellular aspects that govern the internalization mechanisms of arginine-rich cell-penetrating peptides, Adv. Drug Deliv. Rev. 60 (2008) 598–607.
[30] D.J. Mitchell, D.T. Kim, L. Steinman, C.G. Fathman, J.B. Rothbard, Polyarginine enters cells more efficiently than other polycationic homopolymers, J. Pept. Res. 56 (2000) 318–325.
[31] P.A. Wender, D.J. Mitchell, K. Pattabiraman, E.T. Pelkey, L. Steinman, et al., The design, synthesis, and evaluation of molecules that enable or enhance cellular uptake: Peptoid molecular transporters, Proc. Natl. Acad. Sci. U. S. A. 97 (2000) 13003–13008.
[32] D. Derossi, S. Calvet, A. Trembleau, A. Brunissen, G. Chassaing, et al., Cell internalization of the third helix of the antennapedia homeodomain is receptor-independent, J. Biol. Chem. 271 (1996) 18188–18193.
[33] M. Rizzuti, M. Nizzardo, C. Zanetta, A. Ramirez, S. Corti, Therapeutic applications of the cell-penetrating HIV-1 Tat peptide, Drug Discov. Today 20 (2015) 76–85.
[34] T.N.M. Schumacher, L.M. Mayr, D.L. Minor, M.A. Milhollen, M.W. Burgess, et al., Identification of D-peptide ligands through mirror-image phage display, Science 271 (1996) 1854–1857.
[35] K. Wiesehan, D. Willbold, Mirror-image phage display: aiming at the mirror, Chembiochem 4 (2003) 811–815.
[36] S.A. Funke, T. van Groen, I. Kadish, D. Bartnik, L. Nagel-Steger, et al., Oral treatment with the D-enantiomeric peptide D3 improves the pathology and behavior of Alzheimer's disease transgenic mice, ACS Chem. Neurosci. 1 (2010) 639–648.
[37] T. van Groen, K. Wiesehann, S.A. Funke, I. Kadish, L. Nagel-Steger, et al., Reduction of Alzheimer's disease amyloid plaque load in transgenic mice by D3, a D-enantiomeric peptide identified by mirror image phage display, ChemMedChem 3 (2008) 1848–1852.
[38] T. van Groen, I. Kadish, K. Wiesehan, S.A. Funke, D. Willbold, In vitro and in vivo staining characteristics of small, fluorescent, Abeta42-binding D-enantiomeric peptides in transgenic AD mouse models, ChemMedChem 4 (2009) 276–282.
[39] T. van Groen, I. Kadish, S.A. Funke, D. Bartnik, D. Willbold, Treatment with D3 removes amyloid deposits, reduces inflammation, and improves cognition in aged AbetaPP/PS1 double transgenic mice, J. Alzheimers Dis. 34 (2013) 609–620.
[40] T. van Groen, I. Kadish, A. Funke, D. Bartnik, D. Willbold, Treatment with Abeta42 binding D-amino acid peptides reduce amyloid deposition and inflammation in APP/PS1 double transgenic mice, Adv. Protein Chem. Struc. Biol. 88 (2012) 133–152.
[41] S. Aileen Funke, T. van Groen, I. Kadish, D. Bartnik, L. Nagel-Steger, et al., Oral treatment with the d-enantiomeric peptide D3 improves the pathology and behavior of Alzheimer's disease transgenic mice, ACS Chem. Neurosci. 1 (2010) 639–648.
[42] T. van Groen, K. Wiesehan, S.A. Funke, I. Kadish, L. Nagel-Steger, et al., Reduction of Alzheimer's disease amyloid plaque load in transgenic mice by D3, a D-enantiomeric peptide identified by mirror image phage display, ChemMedChem 3 (2008) 1848–1852.
[43] H.M. Liu, S.A. Funke, D. Willbold, Transport of Alzheimer disease amyloid-beta-binding D-amino acid peptides across an in vitro blood-brain barrier model, Rejuvenation Res. 13 (2010) 210–213.
[44] A.G. Fisher, E. Collalti, L. Ratner, R.C. Gallo, F. Wong-Staal, A molecular clone of HTLV-III with biological activity, Nature 316 (1985) 262–265.
[45] B. Korber, B. Gaschen, K. Yusim, R. Thakallapally, C. Kesmir, et al., Evolutionary and immunological implications of contemporary HIV-1 variation, Br. Med. Bull. 58 (2001) 19–42.
[46] B.H. Hahn, G.M. Shaw, S.K. Arya, M. Popovic, R.C. Gallo, et al., Molecular cloning and characterization of the HTLV-III virus associated with AIDS, Nature 312 (1984) 166–169.

[47] J.L. Jankowsky, D.J. Fadale, J. Anderson, G.M. Xu, V. Gonzales, et al., Mutant presenilins specifically elevate the levels of the 42 residue beta-amyloid peptide in vivo: evidence for augmentation of a 42-specific gamma secretase, Hum. Mol. Genet. 13 (2004) 159–170.
[48] T. Malm, J. Koistinaho, K. Kanninen, Utilization of APPswe/PS1dE9 transgenic mice in research of Alzheimer's disease: focus on Gene therapy and cell-based therapy applications, Int. J. Alzheimers Dis. 2011 (2011) 517160.
[49] M. Garcia-Alloza, E.M. Robbins, S.X. Zhang-Nunes, S.M. Purcell, R.A. Betensky, et al., Characterization of amyloid deposition in the APPswe/PS1dE9 mouse model of Alzheimer disease, Neurobiol. Dis. 24 (2006) 516–524.
[50] C. Kilkenny, W.J. Browne, I.C. Cuthill, M. Emerson, D.G. Altman, Improving bioscience research reporting: the ARRIVE guidelines for reporting animal research, PLoS Biol. 8 (2010).
[51] L. Liu, K. Duff, A technique for serial collection of cerebrospinal fluid from the cisterna magna in mouse, J. Vis. Exp. (2008).
[52] A. Willuweit, J. Velden, R. Godemann, A. Manook, F. Jetzek, et al., Early-onset and robust amyloid pathology in a new homozygous mouse model of Alzheimer's disease, PLoS One 4 (2009).
[53] V. Vergote, S. Van Dorpe, K. Peremans, C. Burvenich, B. De Spiegeleer, In vitro metabolic stability of obestatin: kinetics and identification of cleavage products, Peptides 29 (2008) 1740–1748.
[54] S. Stalmans, N. Bracke, E. Wynendaele, B. Gevaert, K. Peremans, et al., Cell-penetrating peptides selectively cross the blood-brain barrier in vivo, PLoS One 10 (2015), e0139652.
[55] A. Manook, B.H. Yousefi, A. Willuweit, S. Platzer, S. Reder, et al., Small-animal PET imaging of amyloid-beta plaques with [11C]PiB and its multi-modal validation in an APP/PS1 mouse model of Alzheimer's disease, PLoS One 7 (2012), e31310.
[56] A. Sun, X.V. Nguyen, G. Bing, Comparative analysis of an improved thioflavin-s stain, Gallyas silver stain, and immunohistochemistry for neurofibrillary tangle demonstration on the same sections, J. Histochem. Cytochem. 50 (2002) 463–472.
[57] J.B. Rothbard, E. Kreider, C.L. VanDeusen, L. Wright, B.L. Wylie, et al., Arginine-rich molecular transporters for drug delivery: role of backbone spacing in cellular uptake, J. Med. Chem. 45 (2002) 3612–3618.
[58] G. Lattig-Tunnemann, M. Prinz, D. Hoffmann, J. Behlke, C. Palm-Apergi, et al., Backbone rigidity and static presentation of guanidinium groups increases cellular uptake of arginine-rich cell-penetrating peptides, Nat. Commun. 2 (2011) 453.
[59] A.J. de Crespigny, J. Rother, C. Beaulieu, T. Neumann-Haefelin, M.E. Moseley, Comparison of diffusion, blood oxygenation, and blood volume changes during global ischemia in rats, Magn. Reson. Med. 45 (2001) 10–16.
[60] A. Lalatsa, A.G. Schatzlein, I.F. Uchegbu, Strategies to deliver peptide drugs to the brain, Mol. Pharm. 11 (2014) 1081–1093.
[61] R. Nau, F. Sorgel, H. Eiffert, Penetration of drugs through the blood-cerebrospinal fluid/blood-brain barrier for treatment of central nervous system infections, Clin. Microbiol. Rev. 23 (2010) (858−+).
[62] W.M. Pardridge, Drug transport in brain via the cerebrospinal fluid, Fluids Barriers CNS, 8, 2011, p. 7.
[63] D.D. Shen, A.A. Artru, K.K. Adkison, Principles and applicability of CSF sampling for the assessment of CNS drug delivery and pharmacodynamics, Adv. Drug Deliv. Rev. 56 (2004) 1825–1857.
[64] J.H. Lin, CSF as a surrogate for assessing CNS exposure: an industrial perspective, Curr. Drug Metab. 9 (2008) 46–59.
[65] C.L. Joachim, L.K. Duffy, J.H. Morris, D.J. Selkoe, Protein chemical and immunocytochemical studies of meningovascular beta-amyloid protein in Alzheimer's disease and normal aging, Brain Res. 474 (1988) 100–111.
[66] F. Prelli, E. Castano, G.G. Glenner, B. Frangione, Differences between vascular and plaque core amyloid in Alzheimers-disease, J. Neurochem. 51 (1988) 648–651.
[67] C. Humpel, Organotypic vibrosections from whole brain adult Alzheimer mice (overexpressing amyloid-precursor-protein with the Swedish-Dutch-Iowa mutations) as a model to study clearance of beta-amyloid plaques, Front. Aging Neurosci. 7 (2015) 47.
[68] L. Bouman, Über die entwicklung der senilen plaques, Zeitschrift für Die Gesamte Neurologie Und Psychiatrie, 94, 1925, pp. 267–274.
[69] B.V. Zlokovic, Cerebrovascular permeability to peptides - manipulations of transport-Systems at the Blood-Brain-Barrier, Pharm. Res. 12 (1995) 1395–1406.
[70] P. Chiodelli, C. Urbinati, S. Mitola, E. Tanghetti, M. Rusnati, Sialic acid associated with alphavbeta3 integrin mediates HIV-1 Tat protein interaction and endothelial cell proangiogenic activation, J. Biol. Chem. 287 (2012) 20456–20466.
[71] M. Tyagi, M. Rusnati, M. Presta, M. Giacca, Internalization of HIV-1 tat requires cell surface heparan sulfate proteoglycans, J. Biol. Chem. 276 (2001) 3254–3261.
[72] C. Urbinati, S. Nicoli, M. Giacca, G. David, S. Fiorentini, et al., HIV-1 Tat and heparan sulfate proteoglycan interaction: a novel mechanism of lymphocyte adhesion and migration across the endothelium, Blood 114 (2009) 3335–3342.
[73] G. Tunnemann, G. Ter-Avetisyan, R.M. Martin, M. Stockl, A. Herrmann, et al., Live-cell analysis of cell penetration ability and toxicity of oligo-arginines, J. Pept. Sci. 14 (2008) 469–476.
[74] S. Futaki, S. Goto, Y. Sugiura, Membrane permeability commonly shared among arginine-rich peptides, J. Mol. Recognit. 16 (2003) 260–264.
[75] T. Suzuki, S. Futaki, M. Niwa, S. Tanaka, K. Ueda, et al., Possible existence of common internalization mechanisms among arginine-rich peptides, J. Biol. Chem. 277 (2002) 2437–2443.
[76] S.W. Jones, R. Christison, K. Bundell, C.J. Voyce, S.M. Brockbank, et al., Characterisation of cell-penetrating peptide-mediated peptide delivery, Br. J. Pharmacol. 145 (2005) 1093–1102.
[77] G. Ter-Avetisyan, G. Tunnemann, D. Nowak, M. Nitschke, A. Herrmann, et al., Cell entry of arginine-rich peptides is independent of endocytosis, J. Biol. Chem. 284 (2009) 3370–3378.

2.6 A selective retrograde transport of Aβ-binding D-enantiomeric peptides in mouse models of Alzheimer's disease following intra-hippocampal injection

Manuscript ready for submission to: ACS Chemical Neuroscience

Impact Factor: 4.36

Contributions: 75%

Involved in the conception and design of the experiments; except for section-staining, conducted all the rest of experimental parts and data analysis; involved in writing the manuscript.

A selective retrograde transport of Aβ-binding D-enantiomeric peptides in mouse models of Alzheimer's disease following intra-hippocampal injection

Nan Jiang[1], Thomas van Groen[2], Inga Kadish[2], N. Jon Shah[3,4], Karl-Josef Langen[3], Antje Willuweit[3], Dieter Willbold[1,5]

[1]Forschungszentrum Jülich, ICS-6, 52425 Jülich, Germany

[2]Department of Cell, Developmental and Integrative Biology, University of Alabama at Birmingham, Birmingham, AL 35294, USA

[3]Forschungszentrum Jülich, INM-4 Medical Imaging Physics, 52428 Jülich, Germany

[4]Department of Neurology, Faculty of Medicine, JARA, RWTH Aachen University, Aachen, Germany

[5]Heinrich-Heine-Universität Düsseldorf, Institut für Physikalische Biologie, 40225 Düsseldorf, Germany

Corresponding author:

Email: D.Willbold@fz-juelich.de (DW)

Abstract

Increasing evidence indicates that soluble amyloid-beta (Aβ) oligomers induce neurotoxicity including oxidative stress, synaptic dysfunction and axonal transport deficits in Alzheimer's disease (AD). Using a mirror-image phage display screen against Aβ (1-42), we have identified several peptides consisting solely of D-enantiomeric amino acid residues that prevent fibril formation and eliminate Aβ oligomers *in vitro*. These D-peptides have already proven therapeutic efficacy *in vivo* with reduction of amyloid plaque load and inflammation in brain, and reversing cognitive deficits in transgenic mouse models. In our recent studies, the D-peptide D3 showed blood-brain barrier permeability and specific binding to Aβ plaques after systemic administration in transgenic AD mice, as well as high oral availability. But little is known about the distribution within the brain. This study demonstrates the distribution and especially the axonal transport pattern of fluorescently labelled D3 and its derivative D3D3 after intra-hippocampal injection into brains of AD transgenic and wild type mice. Results show that in comparison to other standard retrograde tracers, the fluorescently labelled D3 and D3D3 demonstrate a significantly enhanced retrograde transport in the perforant pathway in AD transgenic mice. We suggest that this may reflect a co-transport of the fluorescently labelled D3 and D3D3 with Aβ species in the axons of the perforant pathway underlying AD pathology.

Introduction

Alzheimer's disease (AD) is the most common cause of dementia (estimated 60 to 80% of all cases) [1]. Its neuropathological changes are predominantly found in the limbic and association cortices, as well as in certain subcortical nuclei that project to them [2, 3]. The AD pathology expands hierarchically during disease progression, which, at least partially follows neuronal pathways anterogradely from affected to unaffected regions, resulting in corresponding clinical signs and symptoms of cognitive and behavioural changes [4-7]. The extracellular senile plaque is mainly composed of aggregated amyloid beta-protein (Aβ) and is together with neurofibrillary tangles and neurodegeneration as one important hallmark of AD. It was described that Aβ can also be found in many intracellular sites of neurons, such as ER, Golgi complexes, mitochondria, endosomes, lysosomes, multivesicular bodies (MVB), and in cytosol [8]. Increasing evidences suggest the accumulation of intraneuronal Aβ, which ends up as extracellular deposition, directly causes neurotoxicity and initiates AD pathology [8-10]. Studies indicate that the hippocampal formation is mostly implicated in the early stage of AD [11, 12], and the perforant pathway, projecting from the entorhinal cortex to the dentate gyrus, hippocampus proper and subiculum, is considered as one of the first and most affected neuronal fibre pathways in AD [13-15]. In those regions, axonal dysfunction and degeneration can be observed before detectable deposition of tau and Aβ [16, 17]. The alteration of cytoskeleton, which disturbs axonal transport, is suggested to be the cause of AD [18]. Impairment of the endocytic pathway which is associated with amyloidogenesis is also among the earliest neuropathological changes of AD and may lead to neuronal dysfunction and cell death [19]. In spite of many investigations, as listed above, there is currently no reliable diagnosis of the disease in its early stages [20, 21].

Recent studies have identified that soluble Aβ oligomers are the key neurotoxic species causing oxidative stress, synaptic dysfunction and axonal transport deficits in AD [22-28]. Using a mirror-image phage display screen against Aβ (1-42) [29, 30], we have identified several peptides consisting solely of D-enantiomeric amino acid residues as potential new drug candidates for the treatment of AD. These D-peptides are able to prevent fibril formation and to eliminate neurotoxic Aβ oligomers *in vitro*, as well as to reduce amyloid plaques and inflammation in the brain, and to reverse cognitive deficits *in vivo* [31-35]. Our recent research showed that, one of those D-peptides, D3, demonstrated high oral availability and long plasma half-life in a preclinical pharmacokinetic study [36], as well as blood-brain barrier permeability. But little is known about their distribution, and the transport pattern within the brain. In this study, fluorescently labelled D-peptides D3 and its derivative D3D3, as well as FITC as a control substance were injected into the hippocampus of two AD mouse models and their transport patterns were characterized by tracking fluorescence. Besides binding to Aβ deposits *in vivo*, the fluorescently labelled D3 and D3D3 also demonstrated special axonal transport features in AD transgenic mice.

Materials and methods

Materials

FAM-D3 (H-rprtrlhthrnr-Lys(5(6)-carboxyfluorescein)-NH2), FITC-D3D3 (rprtrlhthrnrrprtrlhthrnr-Lys(fluorescein isothiocyanate)-NH2) and FITC were purchased from JPT peptide Technologies GmbH (Berlin, Germany). All other chemicals were supplied by Fluka Chemie AG (Buchs, Switzerland), Merck (Darmstadt, Germany), AppliChem (Darmstadt, Germany) and VWR (Darmstadt, Germany) in research grade.

Animals

The male APPSwe/PSEN1ΔE9 (APP Swedish mutation/PSEN1 lacking exon 9), male Tg-SwDI (human APP gene containing the Swedish, Dutch and Iowa mutations), and wild type C57BL/6 mice were purchased from Jackson Laboratories. The mice were housed in 4/cage until the treatments (at the age around 9 months) in a controlled environment (temperature 22 °C, humidity 50-60%, light from 06:00-18:00), food and water were available *ad libitum*. This experiment was conducted according with the local Institutional Animal Care and Use Committee (IACUC) guidelines.

Intra-hippocampal injection

The mice were separated into different groups according to injected substances, incubation time and mouse models. For studying differences among substances and of temporal influence, FAM-D3 and FITC were injected into the right hippocampus of transgenic APPSwe/PSEN1ΔE9 mice for 3 and 48 hours' incubation, respectively. For studying differences between two D-peptides, FAM-D3 and FITC-D3D3 were injected into the right hippocampus of Tg-SwDI mice for 48 hours' incubation, respectively. Wild type mice were used for controls with corresponding treatments.

The mice were anesthetized with ketamine/xylazine (100/10 mg/kg) and placed in a stereotaxic head frame. The microinjections were performed with a 2-µl Hamilton syringe. All the substances were dissolved in phosphate buffer (pH 8.0) to a concentration of 10 µg/µl. Notice that FITC was injected as a suspension solution, due to its low solubility in phosphate buffer. Following coordinates based on Paxinos and Franklin's the Mouse Brain in Stereotaxic Coordinates were used for intra-hippocampal injection: anterior-posterior (AP) 1.9 mm, medial-lateral (ML) 1.3 mm and dorsal-ventral (DV) 1.8 mm; for intra-ventricular injection: AP 0.8 mm, ML 1.0 mm and DV 2.5 mm. 1 µl of each substance was injected in a controlled speed about 0.1 µl/min. Then the needle was kept in the brain for 5 min before slow withdrawal. The skin was then sutured, and the mice were subcutaneously injected with 1 ml 0.9 % saline solution and placed on a warm water blanket in order to hydrate and sustain body temperature. Each mouse was housed individually after surgery and allowed to recover with water and food *ad libitum*.

Preparation of mouse brain samples

Mice were anesthetized with ketamine/xylazine and then transcardially perfused with ice-cold 0.9 % saline for 5 min followed by 4% paraformaldehyde in 0.1 M sodium phosphate buffer for 7 min. The brains were harvested and stored in the fixative (4% buffered (pH 7.4) paraformaldehyde solution to which 0.5% picric acid had been added) for 24 hours; thereafter they were transferred to a 30% sucrose solution at 4 °C for two days. Six series of coronal sections (35 µm) were cut on a freezing microtome. The first series of sections were mounted on gelatine-coated slides immediately, dried and coverslipped for microscopic image analysis using a Nikon Eclipse E600 microscope with camera under fluorescein channel. One half of the second series were used for immunostaining.

Immunostaining

Brain sections were immunohistochemically stained for Aβ (monoclonal mouse anti-human Aβ4-10 (W0-2), EMD Millipore). In short, the sections were rinsed overnight in a solution of Tris buffered saline (TBS); then the sections were treated for 30 min in a heated (85 °C) sodium citrate solution (0.05 M, pH 6.0). Following cooling and rinsing, the series of sections were transferred to a solution containing the primary antibody. This solution consists of TBS with 0.5% Triton X-100 added (TBS-T). Following incubation with primary antibody for 24 hours on a shaker table at room temperature (20 °C) in the dark, the sections were three times rinsed in TBS-T and transferred to the solution containing the secondary antibody (biotinylated goat anti-mouse; Sigma, 1:400) for 2 hours. The sections were rinsed three times with TBS-T and transferred to a solution containing ExtrAvidin for 2 hours; then the sections were incubated for approximately 3 min with Ni-enhanced diaminobenzidine (DAB) (12.5 mg DAB in 25 ml 0.1 M phosphate buffer, pH 7.4, 30 µl H_2O_2 (30%), with 1 ml of a 15% ammonium Ni-sulfate solution added). The stained sections were mounted on gelatinized slides and coverslipped.

Activated microglia were detected with rabbit polyclonal antibody to ionized calcium binding adaptor molecule-1 (Iba-1; Wako, 1:2500), activated astrocytes were detected using rabbit polyclonal antibody to glial fibrillary acidic protein (GFAP; Sigma, 1:1000), separately. The staining procedure was similar as described above, except there was no pretreatment and a red fluorescent secondary antibody (goat anti rabbit, Jackson ImmunoResearch) was added for visualization. The stained sections were mounted on gelatinized slides and coverslipped. Images were acquired and processed with cellSens Standard (Olympus) and ImageJ (1.48 s).

Results

FAM-D3 labelled Aβ plaques in both ipsi- and contralateral sides already 3 hours after intra-hippocampal injection into the transgenic mouse brain. As illustrated in Fig. 1, plaque-labelling was verified by anti-Aβ antibody (W0-2), activated astrocytes (GFAP) and microglia (Iba-1) staining, on the transgenic mouse brains injected with FAM-D3.

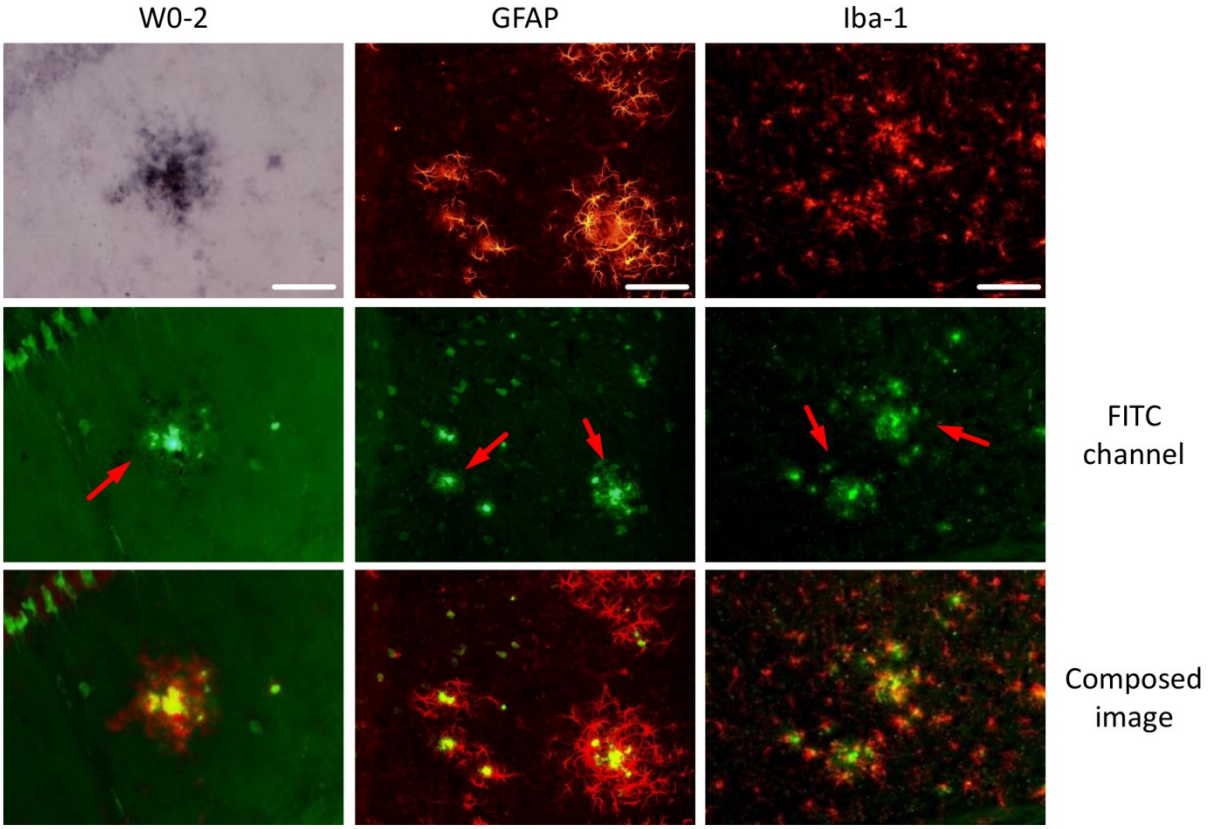

Fig. 1. Immunostaining with anti-Aβ antibody (W0-2), against activated astrocytes (GFAP) and microglia (Iba-1) on transgenic (APPSwe/PSEN1ΔE9) mouse brain sections 3 hours after intra-hippocampal injection of FAM-D3. Images in the first row show respective antibody staining (W0-2 was visualized with immunohistochemistry (DAB) in black-brown; GFAP and Iba-1 were visualized with immunofluorescence in red, respectively). The second row shows the same sections in FITC channel visualizing FAM-D3. The last row shows composed images of the above two channels. The image of W0-2 stain was converted to red colour before channel combination. Red arrows demonstrate FAM-fluorescence stains Aβ plaques in the corresponding sections. Scale bar: 20 µm.

Except for the plaque labelling, the distribution pattern of FAM-D3 post-injection was similar between wild type and transgenic mice. As shown in Fig. 2, local diffusion and a wide spread (anterior and posterior) of FAM-D3 within the hippocampus was found at the injection site 3 hours post-injection. Distribution of FAM-D3 in the corpus callosum was also observed, but its spread was limited (i.e., only a short distance). Ipsilateral to the injection, the granule and pyramidal cell layers of the dentate gyrus and hippocampus were intensively labelled with fluorescence. 48 hours post-injection, the local concentration of fluorescence on the injection side became lower due to further dispersion and/or clearance. On the ipsilateral

side, mossy fibres and hilar cells showed fluorescence; on the contralateral side, more FAM-D3 was observed in the pyramidal cells of CA areas, especially in CA3. On the contrary, FITC, which was injected as control, did not show neither fluorescence in the pyramidal nor in granule cells on the ipsilateral side, nor transport to the contralateral CA3 area (Fig. 3).

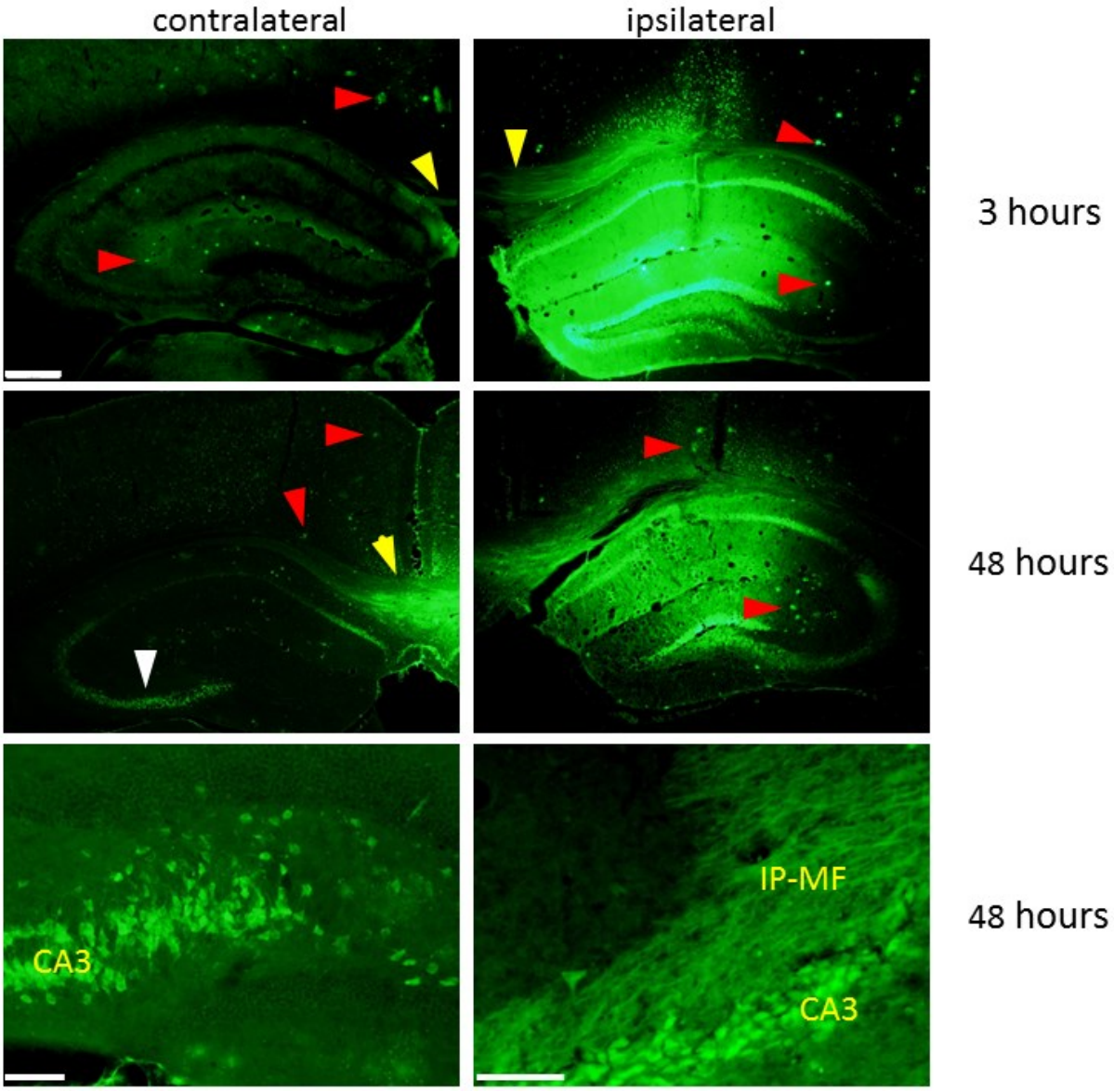

Fig. 2. Distribution of FAM-D3 in the transgenic mouse brain following intra-hippocampal injection. Illustrated are coronal sections showing right and left hippocampi of APPSwe/PSEN1ΔE9 transgenic mice after different incubation time post-injection with FAM-D3. FAM-D3 labelled plaques are shown with red arrows. Spread of FAM-D3 to the contralateral side via corpus callosum is indicated with yellow arrows. White arrow shows the fluorescently labelled pyramidal neurons (predominantly in CA3 area) found on the contralateral side. Higher magnification images show fluorescently labelled pyramidal neurons in CA3 (bottom left) and infrapyramidal mossy fibre (IP-MF) in stratum lucidum (bottom right). Scale bars of upper four images: 200 µm, of bottom two images: 50 µm.

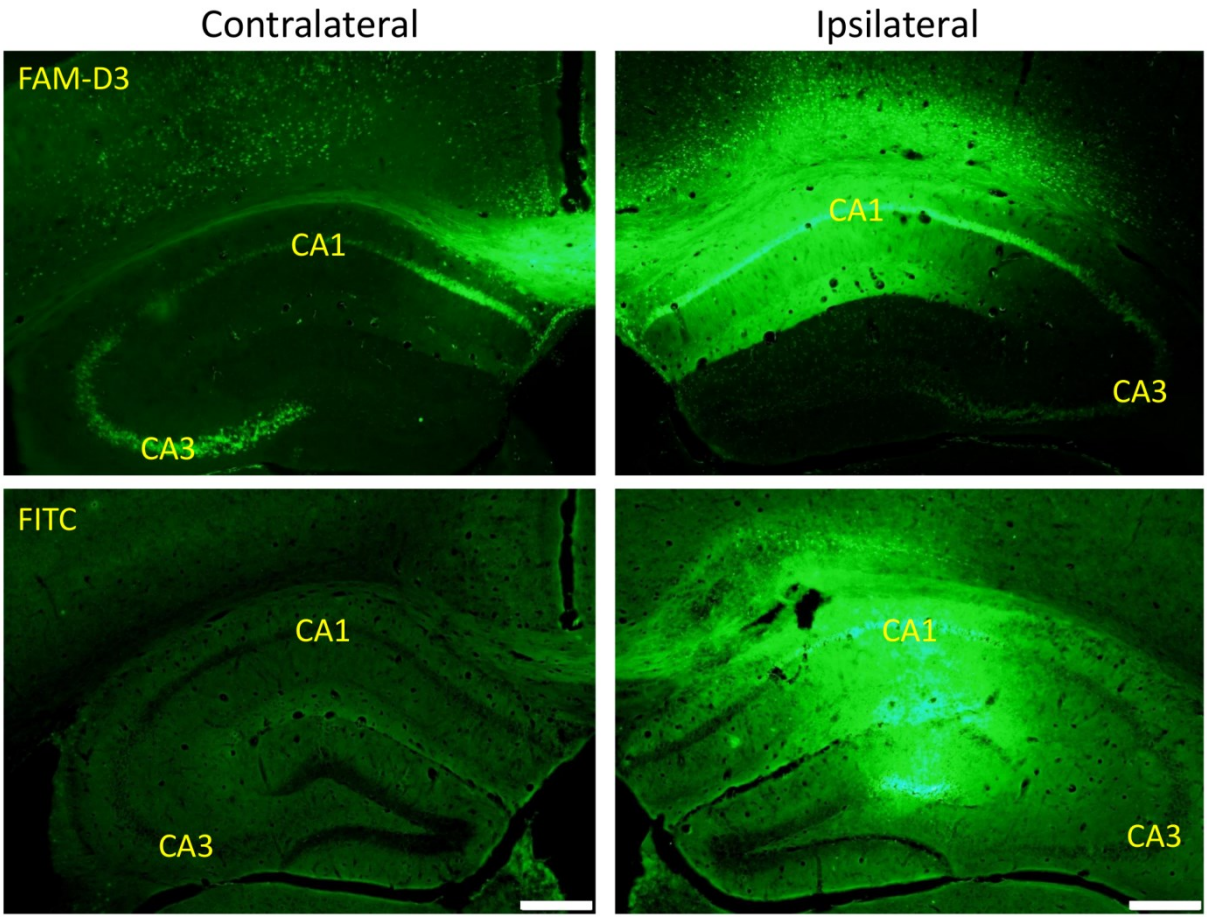

Fig. 3. Distribution of FAM-D3 and FITC in the contralateral hippocampus of wild type mouse brain. Illustrated are coronal sections of mouse brains after 48 hours intra-hippocampal injection of FAM-D3 (upper) and FITC (lower) respectively. CA1 and CA3 areas are indicated in yellow, respectively. Scale bar: 200 µm.

Besides the above stated observations, FAM-D3 also showed another unique property. In wild type mice, retrograde axonal transport of FAM-D3 to the temporal association and entorhinal areas was observed. But the fluorescence in those areas was generally weak. Whereas highly intensive fluorescence of FAM-D3 in layer II cells (small number of layer III cells were also involved) in entorhinal cortex was observed in both of the transgenic mouse lines expressing human Aβ (Fig. 4). In order to check whether this finding is due to D3 molecule alone or due to the FAM-labelling, control group with FITC injection was examed. There were no labelled neurons in the entorhinal cortex.

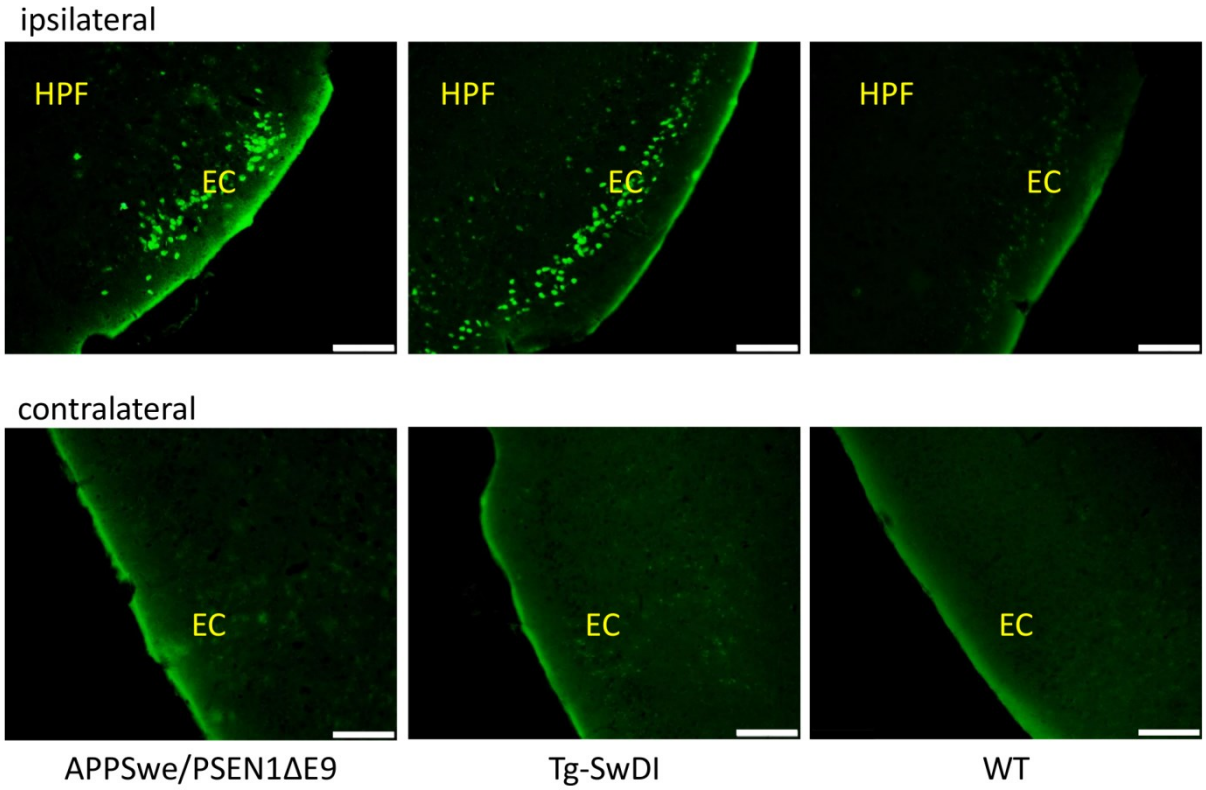

Fig. 4. Retrograde axonal transport of FAM-D3 in wild type and two AD transgenic mouse models 48 hours post intra-hippocampal injection. Images in upper row show FAM-D3 distribution in the ipsilateral entorhinal cortex, lower row show its distribution in the contralateral entorhinal cortex of transgenic APPSwe/PSEN1ΔE9 mouse (left), transgenic Tg-SwDI mouse (middle) and wild type mouse (right) brain, respectively. EC: entorhinal cortex, HPF: hippocampal formation. Scale bars: 100 µm.

Interestingly, co-localization of W0-2 antibody and FAM-D3 was found on the Aβ plaques as mentioned above, whereas no obvious W0-2 positive staining was observed in the layer II (and III) cells of entorhinal cortex, as well as in the pyramidal cells of CA areas and granule cells in dentate gyrus, where highly intensive fluorescence of FAM-D3 was found (Fig. 5).

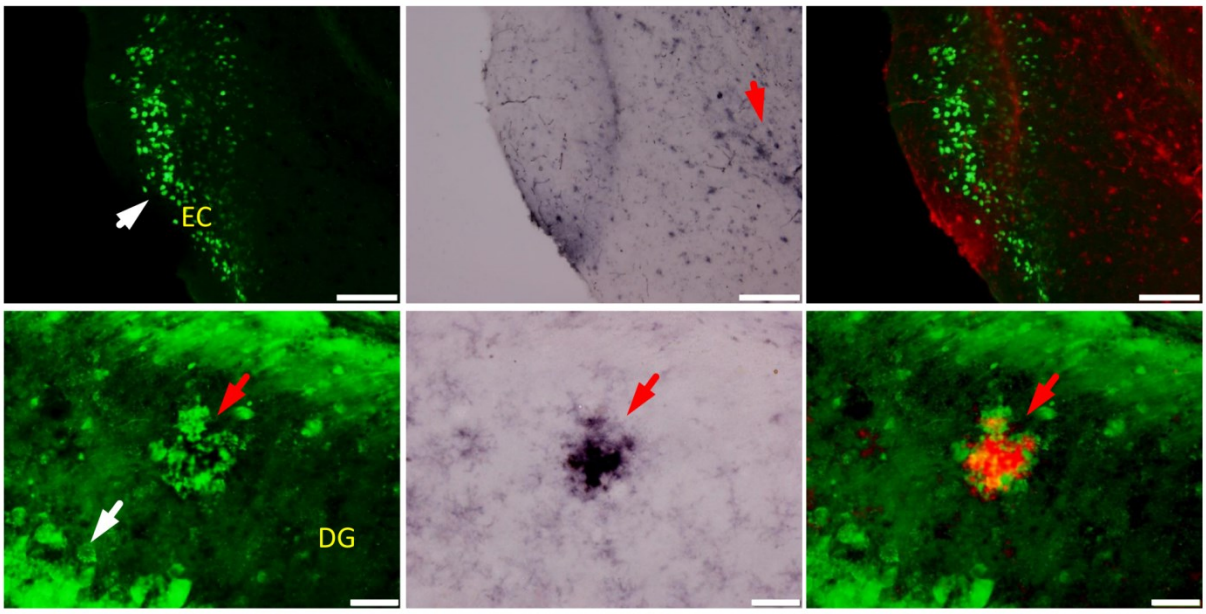

Fig. 5. Anti-Aβ (W0-2) antibody staining on sections from transgenic brain injected with FAM-D3. Upper row shows the entorhinal cortex (EC) of Tg-SwDI transgenic mouse brain 48 hours post-injection. Lower row shows the dentate gyrus (DG) of APPSwe/PSEN1ΔE9 transgenic mouse brain 3 hours post-injection. A co-localization of FAM-D3 and W0-2 antibody was found on Aβ plaques but not on the neurons with highly intensive fluorescence. Red arrows show Aβ deposits in both transgenic mouse models. Scale bar in upper row: 100 µm; lower row: 20 µm.

To investigate, whether the observed properties of FAM-D3 correlate with the affinity of D3 to Aβ species, we investigated the properties of FITC labelled D3D3, a linear tandem version of D3 [37]. On the first sight, no obvious difference was found between fluorescently labelled D3 and D3D3, as they both showed high accumulation in cellular layers of dentate gyrus and hippocampus in the ipsilateral side; a commissural transport to the contralateral side, especially to the pyramidal cells in CA3; labelling plaques on both sides of brain; specific retrograde axonal transport from hippocampal formation to layer II cells in entorhinal cortex (Fig. 6). However, FITC-D3D3 seemed to label fibre tracks more intensively than FAM-D3 did and it seemed to be transported faster within axons. Under higher magnification, fluorescence was found evenly distributed in distal axons, but heterogeneously distributed in the proximal axons and somata (Fig. 7).

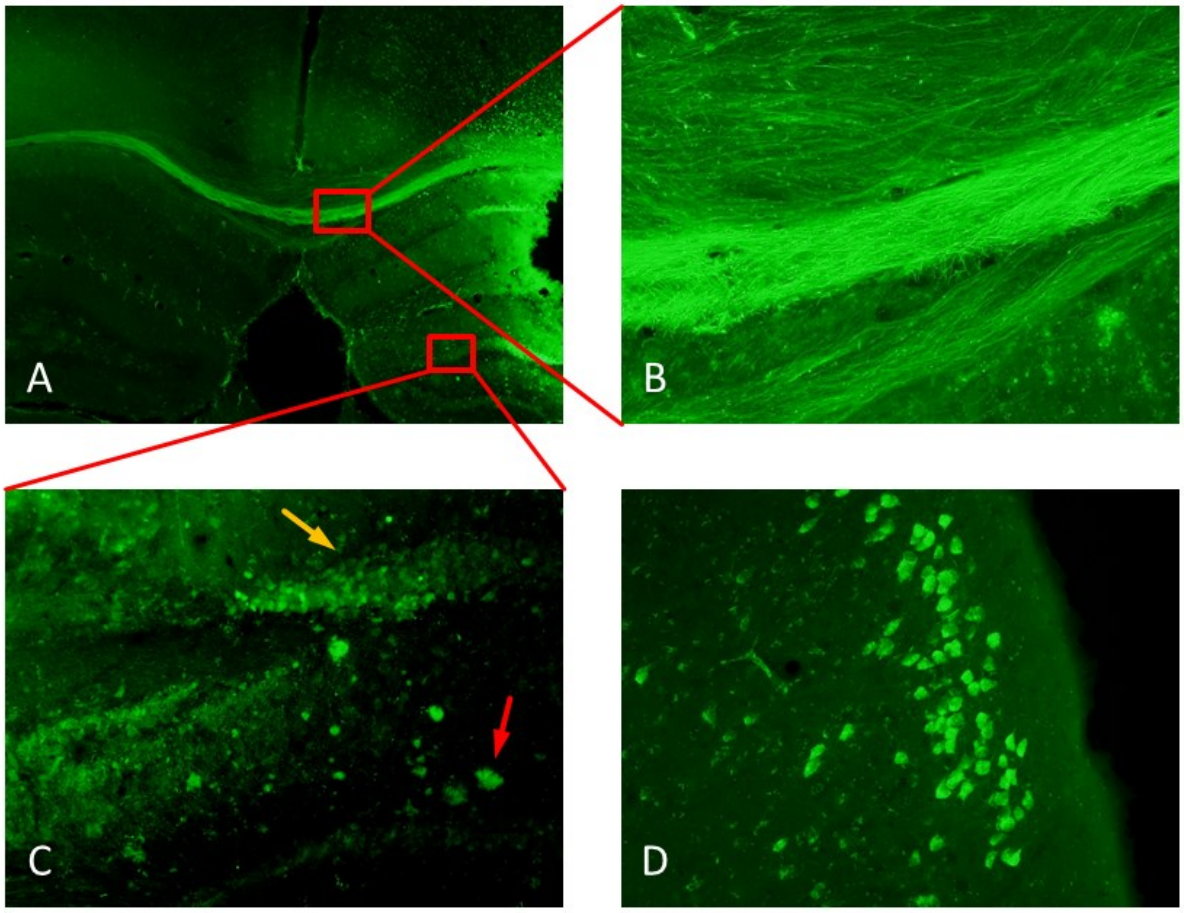

Fig. 6. Tracking of FITC-D3D3 following intra-hippocampal injection in a transgenic Tg-SwDI mouse 48 hours post-injection. Illustrated are characteristic labelling features of FITC-D3D3: (A) a global view of a coronal section at the midline showing hippocampi, (B) labelled neurofibres in corpus callosum or alveus, (C) labelled granule cells in dentate gyrus were shown with yellow arrow and amyloid deposits with red arrow, (D) retrograde transport to layer II pyramidal cells in entorhinal cortex.

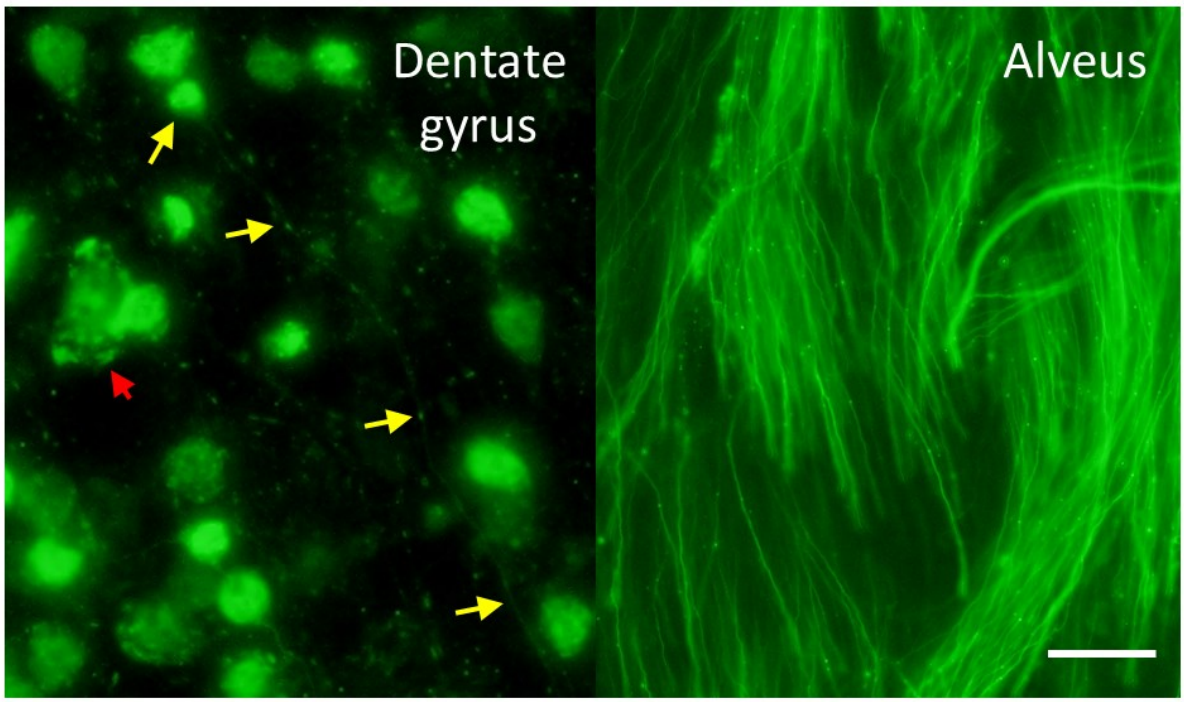

Fig. 7. Fluorescently labelled neurons (soma) and axons under high magnification with FITC-D3D3 injected in Tg-SwDI transgenic mouse brain. Left: Granule cells in dentate gyrus, right: axons in alveus. Yellow arrows highlight a neuron with its axon. Red arrow shows heterogeneous distribution of fluorescence in the soma of a neuron on the same section. Scale bar: 50 µm.

Discussion

Two different D-peptides were tested in this study, D3 and its tandem derivative D3D3. The rationale for the design of D3D3 was that the multivalent D-peptide can be expected to bind the multivalent Aβ target assembly with increased avidity and thus with increased binding affinity. Two main factors are suggested to be involved in the distribution of the fluorescently labelled D3 and D3D3: extracellular diffusion and intracellular transport (axonal transport). As we could show in this study, extracellular diffusion of the fluorescently labelled D3 and D3D3 after intra-hippocampal injection was limited within the hippocampal formation on the ipsilateral side by the naturally existing boundary around it. Axonal transport within white matter tracks might provide rapid and long distance spreading of the fluorescently labelled D3 and D3D3 to the whole brain. Both of the fluorescently labelled D3 and D3D3 showed transport within the major commissural fibres, the corpus callosum and were able to label Aβ plaques all around the brain (Fig. 1 and 2). Here D3D3 showed a more intensive labelling of axons and seemed to be transported in axons faster and more efficiently than D3 (Fig. 7). Besides that, the other observed properties of D3 and D3D3 were comparable.

The fluorescently labelled D3 and D3D3 were found 48 hours post-injection in the contralateral pyramidal cells of CA3 area of both transgenic and wild type mice, which suggests that they were transported retrogradely by neurons (Fig. 2 and 3). Remarkably, both fluorescently labelled D3 and D3D3 showed intensive labelling of layer II (and III) cells in entorhinal cortex in both transgenic mouse models (APPSwe/PSEN1ΔE9 and Tg-SwDI), but significantly less intensive in wild type mice (Fig. 4). Based on these results, we postulate that the retrograde transport of D3 and D3D3 from hippocampal formation to entorhinal cortices of both brain hemispheres following two pathways: 1) through retrograde trisynaptic pathway, namely CA1 (Schaffer collaterals)→CA3 (Mossy fibres)→dentate gyrus (perforant pathway)→layer II cells of the ipsilateral entorhinal cortex; 2) CA1 of injection site (retrogradely transported through commissural fibres)→CA3 of contralateral side and finally to the layer II cells of the contralateral entorhinal cortex through the retrograde perforant pathway. The latter pathway might explain why D3 and D3D3 were found mostly at the CA3 area of the contralateral side. This retrograde transport through commissural fibres was not dependent on the presence of human Aβ or AD pathology, because it was observed in both transgenic and wild type mice. Thus the conclusion might be drawn, that D3 and D3D3 showed significantly enhanced retrograde transport in the perforant pathway in AD transgenic mice in comparison to that in wild type mice. Whereas there was obvious co-localization of the fluorescently labelled D3 and D3D3 with Aβ plaques, the strongly fluorescence labelled layer II pyramidal cells in the entorhinal cortex were not stained by the anti-Aβ antibody W02 (Fig. 5). One explanation is that D3 and D3D3 are taken up by these cells independent of Aβ. The other explanation is that D3 and D3D3 are taken up with Aβ species followed by a retrograde transport to neuronal cell bodies for further processing, as some studies reported that Aβ located in autophagosomes or endosomes is transported

retrogradely towards the neuronal cell body where lysosomes are most concentrated, and is there subsequently degraded by lysosomes there [38, 39]. The latter explanation would be in accordance with the observation that the retrograde transport is less efficient in wild type mice, possibly because they express only endogenous levels of Aβ.

Accumulating studies describe the intracellular Aβ and Aβ oligomers as the early neurotoxic species in AD pathology [40-42], as well as their effects on axonal transport [43, 44]. Different therapeutic strategies against those Aβ species are developed [45-47]. Besides the therapeutic effectiveness of our D-peptides mentioned above, this study shows enhanced retrograde transport of D3 and D3D3 in AD transgenic mouse models. As the perforant pathway is considered to be the first and most affected during disease progression, the fluorescently labelled D3 and D3D3 will be useful to investigate the neuropathological changes in this pathway in early AD.

Acknowledgements

We thank Ashish Kumar and Monique Dozier-Sharpe for the excellent technical assistance.

References

1. Fletcher LC, Burke KE, Caine PL, Rinne NL, Braniff CA, Davis HR, et al. Diagnosing Alzheimer's disease: are we any nearer to useful biomarker-based, non-invasive tests? GMS health technology assessment. 2013;9:Doc01. Epub 2013/06/12. doi: 10.3205/hta000107. PubMed PMID: 23755087; PubMed Central PMCID: PMC3677379.
2. MacDonald AB. Alzheimer's disease Braak Stage progressions: reexamined and redefined as Borrelia infection transmission through neural circuits. Medical hypotheses. 2007;68(5):1059-64.
3. Selkoe DJ. The molecular pathology of Alzheimer's disease. Neuron. 1991;6(4):487-98. Epub 1991/04/01. PubMed PMID: 1673054.
4. Riedel G, Micheau J. Function of the hippocampus in memory formation: desperately seeking resolution. Progress in neuro-psychopharmacology & biological psychiatry. 2001;25(4):835-53.
5. Jonas P, Lisman J. Structure, function, and plasticity of hippocampal dentate gyrus microcircuits. Frontiers in Neural Circuits. 2014;8:107. doi: 10.3389/fncir.2014.00107. PubMed PMID: PMC4159971.
6. Hardy J. An 'anatomical cascade hypothesis' for Alzheimer's disease. Trends in neurosciences. 1992;15(6):200-1.
7. Hardy JA, Higgins GA. Alzheimer's disease: the amyloid cascade hypothesis. Science. 1992;256(5054):184-5.
8. LaFerla FM, Green KN, Oddo S. Intracellular amyloid-beta in Alzheimer's disease. Nature reviews Neuroscience. 2007;8(7):499-509. Epub 2007/06/07. doi: 10.1038/nrn2168. PubMed PMID: 17551515.
9. Gouras GK, Tampellini D, Takahashi RH, Capetillo-Zarate E. Intraneuronal β-amyloid accumulation and synapse pathology in Alzheimer's disease. Acta neuropathologica. 2010;119(5):523-41. doi: 10.1007/s00401-010-0679-9. PubMed PMID: PMC3183823.
10. Gouras GK, Tsai J, Naslund J, Vincent B, Edgar M, Checler F, et al. Intraneuronal Abeta42 accumulation in human brain. The American journal of pathology. 2000;156(1):15-20. Epub 2000/01/07. PubMed PMID: 10623648; PubMed Central PMCID: PMC1868613.
11. Khan UA, Liu L, Provenzano FA, Berman DE, Profaci CP, Sloan R, et al. Molecular drivers and cortical spread of lateral entorhinal cortex dysfunction in preclinical Alzheimer's disease. Nature neuroscience. 2014;17(2):304-11. doi: 10.1038/nn.3606.
12. Mu Y, Gage FH. Adult hippocampal neurogenesis and its role in Alzheimer's disease. Molecular neurodegeneration. 2011;6:85. Epub 2011/12/24. doi: 10.1186/1750-1326-6-85. PubMed PMID: 22192775; PubMed Central PMCID: PMC3261815.
13. Kalus P, Slotboom J, Gallinat J, Mahlberg R, Cattapan-Ludewig K, Wiest R, et al. Examining the gateway to the limbic system with diffusion tensor imaging: the perforant pathway in dementia. NeuroImage. 2006;30(3):713-20. Epub 2005/12/13. doi: 10.1016/j.neuroimage.2005.10.035. PubMed PMID: 16337815.
14. Rogalski EJ, Murphy CM, deToledo-Morrell L, Shah RC, Moseley ME, Bammer R, et al. Changes in parahippocampal white matter integrity in amnestic mild cognitive impairment: a diffusion tensor imaging study. Behavioural neurology. 2009;21(1):51-61. Epub 2009/10/23. doi: 10.3233/BEN-2009-0235. PubMed PMID: 19847045; PubMed Central PMCID: PMC2819387.
15. Stoub TR, deToledo-Morrell L, Stebbins GT, Leurgans S, Bennett DA, Shah RC. Hippocampal disconnection contributes to memory dysfunction in individuals at risk for Alzheimer's disease. Proceedings of the National Academy of Sciences of the United States of America. 2006;103(26):10041-5. Epub 2006/06/21. doi: 10.1073/pnas.0603414103. PubMed PMID: 16785436; PubMed Central PMCID: PMC1479867.
16. Kanaan NM, Pigino GF, Brady ST, Lazarov O, Binder LI, Morfini GA. Axonal degeneration in Alzheimer's disease: When signaling abnormalities meet the axonal transport system. Experimental neurology. 2013;246:44-53. doi: 10.1016/j.expneurol.2012.06.003. PubMed PMID: PMC3465504.

17. Kowall NW, Kosik KS. Axonal disruption and aberrant localization of tau protein characterize the neuropil pathology of Alzheimer's disease. Annals of neurology. 1987;22(5):639-43. Epub 1987/11/01. doi: 10.1002/ana.410220514. PubMed PMID: 3122646.
18. Terry RD. The pathogenesis of Alzheimer disease: an alternative to the amyloid hypothesis. Journal of neuropathology and experimental neurology. 1996;55(10):1023-5. Epub 1996/10/01. PubMed PMID: 8857998.
19. Nixon RA. Endosome function and dysfunction in Alzheimer's disease and other neurodegenerative diseases. Neurobiology of aging. 2005;26(3):373-82. Epub 2005/01/11. doi: 10.1016/j.neurobiolaging.2004.09.018. PubMed PMID: 15639316.
20. Chetelat G, Baron JC. Early diagnosis of Alzheimer's disease: contribution of structural neuroimaging. NeuroImage. 2003;18(2):525-41. Epub 2003/02/22. PubMed PMID: 12595205.
21. Petrella JR, Coleman RE, Doraiswamy PM. Neuroimaging and early diagnosis of Alzheimer disease: a look to the future. Radiology. 2003;226(2):315-36. Epub 2003/02/04. doi: 10.1148/radiol.2262011600. PubMed PMID: 12563122.
22. Barghorn S, Nimmrich V, Striebinger A, Krantz C, Keller P, Janson B, et al. Globular amyloid beta-peptide oligomer - a homogenous and stable neuropathological protein in Alzheimer's disease. Journal of neurochemistry. 2005;95(3):834-47. Epub 2005/09/02. doi: 10.1111/j.1471-4159.2005.03407.x. PubMed PMID: 16135089.
23. Walsh DM, Klyubin I, Shankar GM, Townsend M, Fadeeva JV, Betts V, et al. The role of cell-derived oligomers of Abeta in Alzheimer's disease and avenues for therapeutic intervention. Biochemical Society transactions. 2005;33(Pt 5):1087-90. Epub 2005/10/26. doi: 10.1042/BST20051087. PubMed PMID: 16246051.
24. Townsend M, Shankar GM, Mehta T, Walsh DM, Selkoe DJ. Effects of secreted oligomers of amyloid beta-protein on hippocampal synaptic plasticity: a potent role for trimers. The Journal of physiology. 2006;572(Pt 2):477-92. Epub 2006/02/14. doi: 10.1113/jphysiol.2005.103754. PubMed PMID: 16469784; PubMed Central PMCID: PMC1779683.
25. Kayed R, Head E, Thompson JL, McIntire TM, Milton SC, Cotman CW, et al. Common structure of soluble amyloid oligomers implies common mechanism of pathogenesis. Science. 2003;300(5618):486-9. Epub 2003/04/19. doi: 10.1126/science.1079469. PubMed PMID: 12702875.
26. Kayed R, Head E, Sarsoza F, Saing T, Cotman CW, Necula M, et al. Fibril specific, conformation dependent antibodies recognize a generic epitope common to amyloid fibrils and fibrillar oligomers that is absent in prefibrillar oligomers. Molecular neurodegeneration. 2007;2:18. Epub 2007/09/28. doi: 10.1186/1750-1326-2-18. PubMed PMID: 17897471; PubMed Central PMCID: PMC2100048.
27. Lesné S, Koh MT, Kotilinek L, Kayed R, Glabe CG, Yang A, et al. A specific amyloid-[beta] protein assembly in the brain impairs memory. Nature. 2006;440(7082):352-7. doi: http://www.nature.com/nature/journal/v440/n7082/suppinfo/nature04533_S1.html.
28. Haass C, Selkoe DJ. Soluble protein oligomers in neurodegeneration: lessons from the Alzheimer's amyloid [beta]-peptide. Nat Rev Mol Cell Biol. 2007;8(2):101-12.
29. Wiesehan K, Willbold D. Mirror-image phage display: aiming at the mirror. Chembiochem : a European journal of chemical biology. 2003;4(9):811-5. Epub 2003/09/10. doi: 10.1002/cbic.200300570. PubMed PMID: 12964153.
30. Schumacher TN, Mayr LM, Minor DL, Jr., Milhollen MA, Burgess MW, Kim PS. Identification of D-peptide ligands through mirror-image phage display. Science. 1996;271(5257):1854-7.
31. van Groen T, Kadish I, Funke SA, Bartnik D, Willbold D. Treatment with D3 removes amyloid deposits, reduces inflammation, and improves cognition in aged AbetaPP/PS1 double transgenic mice. J Alzheimers Dis. 2013;34(3):609-20. Epub 2012/12/29. doi: 10.3233/JAD-121792. PubMed PMID: 23271316.
32. van Groen T, Kadish I, Funke A, Bartnik D, Willbold D. Treatment with Abeta42 binding D-amino acid peptides reduce amyloid deposition and inflammation in APP/PS1 double transgenic mice. Advances in protein chemistry and structural biology. 2012;88:133-52. Epub 2012/07/21. doi: 10.1016/B978-0-12-398314-5.00005-2. PubMed PMID: 22814708.
33. Aileen Funke S, van Groen T, Kadish I, Bartnik D, Nagel-Steger L, Brener O, et al. Oral treatment with the d-enantiomeric peptide D3 improves the pathology and behavior of Alzheimer's

Disease transgenic mice. ACS chemical neuroscience. 2010;1(9):639-48. Epub 2010/09/15. doi: 10.1021/cn100057j. PubMed PMID: 22778851; PubMed Central PMCID: PMC3368690.
34. van Groen T, Wiesehan K, Funke SA, Kadish I, Nagel-Steger L, Willbold D. Reduction of Alzheimer's disease amyloid plaque load in transgenic mice by D3, A D-enantiomeric peptide identified by mirror image phage display. ChemMedChem. 2008;3(12):1848-52. Epub 2008/11/19. doi: 10.1002/cmdc.200800273. PubMed PMID: 19016284.
35. van Groen T, Kadish I, Wiesehan K, Funke SA, Willbold D. In vitro and in vivo staining characteristics of small, fluorescent, Abeta42-binding D-enantiomeric peptides in transgenic AD mouse models. ChemMedChem. 2009;4(2):276-82. Epub 2008/12/17. doi: 10.1002/cmdc.200800289. PubMed PMID: 19072935.
36. Jiang N, Leithold LH, Post J, Ziehm T, Mauler J, Gremer L, et al. Preclinical Pharmacokinetic Studies of the Tritium Labelled D-Enantiomeric Peptide D3 Developed for the Treatment of Alzheimer s Disease. PloS one. 2015;10(6):e0128553. Epub 2015/06/06. doi: 10.1371/journal.pone.0128553. PubMed PMID: 26046986; PubMed Central PMCID: PMC4457900.
37. Brener O DT, Gremer L, van Groen T, Mirecka EA, Kadish I, Willuweit A, Kutzsche J, Jürgens D, Rudolph S, Tusche M, Bongen P, Pietruszka J, Oesterhelt F, Langen K-J, Demuth H-U, Janssen A, Hoyer W, Funke SA, Nagel-Steger L, Willbold D. . QIAD assay for quantitating a compound's efficacy in elimination of toxic Aβ oligomers Scientific reports. 2015;5(13222). doi: 10.1038/srep13222.
38. Nixon RA. Autophagy, amyloidogenesis and Alzheimer disease. Journal of cell science. 2007;120(Pt 23):4081-91. Epub 2007/11/23. doi: 10.1242/jcs.019265. PubMed PMID: 18032783.
39. LaFerla FM, Green KN, Oddo S. Intracellular amyloid-[beta] in Alzheimer's disease. Nature reviews Neuroscience. 2007;8(7):499-509.
40. Pigino G, Morfini G, Atagi Y, Deshpande A, Yu C, Jungbauer L, et al. Disruption of fast axonal transport is a pathogenic mechanism for intraneuronal amyloid beta. Proceedings of the National Academy of Sciences of the United States of America. 2009;106(14):5907-12. doi: 10.1073/pnas.0901229106. PubMed PMID: PMC2667037.
41. Takahashi RH, Milner TA, Li F, Nam EE, Edgar MA, Yamaguchi H, et al. Intraneuronal Alzheimer abeta42 accumulates in multivesicular bodies and is associated with synaptic pathology. The American journal of pathology. 2002;161(5):1869-79. Epub 2002/11/05. PubMed PMID: 12414533; PubMed Central PMCID: PMC1850783.
42. Crowther DC, Kinghorn KJ, Miranda E, Page R, Curry JA, Duthie FA, et al. Intraneuronal Abeta, non-amyloid aggregates and neurodegeneration in a Drosophila model of Alzheimer's disease. Neuroscience. 2005;132(1):123-35. Epub 2005/03/23. doi: 10.1016/j.neuroscience.2004.12.025. PubMed PMID: 15780472.
43. Calkins MJ, Reddy PH. Amyloid Beta Impairs Mitochondrial Anterograde Transport and Degenerates Synapses in Alzheimer’s Disease Neurons. Biochimica et biophysica acta. 2011;1812(4):507-13. doi: 10.1016/j.bbadis.2011.01.007. PubMed PMID: PMC3042500.
44. Millecamps S, Julien J-P. Axonal transport deficits and neurodegenerative diseases. Nature reviews Neuroscience. 2013;14(3):161-76.
45. Eleuteri S, Di Giovanni S, Rockenstein E, Mante M, Adame A, Trejo M, et al. Novel therapeutic strategy for neurodegeneration by blocking Abeta seeding mediated aggregation in models of Alzheimer's disease. Neurobiology of disease. 2015;74:144-57. Epub 2014/09/01. doi: 10.1016/j.nbd.2014.08.017. PubMed PMID: 25173807; PubMed Central PMCID: PMC4323687.
46. Dwivedi AK, Iyer PK. Therapeutic Strategies to Prevent Alzheimer's Disease Pathogenesis Using A Fluorescent Conjugated Polyelectrolyte. Macromolecular bioscience. 2014;14(4):508-14. doi: 10.1002/mabi.201300107.
47. Soto C, Martin Z. Therapeutic strategies against protein misfolding in neurodegenerative diseases. Expert opinion on drug discovery. 2009;4(1):71-84. Epub 2009/01/01. doi: 10.1517/13543770802630455. PubMed PMID: 23480338.

2.7 Characterization of a Single-Chain Variable Fragment Recognizing a Linear Epitope of Ab: A Biotechnical Tool for Studies on Alzheimer's Disease?

Published in: PloS ONE

Impact Factor: 3.23

Contributions: 20%

Involved in the conception and design of the experiments; involved in the conduction of experiments (animal experiment, cryosectioning, immunostaining, fluorescence microscopy, image processing and analysis); involved in writing the manuscript.

OPEN ACCESS Freely available online

PLOS ONE

Characterization of a Single-Chain Variable Fragment Recognizing a Linear Epitope of Aβ: A Biotechnical Tool for Studies on Alzheimer's Disease?

Silke Dornieden[1], Andreas Müller-Schiffmann[2], Heinrich Sticht[3], Nan Jiang[1], Yeliz Cinar[1], Michael Wördehoff[5], Carsten Korth[2], Susanne Aileen Funke[1,4]*, Dieter Willbold[1,5]

1 Institute of Complex Systems (ICS-6), Forschungszentrum Jülich, Jülich, Germany, **2** Institut für Neuropathologie, Heinrich-Heine-Universität, Düsseldorf, Germany, **3** Institut für Biochemie, Friedrich-Alexander-Universität Erlangen-Nürnberg, Erlangen, Germany, **4** Bioanalytik, Hochschule für Angewandte Wissenschaften, Coburg, Germany, **5** Institut für Physikalische Biologie and BMFZ, Heinrich-Heine-Universität, Düsseldorf, Germany

Abstract

Alzheimer's disease (AD) is a progressive neurodegenerative disorder with devastating effects. Currently, therapeutic options are limited to symptomatic treatment. For more than a decade, research focused on immunotherapy for the causal treatment of AD. However, clinical trials with active immunization using Aβ encountered severe complications, for example meningoencephalitis. Consequently, attention focused on passive immunization using antibodies. As an alternative to large immunoglobulins (IgGs), Aβ binding single-chain variable fragments (scFvs) were used for diagnostic and therapeutic research approaches. scFvs can be expressed in *E. coli* and may provide improved pharmacokinetic properties like increased blood-brain barrier permeability or reduced side-effects in vivo. In this study, we constructed an scFv from an Aβ binding IgG, designated IC16, which binds the N-terminal region of Aβ (Aβ(1-8)). scFv-IC16 was expressed in *E. coli*, purified and characterized with respect to its interaction with different Aβ species and its influence on Aβ fibril formation. We were able to show that scFv-IC16 strongly influenced the aggregation behavior of Aβ and could be applied as an Aβ detection probe for plaque staining in the brains of transgenic AD model mice. The results indicate potential for therapy and diagnosis of AD.

Citation: Dornieden S, Müller-Schiffmann A, Sticht H, Jiang N, Cinar Y, et al. (2013) Characterization of a Single-Chain Variable Fragment Recognizing a Linear Epitope of Aβ: A Biotechnical Tool for Studies on Alzheimer's Disease? PLoS ONE 8(3): e59820. doi:10.1371/journal.pone.0059820

Editor: Riqiang Yan, Cleveland Clnic Foundation, United States of America

Received November 26, 2012; **Accepted** February 19, 2013; **Published** March 26, 2013

Funding: SD was supported by a fellowship of the International Helmholtz Research School on Biophysics and Soft Matter (BioSoft) granted to DW. CK was supported by EU-FP7 grant PRIORITY. SAF, CK and DW were supported by a grant from the KNDD/rpAD (BMBF 01ED1201B). The funders had no role in study design, data collection and analysis, decision to publish, or preparation of the manuscript.

Competing Interests: The authors have declared that no competing interests exist.

* E-mail: a.funke@fz-juelich.de

Introduction

Alzheimer's disease (AD) is a devastating, progressive, neurodegenerative disorder, which affects more than 35 million people world-wide [1]. Currently, AD treatment is restricted to palliative care due to the lack of disease arresting or modifying therapies [2]. Several lines of evidence have indicated that the amyloid-β-peptide (Aβ) plays a pivotal role in the pathology of AD. Aβ is produced throughout life as a 38 to 43 residue peptide derived from the amyloid precursor protein (APP) after cleavage by two distinct proteases, called β- and γ-secretase [3,4,5]. The function of Aβ needs to be clarified, but recent studies suggest neuroprotective effects of monomeric Aβ (for review, see ref. [6]). Senile plaques in the brain of the patient, one of the typical histopathological hallmarks of AD, consist mainly of Aβ(1-42). They are thought to play a crucial role in the pathology of AD, and according to the original amyloid cascade hypothesis, Aβ deposited in plaques has been thought to be responsible for neuronal dysfunction [7,8]. However, Aβ can adopt a variety of neurotoxic conformers (for review, see ref. [9]), and more recent studies indicate that diffusible Aβ oligomers are the major toxic species during disease development and progression [10,11,12,13]. Consequently, agents that interfere with Aβ oligomerization or increase Aβ clearance from the brain are expected to be valuable for application in therapy or prevention of AD. Passive immunotherapeutic approaches, i.e. direct administration of Aβ antibodies peripherally, were shown to be effective in transgenic mouse models of AD [14,15,16,17]. A variety of humanized monoclonal antibodies are currently investigated in clinical trials (for review, see ref. [18]). However, two phase III clinical trials with antibodies were discontinued as they failed to improve cognitive functions in the treated patients [19].

Additionally, Aβ binding ligands can be valuable for the investigation of the plaque load by *in vivo* imaging methods. Currently, only a few amyloid PET ligands have been applied in clinical studies (for review, see ref. [20,21]). Numerous efforts are devoted to develop new, target-specific imaging agents for the detection of amyloid plaques *in vivo*. To be suitable, such substances should exhibit highly specific binding to Aβ aggregates, very selective labeling and efficient brain penetration.

Targeting Aβ using scFvs have been shown to be a suitable alternative to IgGs [22]. ScFvs are genetically engineered constructs composed of the variable regions of the heavy-(V_H) and light chain (V_L) domains of a respective antibody, connected by a flexible linker to prevent dissociation. They usually retain the

specific and monovalent antigenic binding affinity of the parent IgG, but can exhibit improved pharmacokinetic properties like increased blood-brain barrier permeability [23]. Because of their small size, they can be recombinantly expressed in living systems, offering advantages for protein expression in microbial hosts and purification with high yield [24], as well as for gene therapeutic approaches that could avoid repeated infusions of expensive antibodies like performed in passive immunotherapy. Due to the lack of the constant domain (F_C) in scFvs, F_C induced cellular responses, microhemorrhages and inflammatory processes are prevented [25]. These advantages prompted the generation of several Aβ-binding scFvs that interact with Aβ, influence Aβ aggregation and partially reduce Aβ cytotoxicity in cell culture [26,27,28]. Recently, adeno-associated virus (AAV)-mediated intramuscular expression of a gene encoding for a scFv against the N-terminal part of Aβ, isolated from a human scFv library [29], was demonstrated to be effective in removing Aβ from the brain of AD transgenic mice without inducing hemorrhages or inflammation. Additionally, the cognitive performance of treated mice was improved in comparison with control mice [30]. Furthermore, another scFv binding to the C-terminus of Aβ, constructed using an antibody that was generated by immunizing mice with Aβ(30-42), has been shown to reduce congiophilic angiopathy as well as plaque burden in APP transgenic mice after direct chronic intranasal treatment [31].

We have constructed a scFv derived from an Aβ binding monoclonal antibody IC16, designated scFv-IC16. ScFv-IC16 was expressed in *E. coli*, purified and characterized with respect to its interaction with different Aβ species and its influence on Aβ fibrilization. Additionally, scFv-IC16 was used to stain and characterize plaques in brain slices of transgenic AD model mice by immunohistochemistry. scFv-IC16 was conclusively found to be a remarkable antibody fragment for the investigation of molecular pathological mechanisms, therapy or diagnosis of AD.

Materials and Methods

Molecular Modeling

The structure of IC16 in complex with Aβ(1-8) was generated with Modeller [32] using the crystal structure of the Aβ(1-8)-bound antibody PFA1 as template (pdb code 2IPU; [33]). The model was completed using Sybyl7.3 (Tripos Inc., St. Louis, MO, USA) by addition of Aβ-residue D1, which was not resolved in the PFA-Aβ crystal structure, followed by 100 steps of conjugate gradient energy minimization. The quality of the resulting model was checked using WhatCheck [34] and intermolecular contacts were analyzed with LigPlot [35].

Materials

All chemicals were supplied by AppliChem GmbH (Darmstadt, Germany), Merck (Darmstadt, Germany), Sigma Aldrich (St. Louis, MO, USA), and Roth (Karlsruhe, Germany) in research grade. All peptides were purchased as reversed phase high performance liquid chromatography purified products (purity > 95%). Synthetic human Aβ(1-42) was purchased from Bachem (Bubendorf, Switzerland). N-terminally biotinylated Aβ(1-42) was purchased from Anaspec (Fremont, CA, USA). Aβ peptides Aβ(1-8)-GSGSC, Aβ(2-8)-GSGSC, Aβ(3-8)-GSGSC, and Aβ(8-15)-GSGSC were purchased from JPT (Berlin, Germany).

Construction of an IC16 Single-chain Variable Fragment (scFv-IC16) Expression Plasmid

The monoclonal IgG2a antibody IC16 recognizes Aβ(1-8) and has been described earlier [36]. Briefly, an IC16 hybridoma was generated by standard fusion procedure of myeloma cells with splenocytes from a PrP knockout mouse [37] immunized with KLH Aβ(1-16). A scFv was constructed with mRNA purified from IC16 hybridoma used for PCR amplification with primers specific for variable regions of the heavy (V_H) and light chain (V_L): V_H forward: 5′- AAAACCATGGCGCAGGTTACTCTGAAA-GAGTC-3′; V_H reverse: 5′ TTTTGCCGGCCAG TGGATA-GACCGATGGGGCTGTTGTTTTGGT-3′; V_L forward: 5′ AAAAGGATCCGATGTTTTGATGACCCAAACT-3′;V_L re-verse: 5- AAAAGCGGCCGCGGATACAGTTGGTGCAG-CATC-3′. PCR products were digested with *Ngo*MIV (V_H) or *Bam*HI (V_L) and ligated to a oligonucleotide coding for a $(Gly_4Ser)_3$ linker domain [38]. The resulting 800 bp product was eluted from agarose gel and amplified with V_H forward and V_L reverse primer. The amplificate was digested with *Nco*I and *Eag*I and ligated into pET22b (Merck, Darmstadt, Germany), allowing periplasmic expression of the IC16-scFv fused to a His_6- and Myc-tag. The complete amino acid sequence of scFv-IC16 is as follows:
MKYLLPTAAAGLLLLAAQPAMAMAQVTLKESGP-GILQPSQTLSLTCSFSGFSLSTSGMGV.
SWIRQPSGKGLEWLAHIFWDDD-KNYNPSLKSRLTVSKDTSRNQVFLKITSVDTSDTATYY.
CARSPHLRGYDVDFDYWGQGTTLTVSSAKTTAPSVY-PLAGGGGSGGGGSGGGGSDVLMTQ.
TPLSLPVSLGDQASISCRSSQSLVHSNGNTYLH-WYLQKPGQSPKVLIYKVSNRFSGVPDR.
FSGSGSGTDFTLKISRVEAEDLGVYFCSQSTHVPLTF-GAGTKLELKRADAAPTVSAAEEQ.
KLISEEDLEEEEEEGTLEHHHHHH.

Generation of Aβ(1-16)-GB1-NHS-Sepharose for Purification of scFv-IC16

For expression of Aβ(1-16)-GB1 (Aβ-GB1), human Aβ(1-16) was ligated into the *Nde*1 site of pET22b-GB1 [39]. Aβ-GB1 was expressed at 37°C in BL21(DE3) Rosetta (Merck, Darmstadt, Germany) grown to mid-logarithmic phase in 2YT-medium. Expression was induced by the addition of IPTG to a final concentration of 1 mM, and cells were then grown for a further 4 h. After harvesting cells by centrifugation, they were lysed in 50 mM Tris-HCl (pH 8.0), 5 mM EDTA, 1% Triton X-100, 2 mM phenylmethanesulfonyl fluoride (PMSF), 20 mM $MgCl_2$, 200 U DNase1 and 0,25 mg/ml lysozyme. The cleared lysate was first dialyzed to 20 mM Tris-HCl (pH 8.0) and 1 mM EDTA and the first purification step was then performed via Q-Sepharose (GE Healthcare, Little Chalfont, UK). The column was washed with dialysis buffer and bound Aβ-GB1 was eluted with 20 mM Tris-HCl (pH 8.0), 1 mM EDTA and 75 mM NaCl. In a final purification step, Aβ-GB1 was separated from minor impurities using IgG-Sepharose (GE Healthcare). After washing with 20 mM Tris-HCl (pH 8.0), 150 mM NaCl and 1 mM EDTA, Aβ-GB1 was eluted with 50 mM glycine pH 2.5 and immediately neutralized by adding Tris-HCl (pH 8.0) to a final concentration on 100 mM. After dialysis against PBS the protein was coupled to NHS-Sepharose (GE Healthcare, Little Chalfont, UK) according to the manufacturer's recommendations.

Expression and Purification of scFv-IC16

Escherichia coli strain BL21(DE3)pRARE2 was used as an expression host. Bacteria were grown to high density (OD600≥1.6) at 37°C, and cooled on ice for 1 h before induction with IPTG at a final concentration of 0.1 mM. Cells were further incubated for 24 h at 18°C, and subsequently harvested by centrifuging for 30 min at room temperature at 5000×g. Cells were lysed in 20 mM Tris-HCl pH 8.0, 0.4 mM EDTA, 5 mM

imidazole, 500 mM NaCl, 20 mM $MgCl_2$, 10 mM $CaCl_2$, Protease Inhibitor Cocktail Tablet Complete EDTA free (Roche, Grenzach-Wyhlen, Germany), 1 mg/ml lysozyme and 500 U DNase. The lysate was cleared by centrifugation at 20 000×g, and the soluble protein in the supernatant was purified via Ni-NTA chromatography (Ni-NTA Agarose, AppliChem GmbH, Darmstadt, Germany). After loading the sample onto the Ni-NTA Agarose, the column (3 ml) was washed with 10 column volumes (CV) 20 mM Tris-HCl pH 8.0, 5 mM imidazole, 500 mM NaCl and 1% TX-100, followed by a second wash with 10 CV 20 mM Tris-HCl pH 8.0, 5 mM imidazole, 500 mM NaCl. Bound scFv-IC16 was eluted by four CV elution buffer (20 mM Tris-HCl pH 8.0, 300 mM imidazole, and 300 mM NaCl). A second purification step using affinity chromatography was performed, because the purity of the eluted protein was lower than 50%. The previously generated Aβ1-16-GB1 NHS sepharose was used for a subsequent purification step. After loading scFv-IC16 (in elution buffer), the column was washed with 10 CV TBS (137 mM NaCl, 2.7 mM KCl, 2.5 mM Tris-HCl, pH 7.4). The protein was eluted with 50 mM glycine, pH 2.5 and immediately neutralized with a final concentration of 100 mM Tris-HCl, pH 8.0. ScFv-IC16 was dialyzed against PBS (137 mM NaCl, 2.7 mM KCl, 1.8 mM KH_2PO_4, 10 mM Na_2HPO_4, pH 7.4) and stored at −20°C until further usage.

Binding Constant Determination Using Surface Plasmon Resonance (SPR)

Binding kinetics were determined by SPR using a Biacore™ X (GE Healthcare, UK). Synthetic Aβ peptides were dissolved in 10 mM NaAc, pH 4.0. The CM5 sensor chip surface (GE Healthcare, UK) was activated using N-ethyl-N′-3 (diethylaminopropyl) carbodiimide (EDC) and N-hydroxysuccinimide (NHS) chemistry followed by 2-(2-pyridinyldithio)ethaneamine hydrochloride (PDEA), in order to introduce a reactive thiol group. Aβ was coupled via the C-terminal cysteine to the chip at a flow rate of 5 µl/min, and the remaining active groups were blocked by injecting cysteine. The immobilization procedure was performed according to manufacturer's recommendation. All kinetic analyses were performed at a flow rate of 20 µl/min in PBS. Varying concentrations of scFv-IC16 (10 to 5000 nM) and IC16 (10 to 1000 nM) were injected. Association was observed for 180 s whereas the dissociation was observed for 120 to 360 s. When required, the surface was regenerated by injecting 20 µl 50 mM glycine, pH 11.0. The data evaluation was performed using Biaevaluation Software 4.1.1. ScFv-IC16 data were fitted according to the Langmuir 1:1 binding model, whereas IC16 data were fitted according to the bivalent binding model. Standard errors of equilibrium dissociation constants (K_D) were calculated using standard errors of the corresponding association and dissociation rate constants [40].

Thioflavin T (ThT) Assays

7.5 µM Aβ(1-42) (stock solution of 190 µM in DMSO, freshly prepared before usage) were incubated with 10 µM ThT in PBS in absence or presence of different concentrations of scFv-IC16 (1.5, 3.75 and 7.5 µM) at room temperature for 24 h. In addition, scFv-IC16 (7.5 µM) without Aβ(1-42) was tested under the same conditions as the negative control. For all samples a reference value, generated with PBS and ThT only, was subtracted. Each sample had a volume of 50 µl and was incubated and measured in a 384 well plate (Greiner 384 Well polypropylene Greiner Bio-One GmbH, Frickenhausen, Germany). The plate was covered by an adhesive film preventing evaporation of the sample buffer. Fluorescence recordings were performed every 30 min for 22 h (excitation wavelength 440 nm, emission wavelength 490 nm, Polarstar Optima, BMG, Ortenberg, Germany). The experiments were performed five-fold, and the average of the obtained values as well as the standard deviation was calculated.

Seedless-preparation of Aβ1-42

1 mg of Aβ(1-42) or N-terminally/C-terminally biotinylated Aβ(1-42) was dissolved in 1 ml 1,1,1,3,3,3-hexafluorosiopropanol (HFIP) and incubated overnight at room temperature. Afterwards, Aβ(1-42) was mixed in the favored ratio with N-terminally/C-terminally biotinylated Aβ(1-42) and aliquoted. HFIP was evaporated using a SpeedVac (Concentrator 5301, Eppendorf, Germany) at room temperature for 30 min. To evaporate remaining HFIP, the sample was incubated overnight at room temperature with an open lid.

Preparation of Aβ(1-42) Monomers, Oligomers and Fibrils

The preparation of Aβ(1-42) monomers and oligomers was carried out by size exclusion chromatography (SEC) as already described by Johansson et al [41] with minor modifications. 250 µg of Aβ peptide was dissolved in 130 µl SEC buffer (50 mM NaPi, pH 7.4; 150 mM NaCl; 0.6% Tween-20) and briefly centrifuged (1 min, 16 100×g, room temperature) to remove insoluble fibrillar material. 100 µl of the supernatant was applied on a Superdex75 10/300 column (GE Healthcare, UK) connected to an Äkta purifier system (GE Healthcare, UK). The sample was eluted at a flow rate of 0.6 ml per min at room temperature and detected at wavelengths of 214, 250 and 278 nm. Fractions of 200 µl were collected. For the preparation of Aβ fibrils, 125 µg of Aβ(1-42) peptide was dissolved in 200 µl PBS and incubated for 24 h (300×g, 37°C). Samples were centrifuged (16 100×g, 20 min, room temperature) and the supernatant containing soluble Aβ species was discarded. Insoluble fibrils were resuspended in 200 µl SEC buffer. The concentration of the Aβ preparations was determined using the Micro BCA Protein Assay Kit (Thermo Scientific, Waltham, MA, USA). Before performing the standard protocol recommended by the manufacturer, 80 µl 6 M urea was mixed with 80 µl monomer- and oligomer preparation, respectively. As the concentration of the fibril preparation was usually high, 80 µl 6 M Urea was mixed with 40 µl SEC buffer and 40 µl fibril fraction. The samples were incubated at 60°C for 30 min. Afterwards they were mixed with BCA reagent at a ratio of one to one and again incubated at 60°C for 20 to 30 min. Bovine serum albumin (BSA) at concentrations of 10, 20 and 40 µg per ml was used as a standard. The samples were measured at a wavelength of 570 nm with a Polarstar Optima plate reader (BMG, Ortenberg, Germany).

Enzyme-linked Immunosorbent Assay (ELISA) Analysis of scFv-IC16 Binding to Aβ-monomers, -oligomers and -fibrils

An ELISA was applied to characterize the binding affinity of scFv-IC16 to different Aβ conformers. After concentration determination of the Aβ(1-42) monomer, oligomer and fibril preparations, each conformer was diluted in immobilization buffer (0.1 M $NaHCO_3$, pH 9.3) to a concentration of 5 µg/ml, and coated on Nunc immobilizer streptavidin F96 clear plates (250 ng/well) (Nunc, Thermo Scientific, Waltham, MA, USA). Alternatively, Aβ monomers were prepared seedless in the same concentration by dissolving 50 µg N-terminally biotinylated Aβ(1-42) in 1 ml immobilization buffer and diluting it further to 5 µg/ml. N- or C-terminally biotinylated Aβ(1-10) peptides were dissolved in immobilization buffer to a final concentration of

1.2 µg/ml (60 ng/well). 50 µl of these Aβ solutions were incubated in the well for 1 h. Each well was washed with 100 µl immobilization buffer and the plate was stored at 4°C overnight in 100 µl immobilization buffer per well. Unspecific binding sites were blocked with 50 µl blocking buffer (PBS, 1% BSA) at room temperature for 1 h. After removal of the blocking buffer, a solution of either scFv-IC16 (12 and 23 nM in PBS-T (0.1% Tween-20) and 0.1% BSA respectively), IC16 (0.67 nM PBS-T and 0.1% BSA) or mAB-6E10 (0.67 nM PBS-T and 0.1% BSA) was added to each conformer and incubated for 1 h. Subsequently, each well was washed with PBS-T (three times, 100 µl) and incubated with Penta-His antibody (Qiagen, Hilden, Germany, dilution 1:500, in 2 ml TBS-T) for 1 h at room temperature. This was followed by another three washing steps with PBS-T and detection of the antibodies with HRP-conjugated anti-mouse IgG (Thermo Scientific, Waltham, MA, USA, dilution 1:10000, in 2 ml TBS-T). 3,3,5,5-tetramethylbenzidine (Sigma Aldrich, St. Louis, MO, USA) was used as the substrate for the HRP. The reaction was terminated by adding sulfuric acid to a final concentration of 1 M. The absorbance was recorded at 450 nm on Polarstar Optima plate reader (BMG, Ortenberg, Germany).

Immunoprecipitation of Cell Culture Derived Aβ

Purified scFv-IC16 was dialyzed against PBS and coupled to NHS-Sepharose (GE, Buckinghamshire, UK) according to the manufacturers recommendations. Conditioned medium (CM) was prepared from confluent wild type CHO cells or 7PA2 cells cultured in DMEM (Life Technologies, UK) in presence or absence of FCS. Aβ was immune-precipitated from cleared CM with scFv-IC16-NHS-Sepharose overnight at 4°C. After washing with PBS, captured proteins were separated by 10–20% tricine peptide PAGE (Biorad, Hercules, CA) and transferred onto a 0.2 µm nitrocellulose membrane at 400 mA for 2 h. The filter was boiled for 5 min in PBS [42] and blocked overnight at 4°C with 5% fat-free milk in PBS containing 0.05% Tween 20 (PBS-T). After washing in PBS-T, the membrane was probed with 1:200 diluted monoclonal 4G8 (Signet, Dedhem, MA). Bound antibody was detected with horseradish peroxidase conjugated goat anti-mouse Ig (at 1:25000) (Thermo Scientific, Bonn, Germany). Subsequently, the Amersham ECL Western Blotting Detection Reagent (GE, Buckinghamshire, UK) was applied for visualization.

Ex vivo Staining of Plaques in Mouse Brain Slices

Deep frozen horizontal brain cryosections (20 µm thickness) from 9 or 12 months old Tg2576 mice and the respective wildtype control were dried in ambient air for 15 min, and then fixed in ice-cold 4% (w/v) paraformaldehyde for 20 min. Incubation with 70% formic acid for 5 min was performed to enhance immunoreactivity. Sections were permeabilized with 1% Triton X-100 in TBS for 10 min, followed by blocking with Mouse on mouse (M.O.M.) Basic Kit (Vector Laboratories) in TBS-Triton (1%, v/v) for 30 min. Primary antibodies were diluted in 1% BSA/TBS-Triton (working concentration of ScFv: 400 nM, 6E10:33 nM, 1-11-3 (Covance, USA) in 1:200 dilution) and probed on the sections for 1 h, incubating at room temperature. For double staining of scFv-IC16 and 1-11-3, the respective antibodies were mixed directly in 1% BSA/TBS-Triton buffer. Subsequently, the slices were incubated overnight at 8°C in a humid chamber. For His-tagged scFv, sections were incubated with anti Penta-His Mouse antibody (Qiagen) 1:10 diluted in 1% BSA/TBST for 2 h at room temperature. A secondary antibody (Goat anti Mouse Alexa 488, Invitrogen), diluted 1:300 in 1% BSA/TBST, was incubated for 2 hours at room temperature. For double staining, two secondary antibodies (goat anti mouse-Alexa488 and goat anti rabbit-Alexa-568 were mixed directly (working concentration of goat anti rabbit-Alexa568:1.300). After 1 min of incubation with 0.5 µg/ml DAPI, the sections were coverslip-mounted with Aqua Poly/Mont (Polysciences Inc, Worrington, PA, USA). Sections were examined under a fluorescence microscope (Leica LMD6000 (Leica, Solms, Germany). Excitation Range: UV; blue; green. Excitation Filter: Bp 420/30; Bp 495/15; Bp 570/20) with camera (Leica DFC 310 FX). Images were processed with LAS software (Leica Application Suite, V.4.0.0) and ImageJ (1.45 s).

Results

Expression of scFv-IC16 in *E. coli* and Purification via Ni-NTA and Aβ-affinity Chromatography

To characterize scFv-IC16, the protein was produced in *E. coli* and purified via Ni-NTA and Aβ-affinity chromatography. Expression was performed using the BL21DE3 pRARE2 strain. ScFv expression often results in formation of inclusion bodies [43,44]. Therefore, we have developed a protocol for slow expression, leading to an increase of correctly folded and soluble protein. Cells were shocked on ice for 1 h after reaching the stationary phase ($OD_{600} \geq 1.6$) in order to slow down the metabolism. Protein expression was induced with a final IPTG concentration of 0.1 mM. Under these conditions more than 10% of the expressed protein was soluble. Attempts to purify the remaining unsoluble protein after denaturation were successful and yielded pure protein after Ni-NTA affinity chromatography. However, refolding attempts remained unsuccessful. Purification of natively folded protein was performed using Ni-NTA affinity chromatography, followed by Aβ affinity chromatography using Aβ(1-16)-GB1 NHS Sepharose. IC16 was originally raised against Aβ(1-16). Therefore, the fusion protein contains the binding epitope of scFv-IC16. In addition, this step ensured that only active and correctly folded scFv was purified and thus used for further studies. The complete procedure resulted in 0.4 ± 0.1 mg of pure protein as judged by SDS-PAGE (Fig. 1) and UV/Vis spectrometry, derived from 1 L cell culture.

Characterization of the Binding Site of scFv-IC16 at Aβ(1-16) – Homology Modeling and Surface Plasmon Resonance Measurements

The amino acid sequence of the constructed scFv-IC16 was compared to antibody fragments that were already described in the literature. The IgG2a monoclonal anti-Aβ protofibril antibodies PFA1 and PFA2 were derived from mice challenged with a stabilized protofibril form of Aβ(1-40). The derived Fab fragments exhibit binding to Aβ monomers in the nM range, but the binding to aggregated Aβ forms is significantly impaired in comparison to the full IgG molecules. Structural characterization of the Fabs in complex with the Aβ(1-8) peptide as well as binding studies revealed a significant influence of N-terminal Aβ truncations on binding [33]. Our alignments exhibited sequence identities of 82% and 94% for the V_H and V_L regions of scFv-IC16 and the Fab fragment PFA1, respectively (Fig. 2, [33]). In addition, the complementary determining regions (CDR), which are hypervariable and mainly determine the binding properties of an antibody [45], showed high similarity of scFv-IC16 to PFA1 (see also Tables 1 and 2). Therefore, we assume that the binding of scFv-IC16 is similar to Aβ as shown for PFA1 and Aβ(1-8) by X-ray crystallography. To understand the binding of scFv-IC16 to Aβ and the differences to the binding of PFA1 to Aβ in more detail, the structure of scFv-IC16 in complex with Aβ(1-8) was

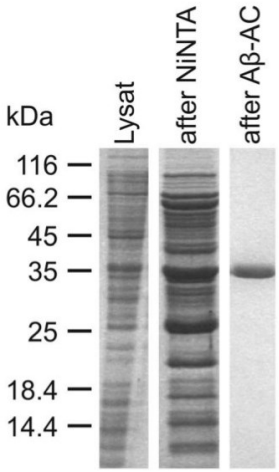

Figure 1. SDS-PAGE analysis of the purification of scFv-IC16 via Ni-NTA and Aβ1-16 GB1 NHS sepharose affinity chromatography. 1 µl of the lysate and 15 µl of the purified fractions were applied to 16% polyacrylamide gels [56]. Lane 1: cell lysate, lane 2: eluate after affinity chromatography via Ni NTA–Agarose, lane 3: eluate after Aβ1-16-GB1-NHS-Sepharose affinity chromatography. Target protein is more than 99% pure after final purification step.
doi:10.1371/journal.pone.0059820.g001

modeled using the crystal structure of the Aβ(1-8)-PFA1 complex [33] as a template. As expected from the high degree of sequence similarity, both antibodies form similar contacts with Aβ(1-8) (Fig. 3). Differences are only detected for sequence positions 100 and 108 of the heavy chain, as well as 98 of the light chain. Of these three sites, only residue 108 forms significant interactions with Aβ(1-8). In PFA1, D108(H) forms a salt-bridge with H6 of Aβ, while V108(H) of IC16 forms nonpolar interactions with H6 (Fig. 3).

Our next aim was to confirm the prediction of the modeling. Consequently, the equilibrium constants (K_D) of scFv-IC16 to various N-terminal Aβ fragments were determined using SPR. For comparison, we also performed the measurements with the monoclonal parent antibody IC16 (Fig. 4 and 5, Table 3). The monoclonal antibody was expected to exhibit more structural stability caused by the constant domains. Additionally, an avidity effect may influence the binding constants of IC16 to the different Aβ peptides. Measurements on both Aβ(1-8) and Aβ(8-15) were used to confirm the localization of the linear binding epitope at the N-terminal. No interaction of IC16 and scFv-IC16 with Aβ(8-15) was observed. For Aβ(1-8) the injection curves showed a fast association rate of IC16 and a very slow dissociation rate. This result is reflected in the low K_D of 51 nM (Table 3, bivalent fit). Comparison of the binding curves of IC16 and scFv-IC16 revealed that the association rates of scFv-IC16 and IC16 to Aβ(1-8) were comparable, whereas the dissociation rate of scFv-IC16 was one order of magnitude higher than the corresponding IC16 dissociation rate. These results are reflected in the K_D for scFv-IC16 (K_D of 0.55 µM, Table 3, Langmuir 1:1 binding model), demonstrating a loss of affinity of the scFv in comparison to the monoclonal antibody, which may be due to the lost avidity of the scFv as compared to the monoclonal antibody.

A comparison of the affinities of both IC16 and scFv-IC16 for N-terminally truncated Aβ-peptides (Table 3) showed that the highest affinities were observed for Aβ(2-8). Deletion of A2 leading to Aβ(3-8) resulted in significant reduction of affinity for scFv-IC16 (Table 3). Truncation of the two N-terminal residues and modification of E3 into pyroE3 led to an extensive loss of affinity and no binding could be detected for scFv-IC16.

Influence of scFv-IC16 on Aβ(1-42) Fibrilization

To characterize the influence of scFv-IC16 on Aβ(1-42) fibrilization, ThioflavinT (ThT) assays were carried out. ThT is a benzothiazole dye, which exhibits a shift and increase in quantum yield while binding to β-sheet rich fibrils [46]. During the fibrilization process of Aβ, an increase of ThT fluorescence can be observed until a saturation level is reached. Whereas the

A

```
          10        20        30        40        50        60
IC16  QVTLKESGPGILQPSQTLSLTCSFSGFSLSTSGMGVSWIRQPSGKGLEWLAHIFWDDDKN
      ::::::::::::.:::::::::::::::::::::::.:::::::::::::::.::::..
PFA1  QVTLKESGPGILKPSQTLSLTCSFSGFSLSTSGMGVGWIRQPSGKGLEWLAHIWWDDDRS

             70        80        90       100       110       120
IC16  YNPSLKSRLTVSKDTSRNQVFLKITSVDTSDTATYYCARSPHLRGYDVDFDYWGQGTTLT
      ::::::::.::.::::.:::::::.:::::::.::::::.:  :      : :::::: .:
PFA1  YNPSLKSQLTISKDAARNQVFLRITSVDTADTATYYCVRRAHTTVLGDWFAYWGQGTLVT

          130
IC16  VSSAKTTAPSVYPLA
      ::.:::::::::::::
PFA1  VSAAKTTAPSVYPLA
```

B

```
          10        20        30        40        50        60
IC16  DVLMTQTPLSLPVSLGDQASISCRSSQSLVHSNGNTYLHWYLQKPGQSPKVLIYKVSNRF
      ::::::::::::::::::::::::::::::.:::::::::.::::::::::::.:::::::::
PFA1  DVLMTQTPLSLPVSLGDQASISCRSSQSIVHSNGNTYLEWYLQKPGQSPKLLIYKVSNRF
```

Figure 2. Sequence alignment of the V_H (a) and V_L (b) region of IC16 and PFA1. Residues belonging to the CDRs are marked in red. Labeling was done according to the sequence of the heavy and light chain used for the scFv-IC16 construct, each starting with residue 1. Residues that interact with Aβ(1-8) are marked in bold and those residues that form hydrogen bonds or salt-bridges with Aβ(1-8) are additionally underlined. D1 of the IC16 light chain is marked in bold and blue, because it forms repulsive interactions with D1 of Aβ.
doi:10.1371/journal.pone.0059820.g002

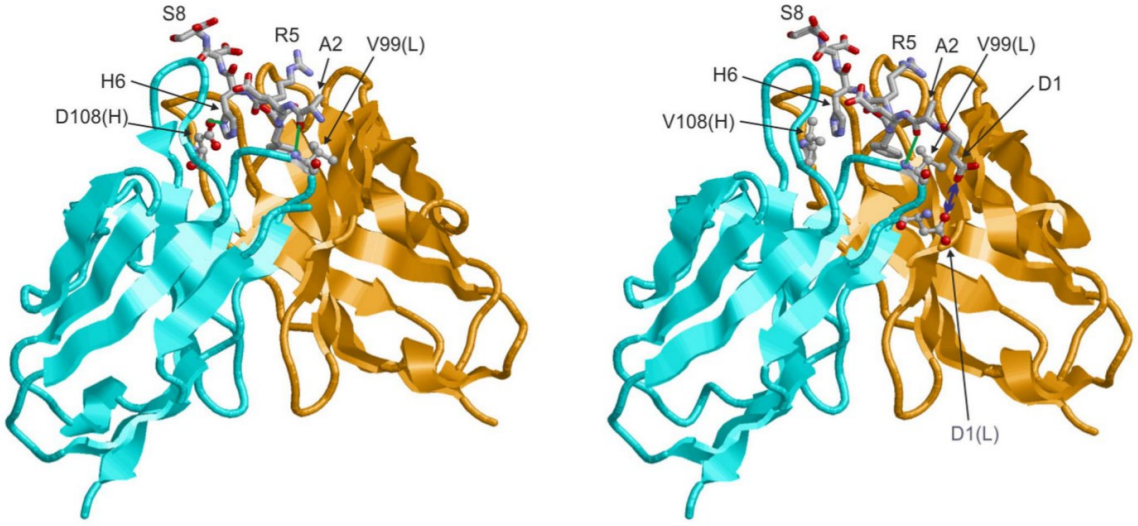

Figure 3. Interaction of monomeric Aβ(1-8) with the antibodies PFA1 (left) and IC16 (right). Residues of Aβ(1-8) are shown in stick presentation and colored according to the atom type (residue D1 of Aβ is not resolved in the PFA1 complex). For clarity, only D1, A2, R5, H6, and S8 of Aβ(1-8) are labeled. Key interacting residues of the antibodies are shown in ball-and-stick presentation and are labeled (chain identifier in parenthesis). Polar attractive interactions formed by these residues are depicted in green line. A repulsive interaction between D1(L) and D1 of Aβ(1-8) is indicated by a blue double-headed arrow.
doi:10.1371/journal.pone.0059820.g003

Aβ sample showed a strong increase in ThT fluorescence after 10 h, ThT assays with Aβ and scFv-IC16 yielded a scFv-IC16 dose-dependent lower ThT signal (Fig. 6A), indicating a strong influence of scFv-IC16 on Aβ fibril formation. With the ratio of 1:1 for Aβ(1-42) and scFv-IC16 the fibrilization of Aβ(1-42) was completely inhibited. At the ratios of 2:1 and 5:1, scFv-IC16 reduced the ThT fluorescence significantly. The sample that contained only scFv-IC16 was used as a negative control and did not show ThT fluorescence after 10 h.

ELISA Analysis of the Binding Activities of scFv-IC16 to Aβ Monomers, Oligomers and Fibrils

The monoclonal antibody IC16 was raised against Aβ(1-16), and binding activity of scFv-IC16 to N-terminal Aβ fragments was confirmed using SPR. Nonetheless, we intended to analyze the binding activities of scFv-IC16 to different Aβ conformers in order to detect potential binding preferences. To perform ELISA studies, Aβ monomers, oligomers and fibrils were prepared and equal molar amounts with respect to monomeric Aβ were immobilized in wells of a 96 well plate. The commercially available monoclonal antibody 6E10 is known to bind to all Aβ conformers with similar affinities as it recognizes human Aβ(3-10) epitope, which is freely accessible in Aβ monomers as well as in oligomers and fibrils [47]. It is frequently used as a standard in ELISA experiments [48,49,50] and was used here as a control to compare the immobilized amounts of Aβ monomers, oligomers and fibrils. The different Aβ conformers were incubated with scFv-IC16. Subsequently, bound scFv-IC16 was detected using an anti-His antibody that was then detected by an HRP conjugated secondary antibody. Fig. 6B depicts the relative quantification of the binding of scFv-IC16 and 6E10 to different Aβ conformers. The 6E10 control demonstrated the presence of similar amounts of Aβ monomers, oligomers and fibrils with respect to monomeric Aβ in the wells of the microtiterplate. Furthermore, scFv-IC16 showed a preferential binding to Aβ fibrils. The highest relative fluorescence was detected for fibril binding; the relative fluorescence for oligomer binding was weaker ($p = 0.0014$, N-bio oligomers to N-bio fibrils). Signals for monomer binding were not detected if Aβ monomers were immobilized onto the streptavidin functionalized surface of the well via an N-terminal biotin tag, indicating interference of the N-terminal biotin tag with the binding of scFv-IC16 to 100% N-terminally biotinylated monomers. Aβ monomers or Aβ(1-10) fragments that were immobilized via a C-terminal biotin tag were bound by scFv-

Table 1. Comparison of the CDR sequences of the heavy chains of different antibody fragments.

Name	CDR1	CDR2	CDR3
scFv-IC16	GFSLSTSGMGV	HIFWDDDKNYNPSLKSR	RSPHLRGYDVDFDY
PFA1	GFSLSTSGMG	IWWDDDR	VRRAHTTVLGDWFAY
PFA2	GFSLRTSGMG	IWWDDDK	VRRAHNVVLGDWFAY

doi:10.1371/journal.pone.0059820.t001

Table 2. Comparison of the CDR sequences of the light chains of antibody fragments.

Name	CDR1	CDR2	CDR3
scFv-IC16	RSSQSLVHSNGNTYLH	YKVSNRFS	SQSTHVPLT
PFA1	QSIVHSNGNTY	KVS	FQGSHVPLTS
PFA2	QSIVHSNGNTY	KVS	FQGSHVPLTS

doi:10.1371/journal.pone.0059820.t002

Table 3. Rate constants and dissociation constants of the interactions of scFv-IC16 and IC16 with N-terminal Aβ fragments.

Analyte	Ligand	k_{on} (M^{-1} s^{-1})	k_{off} (s^{-1})	K_D (M)
scFv-IC16	Aβ(1-8)	$3.10\pm0.02\times10^{4}$	$1.72\pm0.005\times10^{-2}$	$553\pm4\times10^{-9}$
	Aβ(2-8)	$6.84\pm0.03\times10^{4}$	$7.65\pm0.03\times10^{-3}$	$112\pm0.6\times10^{-9}$
	Aβ(3-8)	$8.36\pm0.5\times10^{3}$	$43.9\pm0.3\times10^{-3}$	$5.25\pm0.3\times10^{-6}$
	Aβ(pE3-8)			n.d.
	Aβ(8-15)			n.d.
IC16	Aβ(1-8)	$3.5\pm0.02\times10^{4}$	$1.8\pm0.02\times10^{-3}$	$51\pm0.5\times10^{-9}$
	Aβ(2-8)	$4.85\pm0.01\times10^{4}$	$1.54\pm0.006\times10^{-3}$	$32\pm0.1\times10^{-9}$
	Aβ(3-8)	$4.17\pm0.006\times10^{4}$	$3.43\pm0.007\times10^{-3}$	$82\pm0.2\times10^{-9}$
	Aβ(pE3-8)	$4.21\pm0.008\times10^{4}$	$63\pm0.05\times10^{-3}$	$1.5\pm0.001\times10^{-6}$
	Aβ(8-15)			n.d.

Data were fitted globally. scFv-IC16 data were fitted according to the Langmuir 1:1 binding model, whereas IC16 data were fitted using a bivalent fit. The association rate constants (k_{on}), the dissociation rate constants (k_{off}) and the equilibrium dissociation constants (K_D) are given below. Both, scFv-IC16 and IC16, did not show any detectable binding towards Aβ(8-15). However, they showed binding to all N-terminal peptides, except scFv-IC16 did not bind to Aβ(pE3-8). The lowest K_D value was observed for the interaction of scFv-IC16 and IC16 to Aβ(2-8).

doi:10.1371/journal.pone.0059820.t003

IC16 very similar to Aβ oligomers in the ELISA experiment, which can be shown by similar absorption values ($p = 0.038$, C-bio monomers to N-bio oligomers; $p = 0.19$, C-bio Aβ1-10 to N-bio oligomers).

To confirm that scFv-IC16 also binds Aβ that was naturally secreted by 7PA2 cells, scFv-IC16 was coupled to NHS-Sepharose and incubated with culture medium derived from wildtype CHO cells or 7PA2 cells. 7PA2 cells secrete high amounts of monomeric and lower oligomeric Aβ species. Previously it was demonstrated that serum stabilizes the monomeric form of Aβ, whereas oligomeric Aβ accumulates in the absence of serum [51]. As demonstrated in Fig. 6C, scFv-IC16 efficiently precipitated monomeric Aβ from 7PA2-CM containing FCS as well as lower oligomeric Aβ species from CM of 7PA2 cells cultured without FCS. Thus, scFv-IC16 displays the same binding specificity as the monoclonal antibody IC16 [36].

Ex vivo Staining of Plaques in Mouse Brain Slices

Brain cryosections derived from nine or 12 months old transgenic (tg 2576) mice and the respective non-transgenic control were stained using scFv-IC16. Additionally, anti-Aβ plaque stainings (using the 6E10 antibody) were performed on adjacent sections as well as costainings with scv-IC16 and 1-11-3 anti Aβ(1-42) antibody. DAPI nuclei counterstainings were performed on the same slides, respectively. Photomicrographs of the stained slices and overlay images are shown in Figure 7. scFv-IC16 could readily be used to detect plaques specifically in AD transgenic mice with low background signals, demonstrating potential applicability as a molecular probe. The staining pattern of scFv-IC-16 was very similar to the staining pattern of 6E10, which also binds to the N-terminal part of Aβ and the periphery of the plaques. The staining pattern of 1-11-3 is slightly different as the core of the plaques is stained with higher intensity.

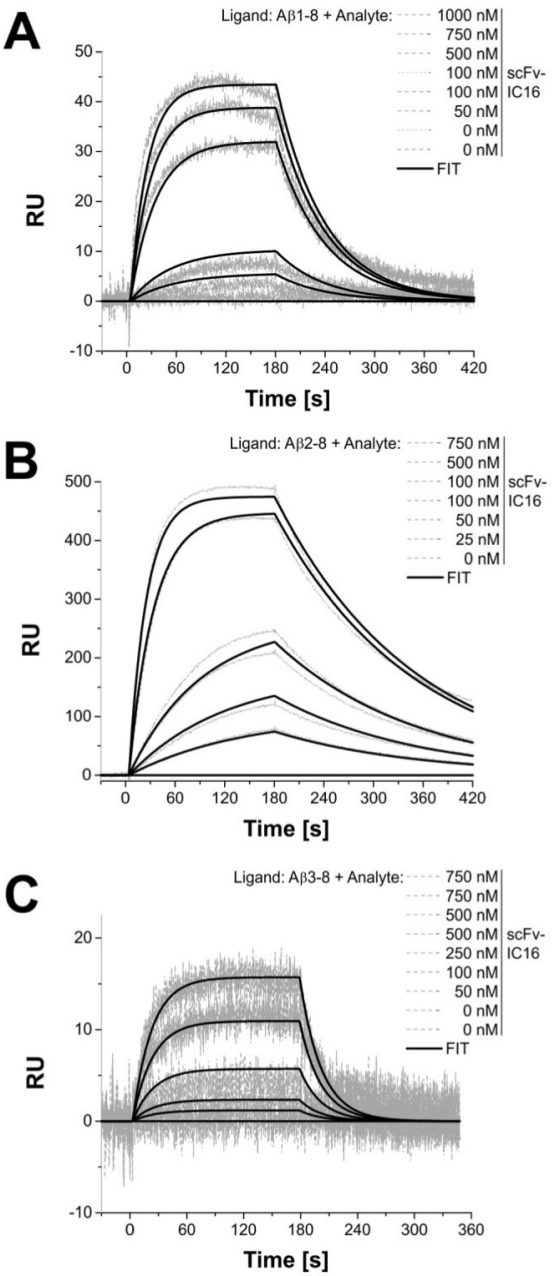

Figure 4. Analysis of the binding affinity of scFv-IC16 to immobilized Aβ peptides. (A: Aβ(1-8), B: Aβ(2-8) and C: Aβ(3-8)) using SPR. Depicted are the overlaid sensorgrams of different injection concentrations of scFv-IC16 onto an Aβ peptide coupled CM5 sensor chip. Each injection was performed for 3 min at a flow rate of 20 µl/min. Concentrations from 0 to 1000 nM were injected (see legend) in consecutive order. Dissociation was observed 2 to 4 min following an injection. Selected concentrations were injected twice as controls. The experimental data were fitted using the Langmuir 1:1 binding model (Ri = 0). [25°C; Running buffer: PBS, RmaxAβ(1-8) = 67.5; RmaxAβ(2-8) = 553; RmaxAβ(3-8) = 126].

doi:10.1371/journal.pone.0059820.g004

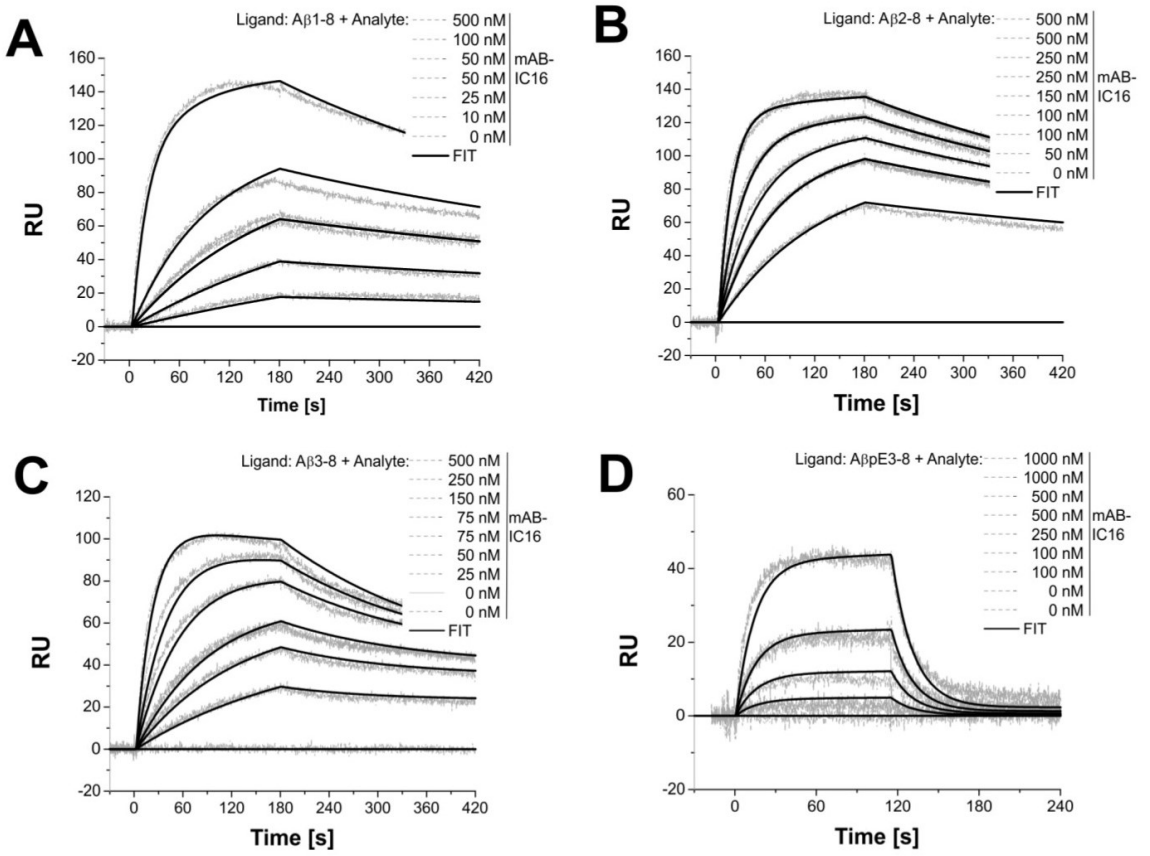

Figure 5. Analysis of the binding affinity of IC16 to immobilized Aβ peptides. (A: Aβ(1-8), B: Aβ(2-8), C: Aβ(3-8) and D: Aβ(pE3-8)) using SPR. Depicted are the overlaid sensorgrams of different injection concentrations of IC16 onto an Aβ peptide coupled CM5 sensor chip. Each injection was performed for 3 min at a flow rate of 20 µl/min. Concentrations from 0 to 1000 nM were injected (see legend) in consecutive order. Dissociation was observed for 2 to 4 min. Selected concentrations were injected twice as additional controls. The experimental data were fitted using the bivalent binding model (Ri = 0). [25°C; Running buffer: PBS; RmaxAβ(1-8) = 169; RmaxAβ(2-8) = 154; RmaxAβ(3-8) = 121; R_{max}Aβ(pE3-8) = 360].
doi:10.1371/journal.pone.0059820.g005

Discussion

Here we have characterized a novel scFv with respect to its binding specificities to different Aβ conformers and its influence on Aβ fibrilization. This scFv-IC16 was constructed from an IgG2a, designated IC16, which was raised in mouse against the antigen Aβ(1-16) and binds to Aβ(2-8) [36].

scFv-IC16 shares 87% sequence identity with of PFA1 and PFA2 (see Figure 2), two Aβ binding Fab fragments described by Gardberg et al. [33]. Especially, the three CDRs of scFv-IC16 are highly similar (see Tables 2 and 3), CDRs 1 of the heavy chain are 100% identical and CDRs 1 and CDRs 2 of the light chain are 91% and 100% identical, respectively. The striking WWDDD motif within CDR2 of PFA1 and PFA2 that recognizes the Aβ binding motif EFRH (Aβ(3-6)) [33,52] is almost completely present in scFv-IC16, too: FWDDD. Because of the high sequence homology between scFv-IC16 and PFA1, we assumed similar interactions between scFv-IC16 and Aβ as described for PFA1 and Aβ. Therefore, a homology modeling for the scFv-IC16-Aβ complex based on the X-ray structure of the Fab PFA1 and Aβ(1-8) was performed (Fig. 3). The model yielded similar binding modes for scFv-IC16 to Aβ(1-8) and PFA1 to Aβ(1-8). However, amino acid D1 of Aβ was not resolved in the X-ray structure of the Aβ(1-8)/PFA1 complex. Our homology modeling placed it in close spatial proximity with the amino acid D1 of the light chain. This close spatial proximity may generate a repulsive force and thus explains the increased affinity (K_D ~112 nM) of scFv-IC16 to Aβ(2-8) as compared to Aβ(1-8) (Tab. 3). The model furthermore offers an explanation why the K_D rises to more than 5 µM when the second amino acid A2 of Aβ is truncated. A2 forms a hydrogen bond with the backbone amide group of V99 of the heavy chain and is therefore important for a tight binding. Deletion of residues one and two and modification of Aβ E3 into pyroE3, as found in several truncated and more aggregation prone Aβ species in the diseased brain [53,54], showed a decrease in affinity and no binding was observed for scFV-IC16.

In comparison, PFA 1 shows the strongest binding to Aβ(1-40) monomers (K_D~39 nM). The binding to Aβ(2-7) is in the same order of magnitude (K_D~60 nM). Similar to scFv-IC16, the binding of PFA1 to Aβ(pE3-8) is decreased, which is reflected in the K_D of ~3 µM [33,52]. pE3 lacks the E3 sidechain carboxyl

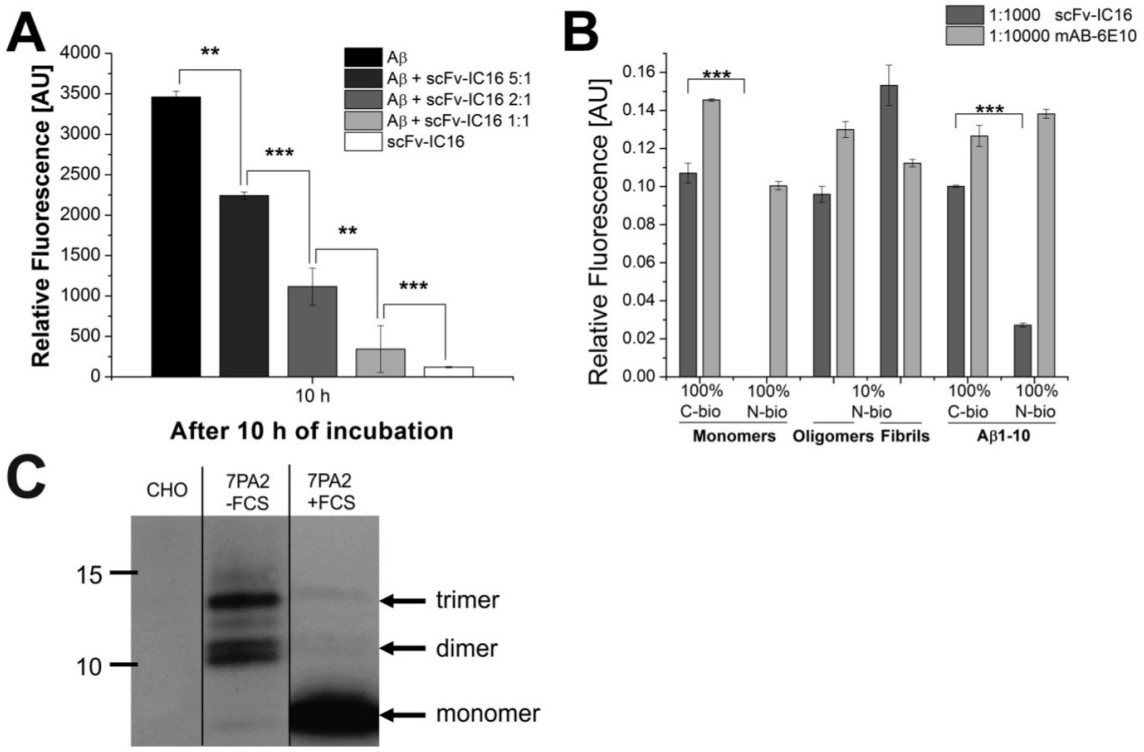

Figure 6. Inhibition of ThT positive Aβ fibril formation in presence of different scFv-IC16 concentrations. (A). ScFv-IC16 was added in concentrations of: 7.5, 3.75, 1.5 and 0 μM (positive control) to 7.5 μM Aβ(1-42) samples. Data were recorded every 30 min during 22 hours of incubation at room temperature. Depicted is the absolute fluorescence value after 10 h of incubation. Upon addition of ThT, fluorescence was measured at 490 nm in relative units (mean +/− standard deviations of results, each measurement was repeated five times). All values are corrected by background fluorescence of ThT in PBS. ScFv-IC16 only control (7.5 μM) does not show any formation of ThT positive fibrils. A statistical significant difference between the fluorescence values of Aβ only and Aβ-scFv-IC16 co incubations was calculated by student's T-test, as indicated (**: $p<0.01$; ***: $p<0.001$). Analysis of an ELISA experiment to quantify the binding specificity of scFv-IC16 to different Aβ1-42 conformers and Aβ1-10 peptides (B). 250 ng Aβ1-42 (100% N-biotinylated monomers, 100% C-terminally biotinylated monomers, 10% N-biotinylated oligomers and fibrils) and 60 ng Aβ peptides 1–10 (100% C-terminally biotinylated Aβ1-10, 100% N-terminally biotinylated Aβ1-10) were immobilized on streptavidin coated 96 well plates. 6E10 was used to monitor the immobilized amount of Aβ conformers. Similar absorption values of 6E10 to the different Aβ conformers except for 100% N-terminally biotinylated monomers, indicate similar molar amounts of immobilized Aβ regarding monomeric Aβ for monomers, oligomers and fibrils. Background absorption was subtracted from all samples. A highly significant difference in the relative fluorescence value between N-biotinylated monomers and C-biotinylated monomers, as well as between C-bio Aβ1-10 and N-bio Aβ1-10 was calculated by Student's t-test (***: $p<0.001$). N-bio = N-terminally biotinylated; C-bio = C-terminally biotinylated. Western Blot of Aβ monomers and low-n oligomers immunoprecipitated by scFv-IC16 from conditioned medium (CM) of CHO or 7PA2 cells (C). The latter were grown either in medium with or without FCS. Monomeric Aβ is stabilized by the presence of FCS, whereas low-n oligomeric Aβ is eriched in CM-FCS. No Aβ was precititated from the supernatants of CHO cells. Monomeric Aβ (CM 7Pa2+ FCS) and low-n oligomeric Aβ (CM 7PA2− FCS) were equally bound by scFv-IC16. Detection antibody: 4G8.
doi:10.1371/journal.pone.0059820.g006

group that forms two hydrogen bonds with S32(H) in the complex crystal structure.

Due to the high sequence similarity between PFA1 and scFv-IC16, similar interactions between scFv-IC16 and E3 of Aβ are also present in our modeled complex structure. Therefore, a loss of the interactions described above may lead to a loss in affinity, so that an interaction between scFv-IC16 and Aβ(pE3-8) could not be detected.

Altogether, the binding of scFv-IC16 to the Aβ fragments is weaker in comparison to PFA1. This may be due to small differences in the binding pocket like the D108V replacement (Fig. 3), but also to the fact that PFA1 is a Fab fragment, consisting of the variable and one constant domain of the heavy chain and the variable and the constant domain of the light chain. The two constant domains may provide more stability for the binding pocket of PFA1 compared with the binding pocket of scFv-IC16, because its two variable domains are connected only via a peptide linker lacking the stability of the two constant domains.

In a series of ELISA experiments, the specificity of scFv-IC16 to different conformers of Aβ, monomers, oligomers and fibrils, was characterized. The non-conformation specific monoclonal antibody 6E10 was used to control the relative amount of bound Aβ conformer in the wells. 6E10 was previously characterized to bind an Aβ N-terminal epitope at residues 3 to 10. Similar ELISA readouts for 6E10 and Aβ monomers, oligomers and fibrils proved that all three conformers were loaded in similar amounts into the wells. The binding of scFv-IC16 to its epitope at residues 2–8 of Aβ monomers that were immobilized using an N-terminal biotin tag was sterically hindered. As soon as the N-terminus was freely accessible, e.g. in C-terminally biotinylated Aβ monomers, scFv-

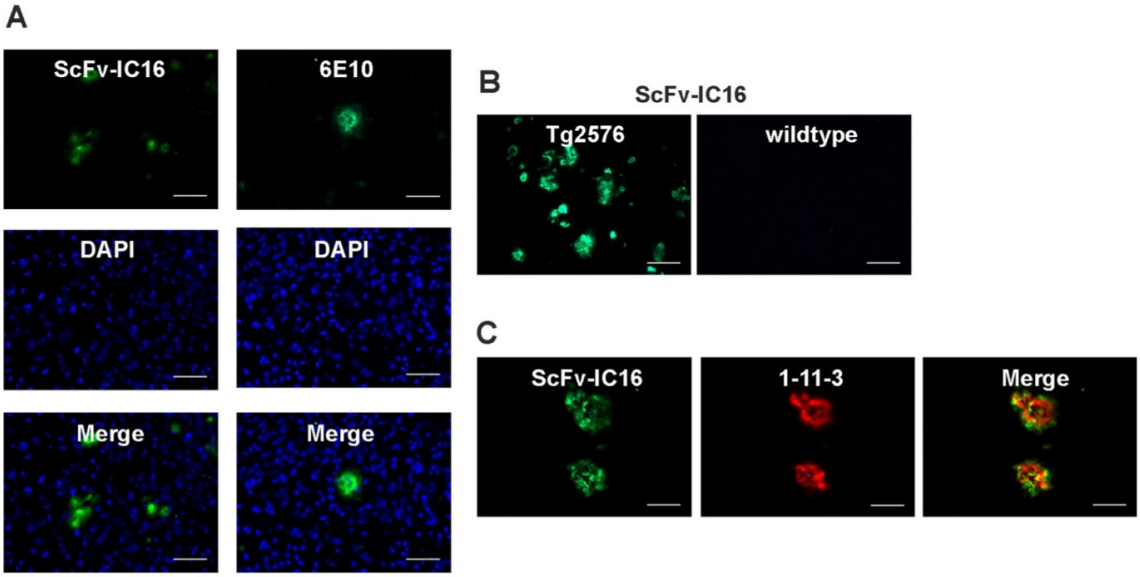

Figure 7. In vitro staining of brain sliced from transgenic 2576 AD mice using scFv-IC16, 6E10-Aβ-antibody and DAPI. (A). Pretreated deep frozen horizontal brain cryosections (20 µm thickness) from 9 months old Tg2576 mice were fixed in 4% paraformaldehyde, treated with 70%formic acid and either incubated with scFv-IC16 in a concentration of 400 nM or 6E10 in a concentration of 33 nM. As scFv-IC16 is fused with a His tag, the respective sections were incubated with Penta-His Mouse antibody. Detection was performed using goat anti mouse-Alexa488 using a fluorescent microscope (Leica LMD6000. Excitation Range: UV; blue; green. Excitation Filter: Bp 420/30; Bp 495/15; Bp 570/20) with camera (Leica DFC 310 FX). Images were processed with LAS software (Leica Application Suite, V.4.0.0) and ImageJ (1.45 s). Scale bar: 50 µm. B: In vitro staining of brain sliced from transgenic 2576 AD mice using scFv-IC16 and a respective wildtype control mouse. Scale bar:100 µm. C: Co-staining of brain sliced from transgenic 2576 AD mice using scFv-IC16 and anti Aβ(1-42) 1-11-3. As secondary antibodies, a mix of goat anti mouse-Alexa488 and goat anti rabbit-Alexa-568 was used. Scale bar: 50 µm.
doi:10.1371/journal.pone.0059820.g007

IC16 bound Aβ monomers with the same affinity as oligomers, as judged by the ELISA results. A slightly higher ELISA signal was detected for the binding to Aβ fibrils. Given the fact that scFv-IC16 binds to residues 2–8 of the N-terminus of Aβ, specificity for a special Aβ conformer was not expected. In aggregated Aβ conformers, the N-terminus of Aβ (Aβ(1-9)) was described to be disordered and accessible, whereas residues 10–22 and 30–40 adopt a β-strand conformation and are involved in fibrilization [55]. As both, scFv-IC16 and 6E10, bind to the N-terminus of Aβ, a similar binding pattern after usage for ex-vivo plaque staining in AD transgenic mice was expected. A significantly higher concentration of scFv-IC16 was needed to perform proper plaque staining in comparison to the monoclonal antibody 6E10. The need of higher amounts of protein, however, can be balanced by the fact that the scFv can be expressed in *E. coli* and produced in reasonable amounts at low costs. An interesting option could also be to enhance the affinity of scFv-IC16 to Aβ by rational design or directed evolution methods. In conclusion, scFv-IC16 has several interesting features. It can be produced recombinantly, a fact that also provides possibilities for sequence optimization. scFv-IC16 prevents the formation of ThT positive Aβ(1-42) fibrils. It recognizes all conformers of Aβ as it binds to a linear N-terminal epitope. Furthermore, it is suitable as a molecular probe, which was demonstrated by ex vivo plaque staining in brain slices of AD transgenic mice. Therefore, scFv-IC16 is interesting for therapeutic, imaging and mechanistic studies.

Author Contributions

Conceived and designed the experiments: SD AMS HS CK SAF DW. Performed the experiments: SD AMS NJ YC MW. Analyzed the data: SD AMS NJ HS CK SAF DW. Wrote the paper: SD SAF DW.

References

1. Brookmeyer R, Johnson E, Ziegler-Graham K, Arrighi HM (2007) Forecasting the global burden of Alzheimer's disease. Alzheimers & Dementia 3: 186–191.
2. Citron M (2010) Alzheimer's disease: strategies for disease modification. Nat Rev Drug Discov 9: 387–398.
3. Haass C, Selkoe DJ (1993) Cellular processing of beta-amyloid precursor protein and the genesis of amyloid beta-peptide. Cell 75: 1039–1042.
4. Kang J, Lemaire HG, Unterbeck A, Salbaum JM, Masters CL, et al. (1987) The precursor of Alzheimer's disease amyloid A4 protein resembles a cell-surface receptor. Nature 325: 733–736.
5. Weidemann A, Konig G, Bunke D, Fischer P, Salbaum JM, et al. (1989) Identification, biogenesis, and localization of precursors of Alzheimer's disease A4 amyloid protein. Cell 57: 115–126.
6. Puzzo D, Arancio O (2012) Amyloid-beta Peptide: Dr. Jekyll or Mr. Hyde? J Alzheimers Dis.
7. Hardy JA, Higgins GA (1992) Alzheimer's disease: the amyloid cascade hypothesis. Science 256: 184–185.
8. Selkoe DJ (1991) The molecular pathology of Alzheimer's disease. Neuron 6: 487–498.
9. Finder VH, Glockshuber R (2007) Amyloid-beta aggregation. Neurodegener Dis 4: 13–27.
10. Haass C, Selkoe DJ (2007) Soluble protein oligomers in neurodegeneration: lessons from the Alzheimer's amyloid beta-peptide. Nat Rev Mol Cell Biol 8: 101–112.
11. Lambert MP, Barlow AK, Chromy BA, Edwards C, Freed R, et al. (1998) Diffusible, nonfibrillar ligands derived from Abeta1–42 are potent central nervous system neurotoxins. Proc Natl Acad Sci U S A 95: 6448–6453.
12. Shankar GM, Bloodgood BL, Townsend M, Walsh DM, Selkoe DJ, et al. (2007) Natural oligomers of the Alzheimer amyloid-beta protein induce reversible

synapse loss by modulating an NMDA-type glutamate receptor-dependent signaling pathway. J Neurosci 27: 2866–2875.
13. Walsh DM, Selkoe DJ (2007) A beta oligomers - a decade of discovery. J Neurochem 101: 1172–1184.
14. Bard F, Cannon C, Barbour R, Burke RL, Games D, et al. (2000) Peripherally administered antibodies against amyloid beta-peptide enter the central nervous system and reduce pathology in a mouse model of Alzheimer disease. Nat Med 6: 916–919.
15. DeMattos RB, Bales KR, Cummins DJ, Dodart JC, Paul SM, et al. (2001) Peripheral anti-A beta antibody alters CNS and plasma A beta clearance and decreases brain A beta burden in a mouse model of Alzheimer's disease. Proc Natl Acad Sci U S A 98: 8850–8855.
16. Lee EB, Leng LZ, Zhang B, Kwong L, Trojanowski JQ, et al. (2006) Targeting amyloid-beta peptide (Abeta) oligomers by passive immunization with a conformation-selective monoclonal antibody improves learning and memory in Abeta precursor protein (APP) transgenic mice. J Biol Chem 281: 4292–4299.
17. Wilcock DM, Rojiani A, Rosenthal A, Levkowitz G, Subbarao S, et al. (2004) Passive amyloid immunotherapy clears amyloid and transiently activates microglia in a transgenic mouse model of amyloid deposition. J Neurosci 24: 6144–6151.
18. Haas C (2012) Strategies, development, and pitfalls of therapeutic options for Alzheimer's disease. J Alzheimers Dis 28: 241–281.
19. Callaway E (2012) Alzheimer's drugs take a new tack. Nature 489: 13–14.
20. Nordberg A (2007) Amyloid imaging in Alzheimer's disease. Curr Opin Neurol 20: 398–402.
21. Nordberg A (2008) Amyloid imaging in Alzheimer's disease. Neuropsychologia 46: 1636–1641.
22. Valadon P, Garnett JD, Testa JE, Bauerle M, Oh P, et al. (2006) Screening phage display libraries for organ-specific vascular immunotargeting in vivo. Proc Natl Acad Sci U S A 103: 407–412.
23. Lichtlen P, Mohajeri MH (2008) Antibody-based approaches in Alzheimer's research: safety, pharmacokinetics, metabolism, and analytical tools. J Neurochem 104: 859–874.
24. Holliger P, Hudson PJ (2005) Engineered antibody fragments and the rise of single domains. Nat Biotechnol 23: 1126–1136.
25. Wang YJ, Zhou HD, Zhou XF (2010) Modified immunotherapies against Alzheimer's disease: toward safer and effective amyloid clearance. J Alzheimers Dis 21: 1065–1075.
26. Liu R, Yuan B, Emadi S, Zameer A, Schulz P, et al. (2004) Single chain variable fragments against beta-amyloid (Abeta) can inhibit Abeta aggregation and prevent abeta-induced neurotoxicity. Biochemistry 43: 6959–6967.
27. Robert R, Dolezal O, Waddington L, Hattarki MK, Cappai R, et al. (2009) Engineered antibody intervention strategies for Alzheimer's disease and related dementias by targeting amyloid and toxic oligomers. Protein Eng Des Sel 22: 199–208.
28. Solorzano-Vargas RS, Vasilevko V, Acero G, Ugen KE, Martinez R, et al. (2008) Epitope mapping and neuroprotective properties of a human single chain FV antibody that binds an internal epitope of amyloid-beta 1–42. Mol Immunol 45: 881–886.
29. Cai J, Wang S, Zhong Y, Cheng J, Ji Z, et al. (2003) Screening and characterization of human single-chain Fv antibody against beta-amyloid peptide 40. Neuroreport 14: 265–268.
30. Wang YJ, Gao CY, Yang M, Liu XH, Sun Y, et al. (2010) Intramuscular delivery of a single chain antibody gene prevents brain Abeta deposition and cognitive impairment in a mouse model of Alzheimer's disease. Brain, behavior, and immunity 24: 1281–1293.
31. Cattepoel S, Hanenberg M, Kulic L, Nitsch RM (2011) Chronic intranasal treatment with an anti-Abeta(30–42) scFv antibody ameliorates amyloid pathology in a transgenic mouse model of Alzheimer's disease. PLoS One 6: e18296.
32. Eswar N, Eramian D, Webb B, Shen MY, Sali A (2008) Protein structure modeling with MODELLER. Methods Mol Biol 426: 145–159.
33. Gardberg AS, Dice LT, Ou S, Rich RL, Helmbrecht E, et al. (2007) Molecular basis for passive immunotherapy of Alzheimer's disease. Proc Natl Acad Sci U S A 104: 15659–15664.
34. Hooft RW, Vriend G, Sander C, Abola EE (1996) Errors in protein structures. Nature 381: 272.
35. Wallace AC, Laskowski RA, Thornton JM (1995) LIGPLOT: a program to generate schematic diagrams of protein-ligand interactions. Protein Eng 8: 127–134.
36. Muller-Schiffmann A, Marz-Berberich J, Andreyeva A, Ronicke R, Bartnik D, et al. (2010) Combining Independent Drug Classes into Superior, Synergistically Acting Hybrid Molecules. Angew Chem Int Ed Engl 49: 8743–8746.
37. Bueler H, Fischer M, Lang Y, Bluethmann H, Lipp HP, et al. (1992) Normal development and behaviour of mice lacking the neuronal cell-surface PrP protein. Nature 356: 577–582.
38. Huston JS, Levinson D, Mudgett-Hunter M, Tai MS, Novotny J, et al. (1988) Protein engineering of antibody binding sites: recovery of specific activity in an anti-digoxin single-chain Fv analogue produced in Escherichia coli. Proc Natl Acad Sci U S A85: 5879–5883.
39. Leliveld SR, Stitz L, Korth C (2008) Expansion of the octarepeat domain alters the misfolding pathway but not the folding pathway of the prion protein. Biochemistry 47: 6267–6278.
40. Schonfeld D, Matschiner G, Chatwell L, Trentmann S, Gille H, et al. (2009) An engineered lipocalin specific for CTLA-4 reveals a combining site with structural and conformational features similar to antibodies. Proc Natl Acad Sci U S A 106: 8198–8203.
41. Johansson AS, Berglind-Dehlin F, Karlsson G, Edwards K, Gellerfors P, et al. (2006) Physiochemical characterization of the Alzheimer's disease-related peptides A beta 1–42Arctic and A beta 1–42wt. FEBS J 273: 2618–2630.
42. Ida N, Hartmann T, Pantel J, Schroder J, Zerfass R, et al. (1996) Analysis of heterogeneous A4 peptides in human cerebrospinal fluid and blood by a newly developed sensitive Western blot assay. J Biol Chem 271: 22908–22914.
43. Kim S, Cheung LH, Zhang W, Rosenblum MG (2007) Improved expression of a soluble single chain antibody fusion protein containing tumor necrosis factor in Escherichia coli. Appl Microbiol Biotechnol 77: 99–106.
44. Muller-Schiffmann A, Petsch B, Leliveld SR, Muyrers J, Salwierz A, et al. (2009) Complementarity determining regions of an anti-prion protein scFv fragment orchestrate conformation specificity and antiprion activity. Mol Immunol 46: 532–540.
45. Hsu E SL (1992) Primary structure of immunoglobulins through evolution. Curr Opin Struct Biol 2: 422–431.
46. LeVine H 3rd (1993) Thioflavine T interaction with synthetic Alzheimer's disease beta-amyloid peptides: detection of amyloid aggregation in solution. Protein Scity 2: 404–410.
47. Tycko R (2006) Molecular structure of amyloid fibrils: insights from solid-state NMR. Q Rev Biophys 39: 1–55.
48. Klaver AC, Finke JM, Digambaranath J, Balasubramaniam M, Loeffler DA (2010) Antibody concentrations to Abeta1–42 monomer and soluble oligomers in untreated and antibody-antigen-dissociated intravenous immunoglobulin preparations. Int Immunopharmacol 10: 115–119.
49. Klaver AC, Patrias LM, Coffey MP, Finke JM, Loeffler DA (2010) Measurement of anti-Abeta1–42 antibodies in intravenous immunoglobulin with indirect ELISA: the problem of nonspecific binding. J Neurosci Methods 187: 263–269.
50. Sohn JH, So JO, Kim H, Nam EJ, Ha HJ, et al. (2007) Reduced serum level of antibodies against amyloid beta peptide is associated with aging in Tg2576 mice. Biochem Biophys Res Commun 361: 800–804.
51. Podlisny MB, Ostaszewski BL, Squazzo SL, Koo EH, Rydell RE, et al. (1995) Aggregation of secreted amyloid beta-protein into sodium dodecyl sulfate-stable oligomers in cell culture. J Biol Chem 270: 9564–9570.
52. Gardberg A, Dice L, Pridgen K, Ko J, Patterson P, et al. (2009) Structures of Abeta-related peptide–monoclonal antibody complexes. Biochemistry 48: 5210–5217.
53. Saido TC, Yamao-Harigaya W, Iwatsubo T, Kawashima S (1996) Amino- and carboxyl-terminal heterogeneity of beta-amyloid peptides deposited in human brain. Neurosci Lett 215: 173–176.
54. Schlenzig D, Manhart S, Cinar Y, Kleinschmidt M, Hause G, et al. (2009) Pyroglutamate formation influences solubility and amyloidogenicity of amyloid peptides. Biochemistry 48: 7072–7078.
55. Tycko R (2006) Molecular structure of amyloid fibrils: insights from solid-state NMR. Quarterly reviews of biophysics 39: 1–55.
56. Laemmli UK (1970) Cleavage of structural proteins during the assembly of the head of bacteriophage T4. Nature 227: 680–685.

3. Syntheses and conclusion

As a matter of fact, neither causal therapy nor accurate and reliable diagnostic methods have been found in the fight against Alzheimer's disease so far. Only recently, some research groups focus on the oligomeric forms of Aβ, the key factors of the modified Aβ cascade theory that are now considered as the neurotoxic species in the AD pathology. Years ago already, our research group has identified several Aβ binding D-peptides have been identified from mirror-image phage display, which are able to prevent the formation of the toxic forms of Aβ. The main theme of this doctoral thesis is to characterize those Aβ binding D-peptides by *in vitro* and *in vivo* experiments with mouse models, as well as to explore their diagnostic suitability for AD.

3.1 Preclinical pharmacokinetic studies of D-peptides

Pharmacokinetics describe how concentration of a drug changes over time, thus it emphasizes the selective and sensitive measurement of drug concentration in complex biological matrix, such as plasma or organ homogenate. The typical bioanalytical methods involve sample extraction with organic solvents and LC/MS or LC/MS/MS separation and detection of drug molecules. However, the extreme hydrophilicity of our D-peptides strongly challenges those standard analytical methods (Publication 2.1). Tritium labelling of D-peptides provides a reasonable solution due to the ease of sample preparation and detection, as well as the minimal modification to the labelled molecules. Because it is an indirect measurement of target molecules based on the assumption that the measured radioactivity represents their non-metabolised forms, any labelled metabolites or impurities for example, can influence their pharmacokinetic results, thus special attention should be paid on the purity (by production) and stability (autoradiolysis and proteolysis) of labelled substances.

	Sequence	MW
D3	H-rprtrlhthrnr-NH_2	1.6 kDa
RD2	H-ptlhthn<u>rrrrr</u>-NH_2	1.6 kDa
D3D3	H-rprtrlhthrnrrprtrlhthrnr-NH_2	3.2 kDa
RD2D3	H-ptlhthn<u>rrrrr</u>rprtrlhthrnr-NH_2	3.2 kDa

Tab. 1. Amino acid sequences of four D-peptides studied in this thesis. The arginine residues in RD2 are consecutively rearranged based on rational design.

Here, we firstly described a systematic pharmacokinetic analysis of the all D-enantiomeric peptide D3 in mice, which is, to the best of our knowledge, the first comprehensive preclinical pharmacokinetic study of a peptide consisting solely of D-enantiomeric amino

acid residues in general and in particular for such a D-peptide developed for the treatment of Alzheimer's disease (Publication 2.2). Then, we investigated the PK profile of another D-peptide RD2, containing the same D amino acid residues but in a rationally reordered sequence with five consecutive arginines at C-terminal, which has already shown enhanced properties *in vitro* and *in silico* (Publication 2.3). The rational design is to concentrate the possible Aβ binding sites which are relevant to the arrangement of arginines and to keep the rest of amino acids which might be involved in hydrophilic and/or hydrophobic interaction with Aβ oligomers [214]. Finally, the pharmacokinetic studies of tandem peptides, D3D3 and RD2D3 were performed. The idea of rationale design is that the multivalent D-peptides can be expected to target the multivalent binding sites presented on the Aβ oligomer, resulting in an increased binding efficiency and affinity. So D3 and/or RD2 are linked head-to-tail as tandem homopeptide (D3D3) and heteropeptide (RD2D3) (Publication 2.4).

For all the D-peptides mentioned here, metabolic stability was investigated through ^{3}H-labelled D-peptides incubated with plasma and organ homogenates followed by detection via thin layer chromatography. Special attention should be paid upon the resulting limitations, as the incubation time for the metabolic stability tests were generally shorter than that for the pharmacokinetic studies. Taking RD2 as an example, its metabolic stability was tested for 24 hours, while its pharmacokinetic studies lasted for 28 days. Thus, partial conversion of D-peptides into metabolites at later time points cannot be excluded. But *in vitro* stability tests using biological samples beyond 24 hours might be less meaningful, because longer incubation time may cause autolysis of enzymes within those samples leading to artefacts. And there is no reason to expect significant metabolism at later time points since not any proteolytic instability was observed at 24 hours. Therefore, the results of the stability tests proved the high protease-resistance of D-peptides, as well as validated that the measured radioactivity could represent the concentration of D-peptides in their original forms.

Individually, single D-peptides (D3 or RD2) showed similar concentration-time profiles with *i.v.* and *i.p.* (and *s.c.* with RD2) administration with the highest concentration in kidney, followed by liver and plasma, whereas oral administration resulted in significantly low concentrations in liver, kidney and plasma. Tandem D-peptides (D3D3 or RD2D3) individually, also showed similar concentration-time curves with *i.v.* and *i.p.* administration, but the highest concentration was found in liver, followed by kidney and plasma. Fig. 11 compared the concentration-time profiles of D3 and RD2D3 in kidney and liver. Diagram showed very high concentration of D3 in kidney and low concentration in liver with *i.v.* and *i.p.* administration, whereas the concentration of RD2D3 in kidney and liver were comparable. In both organs, both D-peptides showed very low concentration after oral administration (Including unpublished data from RD2D3 p.o. displayed in Fig. 12).

A global comparison of D-peptides with concentration-time profiles in brain and plasma, as well as the brain-plasma ratios are shown in Fig. 12. The pharmacokinetic parameters of D-peptides in brain and plasma, which were calculated based on non-compartmental analysis,

are listed in Tab. 2. In general, single D-peptides showed higher concentration (AUC) than tandem peptides in brain and in plasma with different administration routes; RD2 showed higher concentration than D3, and correspondently, RD2D3 showed higher concentration than D3D3. Interestingly, oral administration of all the four D-peptides respectively resulted in similar brain concentration as for the other administration routes.

Two single D-peptides showed relatively long terminal plasma half-lives with different administration routes (RD2: 58-62 hours; D3: 32-41 hours), whereas tandem D-peptides showed short terminal plasma half-lives between 0.7 and 2.7 hours, but still longer than those reported for L-enantiomeric peptides which are typically only a few minutes [215, 216]. The clearance of both tandem D-peptides from plasma were faster than that of single D-peptides (D3D3: 17.9, RD2D3: 10.2, D3: 4.6 and RD2: 1.7 ml/(min*kg)), as a reflection of their terminal plasma half-lives. The plasma terminal phase volume of distribution (Vz) and the steady state phase volume of distribution (Vss) of both single D-peptides were similar in magnitude, respectively. The clearance of RD2 was very slow, so that the concentration in central compartment (plasma) would be nearly in equilibrium with the peripheral compartments, thus its Vz (8.6 l/kg) was very close to its Vss (9.2 l/kg). D3 showed a higher Vz (11.1 l/kg) than Vss (7.6 l/kg), suggesting a higher equilibrium concentration than terminal concentration, and thus a transport of D3 due to this concentration gradient from peripheral compartments to central compartment (plasma) would be suggested. The Vss of both tandem D-peptides were similar to those of the single ones (D3D3: 13.2 and RD2D3: 7.5 l/kg), whereas their Vz were significantly smaller (D3D3: 1.2 and RD2D3: 0.7). Such low values are similar to the extracellular fluid volume (ca. 0.2-0.25 l/kg), which would suggest a poor tissue penetration or an altered tissue binding. As pharmacokinetic parameters in those studies were calculated by non-compartmental analysis (NCA), special attentions should be taken that the limitation or disadvantage of NCA may result in over- or under-estimation of certain values. As shown in the Publication 2.4, the concentration (brain and plasma) of the tandem D-peptides in the elimination phase was kept on a relative constant level, which was still several magnitudes beyond the detection limit of tritium scintillation counting. It would suggest a re-distribution of tandem D-peptides from peripheral compartments (most likely at least the kidney and liver) back into the central compartment (plasma). The brain concentration reflects the corresponding plasma concentration resulting in a relatively constant brain-plasma ratio. In some cases, the concentration at the last time point was even higher than that of its previous ones, therefore the determination of lambda_z is more or less objective and empirical. Because Vss is independent of elimination processes it is thus a more appropriate parameter than Vz in this case [217].

The brain-plasma ratios of D-peptide after 4 hours are in the range of 0.7 and 1.0. Some go even higher at longer time points, especially with tandem peptides after *i.v.* administration (Fig. 12). In the study of continuous dosing of D3 over several days using an i.p. implanted osmotic pump, the brain-plasma ratio increased with time from 0.53 at day 2 to 0.77 at day 6. As substances with a brain-plasma ratio larger than 0.3 are considered to have sufficient access to the central nervous system [218], our results suggest that all the tested D-peptides

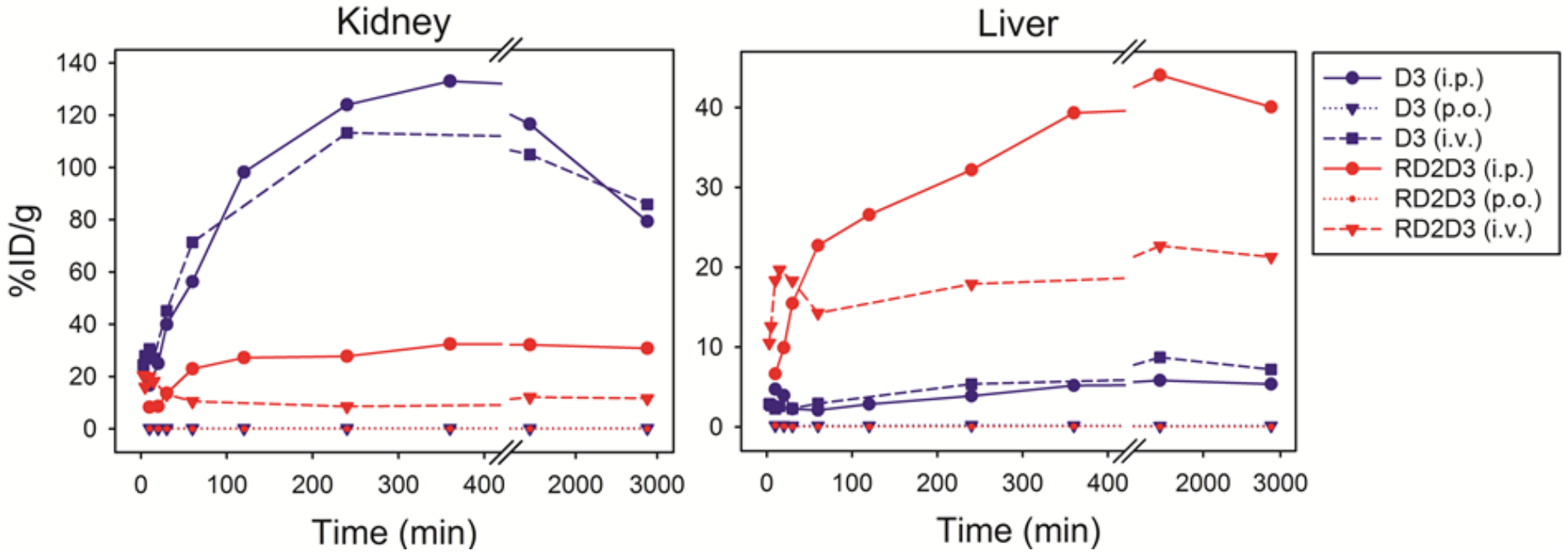

Fig. 11. Comparison of D3 and RD2D3 with concentration-time profiles in kidney and liver. The concentration is given in relative injected dose per gram organ weight (%ID/g).

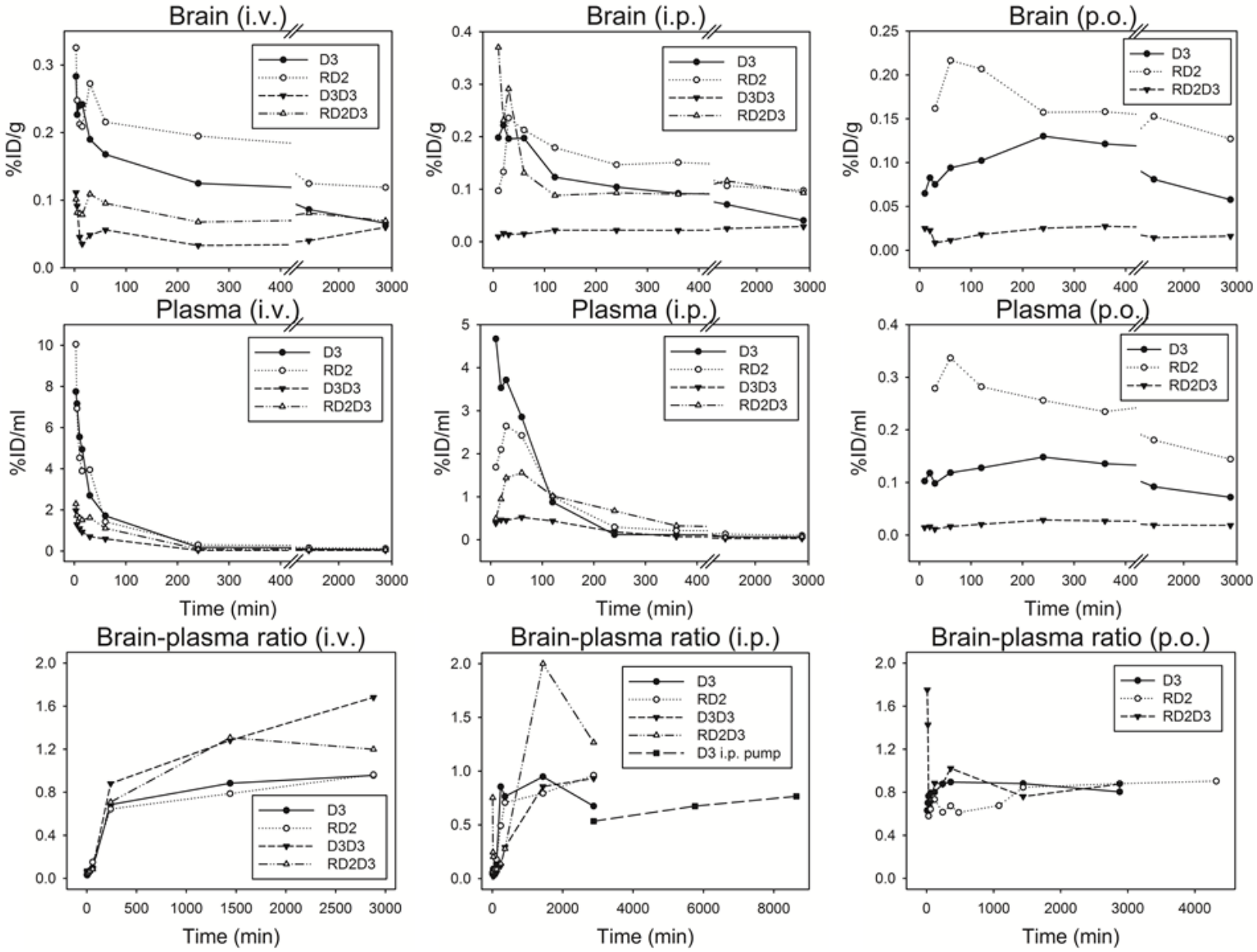

Fig. 12. A global comparison of D-peptides with concentration-time profiles in brain and plasma, as well as the brain-plasma ratios. The concentration is given in relative injected dose per gram organ weight (%ID/g) for brain and per ml (%ID/ml) for plasma. The last time point of plasma and brain was uniformed to be 2880 min for the convenience of comparison.

Plasma

		D3			RD2				D3D3		RD2D3	
Parameter	Units	i.v.	i.p.	p.o.	i.v.	i.p.	s.c.	p.o.	i.v.	i.p.	i.v.	i.p.
Dose (D)	mg/kg	3.5	10.5	10.5	3.3	10	10	10	3.3	10	3.3	10
tmax	min	3	10	240	3	30	30	60	3	60	3	60
Cmax/D	(µg/ml)/(mg/kg)	2.35	1.4	0.04	3.04	0.79	0.98	0.09	0.54	0.16	0.58	0.47
AUC0-last	mg/ml*min	0.7	1.8	1.1	2.0	4.5	5.4	4.5	0.2	0.6	0.3	1.8
MRT0-last	h	9.1	8.8	28.6	84.8	81.4	80.9	86.3	11.9	11.6	11.9	10
λz	min-1	0.00036	0.00028	0.00028	0.0002	0.00019	0.00019	0.0002	0.0155	0.0075	0.0137	0.0043
t1/2	h	32	41	41	59	62	60	58	0.7	1.6	0.9	2.7
AUC0-inf	mg/ml*min	0.9	2.4	1.5	2.0	4.6	5.4	4.5	0.2	0.6	0.3	1.9
MRT0-inf	h	27.6	35.1	57.2	91.4	86.4	84.6	90.8	12.3	12.3	12.3	11.1
Vz	l/kg	11.1	15.6	24	8.6	9.0	8.8	8.5	1.2	2.4	0.7	2.4
Cl	ml/(min*kg)	4.6			1.7				17.9		10.2	
Vss	l/kg	7.6			9.2				13.2		7.5	
FAUC-last	%		92	58		77	91	77		110		187

Brain

		D3			RD2				D3D3		RD2D3	
Parameter	Units	i.v.	i.p.	p.o.	i.v.	i.p.	s.c.	p.o.	i.v.	i.p.	i.v.	i.p.
Dose (D)	mg/kg	3.5	10.5	10.5	3.3	10	10	10	3.3	10	3.3	10
tmax	min	3	20	240	3	30	20	60	3	2880	30	10
Cmax/D	(µg/g)/(mg/kg)	0.09	0.07	0.04	0.06	0.06	0.06	0.06	0.03	0.01	0.03	0.11
AUC0-last	mg/g*min	0.3	0.6	0.9	1.5	3.4	4.5	4.5	0.1	0.2	0.2	0.9
MRT0-last	h	19.6	18.5	28.2	128.4	111.9	116.1	100.3	26.4	25.8	23.9	23.4

Tab. 2. Calculated pharmacokinetic parameters of D-enantiomeric peptides in mouse plasma and brain for different administration routes. Clear fields are not applicable for this respective administration route. For abbreviations please refer to the abbreviation sections.

efficiently overcome the blood-brain barrier. The BBB penetration was observed with cell-penetrating peptides including arginine-rich peptides (also discussed in the next Chapter 3.2). Studies showed a minimum of six consecutive arginines were enough to cause transduction [219, 220], and the flexibility in the position of arginines within a given peptide sequence didn't affect its transduction efficiency [220]. In our study, five arginines are relatively homogeneously distributed in D3, while re-arranged in a consecutive matter in RD2; tandem peptides have 10 arginines and RD2D3 even has six consecutive arginines (five from RD2 and one from D3) in sequence. In the pharmacokinetic studies, RD2 and RD2D3 showed higher brain concentrations than those of D3 and D3D3, respectively, but tandem peptides showed in general lower brain concentrations than single ones due to their likewise lower plasma concentrations. Thus the transduction potency should also associate with the number of arginines per length of the sequence, namely the relative abundance, and brain-plasma ratio should represent the transduction at BBB more suitable than brain concentration, as the application of arginine-rich peptides also influence the cellular uptake in other organs.

Favourable bioavailabilities were observed with all the D-peptides, especially by oral administration with single form of D-peptides, in spite of only a small peptide portion being absorbed via the enteric tract. Bioavailabilities are relatively high in comparison to those of L-peptide drugs, which were described to be less than 1% without delivery enhancement [221-223]. Low concentrations of D-peptides as found in kidney and liver after oral administration are desirable because this lowers the risk of possible intoxication of important organs.

The prediction of plasma protein binding based on binding to HSA and AGP (Tab. 3) showed single D-peptides with favourable plasma unbound fractions. Studies indicated that only the minority of examined drugs developed for the central nervous system exhibit free plasma fractions above 10 % [224]. The tandem D-peptides, however, showed very small unbound fractions, which is in agreement to the low brain concentration of tandem D-peptides, because it is believed that only unbound substance can cross cellular membranes. But this seems to be controversial to their relatively high brain-plasma ratios. One possible explanation would be, that an increased tissue binding, especially in liver, greatly reduced the effective concentration of tandem D-peptides in blood and subsequently in brain.

	D3	RD2	D3D3	RD2D3
fu (%)	8.00	11.50	0.16	0.20

Tab. 3. Free fraction of D-peptides in plasma calculated by in vitro plasma protein binding assay. fu: predicted free or unbound fraction of tested substance in plasma.

The tandem D-peptides, for example D3D3 showed significantly stronger Aβ oligomer elimination than its monomer D3 [214], yet this rational design resulted in unfavourable pharmacokinetics. Thus this example indicates the importance to balance the *in vitro* therapeutic efficiency and the *in vivo* pharmacokinetic properties.

These results demonstrated that 1) the sequence order (when consisted of identical amino acid residues) and 2) the molecular weight and structure (single v/s tandem) of D-peptides significantly influence their pharmacokinetic properties.

3.2 Distribution of D-peptides to and within the brain

D-peptides, to be used for diagnosis and treatment of Alzheimer's disease, need to be delivered to the brain as discussed in Chapter 1.4. Unlike some CNS drugs, especially peptide-based drugs, which need extra modifications to enhance their brain delivery, the here used D-peptides already showed relatively high brain-plasma ratios in the preclinical pharmacokinetic studies suggesting the capability to penetrate the blood-brain barrier and distribution in the brain. The BBB penetrating property of the D-peptides was suggested owing to their similarity to the ARM of HIV-1 Tat protein. However, due to the limitation of pharmacokinetic experimental settings, considerations should be taken, as radioactivity from CSF remaining in ventricles or from blood remaining in cerebrovasculature may contribute to the radioactivity detected in whole brain in some extent, which can result in an over-estimation of the brain concentration. Thus further studies were needed to provide a convincing evidence showing D-peptides in brain parenchyma after administration. By investigation of D3 concentrations in CSF, brain and plasma, as well as exclusion of D3 binding to normal cerebral blood vessels, a conclusion could be drawn, that the D3 concentration detected in the brain likely represents its real concentration in the brain parenchyma (Publication 2.5). Furthermore, the *in vivo* BBB penetration, as well as the Aβ binding ability of D3, were proven by the parenchymal Aβ plaque labelling after oral administration of FAM-D3 in AD transgenic mice. Based on the results of pharmacokinetic studies, it is reasonable to transfer this BBB penetration ability also to other D-peptides, at least to RD2.

However, unlike tritium labelling, fluorescein labelling (as FAM or FITC) might most probably influence the properties of conjugated molecules through introducing this bulky and predominantly hydrophobic structure. Crystal structures of FITC-protein complexes showed that the xanthenonyl ring system of FITC is accommodated in a tight aromatic slot, which is associated with modification of binding sites and affinity of the original molecules [225]. Furthermore, labelling of middle-sized molecules, like peptides, with fluorophores, may also influence their uptake mechanism, intracellular distribution, and cytotoxicity [226, 227]. In a previous study, fluorescein was titrated with Aβ (1-42) in order to rule out fluorescein mediated binding of fluorescently labelled D-peptides to Aβ. It could be demonstrated that the fluorescein fluorescence signal was independent of the Aβ concentration [228]. Consideration should be taken, as the observed BBB penetration of FAM-D3 in APPSwe/PSEN1ΔE9 transgenic mice might also be a result of generally impaired BBB structure. A greater breakdown of the BBB was observed in AD patients in comparison to neurologically healthy controls [229, 230], but no significant alterations in BBB permeability of APPSwe/PSEN1ΔE9 transgenic mice was observed in our laboratory, as well as in other's [231].

The exact BBB penetration mechanism of D-peptides is unknown, as discussed in Publication 2.5, but the guanidinium structure in those arginine-rich D-peptides and the relative abundance of arginines within the peptide might be the decisive factors of their membrane

penetration property [232, 233]. Studies on how the arginine-rich peptides pass the membrane bring controversial results, but there is a clear consensus that it initiates with the electrostatic interactions between cationic sequences and negatively charged glycoproteins on the cellular surface.

After intra-hippocampal injection of fluorescently labelled D-peptides (Publication 2.6), intensive fluorescence was found in certain neurons (axon and soma). The distribution of fluorescently labelled D-peptides in neural fibres at the injection site, especially in the fibres in corpus callosum, could be explained as entrance of axons through damaged places, or as a result of membrane penetration. Remarkably, none of the fluorescently labelled D-peptides was taken up by astrocytes or microglia, which is in agreement with previous observations [234]. All the tested substances, namely fluorescently labelled D-peptides, FITC-Aβ and FITC alone showed Aβ plaque labelling, but only fluorescently labelled D-peptides demonstrated a retrograde axonal transport in both wild type and AD transgenic mouse models. Moreover, a specific retrograde transport in the perforant pathway was found in both AD transgenic mouse models (APPSwe/PSEN1ΔE9 and Tg-SwDI). Significant accumulation of fluorescently labelled D-peptides in the layer II cells of entorhinal cortex was observed. Fluorescence was probably located in lysosomes or late endosomes, whereas those cells showed no intracellular Aβ stained by the W0-2 antibody. The exact mechanism is still unknown, but a co-transport of the fluorescently labelled D-peptides together with certain intracellular Aβ species was suggested. Intracellular APP or Aβ fibrils can be excluded as the main species, as they can be recognized by W0-2 antibody. A previous study indicated that the s-value of Aβ oligomers which can be eliminated by D3 was between 5 to 7, corresponding to a molecular weight from 66 to 150 kDa [235]. Whereas the W0-2 antibody can recognize Aβ oligomers of approx. 45 kDa on western blot of human Alzheimer´s disease brain lysate. This detection difference may explain why there was no co-localization of fluorescently labelled D-peptides and W0-2 in layer II cells of entorhinal cortex, thus the result suggested that fluorescently labelled D-peptides bind to middle to high molecular weight Aβ oligomers, which are then taken up by lysosomes (or endosomes) and transported retrogradely to the neuronal soma.

A difference in transport pattern after intra-hippocampal injection between FAM-D3 and FITC-D3D3 was observed, especially the transport of FITC-D3D3 within axons seemed to be significantly faster than that of FAM-D3. Considering the different performance in the pharmacokinetic studies, it can be concluded that altering the sequence of D3 by rational design dramatically alters its physical, chemical and biological property. As mentioned in Chapter 3.1, whether the rational design really results in an improvement of therapeutic or diagnostic performance under complex biological conditions needs to be further elucidated in the future.

Another Aβ binding substance identified through antibody-based strategy, namely the Aβ binding single-chain variable fragments (scFvs) derived from an Aβ binding IgG recognizing the N-terminal region of Aβ (Aβ(1-8)), was also investigated in this dissertation, as described in Publication 2.7.

3.3 Conclusion

This doctoral thesis has sought to explore the distribution of Aβ binding D-peptides in the body *in vivo*, as well as their entrance into the brain and distribution within the brain of mouse models in particular. In the preclinical pharmacokinetic studies, all the tested D-peptides showed high proteolytic resistance. The single peptides exhibited more favourable pharmacokinetic properties than the tandem peptides, as D3 and RD2 demonstrated long terminal half-lives, high oral bioavailability and high drug exposure to the brain. It is therefore concluded that the sequence order of the amino acid residues has a considerable impact on pharmacokinetic properties of the peptide. However, the poor pharmacokinetics of the tandem peptides may not be accompanied with poor pharmacodynamics, which could possibly be outweighed by their higher Aβ binding efficiency. Among the tested D-peptides, RD2 demonstrated improved pharmacokinetic properties and thus might be a more suitable candidate for the treatment of AD providing that it has already shown encouraging therapeutic effects in the previous *in vivo* studies. However, it needs to be clearly stated that all obtained pharmacokinetic parameters are based on the assumption that the measured radioactivity represents the non-metabolised D-peptides, and those parameters are obtained with non-compartmental analysis which has its limitation under certain conditions. Nevertheless, the preclinical pharmacokinetic studies provide important information that helps to characterize D-peptides within the body, as well as to guide further research during their drug development, and to the best of our knowledge, those are the first pharmacokinetic studies of peptides consisting solely of D-enantiomeric amino acid residues in rodents.

The lead molecule of D-peptides, D3, as well as fluorescently labelled D3 readily penetrated the BBB and specifically bound to Aβ plaques after systemic administration. Furthermore, a selective retrograde transport of fluorescently labelled D3 and D3D3 in the perforant pathway in AD transgenic mouse models was observed. Those evidences accumulated in this dissertation strongly support the potential of D-peptides in the diagnostic aspect, as well as to investigate pathological changes in the neural pathways in early AD. Being middle-sized molecules of synthetic origin, D-peptides allow easy chemical modifications e.g. radioactive or nonradioactive isotope labelling for detection purposes with PET and/or MRT.

Taken together, results strongly suggest the Aβ binding D-peptides as promising substances for diagnostic purpose and therapeutic intervention against Alzheimer's disease.

4. Perspectives

The current pharmacokinetic studies were performed only with wild type mice; it might be interesting to investigate further the fate of D-peptides in AD transgenic mice. In order to gain a global view of the distribution within the body, a quantitative whole-body autoradiography (QWBA) of tested animals is recommended. Modification of D-peptides based on their pharmacokinetics is desired, for example higher oral bioavailability could be achieved by drug formulation. Especially for tandem peptides, modifications should aim to improve their brain delivery and plasma half-lives. As RD2 showed high bioavailability with *s.c.* administration, such administration routes that are commonly accepted in the clinic, e.g. *s.c.*, nasal and intramuscular (*i.m.*) should also be explored with other D-peptides. After obtaining basic pharmacokinetic parameters through a non-compartmental analysis, more detailed analysis using compartmental or physiologically based pharmacokinetic (PBPK) models could be performed.

The mechanism of BBB penetration (or plasma membrane transduction) and the transport of D-peptides within the brain need to be further investigated. Questions need to be answered, like the cellular uptake mechanism (interaction with cellular surface proteins); as membrane-penetrating peptides, are they located in plasma or cellular compartments (endosomes, lysosomes or mitochondria); whether D-peptides are transported alone or with other substances, in case of the latter, what kind of substances are co-transported with D-peptides; why does the perforant pathway show specific retrograde transport of D-peptides in AD mouse models, and so on. Thus experiments with neuronal cell culture or organ culture would be helpful.

Radiolabelling of D-peptides with tracers other than tritium could also be tested for diagnostic purpose. Conjugation of D-peptides with ^{11}C, ^{18}F or metastable nuclear isomer of technetium-99 (^{99m}Tc) could provide promising radioactive tracers for diagnostic imaging, e.g. positron emission tomography (PET) or single photon emission computed tomography (SPECT).

5. Summary

Targeting neurotoxic amyloid beta (Aβ) oligomers is currently a very attractive drug development strategy for treatment of Alzheimer´s disease. Using mirror-image phage display against Aβ (1-42), several arginine-rich peptides have previously been identified consisting solely of D-enantiomeric amino acid residues, which bind to Aβ in different assembly states and eliminate toxic Aβ aggregates. Some of these D-peptides show both diagnostic and therapeutic potential *in vitro* and *in vivo*. This doctoral dissertation investigated the preclinical pharmacokinetics and cerebral distribution of these D-enantiomeric peptides in mouse models.

Generally, little information on the pharmacokinetic behaviour of D-enantiomeric peptides is available, therefore we conducted experiments with tritium labelled D-peptides (^{3}H-D3, -RD2, -D3D3, and –RD2D3) in mice with different administration routes to characterize their distribution in different organs and in plasma, as well as their bioavailability by different administration routes. In addition, their metabolic stability was investigated in liver microsomes, mouse plasma, brain, liver and kidney homogenates, and their plasma protein binding was estimated. The brain-plasma ratio related blood-brain barrier (BBB) permeability of those arginine-rich D-peptides was further studied with the lead D-peptide, D3. By labelling with tritium or a fluorescence marker (FAM), D3's BBB penetration and Aβ plaque binding properties were verified with different *in vitro* and *in vivo* experiments with wild type and AD transgenic mice. Moreover, the cerebral distribution, especially the axonal transport pattern of D-peptides was investigated through tracking fluorescently labelled D-peptides after intra-hippocampal injection into AD transgenic and wild type mouse brains.

The D-peptides tested here, especially the single D-peptides, demonstrated favourable pharmacokinetic properties, such as high protease resistance, long biological half-life and high oral bioavailability. The results support the therapeutic potential of D-peptides in general. D3 rapidly entered the brain where it could be found associated with amyloid plaques suggesting a direct penetration of BBB. In comparison to other standard retrograde tracers, D3 and D3D3 showed significantly enhanced retrograde transport in the perforant pathway in two AD transgenic mouse models (APPSwe/PSEN1ΔE9 and Tg-SwDI), especially in comparison to that in wild type mice. It may indicate a promising potential of those D-peptides for diagnosis of AD as well as for the study of pathological changes in the neural pathways in early AD pathology. Taken together, results strongly suggest the Aβ binding D-peptides as promising substances demonstrating both diagnostic and therapeutic potential in the fight against Alzheimer's disease.

6. Zusammenfassung

Die Entwicklung neuer therapeutischer Substanzen gegen neurotoxische Oligomere des Amyloid-beta-Peptiden (Aβ) ist zurzeit eine sehr attraktive Strategie zur Behandlung der Alzheimer-Demenz (AD). Mit Hilfe des Spiegelbild-Phagen-Displays gegen Aβ (1-42) wurden verschiedene Arginin-haltige, ausschließlich aus D-enantiomeren Aminosäuren bestehende, Peptide identifiziert, die Aβ in verschiedenen, aggregierten Formen binden und toxische Aβ Aggregate eliminieren können. Einige dieser D-Peptide zeigten bereits therapeutisches Wirkpotential in *in vitro* und *in vivo* Studien. Diese Doktorarbeit befasst sich mit der Untersuchung der präklinischen Pharmakokinetik und der zerebralen Verteilung dieser D-enantiomeren Peptide in Mausmodellen.

Über die Pharmakokinetik von D-enantiomeren Peptiden ist im Allgemeinen noch sehr wenig bekannt. Daher wurden Experimente mit Tritium-markierten D-Peptiden (^{3}H-D3, -RD2, -D3D3, and –RD2D3) mit Mäusen und unter Verwendung von verschiedenen Administrationswegen durchgeführt, um die Verteilung in verschiedenen Organen und in Plasma sowie die Bioverfügbarkeit zu untersuchen. Außerdem wurde die metabolische Stabilität in Leber-Mikrosomen, Mausplasma, Gehirn-, Leber- und Nierenhomogenaten untersucht, sowie die Plasmaproteinbindung abgeschätzt. Der Hirn-Plasma-Quotient als Maß für die Bluthirnschranken-(BHS)-Permeabilität der Arginin-haltigen D-Peptide wurde darüber hinaus mit der Leitsubstanz D3 untersucht. Durch Markierung mit Tritium oder einem Fluoreszenzmarker (FAM) konnte in verschiedenen *in vitro* und *in vivo* Experimenten mit Wildtyp bzw. transgenen AD Mäusen überprüft werden, ob D3 die BHS überwinden und an Aβ-Plaques binden kann. Darüber hinaus wurde die Verteilung der D-Peptide im Gehirn, und insbesondere der axonale Transport, mit Hilfe von fluoreszenz-markierten D-Peptiden nach intra-hippokampaler Injektion in transgene AD- und Wildtyp-Mausgehirne untersucht.

Die hier getesteten, und insbesondere die einfachen D-Peptide, zeigten günstige pharmakokinetische Eigenschaften, wie z.B. hohe Proteasenresistenz, lange biologische Halbwertszeit und orale Bioverfügbarkeit. Diese Ergebnisse unterstützen insgesamt das therapeutische Potential der D-Peptide. Es konnte gezeigt werden, dass D3 schnell in das Gehirn eindrang, wo es in Assoziation mit Amyloiden Plaques gefunden werden konnte, was eine direkte Überwindung der BHS impliziert. Im Vergleich zu anderen retrograden Standardtracern, zeigten Fluoreszenz-markiertes D3 und D3D3 eine intensive Markierung von Layer II (und III) Zellen des entorhinalen Kortex nach intra-hippokampaler Injektion in zwei transgenen Mausmodellen (APPSwe/PSEN1ΔE9 und Tg-SwDI). Dieser Effekt fiel signifikant schwächer in Wildtyp-Mäusen aus. Dies weist auf ein vielversprechendes Potential dieser D-Peptide für die Diagnose, sowie für die Untersuchung der pathologischen Veränderungen in den neuronalen Bahnen in frühen AD Stadien hin. Zusammenfassend lassen die Ergebnisse deutlich darauf schließen, dass die Aβ-bindenden D-Peptide vielversprechende Substanzen mit sowohl diagnostischem als auch therapeutischem Potential im Kampf gegen die Alzheimer-Demenz darstellen.

7. References

1. Riley JC. Estimates of Regional and Global Life Expectancy, 1800–2001. Population and Development Review. 2005;31(3):537-43. doi: 10.1111/j.1728-4457.2005.00083.x.
2. Graeber MB, Mehraein P. Reanalysis of the first case of Alzheimer's disease. Eur Arch Psychiatry Clin Neurosci. 1999;3:10-3.
3. Maurer K, Volk S, Gerbaldo H. Auguste D and Alzheimer's disease. Lancet. 1997;349(9064):1546-9.
4. Graeber MB. No man alone: the rediscovery of Alois Alzheimer's original cases. Brain Pathol. 1999;9(2):237-40.
5. Burns A, Byrne EJ, Maurer K. Alzheimer's disease. The Lancet. 360(9327):163-5. doi: 10.1016/s0140-6736(02)09420-5.
6. Graeber MB, Kosel S, Grasbon-Frodl E, Moller HJ, Mehraein P. Histopathology and APOE genotype of the first Alzheimer disease patient, Auguste D. Neurogenetics. 1998;1(3):223-8.
7. Blessed G, Tomlinson BE, Roth M. The association between quantitative measures of dementia and of senile change in the cerebral grey matter of elderly subjects. Br J Psychiatry. 1968;114(512):797-811.
8. Fletcher LC, Burke KE, Caine PL, Rinne NL, Braniff CA, Davis HR, et al. Diagnosing Alzheimer's disease: are we any nearer to useful biomarker-based, non-invasive tests? GMS health technology assessment. 2013;9:Doc01. Epub 2013/06/12. doi: 10.3205/hta000107. PubMed PMID: 23755087; PubMed Central PMCID: PMC3677379.
9. Serrano-Pozo A, Frosch MP, Masliah E, Hyman BT. Neuropathological alterations in Alzheimer disease. Cold Spring Harbor perspectives in medicine. 2011;1(1):a006189. Epub 2012/01/10. doi: 10.1101/cshperspect.a006189. PubMed PMID: 22229116; PubMed Central PMCID: PMC3234452.
10. Brunnstrom HR, Englund EM. Cause of death in patients with dementia disorders. European journal of neurology : the official journal of the European Federation of Neurological Societies. 2009;16(4):488-92. Epub 2009/01/28. doi: 10.1111/j.1468-1331.2008.02503.x. PubMed PMID: 19170740.
11. Mitchell SL, Teno JM, Miller SC, Mor V. A national study of the location of death for older persons with dementia. J Am Geriatr Soc. 2005;53(2):299-305. doi: DOI 10.1111/j.1532-5415.2005.53118.x. PubMed PMID: ISI:000226471900018.
12. Bikbov B, Perico N, Remuzzi G. Mortality landscape in the Global Burden of Diseases, Injuries and Risk Factors Study. Eur J Intern Med. 2014;25(1):1-5. doi: DOI 10.1016/j.ejim.2013.09.002. PubMed PMID: ISI:000329853900011.
13. Murray CJL, Abraham J, Ali MK, Alvarado M, Atkinson C, Baddour LM, et al. The State of US Health, 1990-2010 Burden of Diseases, Injuries, and Risk Factors. Jama-J Am Med Assoc. 2013;310(6):591-608. doi: DOI 10.1001/jama.2013.13805. PubMed PMID: ISI:000323058400015.
14. James BD, Leurgans SE, Hebert LE, Scherr PA, Yaffe K, Bennett DA. Contribution of Alzheimer disease to mortality in the United States. Neurology. 2014;82(12):1045-50. doi: Doi 10.1212/Wnl.0000000000000240. PubMed PMID: ISI:000336500100012.
15. Weuve J, Hebert LE, Scherr PA, Evans DA. Deaths in the United States among persons with Alzheimer's disease (2010-2050). Alzheimer's & dementia : the journal of the Alzheimer's Association. 2014;10(2):004.
16. Schulz R, Obrien AT, Bookwala J, Fleissner K. Psychiatric and Physical Morbidity Effects of Dementia Caregiving - Prevalence, Correlates, and Causes. Gerontologist. 1995;35(6):771-91. PubMed PMID: ISI:A1995TJ54700008.
17. Ornstein K, Gaugler JE. The problem with "problem behaviors": a systematic review of the association between individual patient behavioral and psychological symptoms and caregiver depression and burden within the dementia patient-caregiver dyad. International Psychogeriatrics. 2012;24(10):1536-52. doi: Doi 10.1017/S1041610212000737. PubMed PMID: ISI:000308859000002.
18. Zhu CW, Sano M. Economic considerations in the management of Alzheimer’s disease. Clinical Interventions in Aging. 2006;1(2):143-54. PubMed PMID: PMC2695165.

19. Wimo A, Jonsson L, Bond J, Prince M, Winblad B, Int AD. The worldwide economic impact of dementia 2010. Alzheimers & Dementia. 2013;9(1):1-11. doi: DOI 10.1016/j.jalz.2012.11.006. PubMed PMID: ISI:000314081400001.
20. Perl DP. Neuropathology of Alzheimer's disease. The Mount Sinai journal of medicine, New York. 2010;77(1):32-42. Epub 2010/01/27. doi: 10.1002/msj.20157. PubMed PMID: 20101720; PubMed Central PMCID: PMC2918894.
21. Goedert M. Tau protein and the neurofibrillary pathology of Alzheimer's disease. Annals of the New York Academy of Sciences. 1996;777:121-31. Epub 1996/01/17. PubMed PMID: 8624074.
22. Cowan CM, Quraishe S, Mudher A. What is the pathological significance of tau oligomers? Biochemical Society transactions. 2012;40(4):693-7.
23. Selkoe DJ. Alzheimer's disease: genes, proteins, and therapy. Physiological reviews. 2001;81(2):741-66. Epub 2001/03/29. PubMed PMID: 11274343.
24. Braak H, Braak E, Ohm T, Bohl J. Alzheimer's disease: mismatch between amyloid plaques and neuritic plaques. Neuroscience letters. 1989;103(1):24-8.
25. Westermark P. Amyloid in the islets of Langerhans: thoughts and some historical aspects. Upsala journal of medical sciences. 2011;116(2):81-9. Epub 2011/04/14. doi: 10.3109/03009734.2011.573884. PubMed PMID: 21486192; PubMed Central PMCID: PMC3078536.
26. Virchow R. Ueber den Gang der amyloiden Degeneration. Archiv f pathol Anat. 1855;8(2-3):364-8. doi: 10.1007/bf01935311.
27. Virchow R. Zur Cellulose-Frage. Archiv f pathol Anat. 1855;8(1):140-4. doi: 10.1007/bf01935322.
28. Aterman K. A historical note on the iodine-sulphuric acid reaction of amyloid. Histochemistry. 1976;49(2):131-43. doi: 10.1007/bf00495677.
29. Virchow R. Weitere Mittheilungen über das Vorkommen der pflanzlichen Cellulose beim Menschen. Archiv f pathol Anat. 1854;6(2):268-71. doi: 10.1007/bf01881064.
30. Sipe JD, Cohen AS. Review: history of the amyloid fibril. Journal of structural biology. 2000;130(2-3):88-98. Epub 2000/08/15. doi: 10.1006/jsbi.2000.4221. PubMed PMID: 10940217.
31. Friedreich N, Kekulé A. Zur Amyloidfrage. Archiv f pathol Anat. 1859;16(1-2):50-65. doi: 10.1007/bf01945246.
32. Bennhold H. Eine spezifische Amyloidfärbung mit Kongorot. Med Wochenschrift München. 1922;69:1537-8.
33. Chambers WD. Histo-chemical Study of the Senile Plaques of Redlich-Fischer [Étude histo-chimique des plaques séniles.] (Journ. de Neur. et Psychiat., November, 1927.) Divry, P1928 1928-07-01 00:00:00. 533- p.
34. Jin L-W, Claborn KA, Kurimoto M, Geday MA, Maezawa I, Sohraby F, et al. Imaging linear birefringence and dichroism in cerebral amyloid pathologies. Proceedings of the National Academy of Sciences of the United States of America. 2003;100(26):15294-8. doi: 10.1073/pnas.2534647100. PubMed PMID: PMC307560.
35. Missmahl H-P, Hartwig M. Polarisationsoptische Untersuchungen an der Amyloidsubstanz. Virchows Arch path Anat. 1953;324(4):489-508. doi: 10.1007/bf00954791.
36. Eanes ED, Glenner GG. X-ray diffraction studies on amyloid filaments. The journal of histochemistry and cytochemistry : official journal of the Histochemistry Society. 1968;16(11):673-7. Epub 1968/11/01. PubMed PMID: 5723775.
37. Snow AD, Willmer J, Kisilevsky R. Sulfated glycosaminoglycans: a common constituent of all amyloids? Lab Invest. 1987;56(1):120-3.
38. Snow AD, Sekiguchi R, Nochlin D, Fraser P, Kimata K, Mizutani A, et al. An important role of heparan sulfate proteoglycan (Perlecan) in a model system for the deposition and persistence of fibrillar A beta-amyloid in rat brain. Neuron. 1994;12(1):219-34. Epub 1994/01/01. PubMed PMID: 8292358.
39. Riedel G, Micheau J. Function of the hippocampus in memory formation: desperately seeking resolution. Progress in neuro-psychopharmacology & biological psychiatry. 2001;25(4):835-53.

40. Jonas P, Lisman J. Structure, function, and plasticity of hippocampal dentate gyrus microcircuits. Frontiers in Neural Circuits. 2014;8:107. doi: 10.3389/fncir.2014.00107. PubMed PMID: PMC4159971.
41. Braak H, Braak E. Neuropathological stageing of Alzheimer-related changes. Acta neuropathologica. 1991;82(4):239-59. Epub 1991/01/01. PubMed PMID: 1759558.
42. Grober E, Dickson D, Sliwinski MJ, Buschke H, Katz M, Crystal H, et al. Memory and mental status correlates of modified Braak staging. Neurobiology of aging. 1999;20(6):573-9.
43. Delacourte A, David JP, Sergeant N, Buée L, Wattez A, Vermersch P, et al. The biochemical pathway of neurofibrillary degeneration in aging and Alzheimer's disease. Neurology. 1999;52(6):1158. doi: 10.1212/wnl.52.6.1158.
44. Knezovic A, Osmanovic-Barilar J, Curlin M, Hof PR, Simic G, Riederer P, et al. Staging of cognitive deficits and neuropathological and ultrastructural changes in streptozotocin-induced rat model of Alzheimer's disease. J Neural Transm. 2015;122(4):577-92.
45. Granic I, Masman MF, Luiten PGM, Eisel ULM. Braak Staging in Mouse Models of Alzheimer's Disease. The American journal of pathology. 2010;177(4):1603-5. doi: 10.2353/ajpath.2010.100656. PubMed PMID: PMC2947256.
46. MacDonald AB. Alzheimer's disease Braak Stage progressions: reexamined and redefined as Borrelia infection transmission through neural circuits. Medical hypotheses. 2007;68(5):1059-64.
47. Kang J, Lemaire HG, Unterbeck A, Salbaum JM, Masters CL, Grzeschik KH, et al. The precursor of Alzheimer's disease amyloid A4 protein resembles a cell-surface receptor. Nature. 1987;325(6106):733-6.
48. Dyrks T, Weidemann A, Multhaup G, Salbaum JM, Lemaire HG, Kang J, et al. Identification, transmembrane orientation and biogenesis of the amyloid A4 precursor of Alzheimer's disease. The EMBO journal. 1988;7(4):949-57. Epub 1988/04/01. PubMed PMID: 2900137; PubMed Central PMCID: PMC454420.
49. Sisodia SS, Koo EH, Hoffman PN, Perry G, Price DL. Identification and transport of full-length amyloid precursor proteins in rat peripheral nervous system. The Journal of neuroscience : the official journal of the Society for Neuroscience. 1993;13(7):3136-42. Epub 1993/07/01. PubMed PMID: 8331390.
50. Goldgaber D, Lerman MI, McBride OW, Saffiotti U, Gajdusek DC. Characterization and chromosomal localization of a cDNA encoding brain amyloid of Alzheimer's disease. Science. 1987;235(4791):877-80. Epub 1987/02/20. PubMed PMID: 3810169.
51. Turner PR, O'Connor K, Tate WP, Abraham WC. Roles of amyloid precursor protein and its fragments in regulating neural activity, plasticity and memory. Progress in neurobiology. 2003;70(1):1-32. Epub 2003/08/21. PubMed PMID: 12927332.
52. Haass C. Take five--BACE and the gamma-secretase quartet conduct Alzheimer's amyloid beta-peptide generation. The EMBO journal. 2004;23(3):483-8. Epub 2004/01/30. doi: 10.1038/sj.emboj.7600061. PubMed PMID: 14749724; PubMed Central PMCID: PMC1271800.
53. Haass C, Kaether C, Thinakaran G, Sisodia S. Trafficking and proteolytic processing of APP. Cold Spring Harbor perspectives in medicine. 2012;2(5):a006270. Epub 2012/05/04. doi: 10.1101/cshperspect.a006270. PubMed PMID: 22553493; PubMed Central PMCID: PMC3331683.
54. Yagishita S, Morishima-Kawashima M, Tanimura Y, Ishiura S, Ihara Y. DAPT-induced intracellular accumulations of longer amyloid beta-proteins: further implications for the mechanism of intramembrane cleavage by gamma-secretase. Biochemistry. 2006;45(12):3952-60.
55. Qi-Takahara Y, Morishima-Kawashima M, Tanimura Y, Dolios G, Hirotani N, Horikoshi Y, et al. Longer forms of amyloid beta protein: implications for the mechanism of intramembrane cleavage by gamma-secretase. The Journal of neuroscience : the official journal of the Society for Neuroscience. 2005;25(2):436-45.
56. Yagishita S, Morishima-Kawashima M, Ishiura S, Ihara Y. Abeta46 is processed to Abeta40 and Abeta43, but not to Abeta42, in the low density membrane domains. The Journal of biological chemistry. 2008;283(2):733-8.
57. Jankowsky JL, Fadale DJ, Anderson J, Xu GM, Gonzales V, Jenkins NA, et al. Mutant presenilins specifically elevate the levels of the 42 residue beta-amyloid peptide in vivo: evidence for

augmentation of a 42-specific gamma secretase. Human molecular genetics. 2004;13(2):159-70. Epub 2003/12/03. doi: 10.1093/hmg/ddh019. PubMed PMID: 14645205.
58. Zhao G, Tan J, Mao G, Cui MZ, Xu X. The same gamma-secretase accounts for the multiple intramembrane cleavages of APP. Journal of neurochemistry. 2007;100(5):1234-46. Epub 2007/01/24. doi: 10.1111/j.1471-4159.2006.04302.x. PubMed PMID: 17241131.
59. Haass C, Hung AY, Schlossmacher MG, Teplow DB, Selkoe DJ. beta-Amyloid peptide and a 3-kDa fragment are derived by distinct cellular mechanisms. The Journal of biological chemistry. 1993;268(5):3021-4. Epub 1993/02/15. PubMed PMID: 8428976.
60. Portelius E, Gustavsson MK, Zetterberg H, Andreasson U, Blennow K. Evaluation of the performance of novel Abeta isoforms as theragnostic markers in Alzheimer's disease: from the cell to the patient. Neuro-degenerative diseases. 2012;10(1-4):138-40.
61. Portelius E, Mattsson N, Andreasson U, Blennow K, Zetterberg H. Novel abeta isoforms in Alzheimer's disease - their role in diagnosis and treatment. Current pharmaceutical design. 2011;17(25):2594-602.
62. Portelius E, Price E, Brinkmalm G, Stiteler M, Olsson M, Persson R, et al. A novel pathway for amyloid precursor protein processing. Neurobiology of aging. 2011;32(6):1090-8.
63. Willem M, Tahirovic S, Busche MA, Ovsepian SV, Chafai M, Kootar S, et al. [eegr]-Secretase processing of APP inhibits neuronal activity in the hippocampus. Nature. 2015;advance online publication. doi: 10.1038/nature14864

http://www.nature.com/nature/journal/vaop/ncurrent/abs/nature14864.html#supplementary-information.
64. Brown MS, Ye J, Rawson RB, Goldstein JL. Regulated intramembrane proteolysis: a control mechanism conserved from bacteria to humans. Cell. 2000;100(4):391-8. Epub 2000/02/29. PubMed PMID: 10693756.
65. Rawson RB. Regulated intramembrane proteolysis: from the endoplasmic reticulum to the nucleus. Essays in biochemistry. 2002;38:155-68. Epub 2002/12/05. PubMed PMID: 12463168.
66. Lichtenthaler SF, Haass C, Steiner H. Regulated intramembrane proteolysis--lessons from amyloid precursor protein processing. Journal of neurochemistry. 2011;117(5):779-96. Epub 2011/03/19. doi: 10.1111/j.1471-4159.2011.07248.x. PubMed PMID: 21413990.
67. Vassar R. BACE1: the beta-secretase enzyme in Alzheimer's disease. Journal of molecular neuroscience : MN. 2004;23(1-2):105-14. Epub 2004/05/06. doi: 10.1385/JMN:23:1-2:105. PubMed PMID: 15126696.
68. Cole SL, Vassar R. The Alzheimer's disease beta-secretase enzyme, BACE1. Molecular neurodegeneration. 2007;2:22. Epub 2007/11/17. doi: 10.1186/1750-1326-2-22. PubMed PMID: 18005427; PubMed Central PMCID: PMC2211305.
69. Stockley JH, Ravid R, O'Neill C. Altered beta-secretase enzyme kinetics and levels of both BACE1 and BACE2 in the Alzheimer's disease brain. FEBS letters. 2006;580(28-29):6550-60. Epub 2006/11/23. doi: 10.1016/j.febslet.2006.10.076. PubMed PMID: 17113083.
70. Hong L, Koelsch G, Lin X, Wu S, Terzyan S, Ghosh AK, et al. Structure of the protease domain of memapsin 2 (beta-secretase) complexed with inhibitor. Science. 2000;290(5489):150-3. Epub 2000/10/06. PubMed PMID: 11021803.
71. Skovronsky DM, Pijak DS, Doms RW, Lee VM. A distinct ER/IC gamma-secretase competes with the proteasome for cleavage of APP. Biochemistry. 2000;39(4):810-7.
72. Gregory GC, Halliday GM. What is the dominant Abeta species in human brain tissue? A review. Neurotoxicity research. 2005;7(1-2):29-41.
73. Mori H, Takio K, Ogawara M, Selkoe DJ. Mass spectrometry of purified amyloid beta protein in Alzheimer's disease. The Journal of biological chemistry. 1992;267(24):17082-6. Epub 1992/08/25. PubMed PMID: 1512246.
74. Naslund J, Schierhorn A, Hellman U, Lannfelt L, Roses AD, Tjernberg LO, et al. Relative abundance of Alzheimer A beta amyloid peptide variants in Alzheimer disease and normal aging. Proceedings of the National Academy of Sciences of the United States of America. 1994;91(18):8378-82. Epub 1994/08/30. PubMed PMID: 8078890; PubMed Central PMCID: PMC44609.

75. Yan Y, Wang C. Abeta42 is more rigid than Abeta40 at the C terminus: implications for Abeta aggregation and toxicity. Journal of molecular biology. 2006;364(5):853-62.
76. Barghorn S, Nimmrich V, Striebinger A, Krantz C, Keller P, Janson B, et al. Globular amyloid beta-peptide oligomer - a homogenous and stable neuropathological protein in Alzheimer's disease. Journal of neurochemistry. 2005;95(3):834-47. Epub 2005/09/02. doi: 10.1111/j.1471-4159.2005.03407.x. PubMed PMID: 16135089.
77. Walsh DM, Klyubin I, Shankar GM, Townsend M, Fadeeva JV, Betts V, et al. The role of cell-derived oligomers of Abeta in Alzheimer's disease and avenues for therapeutic intervention. Biochemical Society transactions. 2005;33(Pt 5):1087-90. Epub 2005/10/26. doi: 10.1042/BST20051087. PubMed PMID: 16246051.
78. Townsend M, Shankar GM, Mehta T, Walsh DM, Selkoe DJ. Effects of secreted oligomers of amyloid beta-protein on hippocampal synaptic plasticity: a potent role for trimers. The Journal of physiology. 2006;572(Pt 2):477-92. Epub 2006/02/14. doi: 10.1113/jphysiol.2005.103754. PubMed PMID: 16469784; PubMed Central PMCID: PMC1779683.
79. Kayed R, Head E, Thompson JL, McIntire TM, Milton SC, Cotman CW, et al. Common structure of soluble amyloid oligomers implies common mechanism of pathogenesis. Science. 2003;300(5618):486-9. Epub 2003/04/19. doi: 10.1126/science.1079469. PubMed PMID: 12702875.
80. Kayed R, Head E, Sarsoza F, Saing T, Cotman CW, Necula M, et al. Fibril specific, conformation dependent antibodies recognize a generic epitope common to amyloid fibrils and fibrillar oligomers that is absent in prefibrillar oligomers. Molecular neurodegeneration. 2007;2:18. Epub 2007/09/28. doi: 10.1186/1750-1326-2-18. PubMed PMID: 17897471; PubMed Central PMCID: PMC2100048.
81. Lesné S, Koh MT, Kotilinek L, Kayed R, Glabe CG, Yang A, et al. A specific amyloid-[beta] protein assembly in the brain impairs memory. Nature. 2006;440(7082):352-7. doi: http://www.nature.com/nature/journal/v440/n7082/suppinfo/nature04533_S1.html.
82. Haass C, Selkoe DJ. Soluble protein oligomers in neurodegeneration: lessons from the Alzheimer's amyloid [beta]-peptide. Nat Rev Mol Cell Biol. 2007;8(2):101-12.
83. Bitan G, Kirkitadze MD, Lomakin A, Vollers SS, Benedek GB, Teplow DB. Amyloid β-protein (Aβ) assembly: Aβ40 and Aβ42 oligomerize through distinct pathways. Proceedings of the National Academy of Sciences. 2003;100(1):330-5. doi: 10.1073/pnas.222681699.
84. Selkoe DJ. The molecular pathology of Alzheimer's disease. Neuron. 1991;6(4):487-98. Epub 1991/04/01. PubMed PMID: 1673054.
85. Selkoe DJ. Toward a comprehensive theory for Alzheimer's disease. Hypothesis: Alzheimer's disease is caused by the cerebral accumulation and cytotoxicity of amyloid beta-protein. Annals of the New York Academy of Sciences. 2000;924:17-25. Epub 2001/02/24. PubMed PMID: 11193794.
86. Huang X, Atwood CS, Hartshorn MA, Multhaup G, Goldstein LE, Scarpa RC, et al. The A beta peptide of Alzheimer's disease directly produces hydrogen peroxide through metal ion reduction. Biochemistry. 1999;38(24):7609-16. Epub 1999/07/01. doi: 10.1021/bi990438f. PubMed PMID: 10386999.
87. Lin H, Bhatia R, Lal R. Amyloid beta protein forms ion channels: implications for Alzheimer's disease pathophysiology. FASEB journal : official publication of the Federation of American Societies for Experimental Biology. 2001;15(13):2433-44. Epub 2001/11/02. doi: 10.1096/fj.01-0377com. PubMed PMID: 11689468.
88. Bhatia R, Lin H, Lal R. Fresh and globular amyloid beta protein (1-42) induces rapid cellular degeneration: evidence for AbetaP channel-mediated cellular toxicity. FASEB journal : official publication of the Federation of American Societies for Experimental Biology. 2000;14(9):1233-43. Epub 2000/06/02. PubMed PMID: 10834945.
89. King ME, Kan HM, Baas PW, Erisir A, Glabe CG, Bloom GS. Tau-dependent microtubule disassembly initiated by prefibrillar beta-amyloid. The Journal of cell biology. 2006;175(4):541-6. Epub 2006/11/15. doi: 10.1083/jcb.200605187. PubMed PMID: 17101697; PubMed Central PMCID: PMC2064590.
90. Cole SL, Vassar R. The Basic Biology of BACE1: A Key Therapeutic Target for Alzheimer's Disease. Current genomics. 2007;8(8):509-30. Epub 2007/12/01. doi: 10.2174/138920207783769512. PubMed PMID: 19415126; PubMed Central PMCID: PMC2647160.

91. Prasansuklab A, Tencomnao T. Amyloidosis in Alzheimer's Disease: The Toxicity of Amyloid Beta (A beta), Mechanisms of Its Accumulation and Implications of Medicinal Plants for Therapy. Evidence-based complementary and alternative medicine : eCAM. 2013;2013:413808. Epub 2013/06/14. doi: 10.1155/2013/413808. PubMed PMID: 23762130; PubMed Central PMCID: PMC3671299.
92. Price JM, Chi X, Hellermann G, Sutton ET. Physiological levels of beta-amyloid induce cerebral vessel dysfunction and reduce endothelial nitric oxide production. Neurological research. 2001;23(5):506-12. Epub 2001/07/28. doi: 10.1179/016164101101198758. PubMed PMID: 11474807.
93. Jan A, Hartley DM, Lashuel HA. Preparation and characterization of toxic Abeta aggregates for structural and functional studies in Alzheimer's disease research. Nature protocols. 2010;5(6):1186-209. Epub 2010/06/12. doi: 10.1038/nprot.2010.72. PubMed PMID: 20539293.
94. Zou K, Gong JS, Yanagisawa K, Michikawa M. A novel function of monomeric amyloid beta-protein serving as an antioxidant molecule against metal-induced oxidative damage. The Journal of neuroscience : the official journal of the Society for Neuroscience. 2002;22(12):4833-41. Epub 2002/06/22. PubMed PMID: 12077180.
95. Igbavboa U, Sun GY, Weisman GA, He Y, Wood WG. Amyloid beta-protein stimulates trafficking of cholesterol and caveolin-1 from the plasma membrane to the Golgi complex in mouse primary astrocytes. Neuroscience. 2009;162(2):328-38. Epub 2009/04/30. doi: 10.1016/j.neuroscience.2009.04.049. PubMed PMID: 19401218; PubMed Central PMCID: PMC3083247.
96. Soscia SJ, Kirby JE, Washicosky KJ, Tucker SM, Ingelsson M, Hyman B, et al. The Alzheimer's disease-associated amyloid beta-protein is an antimicrobial peptide. PloS one. 2010;5(3):e9505. Epub 2010/03/09. doi: 10.1371/journal.pone.0009505. PubMed PMID: 20209079; PubMed Central PMCID: PMC2831066.
97. Morley JE, Farr SA, Banks WA, Johnson SN, Yamada KA, Xu L. A physiological role for amyloid-beta protein:enhancement of learning and memory. Journal of Alzheimer's disease : JAD. 2010;19(2):441-9.
98. Sherrington R, Rogaev EI, Liang Y, Rogaeva EA, Levesque G, Ikeda M, et al. Cloning of a gene bearing missense mutations in early-onset familial Alzheimer's disease. Nature. 1995;375(6534):754-60. Epub 1995/06/29. doi: 10.1038/375754a0. PubMed PMID: 7596406.
99. St George-Hyslop PH. Genetic factors in the genesis of Alzheimer's disease. Annals of the New York Academy of Sciences. 2000;924:1-7. Epub 2001/02/24. PubMed PMID: 11193785.
100. Duara R, Lopez-Alberola RF, Barker WW, Loewenstein DA, Zatinsky M, Eisdorfer CE, et al. A comparison of familial and sporadic Alzheimer's disease. Neurology. 1993;43(7):1377-84. Epub 1993/07/01. PubMed PMID: 8327141.
101. Nochlin D, van Belle G, Bird TD, Sumi SM. Comparison of the severity of neuropathologic changes in familial and sporadic Alzheimer's disease. Alzheimer disease and associated disorders. 1993;7(4):212-22. Epub 1993/01/01. PubMed PMID: 8305189.
102. TD. B. Early-Onset Familial Alzheimer Disease. [Internet] G, editor. Seattle (WA): University of Washington, Seattle1999 Sep 24 [Updated 2012 Oct 18].
103. Campion D, Dumanchin C, Hannequin D, Dubois B, Belliard S, Puel M, et al. Early-onset autosomal dominant Alzheimer disease: prevalence, genetic heterogeneity, and mutation spectrum. American journal of human genetics. 1999;65(3):664-70. Epub 1999/08/12. doi: 10.1086/302553. PubMed PMID: 10441572; PubMed Central PMCID: PMC1377972.
104. Larner AJ, Doran M. Clinical phenotypic heterogeneity of Alzheimer's disease associated with mutations of the presenilin-1 gene. Journal of neurology. 2006;253(2):139-58. Epub 2005/11/04. doi: 10.1007/s00415-005-0019-5. PubMed PMID: 16267640.
105. Korenberg JR, Pulst SM, Neve RL, West R. The Alzheimer amyloid precursor protein maps to human chromosome 21 bands q21.105-q21.05. Genomics. 1989;5(1):124-7.
106. Haass C, Hung AY, Selkoe DJ, Teplow DB. Mutations associated with a locus for familial Alzheimer's disease result in alternative processing of amyloid beta-protein precursor. The Journal of biological chemistry. 1994;269(26):17741-8.

107. Citron M, Oltersdorf T, Haass C, McConlogue L, Hung AY, Seubert P, et al. Mutation of the beta-amyloid precursor protein in familial Alzheimer's disease increases beta-protein production. Nature. 1992;360(6405):672-4.
108. Cai XD, Golde TE, Younkin SG. Release of excess amyloid beta protein from a mutant amyloid beta protein precursor. Science. 1993;259(5094):514-6.
109. Corder EH, Saunders AM, Strittmatter WJ, Schmechel DE, Gaskell PC, Small GW, et al. Gene dose of apolipoprotein E type 4 allele and the risk of Alzheimer's disease in late onset families. Science. 1993;261(5123):921-3. Epub 1993/08/13. PubMed PMID: 8346443.
110. Houlston RS, Snowden C, Green F, Alberti KG, Humphries SE. Apolipoprotein (apo) E genotypes by polymerase chain reaction and allele-specific oligonucleotide probes: no detectable linkage disequilibrium between apo E and apo CII. Human genetics. 1989;83(4):364-8. Epub 1989/11/01. PubMed PMID: 2572535.
111. Bu G. Apolipoprotein E and its receptors in Alzheimer's disease: pathways, pathogenesis and therapy. Nature reviews Neuroscience. 2009;10(5):333-44. Epub 2009/04/03. doi: 10.1038/nrn2620. PubMed PMID: 19339974; PubMed Central PMCID: PMC2908393.
112. Blacker D, Tanzi RE. The genetics of Alzheimer disease: current status and future prospects. Archives of neurology. 1998;55(3):294-6. Epub 1998/03/31. PubMed PMID: 9520001.
113. Talbot C, Lendon C, Craddock N, Shears S, Morris JC, Goate A. Protection against Alzheimer's disease with apoE epsilon 2. Lancet. 1994;343(8910):1432-3. Epub 1994/06/04. PubMed PMID: 7910910.
114. Dennis Dickson ROW. Neurodegeneration: The Molecular Pathology of Dementia and Movement Disorders. Second Edition ed: Wiley-Blackwell; 2011 09.09.2011. 432 p.
115. Gerrish A, Russo G, Richards A, Moskvina V, Ivanov D, Harold D, et al. The role of variation at AbetaPP, PSEN1, PSEN2, and MAPT in late onset Alzheimer's disease. Journal of Alzheimer's disease : JAD. 2012;28(2):377-87.
116. Allen M, Kachadoorian M, Quicksall Z, Zou F, Chai HS, Younkin C, et al. Association of MAPT haplotypes with Alzheimer's disease risk and MAPT brain gene expression levels. Alzheimer's research & therapy. 2014;6(4).
117. Desikan RS, Schork AJ, Wang Y, Witoelar A, Sharma M, McEvoy LK, et al. Genetic overlap between Alzheimer's disease and Parkinson's disease at the MAPT locus. Molecular psychiatry. 2015;17(10):6.
118. Woodruff-Pak DS. Animal models of Alzheimer's disease: therapeutic implications. Journal of Alzheimer's disease : JAD. 2008;15(4):507-21.
119. Bryan KJ LH, Perry G, et al. Transgenic Mouse Models of Alzheimer’s Disease: Behavioral Testing and Considerations. In: JJ B, editor. Methods of Behavior Analysis in Neuroscience. 2 nd ed. Boca Raton (FL): CRC Press; 2009.
120. Duff K. Transgenic models for Alzheimer's disease. Neuropathology and applied neurobiology. 1998;24(2):101-3. doi: 10.1046/j.1365-2990.1998.00006.x.
121. Janus C, Westaway D. Transgenic mouse models of Alzheimer's disease. Physiol Behav. 2001;73(5):873-86.
122. Mayeux R, Saunders AM, Shea S, Mirra S, Evans D, Roses AD, et al. Utility of the apolipoprotein E genotype in the diagnosis of Alzheimer's disease. Alzheimer's Disease Centers Consortium on Apolipoprotein E and Alzheimer's Disease. The New England journal of medicine. 1998;338(8):506-11. Epub 1998/02/19. doi: 10.1056/NEJM199802193380804. PubMed PMID: 9468467.
123. McKhann G, Drachman D, Folstein M, Katzman R, Price D, Stadlan EM. Clinical diagnosis of Alzheimer's disease: report of the NINCDS-ADRDA Work Group under the auspices of Department of Health and Human Services Task Force on Alzheimer's Disease. Neurology. 1984;34(7):939-44.
124. Consensus recommendations for the postmortem diagnosis of Alzheimer's disease. The National Institute on Aging, and Reagan Institute Working Group on Diagnostic Criteria for the Neuropathological Assessment of Alzheimer's Disease. Neurobiology of aging. 1997;18(4 Suppl):S1-2. Epub 1997/07/01. PubMed PMID: 9330978.

125. McGleenon BM, Dynan KB, Passmore AP. Acetylcholinesterase inhibitors in Alzheimer's disease. British journal of clinical pharmacology. 1999;48(4):471-80. doi: 10.1046/j.1365-2125.1999.00026.x. PubMed PMID: PMC2014378.
126. Cooper JK. DRug treatment of alzheimer's disease. Archives of internal medicine. 1991;151(2):245-9. doi: 10.1001/archinte.1991.00400020021006.
127. Ballard C, Khan Z, Clack H, Corbett A. Nonpharmacological treatment of Alzheimer disease. Can J Psychiatry. 2011;56(10):589-95.
128. Olazarán J, Reisberg B, Clare L, Cruz I, Peña-Casanova J, del Ser T, et al. Nonpharmacological Therapies in Alzheimer's Disease: A Systematic Review of Efficacy. Dementia and geriatric cognitive disorders. 2010;30(2):161-78.
129. Leinenga G, Gotz J. Scanning ultrasound removes amyloid-beta and restores memory in an Alzheimer's disease mouse model. Science translational medicine. 2015;7(278):278ra33. Epub 2015/03/13. doi: 10.1126/scitranslmed.aaa2512. PubMed PMID: 25761889.
130. Schroeter EH, Kisslinger JA, Kopan R. Notch-1 signalling requires ligand-induced proteolytic release of intracellular domain. Nature. 1998;393(6683):382-6. Epub 1998/06/10. doi: 10.1038/30756. PubMed PMID: 9620803.
131. Milano J, McKay J, Dagenais C, Foster-Brown L, Pognan F, Gadient R, et al. Modulation of notch processing by gamma-secretase inhibitors causes intestinal goblet cell metaplasia and induction of genes known to specify gut secretory lineage differentiation. Toxicological sciences : an official journal of the Society of Toxicology. 2004;82(1):341-58. Epub 2004/08/21. doi: 10.1093/toxsci/kfh254. PubMed PMID: 15319485.
132. Morgan D, Gitter BD. Evidence supporting a role for anti-Abeta antibodies in the treatment of Alzheimer's disease. Neurobiology of aging. 2004;25(5):605-8.
133. Schenk D, Barbour R, Dunn W, Gordon G, Grajeda H, Guido T, et al. Immunization with amyloid-beta attenuates Alzheimer-disease-like pathology in the PDAPP mouse. Nature. 1999;400(6740):173-7. Epub 1999/07/17. doi: 10.1038/22124. PubMed PMID: 10408445.
134. Bard F, Cannon C, Barbour R, Burke RL, Games D, Grajeda H, et al. Peripherally administered antibodies against amyloid beta-peptide enter the central nervous system and reduce pathology in a mouse model of Alzheimer disease. Nature medicine. 2000;6(8):916-9. Epub 2000/08/10. doi: 10.1038/78682. PubMed PMID: 10932230.
135. Orgogozo JM, Gilman S, Dartigues JF, Laurent B, Puel M, Kirby LC, et al. Subacute meningoencephalitis in a subset of patients with AD after Abeta42 immunization. Neurology. 2003;61(1):46-54. Epub 2003/07/09. PubMed PMID: 12847155.
136. Marr R, Hafez D. Amyloid beta and Alzheimer's Disease: The role of neprilysin-2 in amyloid-beta clearance. Frontiers in aging neuroscience. 2014;6. doi: 10.3389/fnagi.2014.00187.
137. Nalivaeva NN, Belyaev ND, Lewis DI, Pickles AR, Makova NZ, Bagrova DI, et al. Effect of sodium valproate administration on brain neprilysin expression and memory in rats. Journal of molecular neuroscience : MN. 2012;46(3):569-77. Epub 2011/09/21. doi: 10.1007/s12031-011-9644-x. PubMed PMID: 21932040.
138. Zhuravin IA, Dubrovskaya NM, Vasilev DS, Tumanova NL, Nalivaeva NN. Epigenetic and pharmacological regulation of the amyloid-degrading enzyme neprilysin results in modulation of cognitive functions in mammals. Doklady biological sciences : proceedings of the Academy of Sciences of the USSR, Biological sciences sections / translated from Russian. 2011;438:145-8. Epub 2011/07/06. doi: 10.1134/S001249661103015X. PubMed PMID: 21728123.
139. Curtain CC, Ali F, Volitakis I, Cherny RA, Norton RS, Beyreuther K, et al. Alzheimer's disease amyloid-beta binds copper and zinc to generate an allosterically ordered membrane-penetrating structure containing superoxide dismutase-like subunits. The Journal of biological chemistry. 2001;276(23):20466-73. Epub 2001/03/29. doi: 10.1074/jbc.M100175200. PubMed PMID: 11274207.
140. Lovell MA, Robertson JD, Teesdale WJ, Campbell JL, Markesbery WR. Copper, iron and zinc in Alzheimer's disease senile plaques. Journal of the neurological sciences. 1998;158(1):47-52. Epub 1998/07/17. PubMed PMID: 9667777.
141. Ritchie CW, Bush AI, Mackinnon A, Macfarlane S, Mastwyk M, MacGregor L, et al. Metal-protein attenuation with iodochlorhydroxyquin (clioquinol) targeting Abeta amyloid deposition and

toxicity in Alzheimer disease: a pilot phase 2 clinical trial. Archives of neurology. 2003;60(12):1685-91. Epub 2003/12/17. doi: 10.1001/archneur.60.12.1685. PubMed PMID: 14676042.
142. Breitner JC, Baker LD, Montine TJ, Meinert CL, Lyketsos CG, Ashe KH, et al. Extended results of the Alzheimer's disease anti-inflammatory prevention trial. Alzheimer's & dementia : the journal of the Alzheimer's Association. 2011;7(4):402-11.
143. Nie Q, Du XG, Geng MY. Small molecule inhibitors of amyloid beta peptide aggregation as a potential therapeutic strategy for Alzheimer's disease. Acta pharmacologica Sinica. 2011;32(5):545-51. Epub 2011/04/19. doi: 10.1038/aps.2011.14. PubMed PMID: 21499284; PubMed Central PMCID: PMC4002509.
144. Reinke AA, Gestwicki JE. Structure-activity relationships of amyloid beta-aggregation inhibitors based on curcumin: influence of linker length and flexibility. Chemical biology & drug design. 2007;70(3):206-15. Epub 2007/08/28. doi: 10.1111/j.1747-0285.2007.00557.x. PubMed PMID: 17718715.
145. Blazer LL, Neubig RR. Small molecule protein-protein interaction inhibitors as CNS therapeutic agents: current progress and future hurdles. Neuropsychopharmacology : official publication of the American College of Neuropsychopharmacology. 2009;34(1):126-41. Epub 2008/09/19. doi: 10.1038/npp.2008.151. PubMed PMID: 18800065.
146. Nakano I. The limbic system: An outline and brief history of its concept. Neuropathology. 1998;18(2):211-4. doi: 10.1111/j.1440-1789.1998.tb00102.x.
147. Bear MF, Connors, Barry W., Paradiso, Michael A. . Neuroscience : exploring the brain. 3rd ed. Lupash E, editor. Maryland: Lippincott Williams&Wilkins; 2006. 898 p.
148. Rajmohan V, Mohandas E. The limbic system. Indian Journal of Psychiatry. 2007;49(2):132-9. doi: 10.4103/0019-5545.33264. PubMed PMID: PMC2917081.
149. Khan UA, Liu L, Provenzano FA, Berman DE, Profaci CP, Sloan R, et al. Molecular drivers and cortical spread of lateral entorhinal cortex dysfunction in preclinical Alzheimer's disease. Nature neuroscience. 2014;17(2):304-11. doi: 10.1038/nn.3606.
150. Mu Y, Gage FH. Adult hippocampal neurogenesis and its role in Alzheimer's disease. Molecular neurodegeneration. 2011;6:85. Epub 2011/12/24. doi: 10.1186/1750-1326-6-85. PubMed PMID: 22192775; PubMed Central PMCID: PMC3261815.
151. H.J. S. Hippocampal Formation. In: Ramachandran VS, editor. The Encyclopedia of Human Behavior. 2: Academic Press; 2012. p. 297-304.
152. Pearce JM. Ammon's horn and the hippocampus. Journal of neurology, neurosurgery, and psychiatry. 2001;71(3):351. Epub 2001/08/21. PubMed PMID: 11511709; PubMed Central PMCID: PMC1737533.
153. Manns JR, Eichenbaum H. Evolution of declarative memory. Hippocampus. 2006;16(9):795-808.
154. Harper A. Mouse models of neurological disorders—A comparison of heritable and acquired traits. Biochimica et Biophysica Acta (BBA) - Molecular Basis of Disease. 2010;1802(10):785-95. doi: http://dx.doi.org/10.1016/j.bbadis.2010.05.009.
155. Deng W, Aimone JB, Gage FH. New neurons and new memories: how does adult hippocampal neurogenesis affect learning and memory? Nature reviews Neuroscience. 2010;11(5):339-50. doi: 10.1038/nrn2822. PubMed PMID: PMC2886712.
156. Oztas E. Neuronal tracing. Neuroanatomy. 2003;2(2).
157. Brown A. Axonal transport of membranous and nonmembranous cargoes: a unified perspective. The Journal of cell biology. 2003;160(6):817-21. Epub 2003/03/19. doi: 10.1083/jcb.200212017. PubMed PMID: 12642609; PubMed Central PMCID: PMC2173776.
158. Katsumata K, Nishiyama J, Inoue T, Mizushima N, Takeda J, Yuzaki M. Dynein- and activity-dependent retrograde transport of autophagosomes in neuronal axons. Autophagy. 2010;6(3):378-85. Epub 2010/02/13. PubMed PMID: 20150763.
159. Rauk A. Why is the amyloid beta peptide of Alzheimer's disease neurotoxic? Dalton Trans. 2008;(10):1273-82. Epub 2008/02/29. doi: 10.1039/b718601k. PubMed PMID: 18305836.
160. Lazarov O, Lee M, Peterson DA, Sisodia SS. Evidence that synaptically released beta-amyloid accumulates as extracellular deposits in the hippocampus of transgenic mice. The Journal of

neuroscience : the official journal of the Society for Neuroscience. 2002;22(22):9785-93. Epub 2002/11/13. PubMed PMID: 12427834.
161. Parameshwaran K, Dhanasekaran M, Suppiramaniam V. Amyloid beta peptides and glutamatergic synaptic dysregulation. Experimental neurology. 2008;210(1):7-13. doi: http://dx.doi.org/10.1016/j.expneurol.2007.10.008.
162. Larson J, Lynch G, Games D, Seubert P. Alterations in synaptic transmission and long-term potentiation in hippocampal slices from young and aged PDAPP mice. Brain research. 1999;840(1-2):23-35. Epub 1999/10/13. PubMed PMID: 10517949.
163. Coleman PD, Yao PJ. Synaptic slaughter in Alzheimer's disease. Neurobiology of aging. 2003;24(8):1023-7. Epub 2003/12/04. PubMed PMID: 14643374.
164. Morfini GA, Burns M, Binder LI, Kanaan NM, LaPointe N, Bosco DA, et al. Axonal transport defects in neurodegenerative diseases. The Journal of neuroscience : the official journal of the Society for Neuroscience. 2009;29(41):12776-86. Epub 2009/10/16. doi: 10.1523/JNEUROSCI.3463-09.2009. PubMed PMID: 19828789; PubMed Central PMCID: PMC2801051.
165. Roy S, Zhang B, Lee VM, Trojanowski JQ. Axonal transport defects: a common theme in neurodegenerative diseases. Acta neuropathologica. 2005;109(1):5-13. Epub 2005/01/13. doi: 10.1007/s00401-004-0952-x. PubMed PMID: 15645263.
166. Urso R, Blardi P, Giorgi G. A short introduction to pharmacokinetics. European review for medical and pharmacological sciences. 2002;6(2-3):33-44. Epub 2003/04/24. PubMed PMID: 12708608.
167. Takimoto CH. Basic pharmacokinetics and pharmacodynamic principles. Cancer treatment and research. 2001;106:85-101. Epub 2001/02/28. PubMed PMID: 11225010.
168. Rasymas A. Basic pharmacology and pharmacokinetics. Clinics in podiatric medicine and surgery. 1992;9(2):211-21. Epub 1992/04/01. PubMed PMID: 1586899.
169. Singer E. [Basic concepts in pharmacology: important terms in pharmacodynamics and pharmacokinetics]. Onkologie. 2008;31 Suppl 2:21-4. Epub 2008/06/14. doi: 10.1159/000113446. PubMed PMID: 18487864.
170. Wedlund PJ, Wilkinson GR. Hepatic tissue binding and the oral first-pass effect. Journal of pharmaceutical sciences. 1984;73(3):422-5. Epub 1984/03/01. PubMed PMID: 6716260.
171. Masimirembwa CM, Bredberg U, Andersson TB. Metabolic stability for drug discovery and development: pharmacokinetic and biochemical challenges. Clinical pharmacokinetics. 2003;42(6):515-28.
172. Schoenemann PT, Yesair DW, Coffey JJ, Bullock FJ. Pharmacokinetic consequences of plasma protein binding of drugs. Annals of the New York Academy of Sciences. 1973;226:162-71. Epub 1973/11/26. PubMed PMID: 4520393.
173. Krieglstein J. [Methods of determination, physico-chemical properties and pharmacokinetic signifance of plasma protein binding of drugs]. Arzneimittel-Forschung. 1973;23(11):1527-9. Epub 1973/11/01. PubMed PMID: 4801656.
174. Barrett PH, Bell BM, Cobelli C, Golde H, Schumitzky A, Vicini P, et al. SAAM II: Simulation, Analysis, and Modeling Software for tracer and pharmacokinetic studies. Metabolism: clinical and experimental. 1998;47(4):484-92. Epub 1998/04/29. PubMed PMID: 9550550.
175. DiStefano JJ, 3rd. Noncompartmental vs. compartmental analysis: some bases for choice. The American journal of physiology. 1982;243(1):R1-6. Epub 1982/07/01. PubMed PMID: 7091383.
176. Gabrielsson J, Weiner D. Non-compartmental analysis. Methods Mol Biol. 2012;929:377-89.
177. Huang X-h, Wang K, Huang J-h, Xu L, Li L-j, Sheng Y-c, et al. Random sparse sampling strategy using stochastic simulation and estimation for a population pharmacokinetic study. Saudi Pharmaceutical Journal. 2014;22(1):63-9. doi: http://dx.doi.org/10.1016/j.jsps.2013.01.010.
178. Walker JR, Pacoma R, Watson J, Ou W, Alves J, Mason DE, et al. Enhanced proteolytic clearance of plasma Abeta by peripherally administered neprilysin does not result in reduced levels of brain Abeta in mice. The Journal of neuroscience : the official journal of the Society for Neuroscience. 2013;33(6):2457-64.

179. Henderson SJ, Andersson C, Narwal R, Janson J, Goldschmidt TJ, Appelkvist P, et al. Sustained peripheral depletion of amyloid-β with a novel form of neprilysin does not affect central levels of amyloid-β2013 2013-11-19 00:00:00.
180. Georgievska B, Gustavsson S, Lundkvist J, Neelissen J, Eketjall S, Ramberg V, et al. Revisiting the peripheral sink hypothesis: inhibiting BACE1 activity in the periphery does not alter beta-amyloid levels in the CNS. Journal of neurochemistry. 2015;132(4):477-86.
181. Ballabh P, Braun A, Nedergaard M. The blood-brain barrier: an overview: structure, regulation, and clinical implications. Neurobiology of disease. 2004;16(1):1-13. Epub 2004/06/23. doi: 10.1016/j.nbd.2003.12.016. PubMed PMID: 15207256.
182. Bazzoni G, Dejana E. Endothelial cell-to-cell junctions: molecular organization and role in vascular homeostasis. Physiological reviews. 2004;84(3):869-901. Epub 2004/07/23. doi: 10.1152/physrev.00035.2003. PubMed PMID: 15269339.
183. Zlokovic BV. The blood-brain barrier in health and chronic neurodegenerative disorders. Neuron. 2008;57(2):178-201. Epub 2008/01/25. doi: 10.1016/j.neuron.2008.01.003. PubMed PMID: 18215617.
184. Abbott NJ, Ronnback L, Hansson E. Astrocyte-endothelial interactions at the blood-brain barrier. Nature reviews Neuroscience. 2006;7(1):41-53. Epub 2005/12/24. doi: 10.1038/nrn1824. PubMed PMID: 16371949.
185. Pardridge WM. CNS drug design based on principles of blood-brain barrier transport. Journal of neurochemistry. 1998;70(5):1781-92. Epub 1998/05/08. PubMed PMID: 9572261.
186. Pardridge WM. Blood-brain barrier delivery. Drug discovery today. 2007;12(1-2):54-61. Epub 2007/01/03. doi: 10.1016/j.drudis.2006.10.013. PubMed PMID: 17198973.
187. Pardridge WM. Molecular biology of the blood-brain barrier. Molecular biotechnology. 2005;30(1):57-70. Epub 2005/04/05. doi: 10.1385/MB:30:1:057. PubMed PMID: 15805577.
188. Brownlees J, Williams CH. Peptidases, peptides, and the mammalian blood-brain barrier. Journal of neurochemistry. 1993;60(3):793-803. Epub 1993/03/01. PubMed PMID: 8436970.
189. Witt KA, Gillespie TJ, Huber JD, Egleton RD, Davis TP. Peptide drug modifications to enhance bioavailability and blood-brain barrier permeability. Peptides. 2001;22(12):2329-43. Epub 2002/01/12. PubMed PMID: 11786210.
190. Nabeshima S, Reese TS, Landis DM, Brightman MW. Junctions in the meninges and marginal glia. The Journal of comparative neurology. 1975;164(2):127-69. Epub 1975/11/15. doi: 10.1002/cne.901640202. PubMed PMID: 810497.
191. Laterra J KR, Betz LA, et al. Blood—Cerebrospinal Fluid Barrier. In: Siegel GJ AB, Albers RW, et al., editor. Basic Neurochemistry: Molecular, Cellular and Medical Aspects. 6th ed. Philadelphia: Lippincott-Raven1999.
192. Dohrmann GJ. The choroid plexus: a historical review. Brain research. 1970;18(2):197-218. Epub 1970/03/03. PubMed PMID: 4929003.
193. Abbott NJ, Patabendige AAK, Dolman DEM, Yusof SR, Begley DJ. Structure and function of the blood–brain barrier. Neurobiology of disease. 2010;37(1):13-25. doi: http://dx.doi.org/10.1016/j.nbd.2009.07.030.
194. Otvos L, Wade JD. Current challenges in peptide-based drug discovery. Frontiers in Chemistry. 2014;2:62. doi: 10.3389/fchem.2014.00062. PubMed PMID: PMC4126357.
195. Vives E, Brodin P, Lebleu B. A truncated HIV-1 Tat protein basic domain rapidly translocates through the plasma membrane and accumulates in the cell nucleus. The Journal of biological chemistry. 1997;272(25):16010-7. Epub 1997/06/20. PubMed PMID: 9188504.
196. Brooks H, Lebleu B, Vives E. Tat peptide-mediated cellular delivery: back to basics. Advanced drug delivery reviews. 2005;57(4):559-77. Epub 2005/02/22. doi: 10.1016/j.addr.2004.12.001. PubMed PMID: 15722164.
197. Zeitler M, Steringer JP, Muller HM, Mayer MP, Nickel W. HIV-Tat Forms Phosphoinositide Dependent Membrane Pores Implicated in Unconventional Protein Secretion. The Journal of biological chemistry. 2015. Epub 2015/07/18. doi: 10.1074/jbc.M115.667097. PubMed PMID: 26183781.

198. Tahirov TH, Babayeva ND, Varzavand K, Cooper JJ, Sedore SC, Price DH. Crystal structure of HIV-1 Tat complexed with human P-TEFb. Nature. 2010;465(7299):747-51. doi: 10.1038/nature09131. PubMed PMID: PMC2885016.
199. Salomone F, Cardarelli F, Di Luca M, Boccardi C, Nifosi R, Bardi G, et al. A novel chimeric cell-penetrating peptide with membrane-disruptive properties for efficient endosomal escape. Journal of controlled release : official journal of the Controlled Release Society. 2012;163(3):293-303. Epub 2012/10/09. doi: 10.1016/j.jconrel.2012.09.019. PubMed PMID: 23041543.
200. Chiodelli P, Urbinati C, Mitola S, Tanghetti E, Rusnati M. Sialic acid associated with alphavbeta3 integrin mediates HIV-1 Tat protein interaction and endothelial cell proangiogenic activation. The Journal of biological chemistry. 2012;287(24):20456-66. Epub 2012/04/25. doi: 10.1074/jbc.M111.337139. PubMed PMID: 22528484; PubMed Central PMCID: PMC3370225.
201. Sun D, Forsman J, Lund M, Woodward CE. Effect of arginine-rich cell penetrating peptides on membrane pore formation and life-times: a molecular simulation study. Physical chemistry chemical physics : PCCP. 2014;16(38):20785-95. Epub 2014/08/29. doi: 10.1039/c4cp02211d. PubMed PMID: 25166723.
202. Schwarze SR, Ho A, Vocero-Akbani A, Dowdy SF. In vivo protein transduction: delivery of a biologically active protein into the mouse. Science. 1999;285(5433):1569-72.
203. Rapoport M, Lorberboum-Galski H. TAT-based drug delivery system--new directions in protein delivery for new hopes? Expert opinion on drug delivery. 2009;6(5):453-63.
204. Liu M, Li C, Pazgier M, Mao Y, Lv Y, Gu B, et al. D-peptide inhibitors of the p53-MDM2 interaction for targeted molecular therapy of malignant neoplasms. Proceedings of the National Academy of Sciences of the United States of America. 2010;107(32):14321-6. Epub 2010/07/28. doi: 10.1073/pnas.1008930107. PubMed PMID: 20660730; PubMed Central PMCID: PMC2922601.
205. Zawadzke LE, Berg JM. A Racemic Protein. Journal of the American Chemical Society. 1992;114(10):4002-3. doi: Doi 10.1021/Ja00036a073. PubMed PMID: ISI:A1992HT80100073.
206. Milton RCD, Milton SCF, Kent SBH. Total Chemical Synthesis of a D-Enzyme - the Enantiomers of Hiv-1 Protease Show Demonstration of Reciprocal Chiral Substrate-Specificity. Science. 1992;256(5062):1445-8. doi: DOI 10.1126/science.1604320. PubMed PMID: ISI:A1992HX33700036.
207. Sun N, Funke SA, Willbold D. A Survey of Peptides with Effective Therapeutic Potential in Alzheimer's Disease Rodent Models or in Human Clinical Studies. Mini-Rev Med Chem. 2012;12(5):388-98. PubMed PMID: ISI:000303103600005.
208. Wiesehan K, Willbold D. Mirror-image phage display: aiming at the mirror. Chembiochem : a European journal of chemical biology. 2003;4(9):811-5. Epub 2003/09/10. doi: 10.1002/cbic.200300570. PubMed PMID: 12964153.
209. Schumacher TN, Mayr LM, Minor DL, Jr., Milhollen MA, Burgess MW, Kim PS. Identification of D-peptide ligands through mirror-image phage display. Science. 1996;271(5257):1854-7.
210. van Groen T, Kadish I, Funke SA, Bartnik D, Willbold D. Treatment with D3 removes amyloid deposits, reduces inflammation, and improves cognition in aged AbetaPP/PS1 double transgenic mice. J Alzheimers Dis. 2013;34(3):609-20. Epub 2012/12/29. doi: 10.3233/JAD-121792. PubMed PMID: 23271316.
211. van Groen T, Kadish I, Funke A, Bartnik D, Willbold D. Treatment with Abeta42 binding D-amino acid peptides reduce amyloid deposition and inflammation in APP/PS1 double transgenic mice. Advances in protein chemistry and structural biology. 2012;88:133-52. Epub 2012/07/21. doi: 10.1016/B978-0-12-398314-5.00005-2. PubMed PMID: 22814708.
212. Aileen Funke S, van Groen T, Kadish I, Bartnik D, Nagel-Steger L, Brener O, et al. Oral treatment with the d-enantiomeric peptide D3 improves the pathology and behavior of Alzheimer's Disease transgenic mice. ACS chemical neuroscience. 2010;1(9):639-48. Epub 2010/09/15. doi: 10.1021/cn100057j. PubMed PMID: 22778851; PubMed Central PMCID: PMC3368690.
213. van Groen T, Wiesehan K, Funke SA, Kadish I, Nagel-Steger L, Willbold D. Reduction of Alzheimer's disease amyloid plaque load in transgenic mice by D3, A D-enantiomeric peptide identified by mirror image phage display. ChemMedChem. 2008;3(12):1848-52. Epub 2008/11/19. doi: 10.1002/cmdc.200800273. PubMed PMID: 19016284.

214. Brener O DT, Gremer L, van Groen T, Mirecka EA, Kadish I, Willuweit A, Kutzsche J, Jürgens D, Rudolph S, Tusche M, Bongen P, Pietruszka J, Oesterhelt F, Langen K-J, Demuth H-U, Janssen A, Hoyer W, Funke SA, Nagel-Steger L, Willbold D. . QIAD assay for quantitating a compound's efficacy in elimination of toxic Aβ oligomers Scientific reports. 2015;5(13222). doi: 10.1038/srep13222.
215. Pollaro L, Heinis C. Strategies to prolong the plasma residence time of peptide drugs. MedChemComm. 2010;1(5):319-24. doi: 10.1039/c0md00111b.
216. Banga AK. Therapeutic peptides and proteins : formulation, processing, and delivery systems. 2nd ed. Boca Raton, FL: CRC/Taylor & Francis; 2006. 354 p. p.
217. Benet LZ. Benet L Z and Galeazzi R L: noncompartmental determination of the steady-state volume of distribution, J Pharm Sci 68, 1071-1074, 1979--the backstory. The AAPS journal. 2012;14(2):164-7. Epub 2012/02/04. doi: 10.1208/s12248-012-9326-9. PubMed PMID: 22302585; PubMed Central PMCID: PMC3326156.
218. Reichel A. The role of blood-brain barrier studies in the pharmaceutical industry. Current drug metabolism. 2006;7(2):183-203. Epub 2006/02/14. PubMed PMID: 16472107.
219. Fischer PM, Zhelev NZ, Wang S, Melville JE, Fahraeus R, Lane DP. Structure-activity relationship of truncated and substituted analogues of the intracellular delivery vector Penetratin. The journal of peptide research : official journal of the American Peptide Society. 2000;55(2):163-72. Epub 2000/04/28. PubMed PMID: 10784032.
220. Futaki S, Suzuki T, Ohashi W, Yagami T, Tanaka S, Ueda K, et al. Arginine-rich peptides. An abundant source of membrane-permeable peptides having potential as carriers for intracellular protein delivery. The Journal of biological chemistry. 2001;276(8):5836-40. Epub 2000/11/21. doi: 10.1074/jbc.M007540200. PubMed PMID: 11084031.
221. Wong TW. Design of oral insulin delivery systems. Journal of drug targeting. 2010;18(2):79-92. Epub 2009/12/09. doi: 10.3109/10611860903302815. PubMed PMID: 19968567.
222. Takagi H, Hiroi T, Hirose S, Yang L, Takaiwa F. Rice seed ER-derived protein body as an efficient delivery vehicle for oral tolerogenic peptides. Peptides. 2010;31(8):1421-5. Epub 2010/05/12. doi: 10.1016/j.peptides.2010.04.032. PubMed PMID: 20457197.
223. Mason JM. Design and development of peptides and peptide mimetics as antagonists for therapeutic intervention. Future medicinal chemistry. 2010;2(12):1813-22. Epub 2011/03/25. doi: 10.4155/fmc.10.259. PubMed PMID: 21428804.
224. Kratochwil NA, Huber W, Muller F, Kansy M, Gerber PR. Predicting plasma protein binding of drugs: a new approach. Biochem Pharmacol. 2002;64(9):1355-74. doi: Pii S0006-2952(02)01074-2

Doi 10.1016/S0006-2952(02)01074-2. PubMed PMID: WOS:000178981800006.
225. Terzyan S, Ramsland PA, Voss EW, Jr., Herron JN, Edmundson AB. Three-dimensional structures of idiotypically related Fabs with intermediate and high affinity for fluorescein. Journal of molecular biology. 2004;339(5):1141-51. Epub 2004/06/05. doi: 10.1016/j.jmb.2004.03.080. PubMed PMID: 15178254.
226. Fischer R, Waizenegger T, Kohler K, Brock R. A quantitative validation of fluorophore-labelled cell-permeable peptide conjugates: fluorophore and cargo dependence of import. Biochimica et biophysica acta. 2002;1564(2):365-74. Epub 2002/08/15. PubMed PMID: 12175919.
227. Lundberg P, El-Andaloussi S, Sutlu T, Johansson H, Langel U. Delivery of short interfering RNA using endosomolytic cell-penetrating peptides. FASEB journal : official publication of the Federation of American Societies for Experimental Biology. 2007;21(11):2664-71. Epub 2007/04/28. doi: 10.1096/fj.06-6502com. PubMed PMID: 17463227.
228. Wiesehan K, Buder K, Linke RP, Patt S, Stoldt M, Unger E, et al. Selection of D-Amino-Acid Peptides That Bind to Alzheimer's Disease Amyloid Peptide Aβ1–42 by Mirror Image Phage Display. Chembiochem : a European journal of chemical biology. 2003;4(8):748-53. doi: 10.1002/cbic.200300631.
229. Sengillo JD, Winkler EA, Walker CT, Sullivan JS, Johnson M, Zlokovic BV. Deficiency in mural vascular cells coincides with blood-brain barrier disruption in Alzheimer's disease. Brain Pathol. 2013;23(3):303-10. Epub 2012/11/07. doi: 10.1111/bpa.12004. PubMed PMID: 23126372; PubMed Central PMCID: PMC3628957.

230. Zlokovic BV. Cerebrovascular Effects of Apolipoprotein E: Implications for Alzheimer's disease. JAMA neurology. 2013;70(4):440-4. doi: 10.1001/jamaneurol.2013.2152. PubMed PMID: PMC4414030.
231. Wengenack TM, Curran GL, Poduslo JF. Targeting Alzheimer amyloid plaques in vivo. Nature biotechnology. 2000;18(8):868-72. PubMed PMID: ISI:000088666800024.
232. Rizzuti M, Nizzardo M, Zanetta C, Ramirez A, Corti S. Therapeutic applications of the cell-penetrating HIV-1 Tat peptide. Drug discovery today. 2015;20(1):76-85. doi: DOI 10.1016/j.drudis.2014.09.017. PubMed PMID: ISI:000349193700009.
233. Vives E, Richard JP, Rispal C, Lebleu B. TAT peptide internalization: seeking the mechanism of entry. Current protein & peptide science. 2003;4(2):125-32. Epub 2003/04/08. PubMed PMID: 12678851.
234. van Groen T, Kadish I, Wiesehan K, Funke SA, Willbold D. In vitro and in vivo staining characteristics of small, fluorescent, Abeta42-binding D-enantiomeric peptides in transgenic AD mouse models. ChemMedChem. 2009;4(2):276-82.
235. Muller-Schiffmann A, Marz-Berberich J, Andreyeva A, Ronicke R, Bartnik D, Brener O, et al. Combining Independent Drug Classes into Superior, Synergistically Acting Hybrid Molecules. Angew Chem Int Edit. 2010;49(46):8743-6. doi: 10.1002/anie.201004437. PubMed PMID: ISI:000284045400042.